NASA Technical Memorandum 81373

PRELIMINARY ANALYSIS OF STS-3 ENTRY FLIGHT DATA

August 1982

NASA

NASA Technical Memorandum 81373

PRELIMINARY ANALYSIS OF STS-3 ENTRY FLIGHT DATA

NASA Ames Research Center
Dryden Flight Research Facility
Edwards, California

National Aeronautics and
Space Administration

1982

SUMMARY

Dryden has completed a preliminary analysis of the data obtained during entry of the STS-3 flight. Three items were of special significance to the data analysis task. First, this flight had planned maneuvers for the sole purpose of improving the Data Base and knowledge of the orbiter's flying qualities. Second, a full set of data were available for the first time. This of course offers a major enhancement of the quality of analysis results. Finally, landing at a remote site enforced our awareness of the benefits derived from real-time telemetry when the orbiter lands at Edwards Air Force Base.

Results of the derivative extraction process are presented for both the lateral-directional and longitudinal axes. Generally, data is shown in comparison to that obtained during flights STS-1, and 2 as well as predictions. Some concerns about the location and calibration of the ACIP package and their potential effect on data analysis is discussed.

An analysis of the landing and roll-out was conducted to look at the flying qualities from the time of the auto to CSS transition through the end of the pitch maneuver during roll-out.

Finally, analysis of surface and structural temperatures is presented and compared to predicted values at selected orbiter cross sections. These measurements are used to support strain gage load measurements during reentry.

NOMENCLATURE

Acronyms

ACIP	aerodynamic coefficient identification package
ADB	aero data book
AGL	above ground level
ASI	aero stick input
C.G.	center of gravity
CSS	control stick steering
DFI	Development Flight Instrumentation
DFRF	Dryden Flight Research Facility
EAFB	Edwards Air Force Base
FS	fuselage station
FPS	feet per second
GPC	general purpose computer
GMT	Greenwich mean time
IMU	inertial measurement unit
JSC	Johnson Space Center
KSC	Kennedy Space Center
MMLE	modified maximum likelihood estimation
OI	operational instrumentation
OV	Orbiter vehicle
PCM	Pulse Code Modulation
PIO	pilot-induced oscillation
PKQ	suppression factor
PSF	pound per square foot
PTI	programmed test input

RCS	reaction control system
RHC	rotational hand controller
SPAR	Structural Performance and Resizing
STS	space transportation system
TC	thermocouple
TPS	Thermal Protection System
WS	Wing Station
VEAS	velocity equivalent airspeed, knots

Symbols

a_n	normal acceleration, g
a_x	longitudinal acceleration, g
a_y	lateral acceleration, g
BF	body flap, deg
b	span, ft
C_ℓ	rolling moment/$\bar{q}Sb$
$C_{\ell_{\delta_a}}$	$= \frac{\partial C_\ell}{\partial \delta_a}$
C_{ℓ_β}	$= \frac{\partial C_\ell}{\partial \beta}$
$C_{l_{\delta_r}}$	$= \frac{\partial C_\ell}{\partial \delta_r}$
C_m	pitching moment/$\bar{q}S\bar{c}$
C_{m_q}	$= \frac{\partial C_m}{\partial q}$
$C_{m_{\delta e}}$	$= \frac{\partial C_m}{\partial \delta_e}$
$C_{m_{BF}}$	$= \frac{\partial C_m}{\partial BF}$
C_{N_α}	$= \frac{\partial C_N}{\partial \alpha}$
C_n	yawing moment/$\bar{q}Sb$
C_{n_β}	$= \frac{\partial C_n}{\partial \beta}$
$C_{n_{\delta a}}$	$= \frac{\partial C_n}{\partial \delta a}$
$C_{n_{\delta r}}$	$= \frac{\partial C_n}{\partial \delta r}$
C_y	yawing moment/$\bar{q}S$

C_{y_β}	$= \frac{\partial C_y}{\partial \beta}$
$C_{y_{\delta_r}}$	$= \frac{\partial C_y}{\partial \delta_r}$
$\bar{c}$	mean aerodynamic chord, ft
com	command
h	altitude
L_{RJ}	rolling moment due to roll jet
L_{YJ}	rolling moment due to yaw jet
M	Mach number
M_{D_J}	pitching moment due to down jet
M_{u_J}	pitching moment due to up jet
N_{RJ}	yawing moment due to roll jet
N_{YJ}	yawing moment due to yaw jet
p	roll velocity, deg/sec
$\dot{p}$	roll acceleration, deg/sec^2
q	pitch velocity, deg/sec
$\bar{q}$	dynamic pressure, psf
r	yaw velocity, deg/sec
$\dot{r}$	yaw acceleration, deg/sec^2
S	wing area, ft^2
SB	speed brake
t_o	plot start time (Greenwich mean time)
V	velocity
x	body axis longitudinal coordinate

Y_{RJ}	yawing force due to roll jet
Y_{YJ}	yawing force due to yaw jets
y	body axis spanwise coordinate
z	body axis vertical coordinate
α	angle of attack, deg
β	angle of sideslip, deg
δ_a	aileron deflection, deg
δ_e	elevator position, deg
$\dot{\delta}_e$	$= \frac{a\delta e}{at}$
δ_r	rudder position
Δ	increment
θ	pitch angle
ϕ	roll angle
γ	flight path angle

Introduction

The STS-3 entry was made on March 30, 1932 to Northrup Strip at White Sands, New Mexico. The primary test objectives were to gather additional stability and control data at the higher Mach numbers and to expand the autoland operational envelope down to 200 feet. A time history of the entire entry is shown in figure 1 and a list of the significant test conditions is shown in table 1. The weight, cg, and inertia characteristics used in the analyses are shown in table 2.

Approach and Landing

The entire approach and landing from about 22,000 feet through rollout is shown in figure 2. The PIO suppressor activity was calculated from the 12.5 sample per second pitch RHC data.

The turn around the heading alignment circle was performed in CSS which is standard practice whenever there is a significant wind in order to reduce the maximum normal acceleration. At about 15000 feet, the nominal trajectory was regained in the CSS mode and a slight pitch oscillation can be seen in the expanded scale time history in figure 3. There was only a slight amount of PIO suppressor activity since the frequency of the oscillation was relatively low (0.2 - 0.3

hertz) and the magnitude of the input was small. The AUTO mode then was engaged and the steep glideslope part of the approach was made in the AUTOLAND mode down to 2500 feet. Speed was maintained at about the desired 285 knot nominal value with a glideslope of about -18 degrees. At 4500 feet, the speedbrake was put into the manual mode and set to the fully closed position. The rest of the system remained in the AUTO mode.

Preflare began at 1800 feet and the speed reached a peak of 304 knots during the 1.4 g preflare. The approach was continued in the AUTO mode to about 150 feet and 280 knots at which time the CSS mode was selected. A more expanded scale time history of the landing is shown in figure 4. The AUTO mode was commanding 1.2 g at the time of disengagement which dropped to 1.0 g when CSS was selected. The pilot made a small nose up correction (about 7 degrees RHC) and then pushed over slightly to regain the desired trajectory. This was followed by about 2 seconds with little pilot activity and then touchdown. Very little PIO suppressor activity was observed during this portion of the landing. Although there was no apparent tendency to PIO, the touchdown conditions were outside desirable limits. A very firm touchdown was made at 225 knots compared to the nominal value of 185 knots.

After touchdown, the speedbrakes were commanded to the fully open position at about 210 knots and reached this commanded value 18 seconds later at a speed of 150 knots. At 190 knots, a 10 degree noseup control input was made in an attempt to hold the nose wheel off and an expanded scale time

history of this maneuver is shown in figure 5. As the nose started up, the pilot removed the nose-up command. However, there was a 1.8 second delay before the positive pitch rate could be arrested because of the rate limiting of the elevator. The nose then came down quite rapidly and the pilot could not keep the nose gear from hitting the ground using full back stick. When the nose gear hit the ground (at 175 knots) the pilot put in a nose down input to keep the nose on the ground. There was significant PIO suppressor activity but it had little effect on the maneuver. The primary purpose of the PIO suppressor is to prevent the tendency for small oscillatory motions to develop into large amplitude motion which can lead to rate limiting and severe PIO. It is not intended to restrict the control authority for a large single input as was made here to arrest the nose-up pitch motion. As a result, even with the PIO suppressor, the pilot had sufficient authority to command more deflection of the elevator than the rate limit would allow. The problem experienced during this maneuver is almost entirely due to an inadequate rate limit to recover from situations that are quite easily attainable with the control authority available.

STS-3 provided a preview of a situation that might be quite likely in the operational setting. The operational situation would be the case in which the pilot must take over due to an autoland malfunction below 200 feet. It is quite likely that this will also be the pilot's first non-simulated

landing as was the case for STS-3 if use of the autoland becomes the normal procedure. It does not appear from the vehicle response data and pilot comments that the shuttle handling qualities are adequate to perform a satisfactory landing in a routine manner under these conditions.

Stability and Control Derivative Extraction Results

The STS-3 flight data includes intentional stability and control maneuvers in addition to the planned bank reversals similar to those on STS-1 and STS-2. The intentional maneuvers included one longitudinal Aero Stick Input (ASI) and five lateral-directional Programmed Test Inputs. The intentional maneuvers resulted in the best stability and control maneuvers for the flight. All of the intentional maneuvers as well as the bank reversals and other miscellaneous maneuvers were analyzed and stability and control derivatives were obtained.

The mathematical formulation of the estimation techniques (MMLE3) used in the following analysis is contained in reference 1. Some of the practical implications of applying the MMLE3 program to flight data are contained in references 2 and 3. The preliminary results for STS-1 and STS-2 are contained in references 4-6.

In general the analysis of STS-3 closely followed that of STS-1 and STS-2 described in references 4-6. The ACIP recorder functioned well on this flight. The functioning of the ACIP recorder improved the value of the estimated stability and control derivatives over STS-2; however the reduced number of PTI's and ASI's provided a disappointingly small amount of information, particularly below Mach 3 where none were performed. The body flap sample rate was increased to 12.5 samples/second on STS-3

(the rate was 1 sample/second on STS-1 and STS-2) which increased the ability to analyze the extremely small longitudinal maneuvers. The ACIP instrumentation package showed significant biases on the angular and linear accelerometers. Some uncertainty still remains in the alignment of the ACIP instruments. A procedure needs to be implemented for keeping the ACIP instruments calibrated and the alignment documented between flights.

Lateral-Directional Analysis

The rotary or rate derivatives were held fixed at the Aero Data Book (ADB) values for the results presented here. It is not believed that fixing the rotary derivatives has a major effect on the results presented.

STS-3 results also showed that reliable information on the sideslip and differential elevon (aileron) derivatives could not be obtained below a dynamic pressure of 10 psf which also had been indicated on previous flights. The sideslip and aileron derivatives for maneuvers performed below a dynamic pressure of 10 psf are fixed at the flight determined value that occured near a dynamic pressure of 10 psf.

In general changes in the effect of the yaw jets below a Mach number of 3 was found to be weak. Thus for most of the analysis of maneuvers in this region the yaw jets were fixed at the ADB values as they were on STS-2. The overall analysis of the data will be enhanced by a good air data system as previously discussed in reference 6.

Figure 6 shows the primary variables effecting the stability and control derivative as a function of the on-board IMU Mach number or V/1000. It is readily seen that the primary differences among the first three flights are the body flap and elevon position above M=10. The body flap and elevon positions differ by about 3° to 4° over a significant portion of the flight.

Lateral-Directional Derivative Results

The lateral-directional derivative estimates are plotted in figures 7 through 10. The derivatives are plotted versus IMU V/1000 or M in figures 7, 8, and 9 and versus GPC dynamic pressure, $\bar{q}$, in figure 10. The symbol is the derivative estimate and the vertical bar is the uncertainty bound (ref. 2 and 3). The poorer the estimate, the larger the uncertainty bound. The dashed line is a fairing of the flight-determined derivative estimates; it is shown as a dotted line where less certainty in the fairing is indicated. The solid line is the ADB value for the derivatives at the same flight conditions as the flight maneuver. The solid ticked lines are the ± 1 variation applied to the ADB values. All data are referenced to 65% of the body length in figures 8, 9, and 10. The squares are for STS-1, the circles for STS-2 and the triangles for STS-3.

The lateral-directional stability and control derivatives are plotted as a function of M for all cases where $\bar{q}$ from GPC is greater than 10 psf in figures 7, 8, and 9. The RCS jet derivatives are plotted against $\bar{q}$ in figure 10. For $\bar{q}$ between 0 and 20 psf, the jet derivatives are plotted versus $\bar{q}$ as the effect is due more to $\bar{q}$ than Mach number at low $\bar{q}$.

Figure 7 shows the lateral directional stability and control derivatives plotted versus M and compared to the ADB derivatives based on STS-3 flight conditions. In general the flight derivatives are showing the same trends with the ADB values as has been indicated in the analysis of STS-1 (ref. 5) and STS-2 (ref. 6). C_{l_β} in figure 7a appears to be double valued at the higher Mach numbers. The estimates from the PTI maneuvers are represented by the shaded symbols. The PTI maneuvers in general contain greater excusions in α and β. The lower values in C_{l_β} are for the most part estimates from the PTI maneuvers, therefore the lower values may be due to the nature of these larger maneuvers. Figure 7 can be used to discern differences between STS-3 flight conditions and STS-1 and STS-2 flight conditions for both predictions (ADB) and flight estimates.

Figure 8 shows all of the estimates from STS-1, 2, and 3 plotted with ADB values and variations of STS-2, because most high quality maneuvers were obtained on STS-2. Above a Mach number of 3 most of the estimates agreed fairly well with those obtained from the first two flights. Figure 8 shows that the fairings are almost the same as those given for STS-1 and STS-2

(ref. 6). For instance, small changes in fairings can be seen for $C_{l_{\delta_a}}$ near a Mach number of 11, for $C_{n_{\delta_a}}$ between Mach numbers of 16 and 21 and for C_{n_β} between Mach numbers of 13 and 17. In addition to these changes in fairings a possible effect of flight condition can be seen at the higher Mach numbers for C_{l_β}, $C_{l_{\delta_a}}$ and $C_{n_{\delta_a}}$. An additional labeled fairing is shown on these three figures. It is not possible to state unequivocally that these effects are due to a change in flight condition until repeat points on future flights are obtained. The primary flight condition changes in this region (figure 5) are in the elevon and body flap positions. They differ by about 1.5° to 2° in this region between STS-2 and STS-3. It should be noted that STS-1 also had a difference of about 1° to 2° more but the fairing shown in reference 6 is based primarily on STS-2. The difference between STS-2 and STS-3 is about - .0003 for C_{l_β}, about +.0003 for $C_{l_{\delta_a}}$, and about -.0003 for $C_{n_{\delta_a}}$. That is, all three derivatives are more effective for the flight conditions flown on STS-3. Referring back to figure 7 and comparing the ADB values for STS-3 with those for STS-2 shown on figure 9, shows an expected change in the same direction although somewhat smaller for $C_{l_{\delta_a}}$ and $C_{n_{\delta_a}}$ and predicts no change at all for C_{l_β}. Although as pointed out earlier the value for C_{l_β} showed these lower values primarily for the PTI maneuvers.

Figure 9 shows the same data as figure 7 for Mach numbers below 4.0. This way some of the changes in the transonic region can be seen more easily. It appears that C_{l_β}, C_{n_β},

$C_{n_{\delta a}}$, $C_{l_{\delta r}}$ and $C_{n_{\delta r}}$ stay within variations in this region, however some of the derivatives get quite close. $C_{l_{\delta r}}$ and $C_{Y_{\delta r}}$ for small deflections and C_{l_β} lie outside the variations. The reason for $C_{l_{\delta r}}$ and $C_{Y_{\delta r}}$ being so effective for small deflections is not well understood. It can also be misleading to say that the derivative is large for small deflections as its overall effect on the total force or moment may not be very large. For this particular nonlinearity it appears that large deflections greater than a degree or two result in fairly well behaved forces and moments and close to the ADB. Since this nonlinearity occurs between M=1.5-1.8 the effects could be largely due to shock placement and their interaction. This is also the region of the quarter hertz wing rock. If these data represent the correct interpretation, the rudder gain may be too high for the small amplitude motions which is a possible explanation of the wing rock.

Figure 10 shows the derivatives against dynamic pressure, $\bar{q}$, for $\bar{q}$ between 0 and 20 psf. The flight data show essentially the same trends as discussed in reference 6. It should be noted that $C_{l_{\delta a}}$ shows a difference for the one $C_{l_{\delta a}}$ flight point shown of increasing effectiveness.

The analysis of the effects of RCS jets shown in the report differs from the way the effect is portrayed in the ADB. The ADB models the yaw jets as the calculated forces and moments that are known plus an interference term that is independent of the number of jets fired. The analysis here assumes that the interference effect is a linear function of the number of jets firing. Although the two models differ in

this way, there is no good way to assure which model is correct as predominantly a fixed number of jets fire during a given maneuver. Therefore the results of one model can be uniquely put in the form of the other model. To date two maneuvers, one on STS-2 and one on STS-3, have been found where a significant number of two and of four jet firings were found within the same maneuver. A study was conducted to see which model worked best. The results of the study was inconclusive as one maneuver slightly favored the model used here and the other model slightly favored the ADB model. Unfortunately these two maneuvers were at greatly different Mach numbers. It would be highly desirable to obtain several maneuvers at a given flight condition that exhibit 2 and 4 jets firing. An easy way to obtain this data would be to initiate a PTI just prior to $\bar{q}$ of 20 psf. The control system would use only two jets below 20 psf and would fire four if needed above 20 psf. By doing a PTI at this condition on subsequent flights the issue can be resolved as to which model is most representative of the flight vehicle. It also would be useful to have repeated maneuvers at other flight conditions as well. For our future analysis Dryden's primary approach to modeling yaw RCS jets will be to use forces and moments proportional to the number of jets for the following reasons; 1) it is consistent with our previous analysis, 2) it is the most consistent with the rawest possible form that the MMLE program can provide and therefore least subject to analyst errors, and 3) the ADB interference model for pitch and roll RCS jets is

dependent on the number of jets firing. The dimensional form of the forces and moments will continue to be used for the reasons discussed in reference 6.

ACIP Package

The ACIP Package consists of two distinct items. The first item is the ACIP instrumentation package and the second item is the ACIP PCM system and associated recorder which hereafter will be referred to as the ACIP recorder. The ACIP instrumentation package consists of rate gyro assembly, a linear accelerometer assembly, and an angular accelerometer assembly and their associated power supplies and signal conditioning boxes. The ACIP recorder records these nine primary signals and various housekeeping parameters from the ACIP instrumentation package. In addition the ACIP recorder currently records high sample rate, high resolution control surface positions and one of the yaw RCS jets. In the future through various ACIP enhancements the recorder will also record many more parameters such as all RCS jets and various IMU signals. There is no doubt that the ACIP recorder is vital to all future parameter estimates on the shuttle to assist in flight envelope expansion and in placard modification or removal. However the ACIP instrumentation package itself in its current environment is not putting out quality measurements. It is not that the ACIP instrumentation package is in itself of poor quality but it is that the quality of the

data reaching the user is not sufficient. There are two major reasons that the data quality is poor.

The first reason is procedural. Any instrument package needs to be properly alligned and calibrated to generate useful information. Misalignment for instance can cause significant errors in $C_{n_{\delta_a}}$ which is a very important derivative in any control system specification. A poor calibration can result in unrepresentative characteristics of the measurements in engineering units. These measurements will result in errors across the board in all of the estimated derivatives. According to Dryden's information the last calibration of the ACIP instrumentation package is nearly two years old. Even on low cost programs of much less importance than the shuttle, periodic checks are made on calibrations of the instrumentation package to assure that high quality data results from its use. The ACIP instrumentation package is perhaps the best instrumentation package of its kind in a flight environment and it seems inconsistent to allow poor procedures on alignment checks and calibrations to render its output questionable. Therefore a procedure needs to be established to provide for periodic alignment and calibration checks of the instrument package.

The second problem in the ACIP instrumentation package involves its location in the vehicle. The package is in a location such that it measures a great amount of structural noise in the 5 to 15 hertz range. In many applications this range of noise would cause no particular problem. In these

cases the noisy signal could be merely low passed or at least notched if it interferred with the data analysis. On the shuttle, however, the measurements can not be low passed or notched as the contaminating structural noise is in the same frequency range as the RCS jets. It would appear that there are two possible solutions to this problem; 1) move the instrumentation package to an area of significantly less structural noise or 2) move the package to an area where the structural noise is of a higher frequency. The first solution seems unlikely as the entire vehicle contains a significant amount of structural vibration. The second solution would seem to be the only remaining choice. In order to put it in a region of higher frequency structural noise a location must be found that is stiffer. The forward portion of the vehicle is stiffer and has smaller dimensions so intuition would say to move the instrument further forward. Perhaps somewhere near the control system accelerometer assembly at the pilot station. These instruments do not appear to have the high amplitude high frequency noise found at the ACIP instrumentation package location. Analysis has been done using the flight control instrumentation in place of the ACIP instrumentation and sometimes the flight control instrumentation analysis has led to superior results.

It is unlikely that the ACIP package could be moved in the current vehicle, but it might be possible to relocate it in subsequent vehicles or perhaps when the current vehicle is down for refurbishment. There is no desire to eliminate the ACIP

instrumentation package completely as it contains the only high resolution, high sample rate data for aerodynamic analysis.

Figure 11 shows an example of the effect of the noise contamination of the ACIP instrumentation package. This maneuver is a planned PTI at Mach 8.2 from STS-3. The problem increases significantly when trying to analyze the more common maneuver with slower responses such as bank or bank reversal maneuvers. The solid line is the actual measured response from the ACIP instrumentation package. The dashed line is the computed response from MMLE-3 on which the estimated stability and control derivatives are based. The MMLE-3 program must get most of its information from the rate gyro signal to obtain the required information on the derivatives. The dashed line through $\dot{p}$, $\dot{r}$, and A_Y seems representative, but moving the fairing 10% will result in an error of 10% in the derivatives. A 10% change would not significantly change the appropriateness of the fairing but would result in meaningless estimates of the derivatives. The way to improve the signals would be to improve the signal to noise ratio. The only way this can be done in this frequency range is to lower the structural noise component.

It is therefore recommended that new locations be investigated for installation of the ACIP instrumentation package that would result in higher frequency noise contamination and also allow easier access for recalibration in between flights.

Summary of Lateral-Directional Derivatives

The derivatives obtained from flight STS-3 agreed fairly well with the derivatives found on previous flights. Slightly different fairings resulted in some of the derivatives where data had been obtained for the first time. This was particularly true for C_{n_β}, $C_{l_{\delta_a}}$ and $C_{n_{\delta_a}}$. Significant changes may also be present in $C_{l_{\delta_a}}$, and $C_{n_{\delta_a}}$ due to the effect of the elevon and/or the body flap at Mach numbers above 10. $C_{l_{\delta_r}}$ and $C_{Y_{\delta_r}}$ may be highly nonlinear for Mach numbers between 1.4 and 1.8. This may be contributing to the quarter hertz oscillation in this region due to too high a rudder gain for low amplitude motions. The ACIP recorder package is vital to future estimation, but the ACIP instrumentation package needs to be periodically calibrated and aligned. In addition, the ACIP recorder should be moved to a diferent vibration environment to provide higher quality data.

Longitudinal Stability and Control Derivatives

All of the longitudinal estimates have significant scatter caused by the use of small incidental maneuvers. In most cases, there is sufficient information to establish a reasonable fairing.

The estimates of normal force and pitching moment due to angle of attack for Mach 1 to 24 are shown in figure 12. The scatter in the C_{N_α} estimates is quite large because the small

longitudinal maneuvers available do not result in sufficient normal force to allow good estimates. The normal force changes due to changing dynamic pressure during a maneuver tend to be large enough to mask the effects of the very small changes in the normal force coefficient. Although the estimates are lower than the predictions in the Mach 2 to 12 area, we would tend to discount these estimates in favor of the predictions because of the small maneuver sizes. The other normal force derivatives exhibit similar or worse scatter and are not presented in this paper. Intentional longitudinal maneuvers will be required to obtain useful normal force derivatives. Cm_{α} agrees reasonably with predictions above Mach 18. Between Mach 4 and 10, the Cm_{α} estimates are less negative then predicted, lying barely within the variations. A fairing is difficult to confidently establish between Mach 10 and 18 and below Mach 4.

Figure 13 shows the estimates of pitching moment due to elevon and body flap from Mach 1 to 24. The estimates from Mach 0 to 4 are plotted on a more expanded scale in figure 14. The $C_{m_{\delta_e}}$ estimates agree well with predictions. For both $C_{m_{\delta_e}}$ and $C_{m_{BF}}$, the estimates from flights 1 and 2 were smaller than predicted between Mach 2 and 4, but the flight 3 estimates are closer to the predicted line. It is likely that the low sample rate for the body flap in the first two flights caused biases in the body flap derivative estimates, and thus indirectly in the elevon derivative estimates. Figure 15 shows the fit of a typical small body flap maneuver from flight 3, where the higher sample rate body flap is available. The fit

in figure 15 is much improved over that in figure 16, which is a maneuver from flight 1 with the low sample rate body flap. It is reasonable to suppose that the estimates from the maneuver of figure 16 are biased. The body flap derivative estimates are smaller than the predictions in the Mach 6 to 12 area.

A few of the maneuvers with large elevon deflections showed strong evidence of nonlinearity in the pitching moment due to elevon. For instance, the fit shown in figure 17 was obtained by allowing a δe^2 derivative in addition to the linear δe derivative used in the analysis. If the same maneuver is analyzed without the δe^2 term, the fit shown in figure 18 is obtained. The fit of pitch rate in figure 17 is improved over that of figure 18 to convince us that the term added for figure 17 is significant.

The pitching moment due to the up and down jets is plotted in figure 19 as a function of dynamic pressure. The units on this plot are foot-pounds of moment per jet. There are three factors contributing to the pitching moment produced by the jets. First is the moment directly produced by the thrust of the jet. This part can be quite accurately predicted. Second is the moment resulting from impingement of the jet plume on the vehicle. There should be no impingement of the up jet plumes, but the impingement effects of the down jets were predicted to be significant. Third is the moment caused by the interference of the jet plume with the air flow around the vehicle. This is the least well understood factor. The

pitching moment from the up jets agrees well with predictions. Since the up jet moment is almost entirely due to the well understood jet thrust term, this good agreement should be expected. Probably the largest contributor to disagreements in the up jet derivatives is the uncertainty in the vehicle moment of inertia, which directly affects the flight estimates. The down jet derivatives agree well with the predictions at 0 dynamic pressure, but show no sign of the predicted large decrease in moment between 0 and 4 psf. The agreement at 0 dynamic pressure indicates that the predictions of the jet thrust term and the impingement term are probably accurate (the impingement term is significant for the down jets; without it the moment would be close to the up jet value of 30,000 foot pounds per jet). There is no flow interference contribution at 0 dynamic pressure. The disagreement between the predictions and flight estimates as dynamic pressure increases indicates that the flow interference contribution is much smaller than predicted.

Structural Temperatures

Background

This section concerns the continuation of work at DFRF Structures' Section in performing surface heating and heat transfer analyses of selected orbiter cross sections to support strain gage load measurement during reentry. The work presents the comparisons of measured and predicted OV 102 structural and TPS surface temperatures for STS-3 flight. The selected cross sections for thermal analyses are WS 134, WS 240, and WS 328.

Trajectory

Figure 20 shows the comparison of the nominal and the measured STS-3 flight trajectory time-histories. The altitude and velocity data lie slightly below the corresponding nominal curves. The angle-of-attack data follow the nominal angle-of-attack curve very nicely during the latter part of flight (i.e., after 1200 sec). The overall TPS surface heating measurements for STS-3 flight are about the same level as that for STS-2 flight. In the thermal analysis, the surface heating was re-calculated based on the measured STS-3 trajectory instead of the nominal trajectory which was used for both the STS-1 and STS-2 thermal analyses.

WS 134 TPS Surface Temperatures

The TPS surface measurement locations (or TC locations) for WS 134 are shown in figure 21. The comparisons of the predicted and the measured TPS surface temperatures are shown in figures 22-30. It is seen that the flight measured data agree quite well with the predicted values. In generating the STS-3 heat input for the lower TPS surface, transitional flow was introduced at time 1200 sec.

WS 134 Structural Temperatures

The structural temperature measurement locations for WS 134 are shown in figure 31, and the predicted and measured structural temperatures are shown in figures 32-39. Some of the flight data between 30 sec. and 80 sec. are either missing (figures 32, 38) or questionable (figure 34). The correlations between the predicted and the measured values are fairly good except for a few locations V09T9205 (figure 32), V09T9126 (figure 34). V09T9160 (figure 36), V09T9159 (figure 39). Excellent agreement occurs at V09T9157 (figure 37).

WS 240 TPS Surface Temperatures

Figure 40 shows a SPAR thermal model for WS 240, and figure 41 shows the temperature measurement locations for WS 240 and WS 254. In figures 42-54, the flight measured data are compared with the predicted surface

temperatures. For WS 240 no transitional flow was introduced in generating lower TPS surface heating. The predicted peak temperatures for the lower TPS surface are slightly higher than the measured data. For V07T9868 (figure 43), V07T9670 (figure 45), V07T9671 (figure 46), V07T9673 (figure 47), V07T9674 (figure 49), the measured data for the initial and final periods of flight were not recovered. Also, questionable data were obtained for V07T9171 (figure 44) and V07T9181 (figure 48) between 100 sec. and 500 sec. For the upper TPS surface, except for V07T9622 (figure 50) and V07T9623 (figure 51), the measured data lie considerably below the predicted curves. Like STS-2, the STS-3 flight data also show flow transition for the lower TPS surface in the vicinity of 1200 seconds.

WS 240 Structural Temperatures

The predicted and the flight measured structural temperatures for WS 240 are shown in figures 54-65. For V09T9147 (figure 56) and V09T9128 (figure 58), only limited data during small time intervals were recovered through telemetering. For V09T9152 (figure 60) and V09T9126 (figure 63) the flight data during the early stage of reentry were not recovered. Also, some questionable flight data were obtained for V09T9159 (figure 61), V09T9112 (figure 64), and V09T9153 (figure 65) during the initial stage of reentry. The data for V09T9116 (figure 62) have shifted considerably upward and are therefore, questionable. For the lower skin (figures 54 and 55) the predicted temperatures (based on the new heat input) are much higher than the measured data. The predicted and measured upper structural temperatures agree reasonably well except for V09T9153 (figure 65).

WS 328 TPS Surface Temperatures

The SPAR thermal model and the temperature measurement locations for WS 328 are shown in figures 66 and 67 respectively. The predicted and the flight measured TPS surface temperatures for WS 328 are compared in figures 68-77. Temperature readings from V07T9700 (figure 68) and V07T9705 (figure 69) gave M-shaped profiles which were not observed in STS-2 flight. Since the structural temperature readings at V09T9142 (figure 78) for both STS-2 and STS-3 are practically the same, it is believed that the above two thermocouples gave false readings during 400 sec. and 1000 sec. For V07T9710 (figure 72) and V07T9711 (figure 74) only the data beginning near the end of the flight were recovered. Overall the prediction is fairly good except for V07T9704 (fig. 73) where the analysis overestimated lower TPS surface temperatures.

WS 328 Structural Temperatures

Figures 78-80 show comparisons of the predicted and the flight measured structural temperatures for WS 328. As shown in figures 78 and 79, the predicted lower skin temperatures are somewhat higher than the measured values except for the early stage of reentry. For the upper skin (figure 80), the predicted and the measured temperatures are fairly close.

Current Status

From the STS-3 flight data and the thermal analyses, it is concluded that:

a) Conclusions drawn for STS-2 flight are reinforced by the STS-3 flight data.

b) The measured wing TPS surface and structural temperatures for STS-3 are quite similar to those of STS-2, indicating that the temperature measurements are definitely repeatable and consistent with the flight trajectories.

c) The revised heat input improved the TPS surface and structural temperature predictions for WS 134. The new heat input computed for STS-3 resulted in a slight overprediciton of the measured TPS surface temperatures at WS 240, whereas, the old heating input, used at WS 240 for STS-2, slightly underpredicted the measured TPS surface temperatures. For WS 328, the prediction for the lower TPS surface temperature is reasonably good except for some bad TC readings.

d) The new heat input overestimates the lower structural temperatures for WS 240 and WS 328 during the latter part of the flight and beyond touchdown. For the upper structural temperatures of WS 240 and WS 328, the predictions agree fairly well with the flight data.

Based on the above observations, the heat transfer models for WS 240 and WS 328 are being revised for STS-4 analysis.

TABLE 1 - STS-3 ENTRY MANEUVERS

Event	GMT (Day 89) (HH:MM:SS)	Velocity (FPS)	Altitude (Feet AGL)	Maneuver Trim Conditions				
				Dynamic Pressure (PSF)	Angle of Attack (Deg)	Elevon (Deg)	Body Flap (Deg)	Speed Brake (Deg)
First Turn	15:40:05	24340	249750	15.2	40.3	4.1	9.2	0
$\bar{q}$=22 Roll PTI-1	15:41:56	23560	239800	22.4	40.1	3.4	10.8	0
M=21 Roll PTI-1	15:45:36	21375	227400	35.5	39.9	3.3	10.8	0
M=21 Pitch ASI	15:45:47	21225	226100	37.5	39.7	3.5	10.8	0
M=18 Roll PTI-1	15:48:24	18740	208400	58.4	39.3	3.2	10.8	0
First Bank Reversal	15:49:08	17800	201250	68.4	39.4	3.0	10.8	0
M=14 Roll PTI-1	15:52:05	12600	173600	94.6	39.6	2.8	5.8	0
Second Bank Reversal	15:53:45	9400	152500	113.8	33.9	3.0	7.1	50.0
M=8.4 Yaw PTI-2	15:54:21	8350	148000	114.5	33.0	3.0	6.8	87.2
Third Bank Reversal	15:56:57	4700	108000	200.0	21.0	4.4	6.8	87.2
Fourth Bank Reversal	15:58:51	2600	83000	212.3	15.0	1.2	2.6	58.0

Table 2

STS-3

WEIGHT, CG, INERTIAS

(Reference: 8 Mar 82 SAS/AERO/82-132)

Weight	209980	Lbs.
IX	933376	Slug-Ft.^{2}
IY	6900754	Slug-Ft.^{2}
IZ	7216749	Slug-Ft.^{2}
IXZ	148133	Slug-Ft.^{2}
IXY	6389	Slug-Ft.^{2}
IYZ	2260	Slug-Ft.^{2}

XCG = 1096.2 ZCG = 372.9 YCG = -.1 inches

These were used as constants for the entire entry.

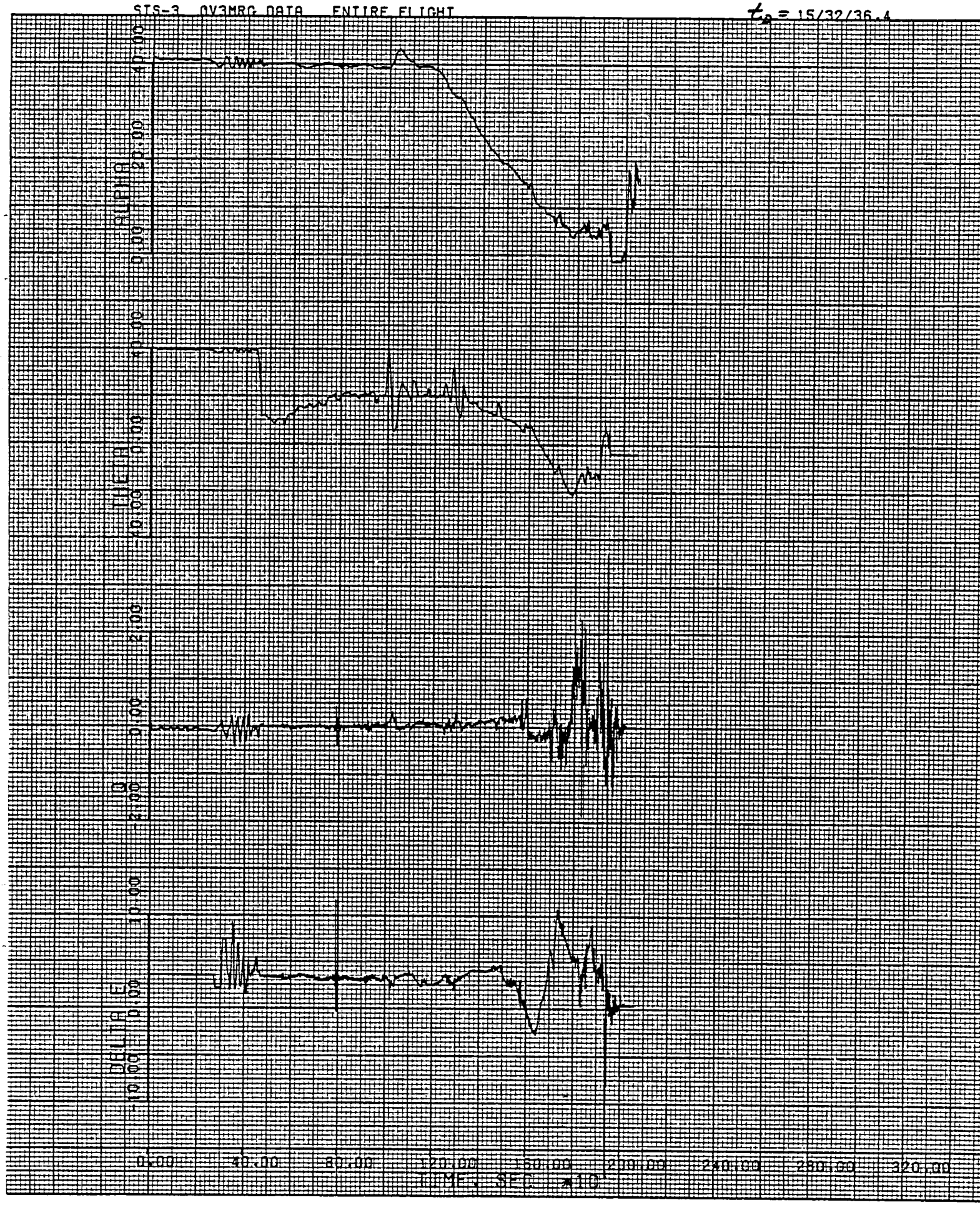

Figure 1a Entry Time History - h=450,000 Feet To Landing

Figure 1b (Continued)

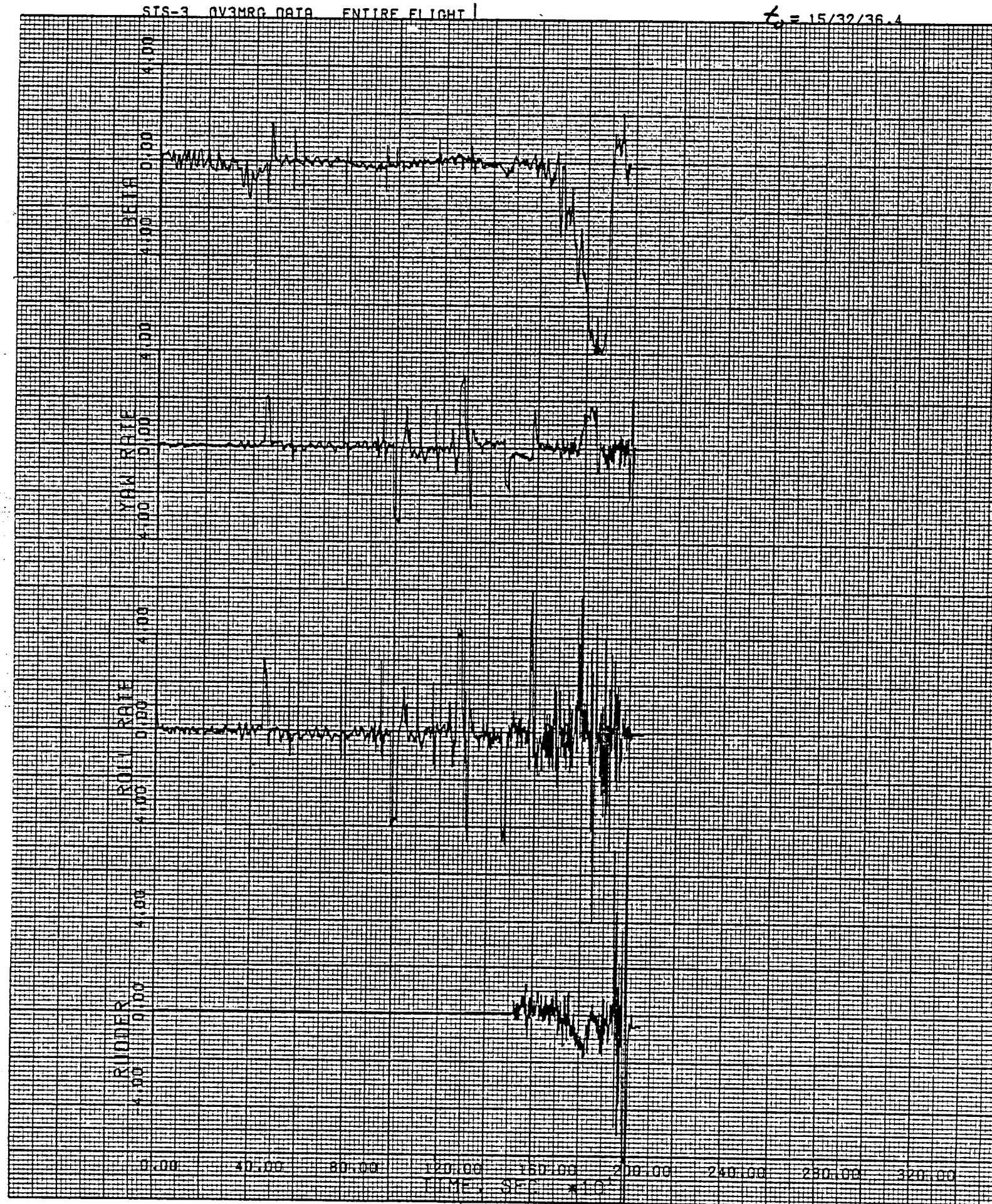

Figure 1c (Continued)

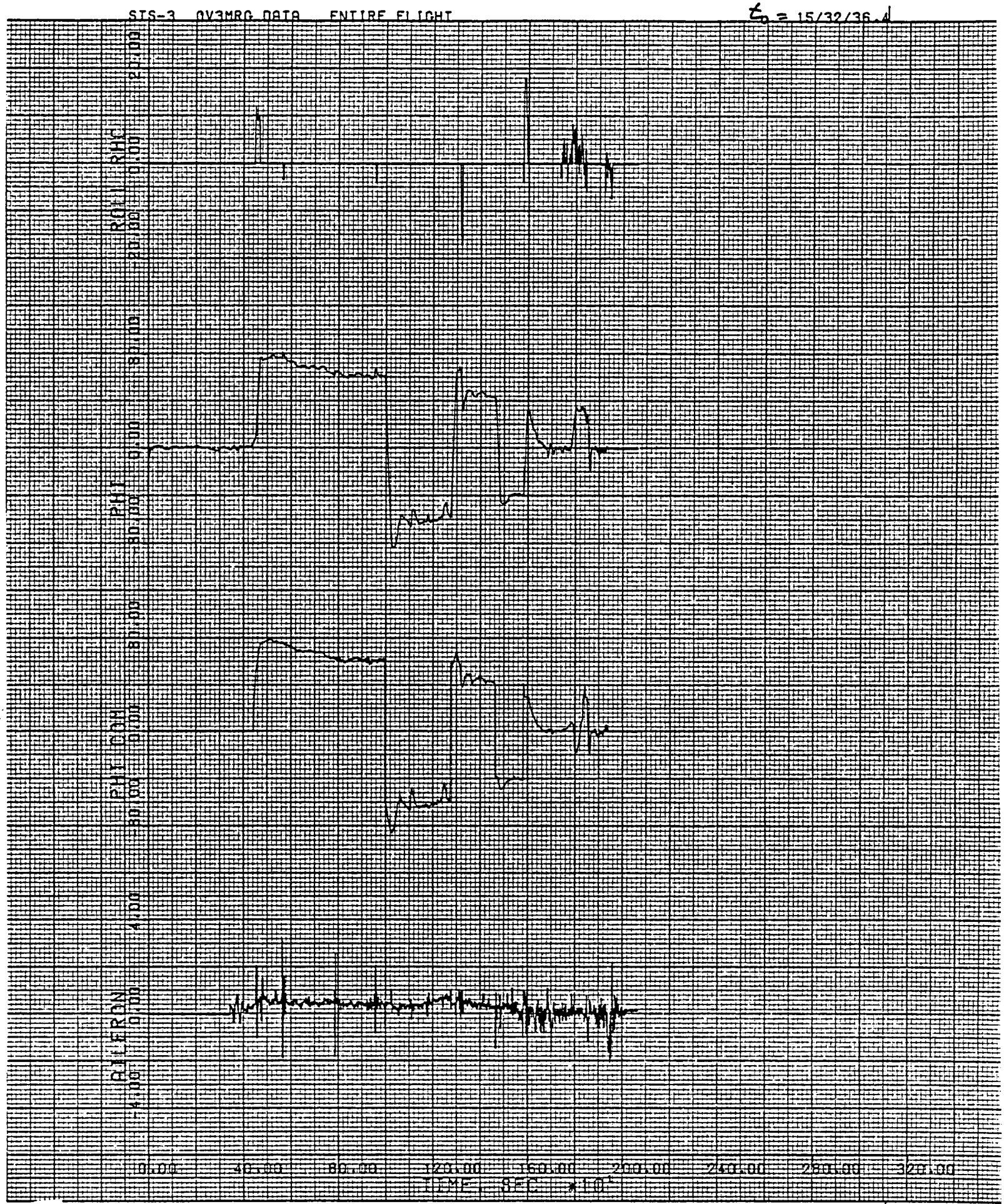

Figure 1d (Continued)

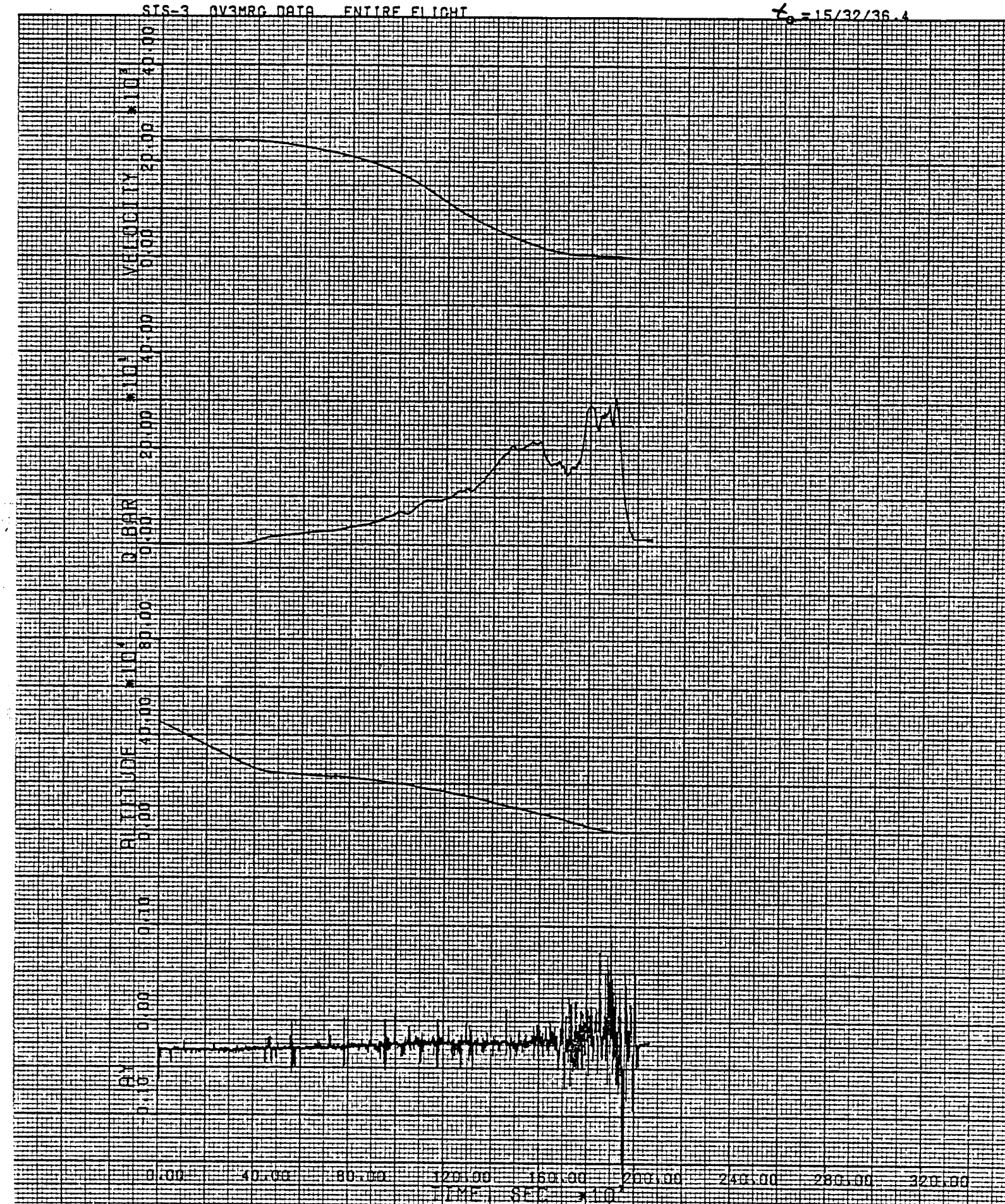

Figure 1e (Continued)

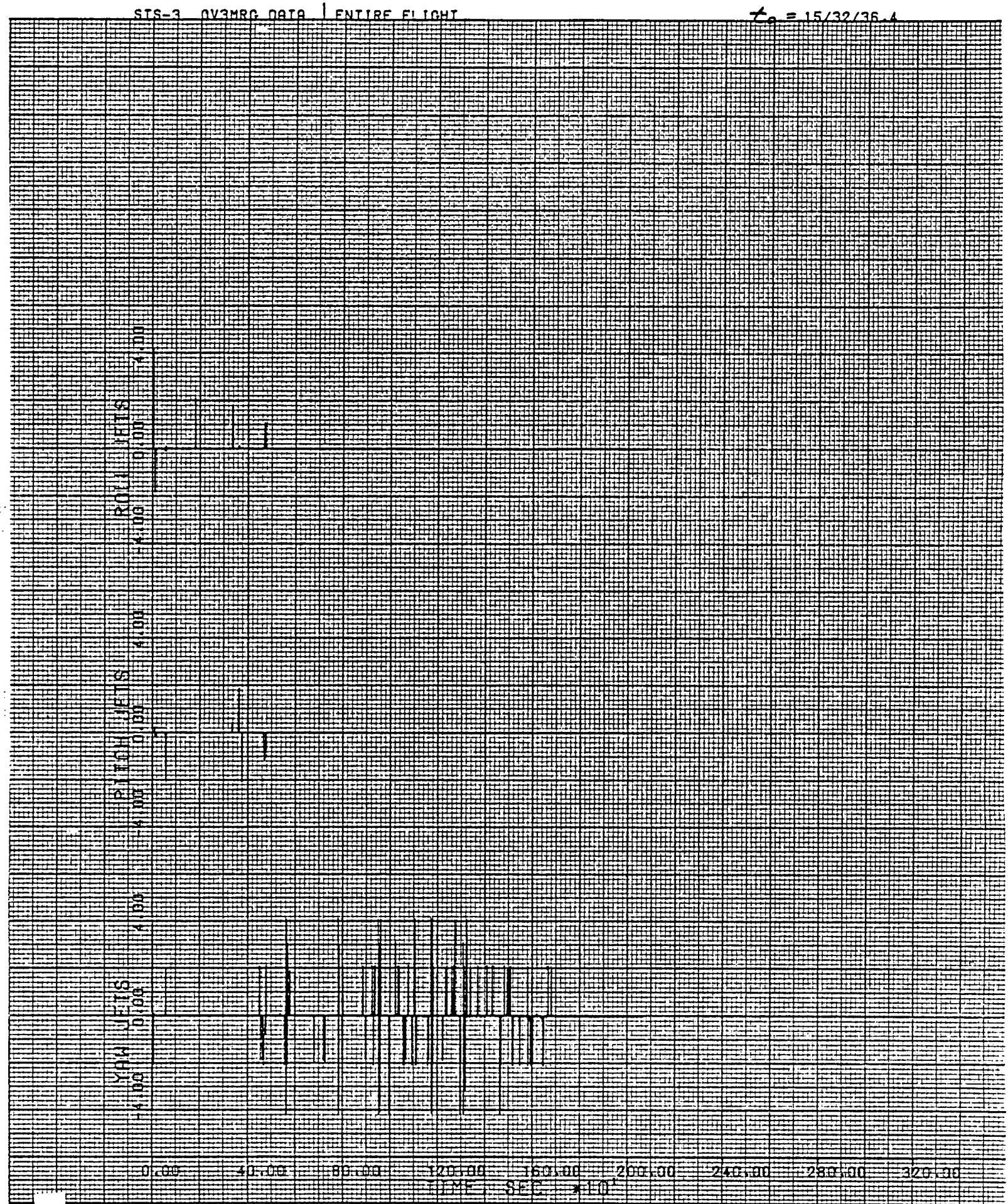

Figure 1f (Concluded)

Figure 2a Approach and Landing - h=22,000 Feet to Landing

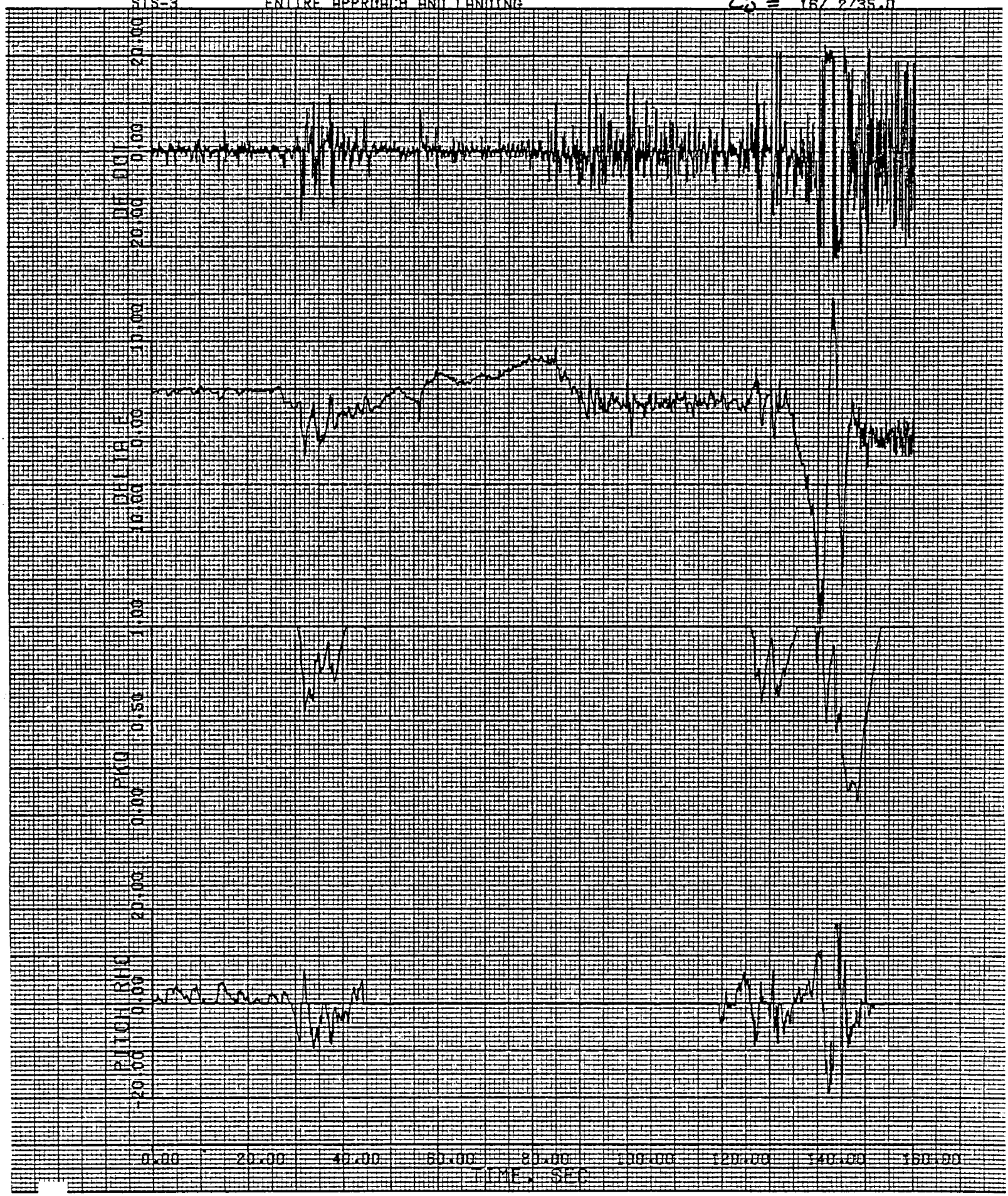

Figure 2b (Continued)

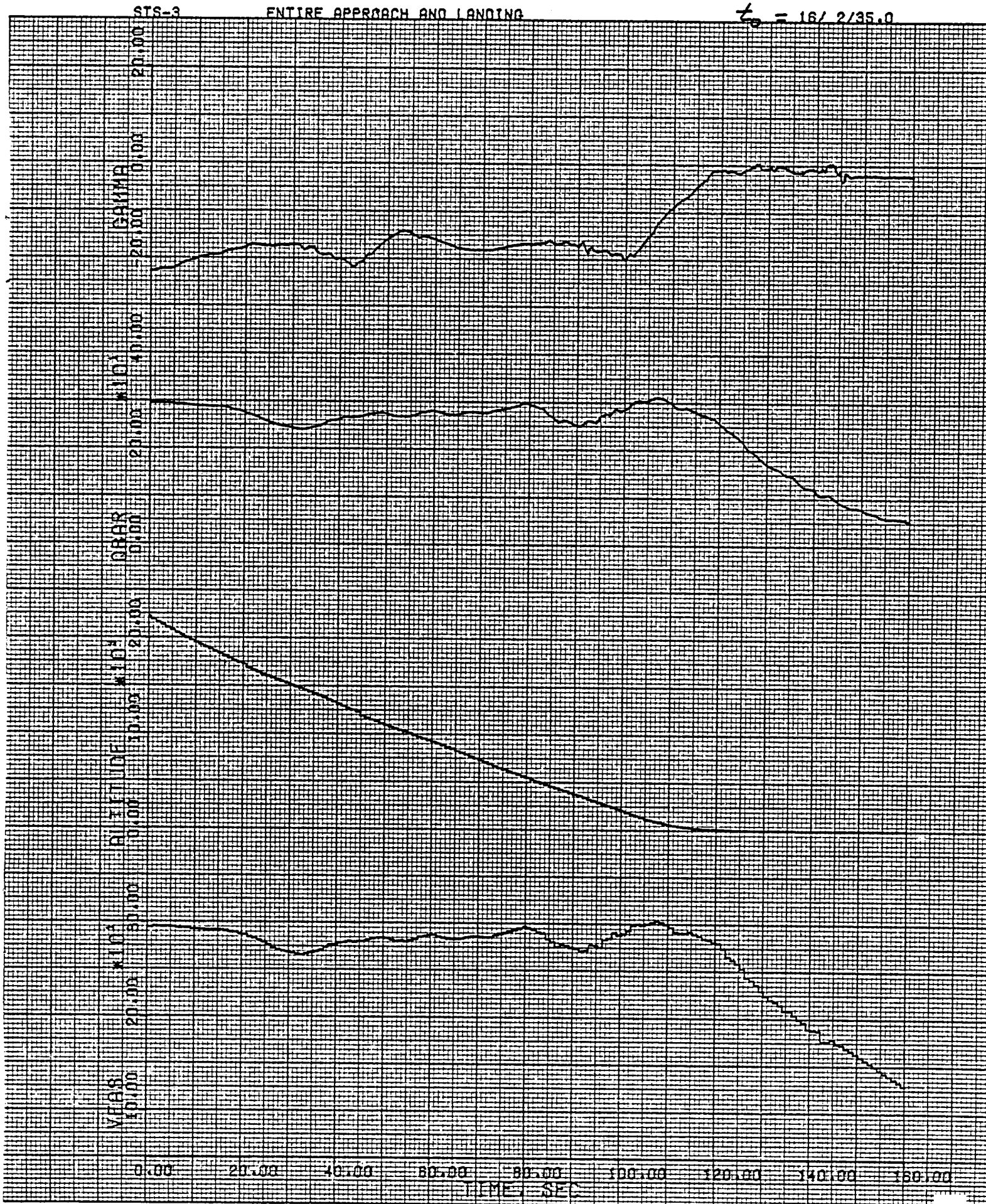

Figure 2c (Continued)

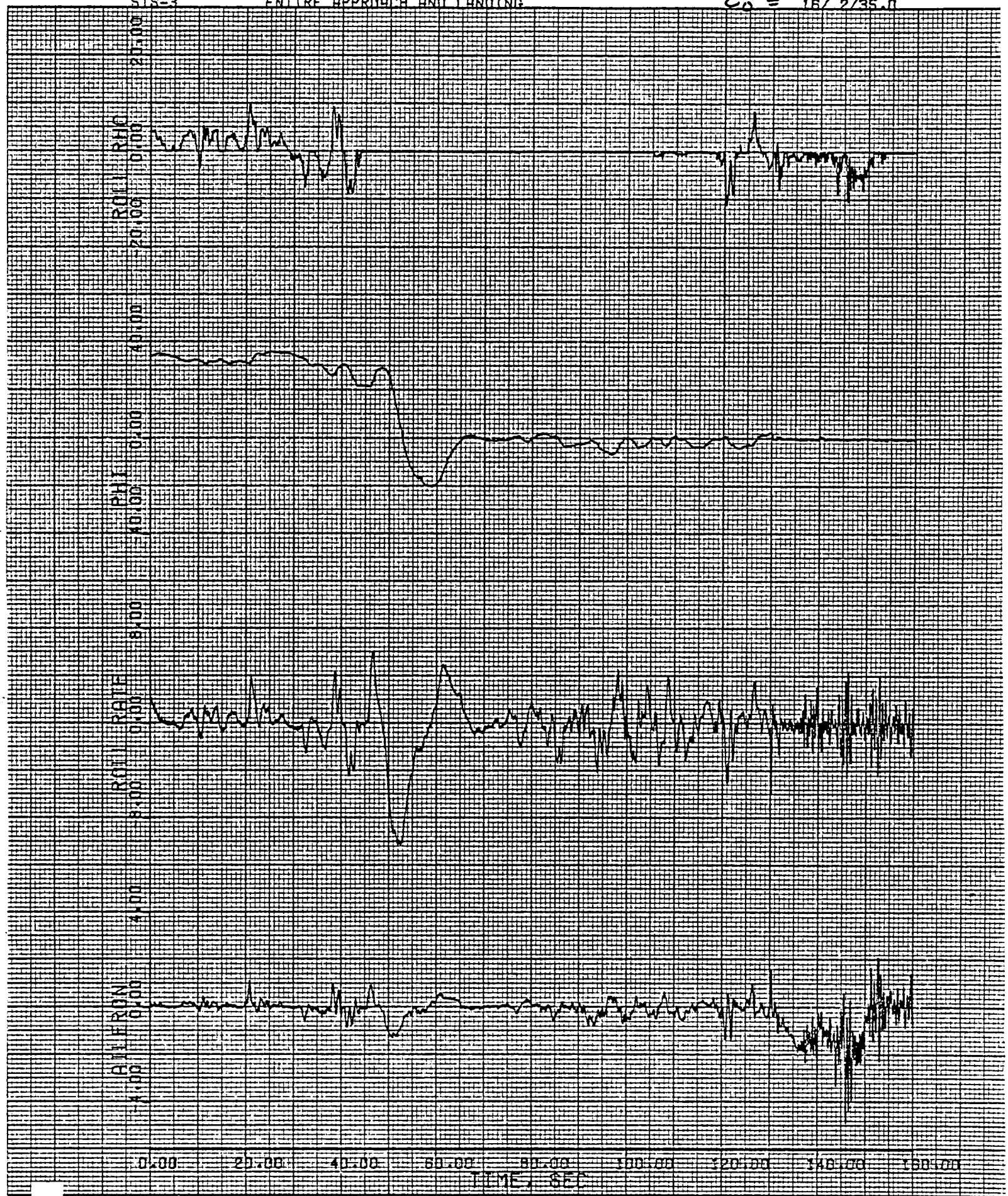

Figure 2d (Continued)

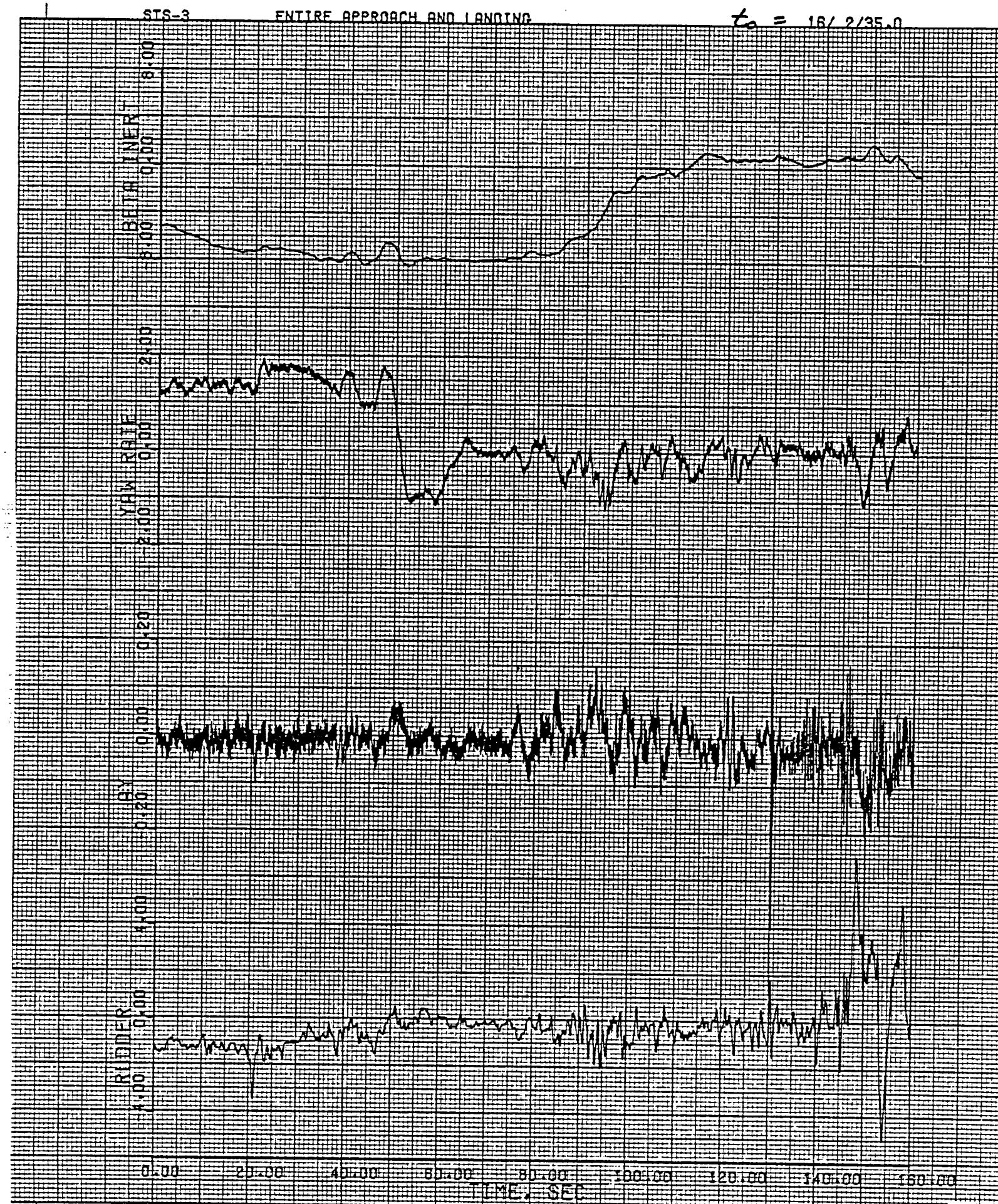

Figure 2e (Continued)

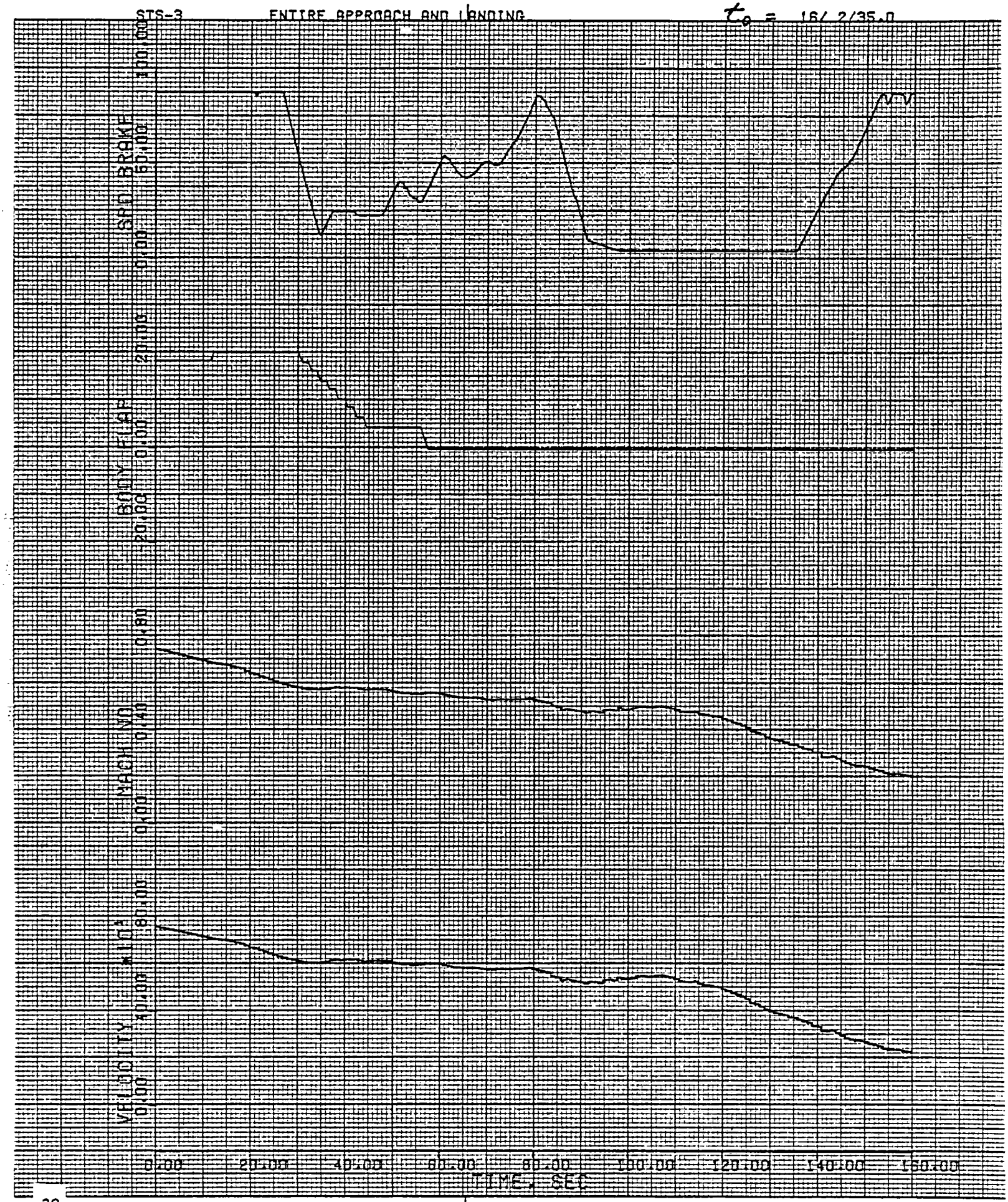

Figure 2f (Concluded)

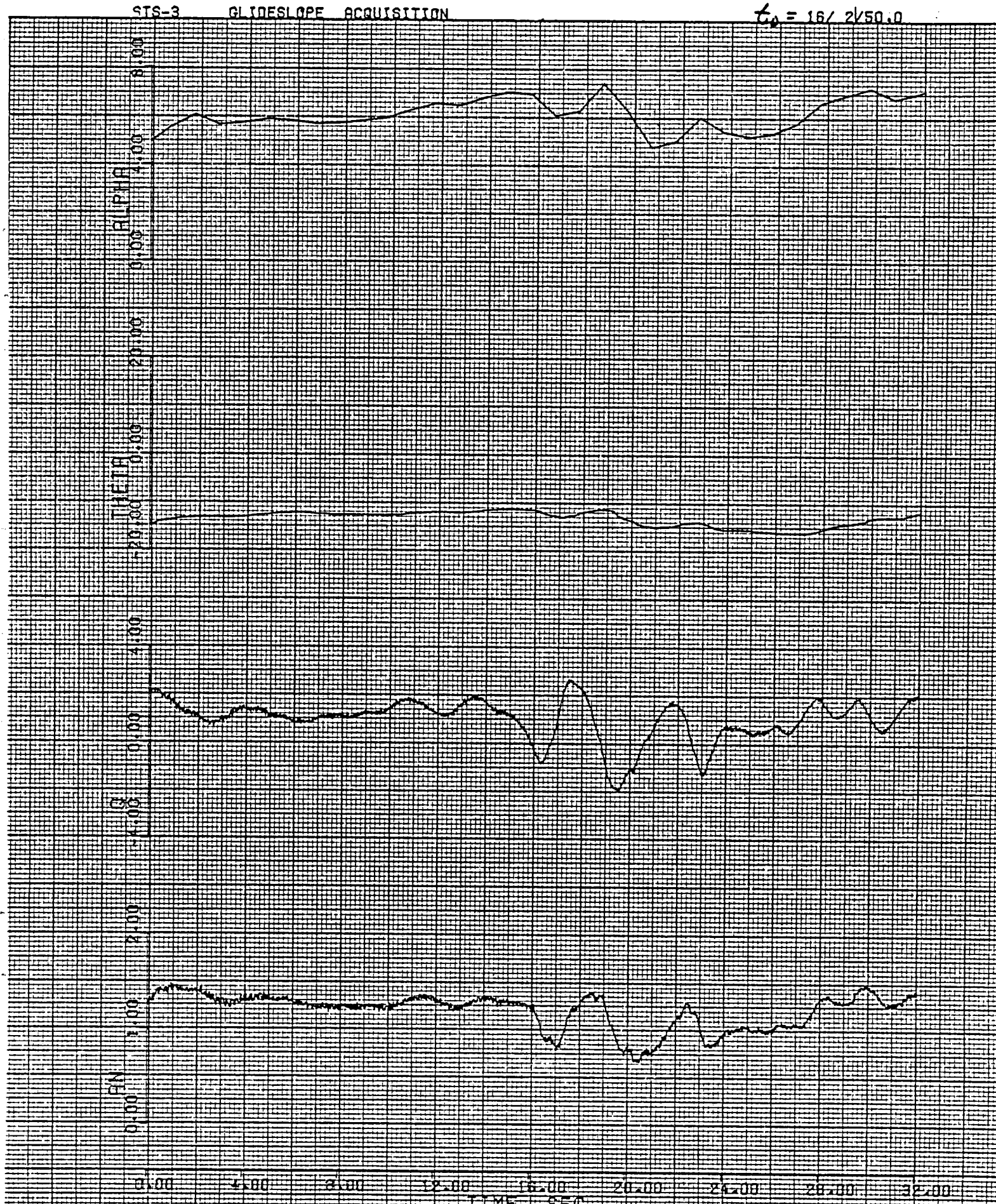

Figure 3a Glideslope Acquisition

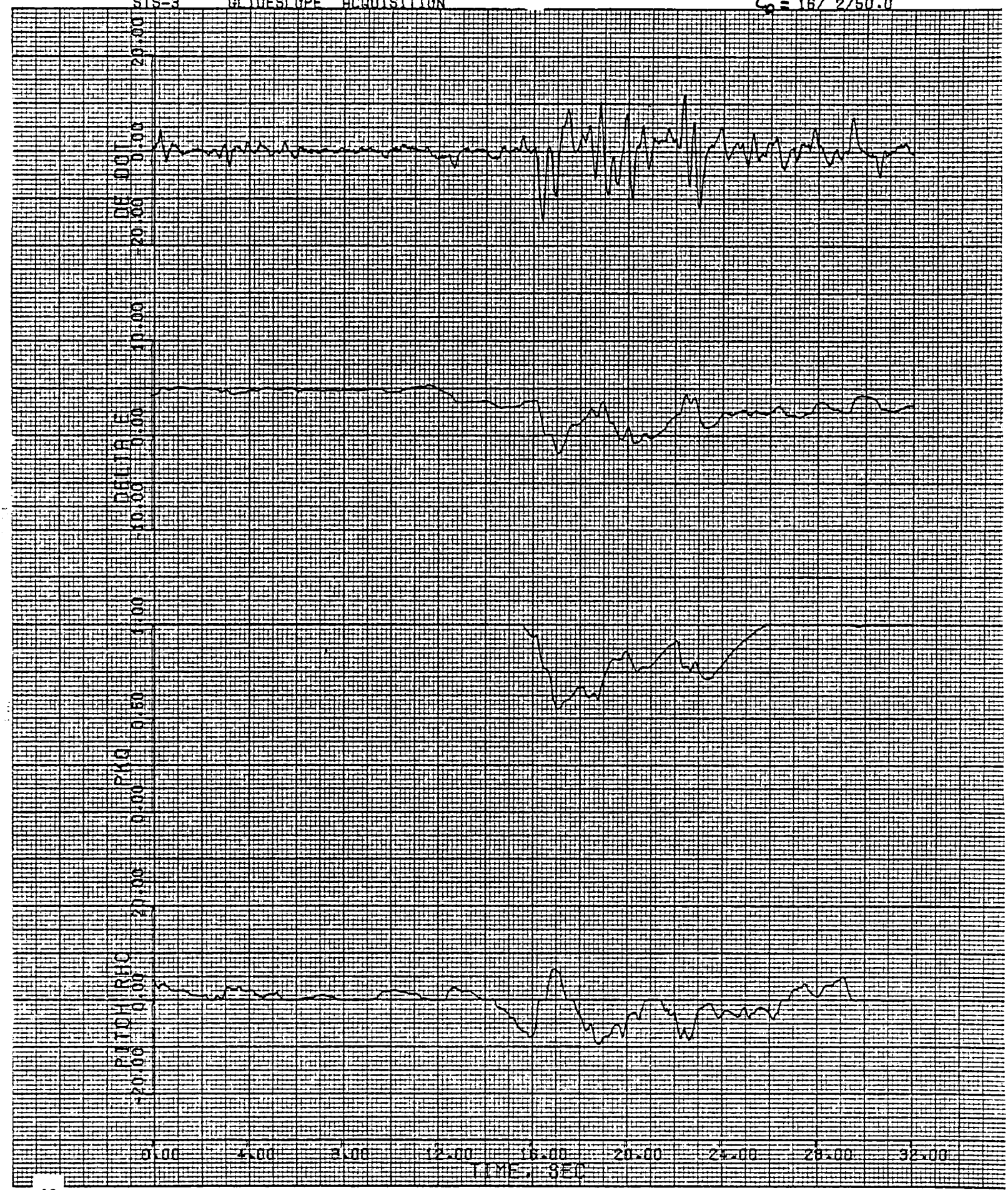

Figure 3b (Continued)

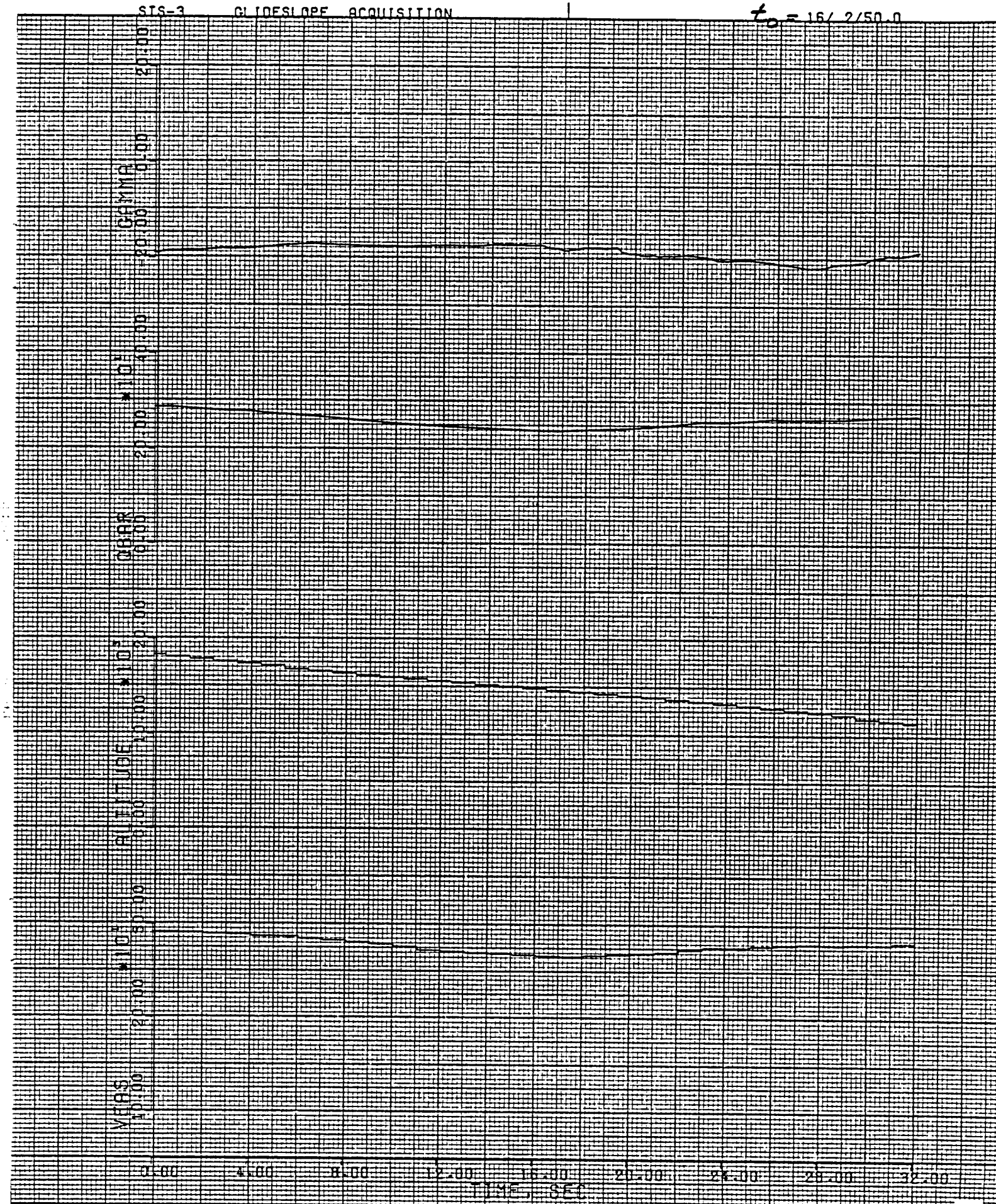

Figure 3c (Continued)

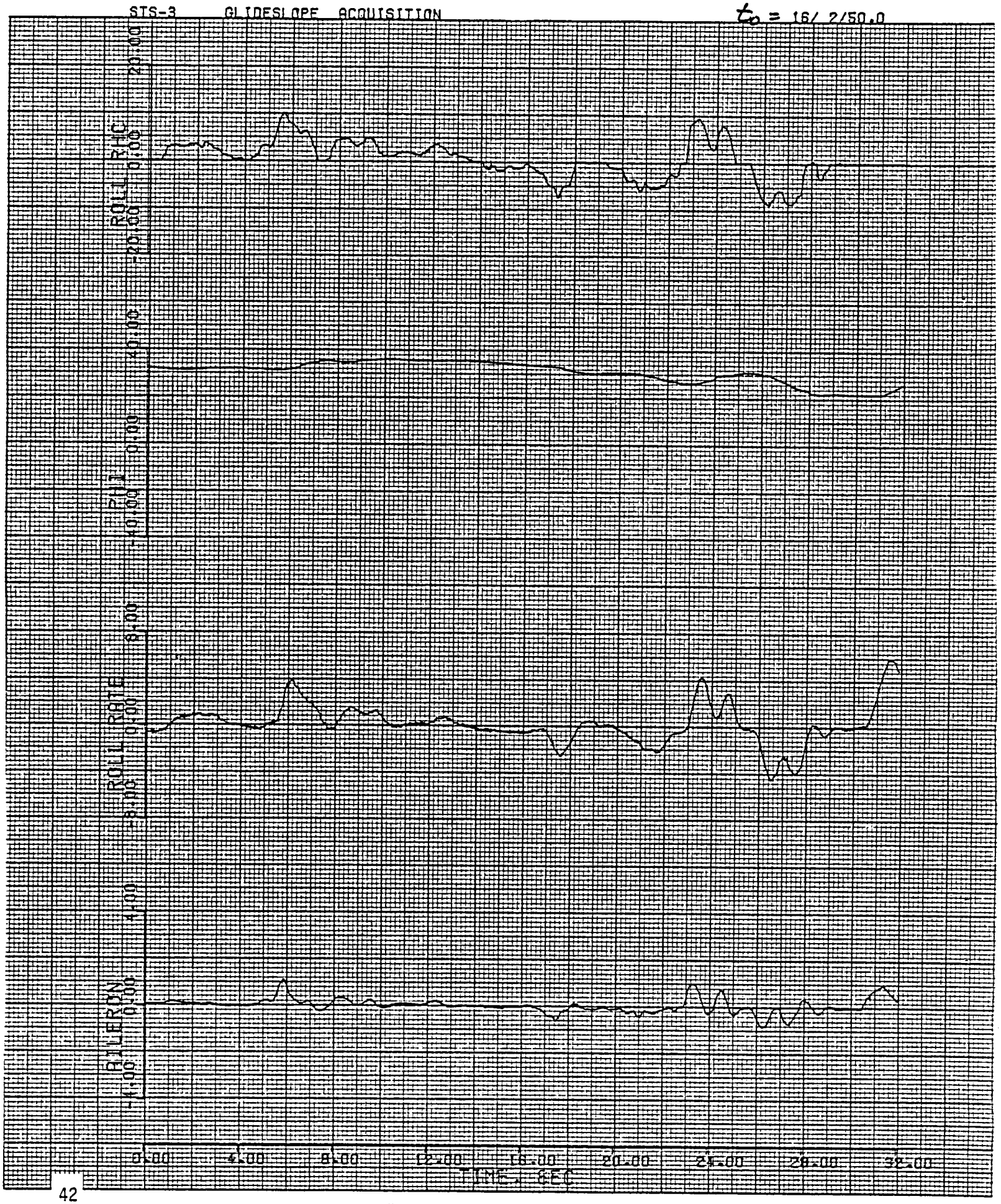

Figure 3d (Continued)

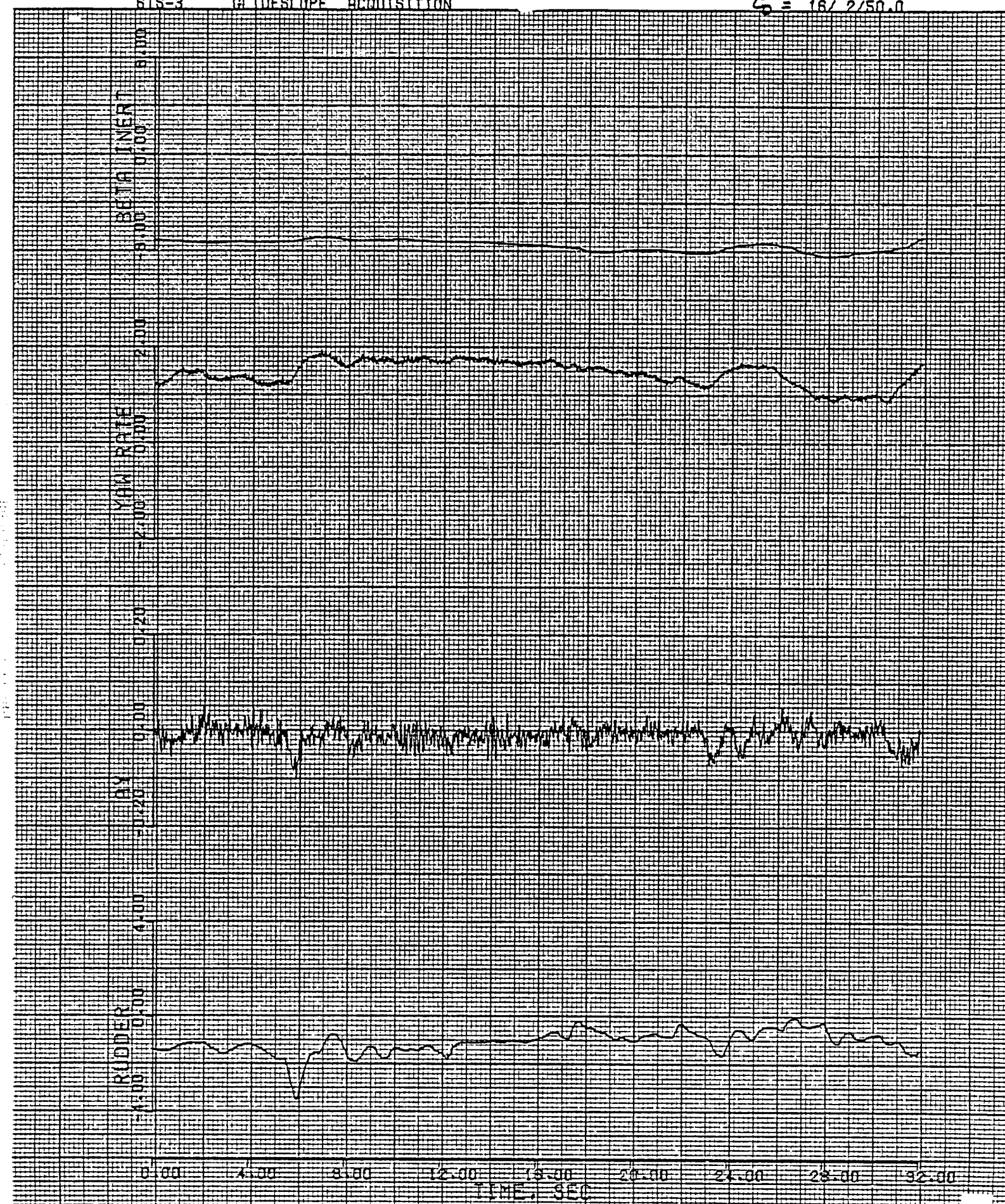

Figure 3e (Continued)

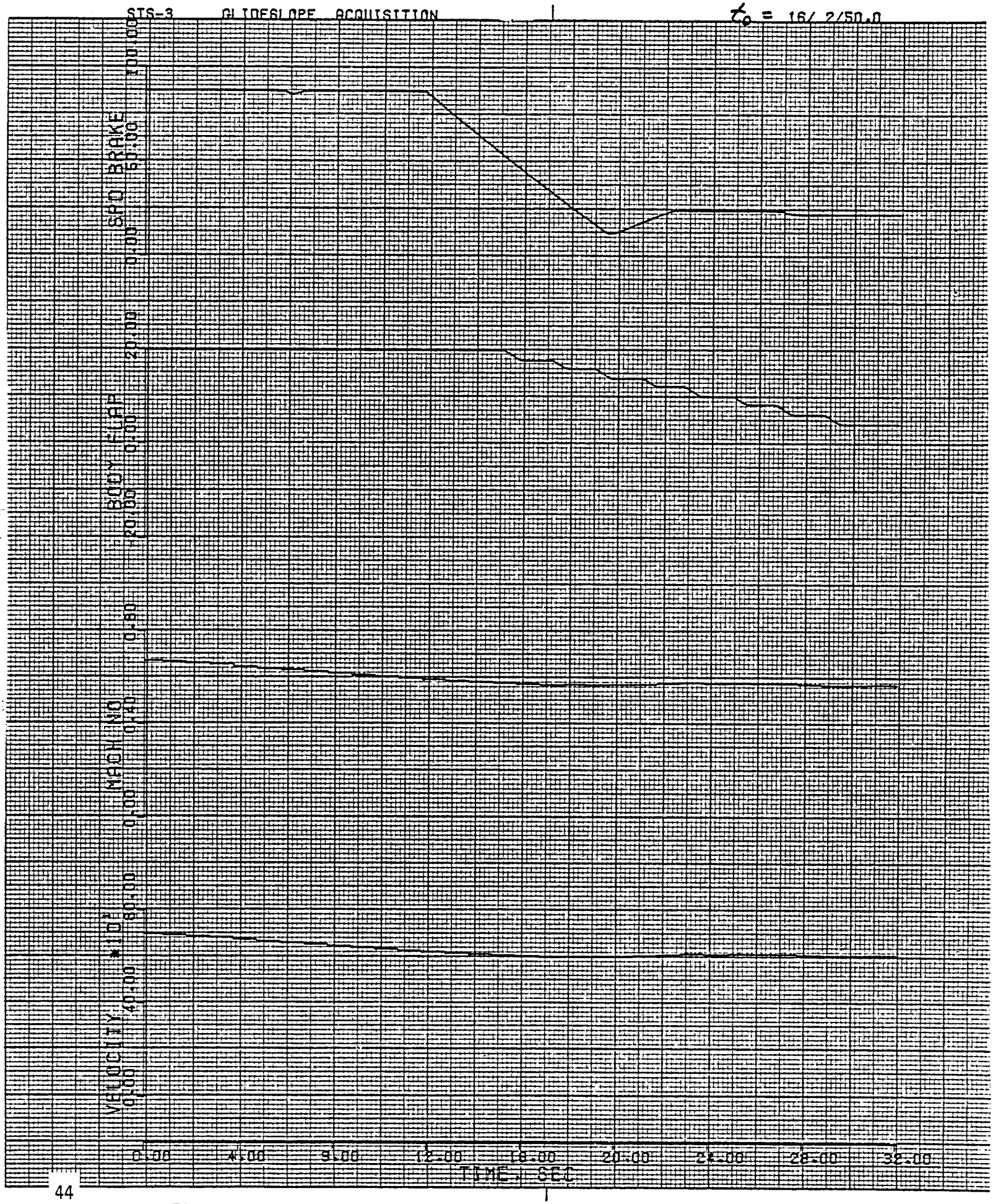

Figure 3f (Concluded)

Figure 4a Final Approach and Landing

Figure 4b (Continued)

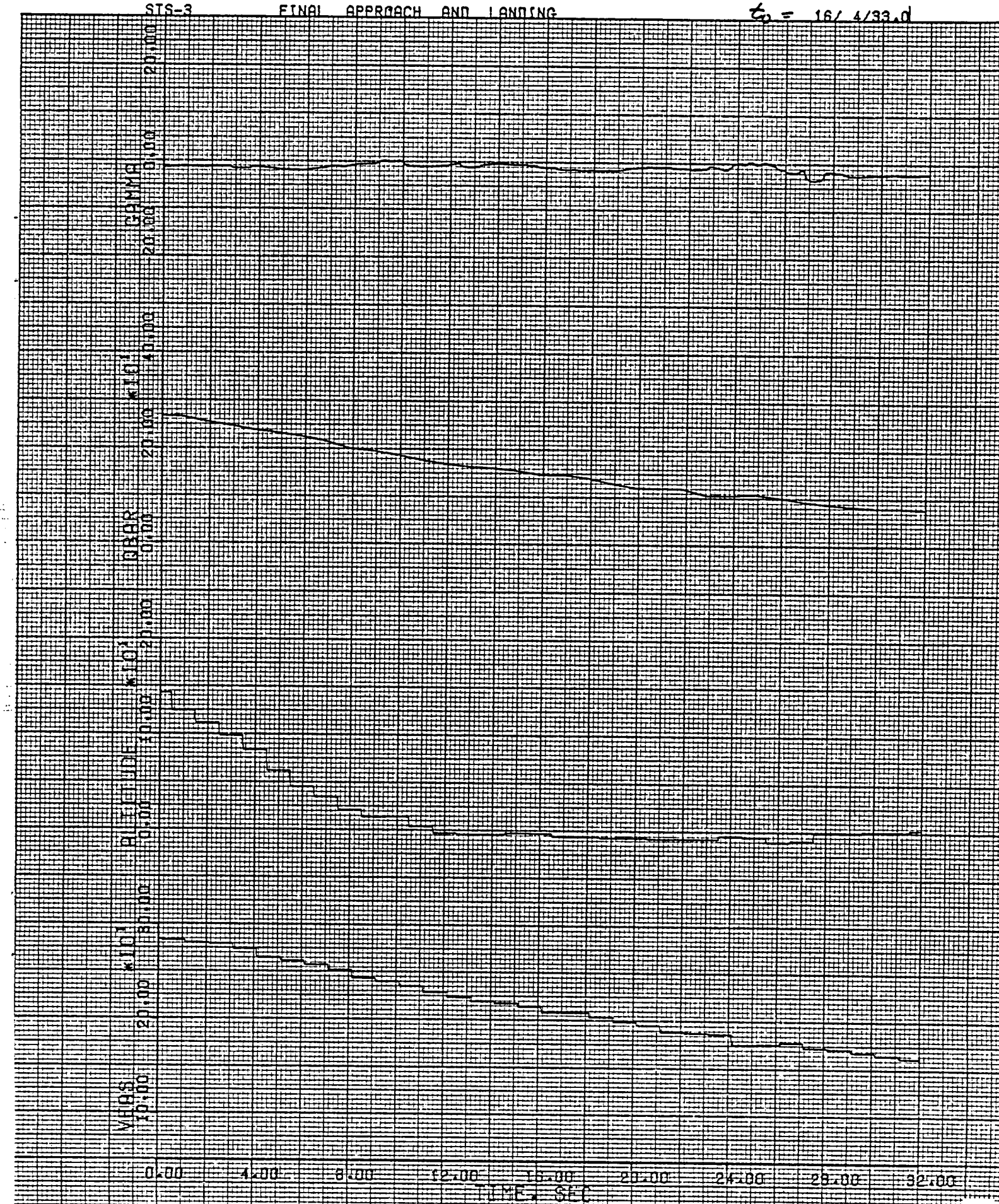

Figure 4c (Continued)

Figure 4d (Continued)

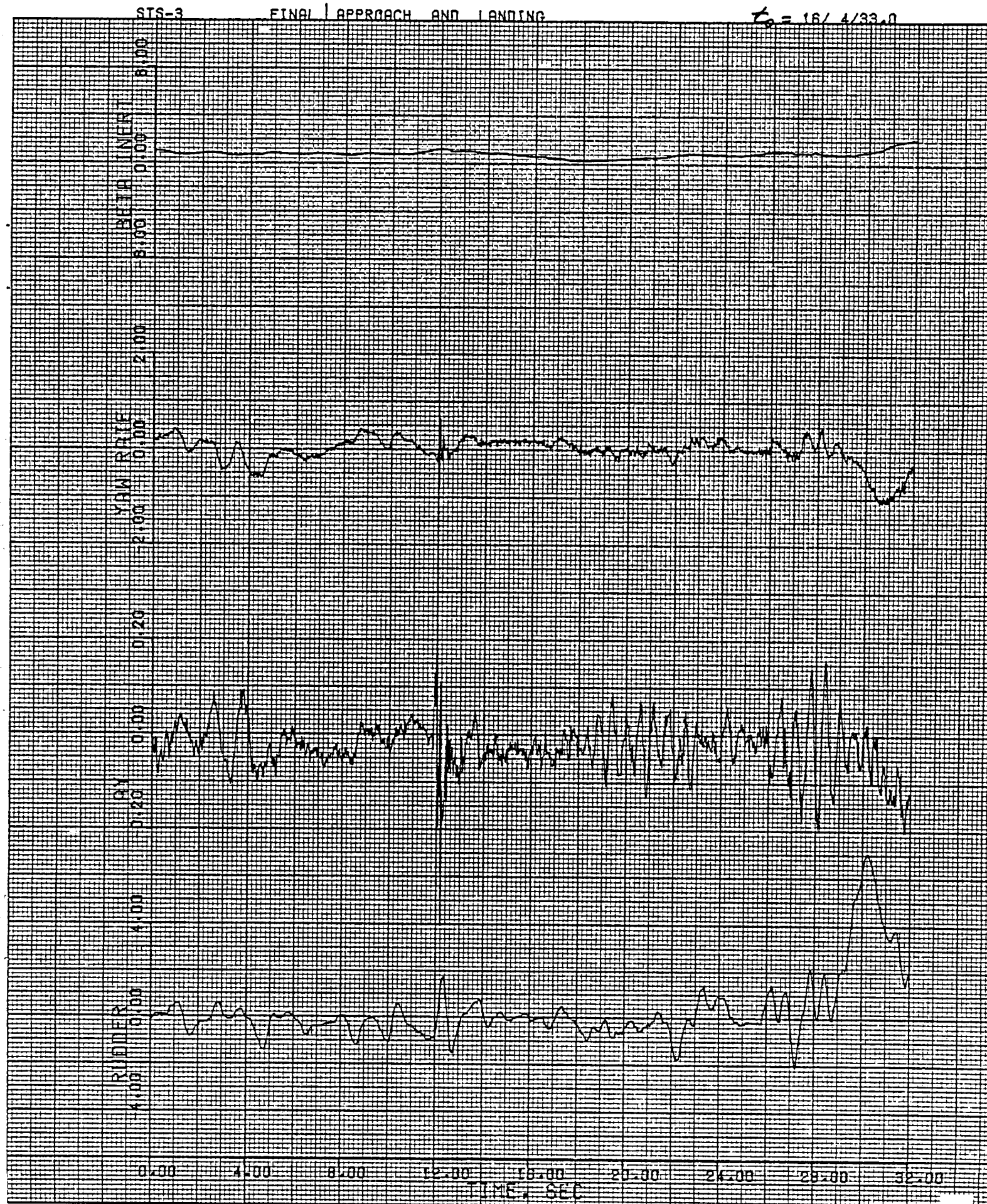

Figure 4e (Continued)

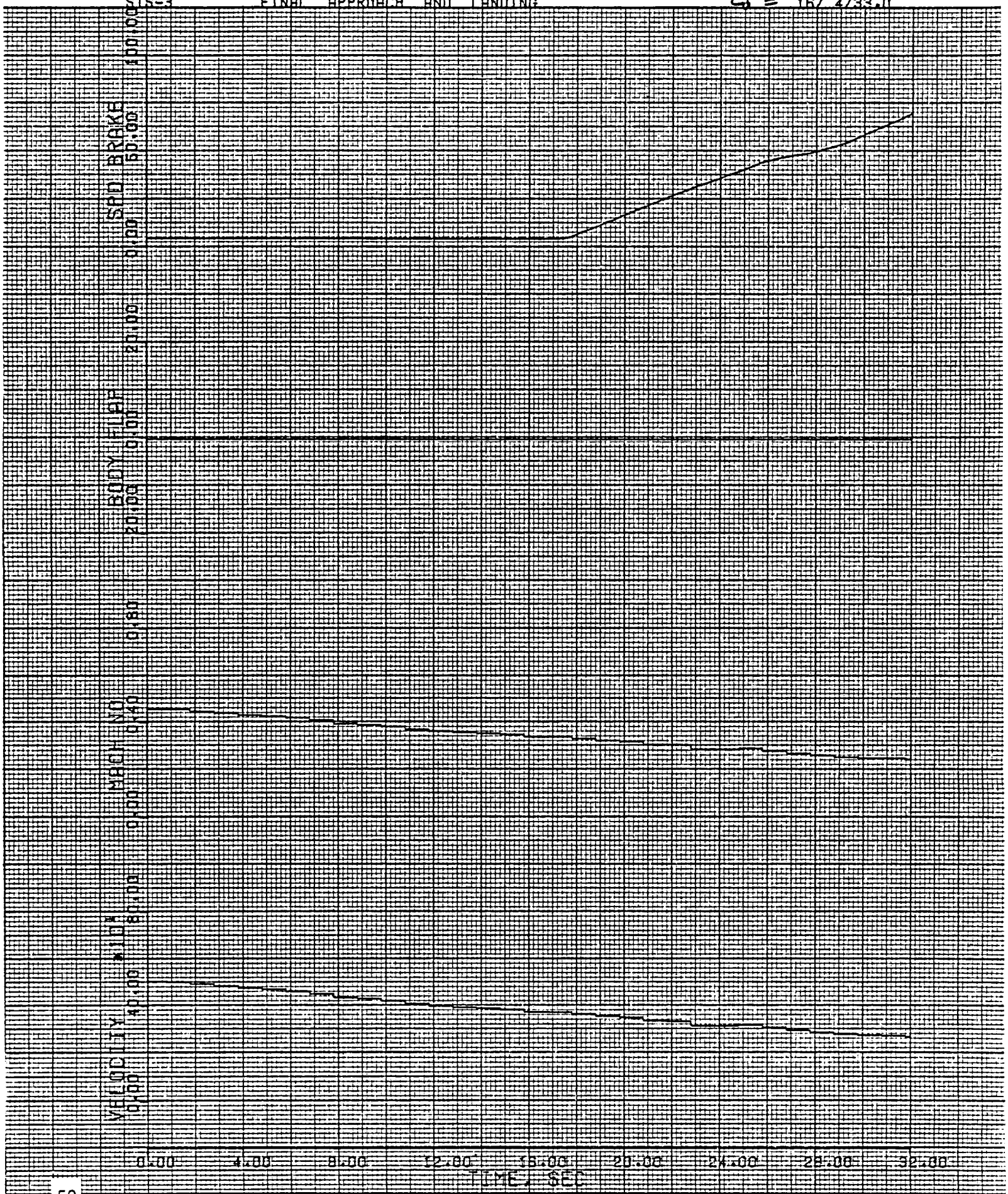

Figure 4f (Concluded)

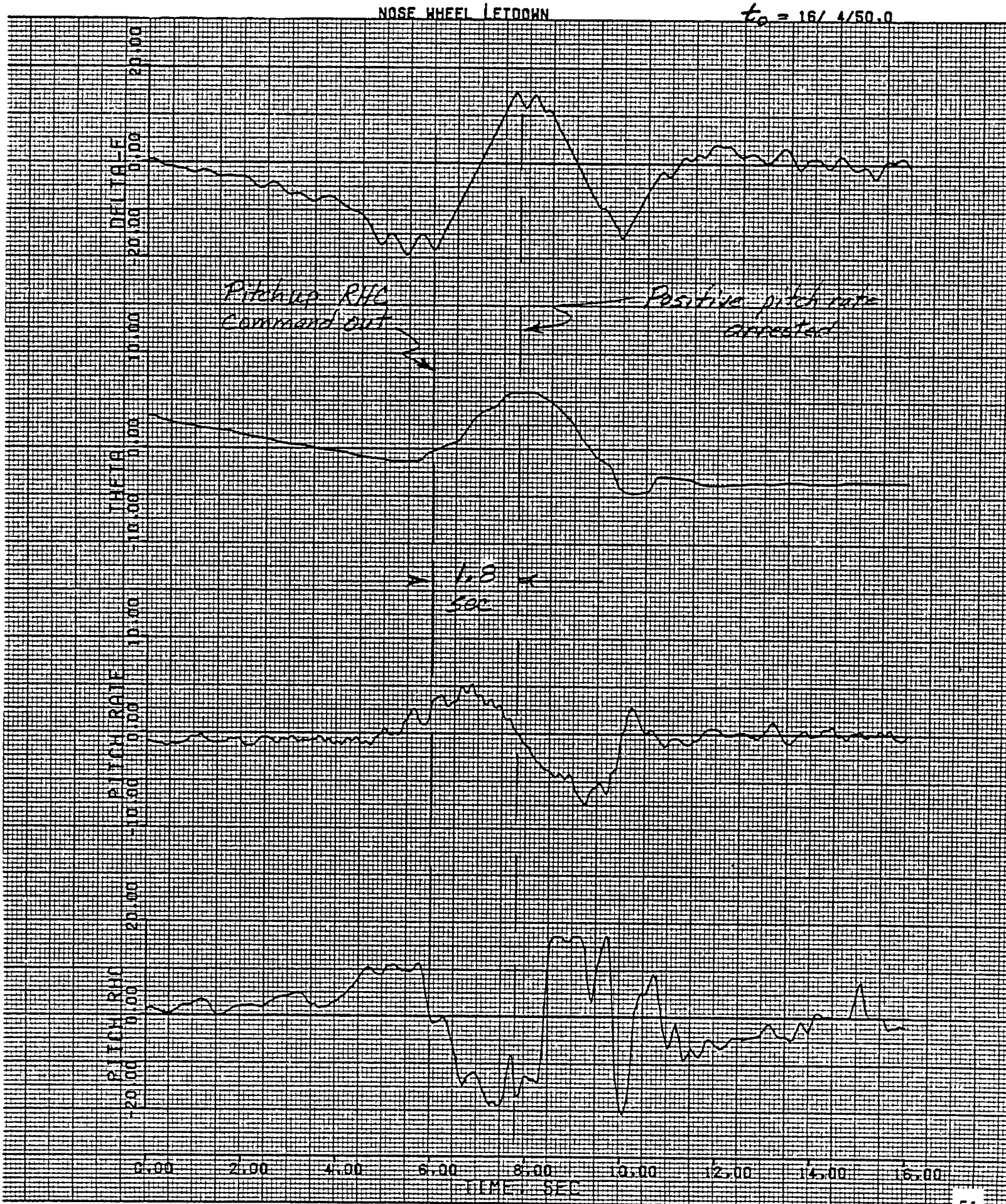

Figure 5 Nosewheel Letdown

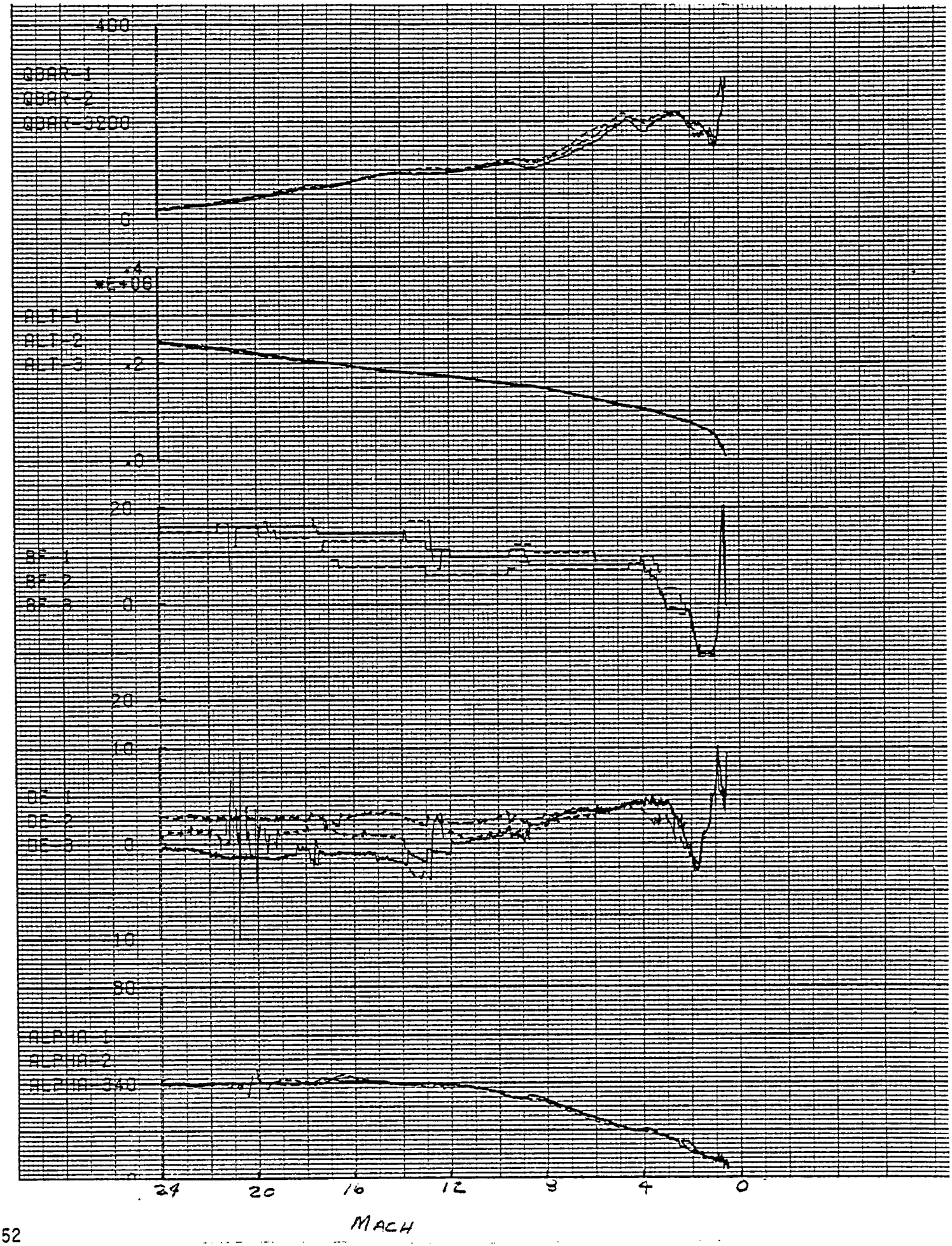

Figure 6 Three-Flight Comparison of Selected Variables

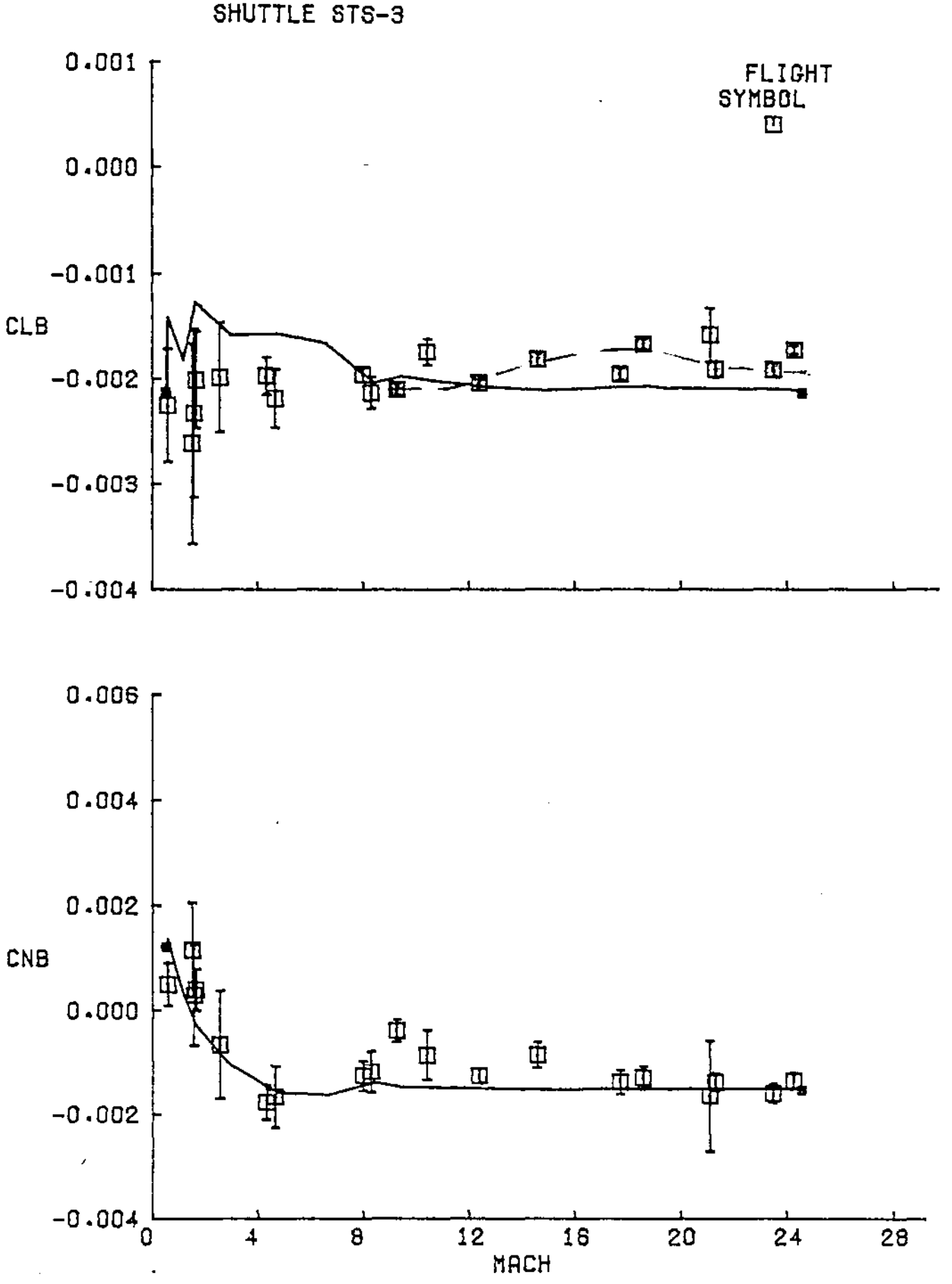

Figure 7a STS-3 Lateral-Directional Flight Derivatives

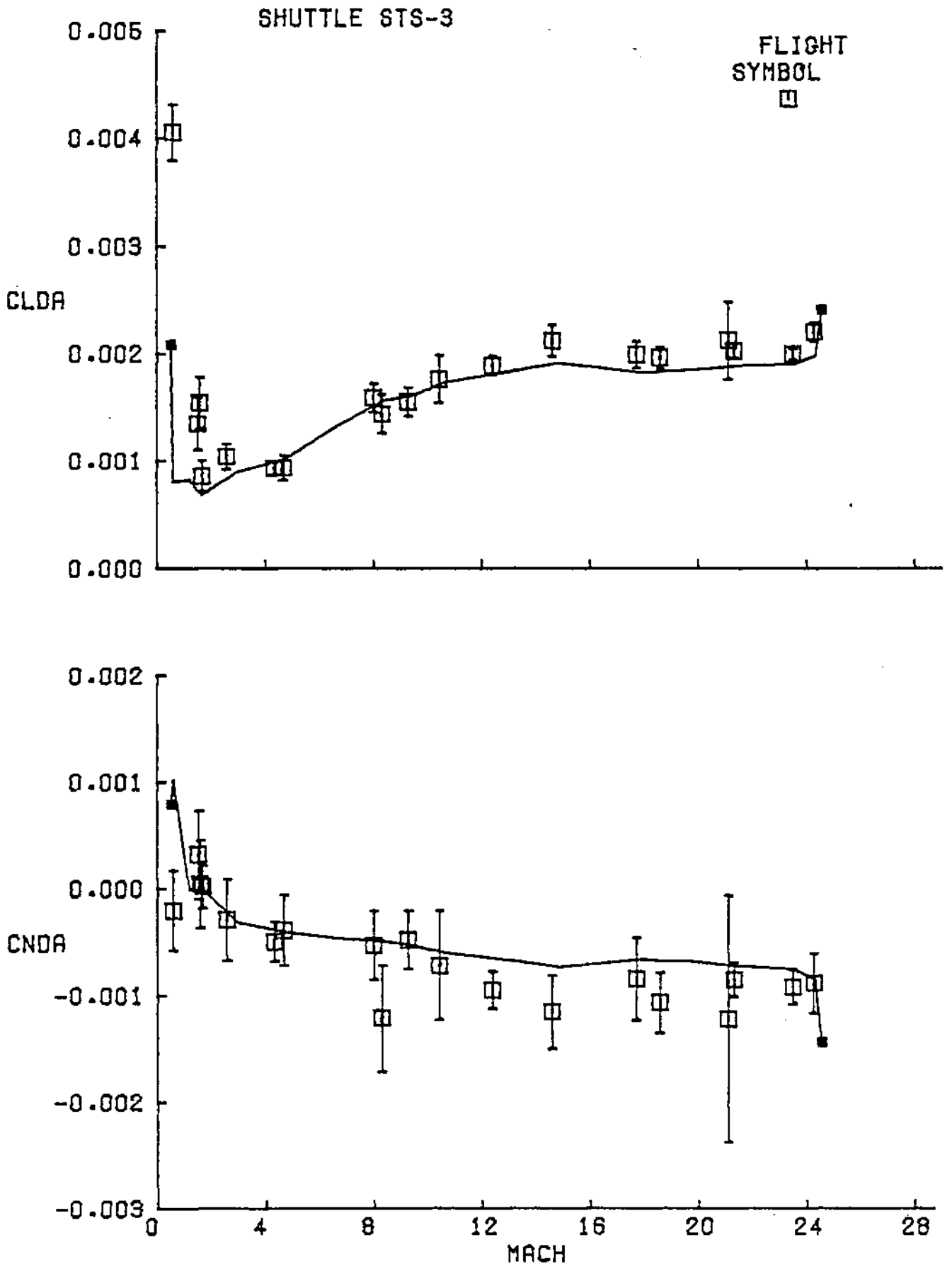

Figure 7b (Continued)

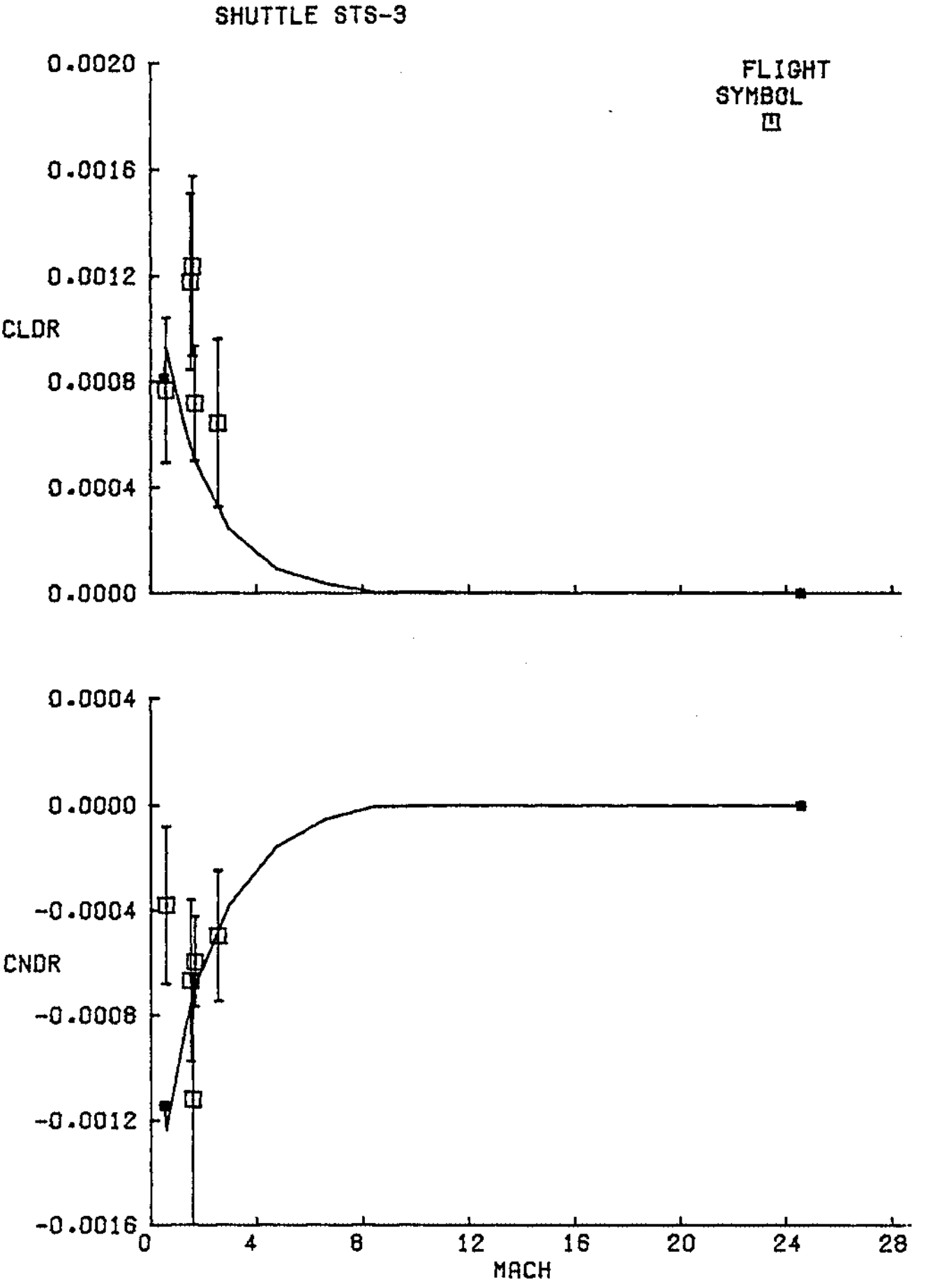

Figure 7c (Continued)

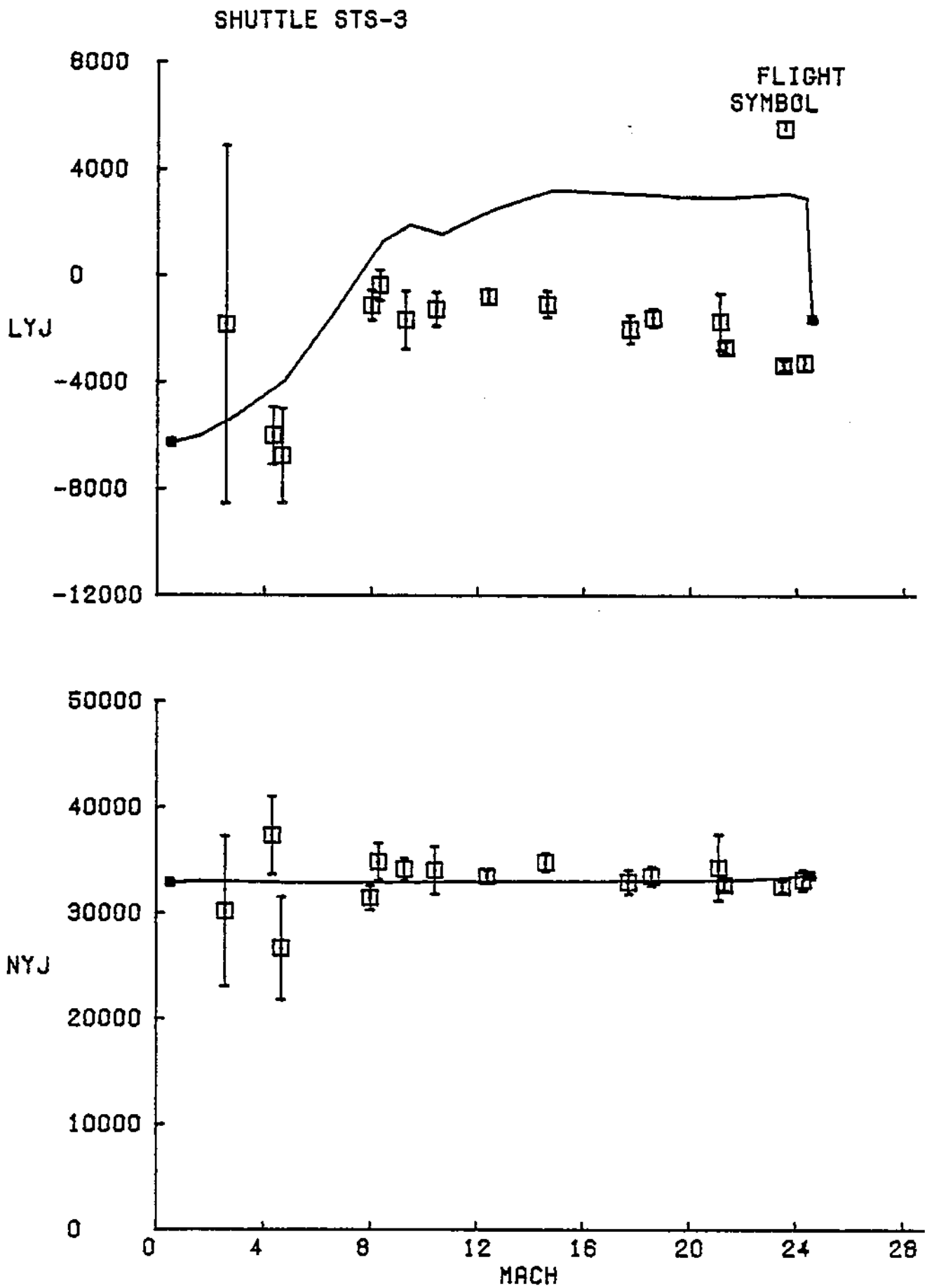

Figure 7d (Continued)

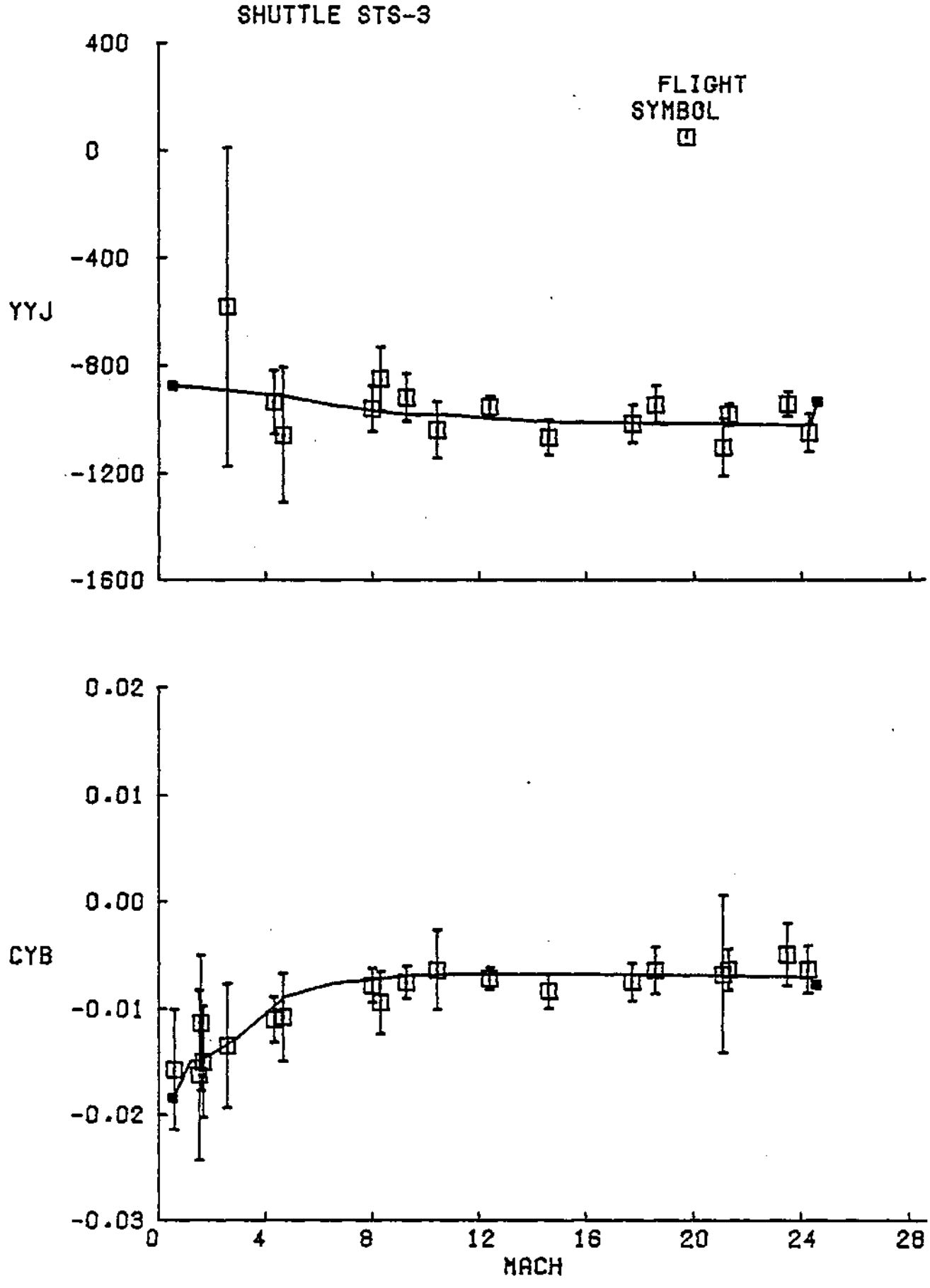

Figure 7e (Concluded)

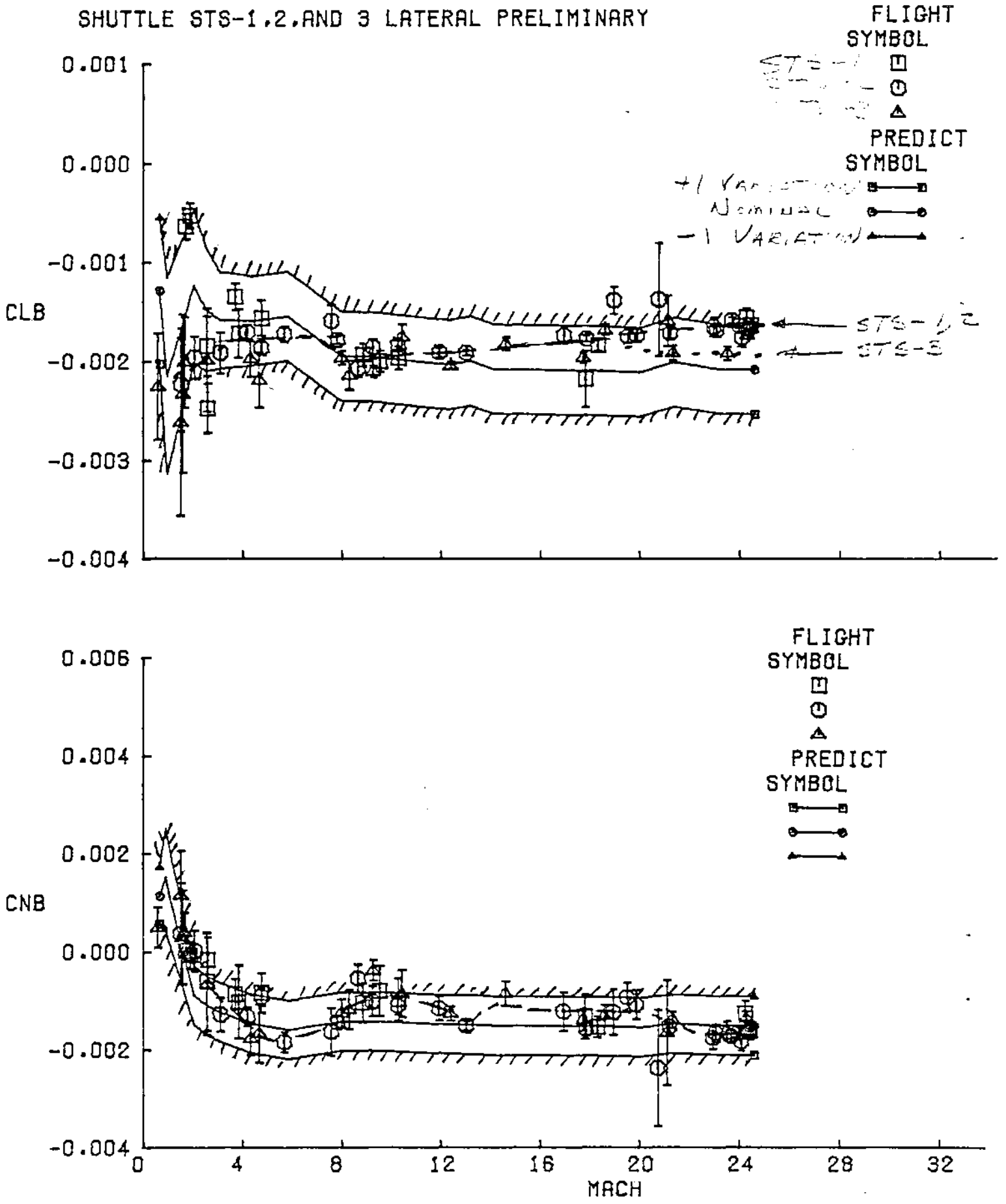

Figure 8a Lateral-Directional Derivative Results From STS-1, 2, and 3

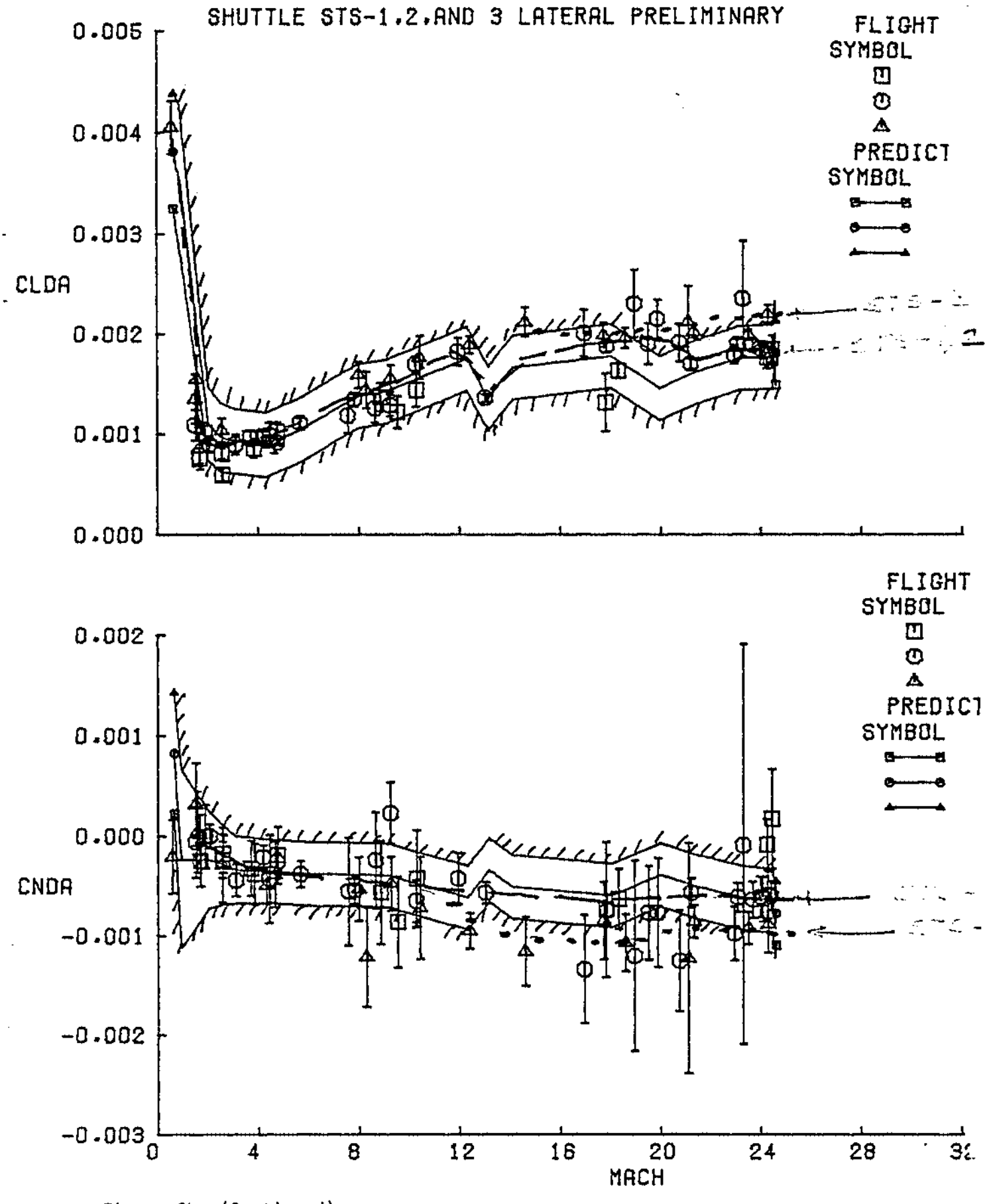

Figure 8b (Continued)

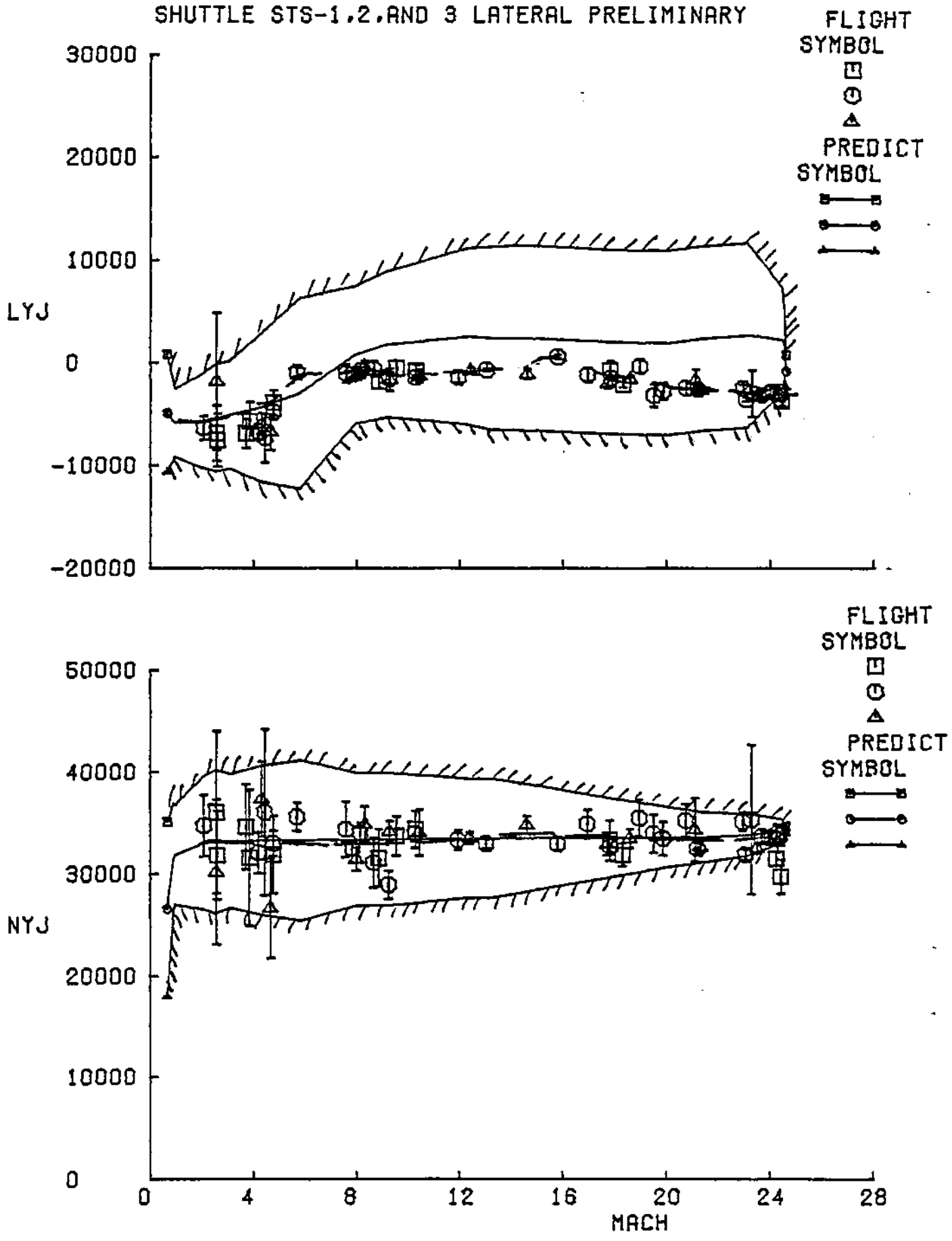

Figure 8c (Continued)

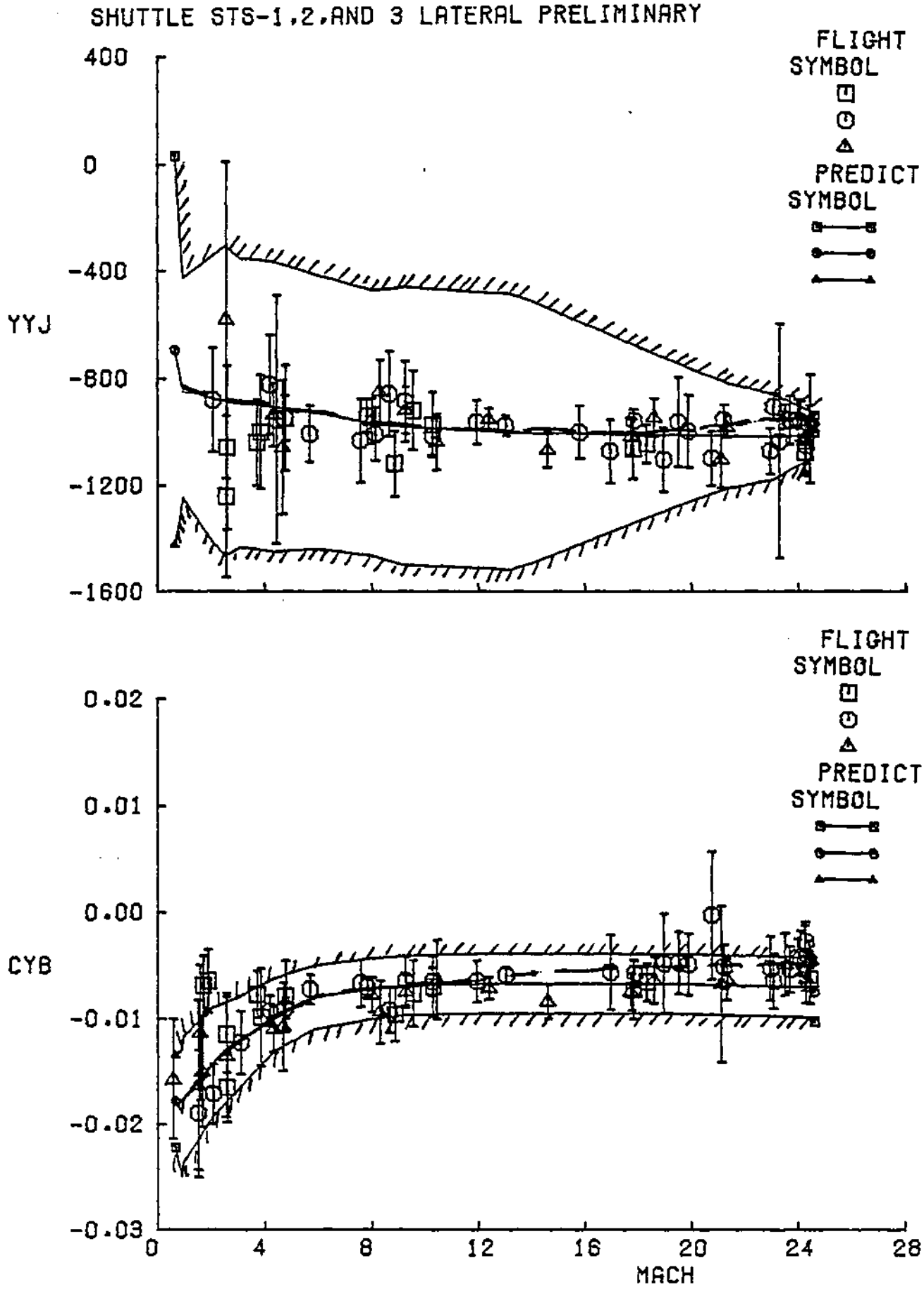

Figure 8d (Concluded)

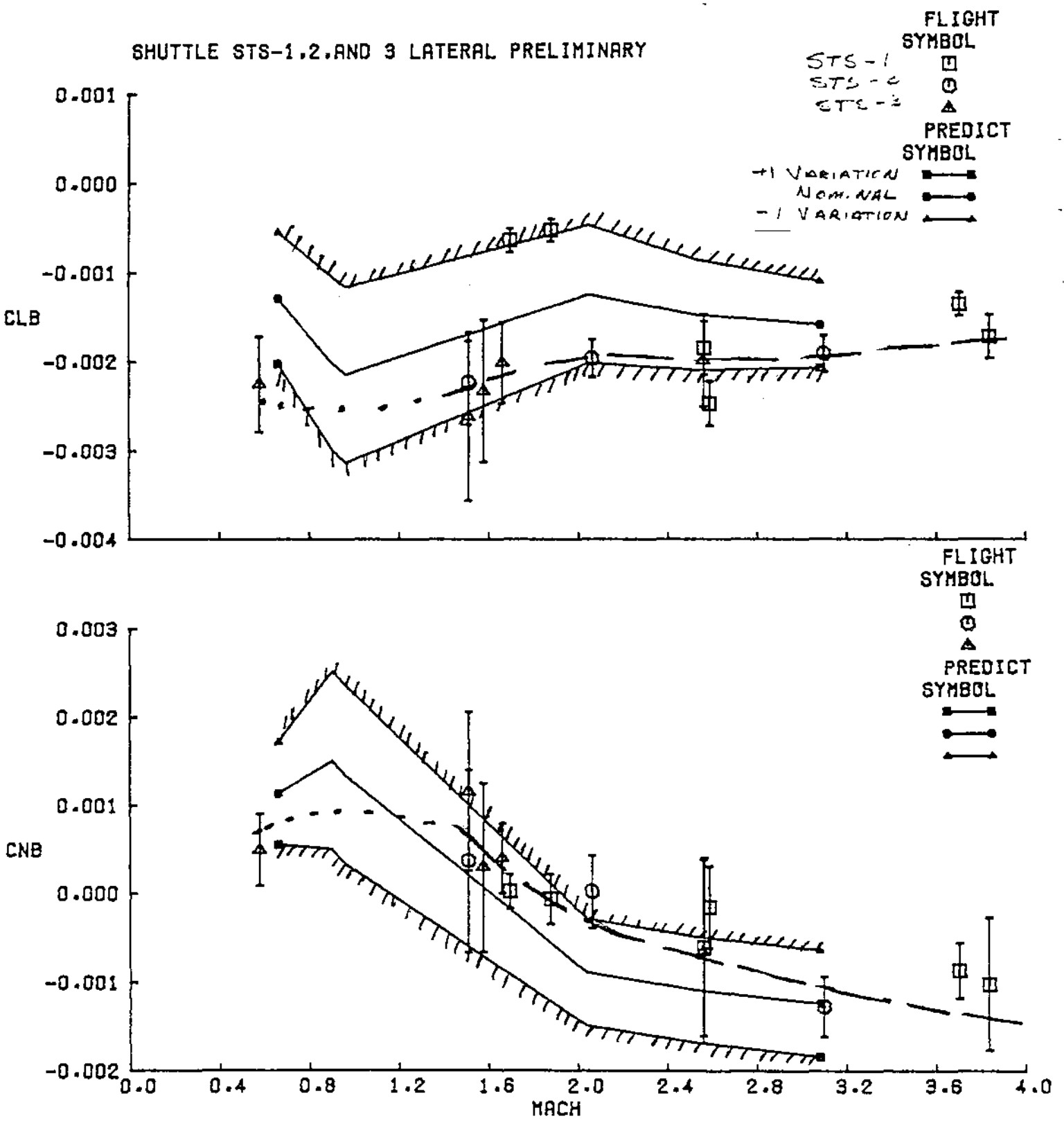

Figure 9a Lateral Directional Derivative Results-Low M Regime

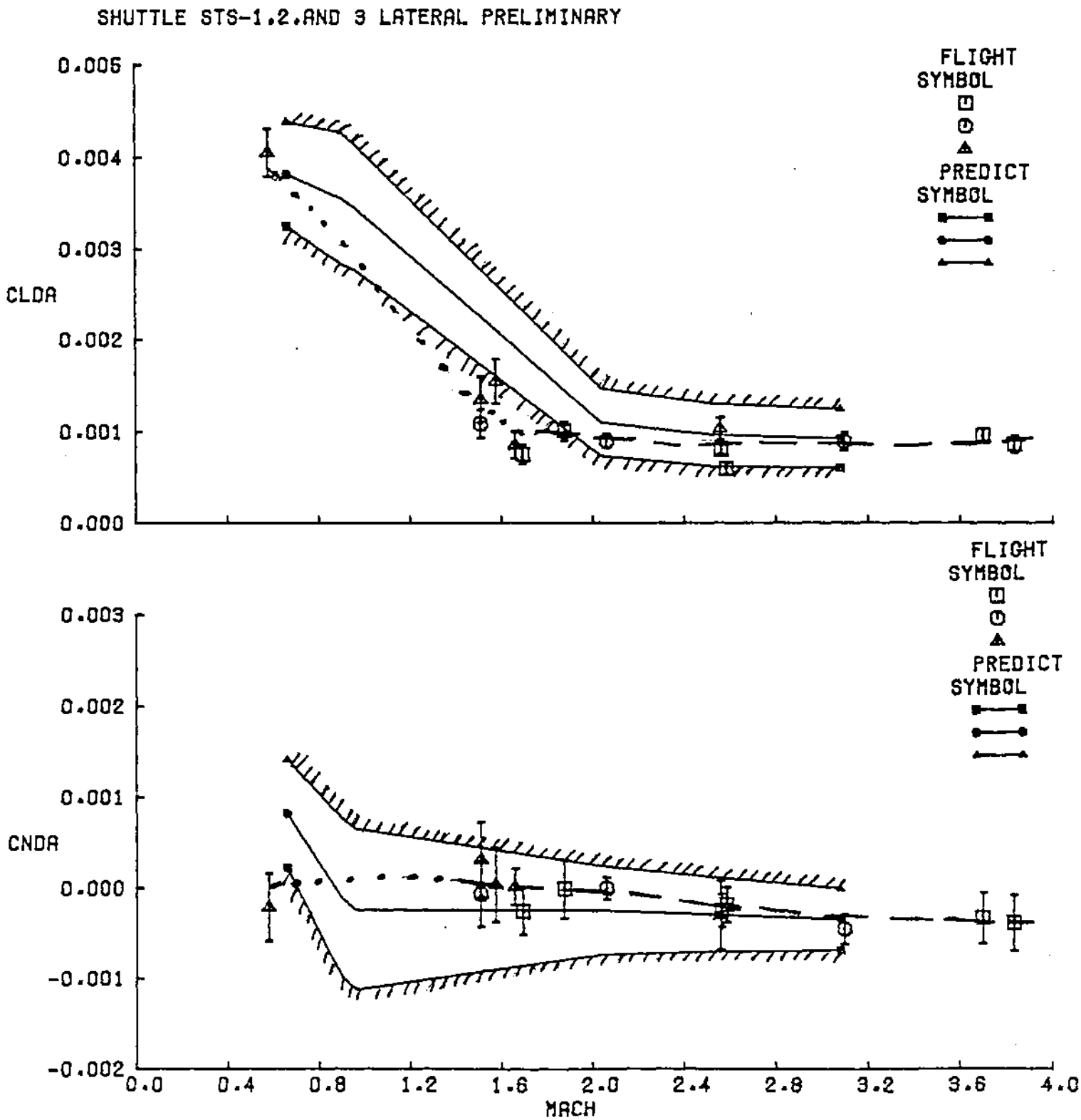

Figure 9b (Continued)

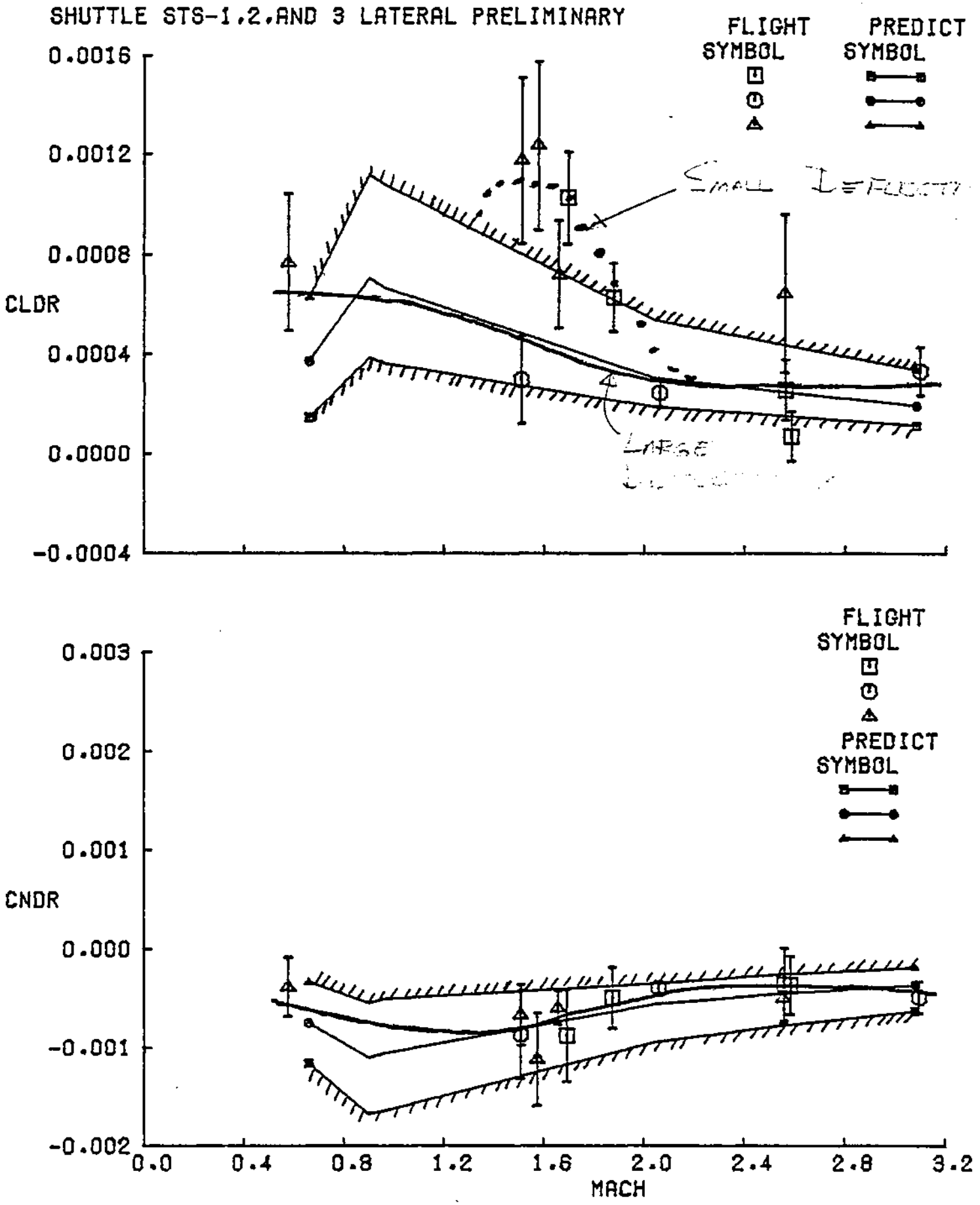

Figure 9c (Continued)

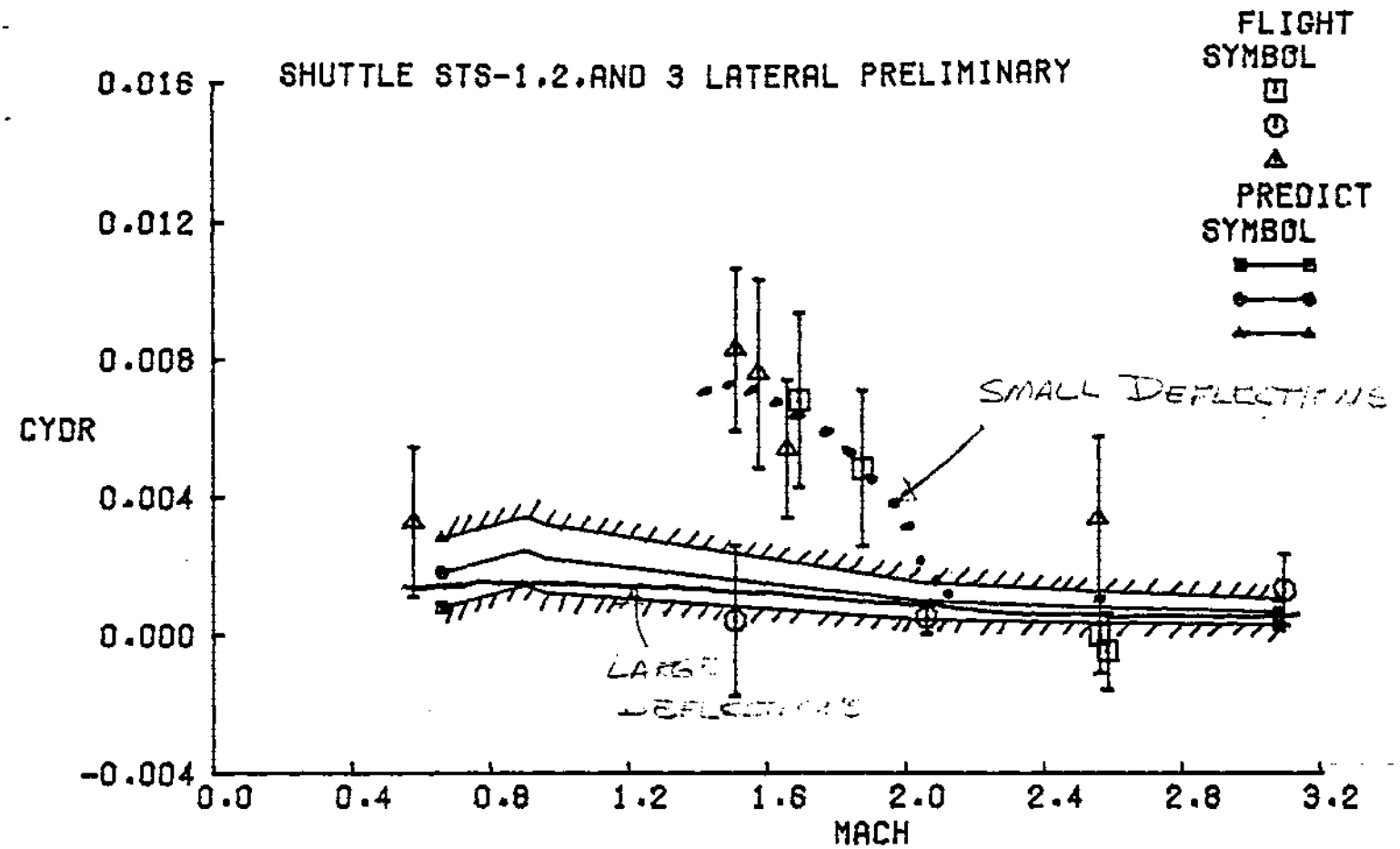

Figure 9d (Concluded)

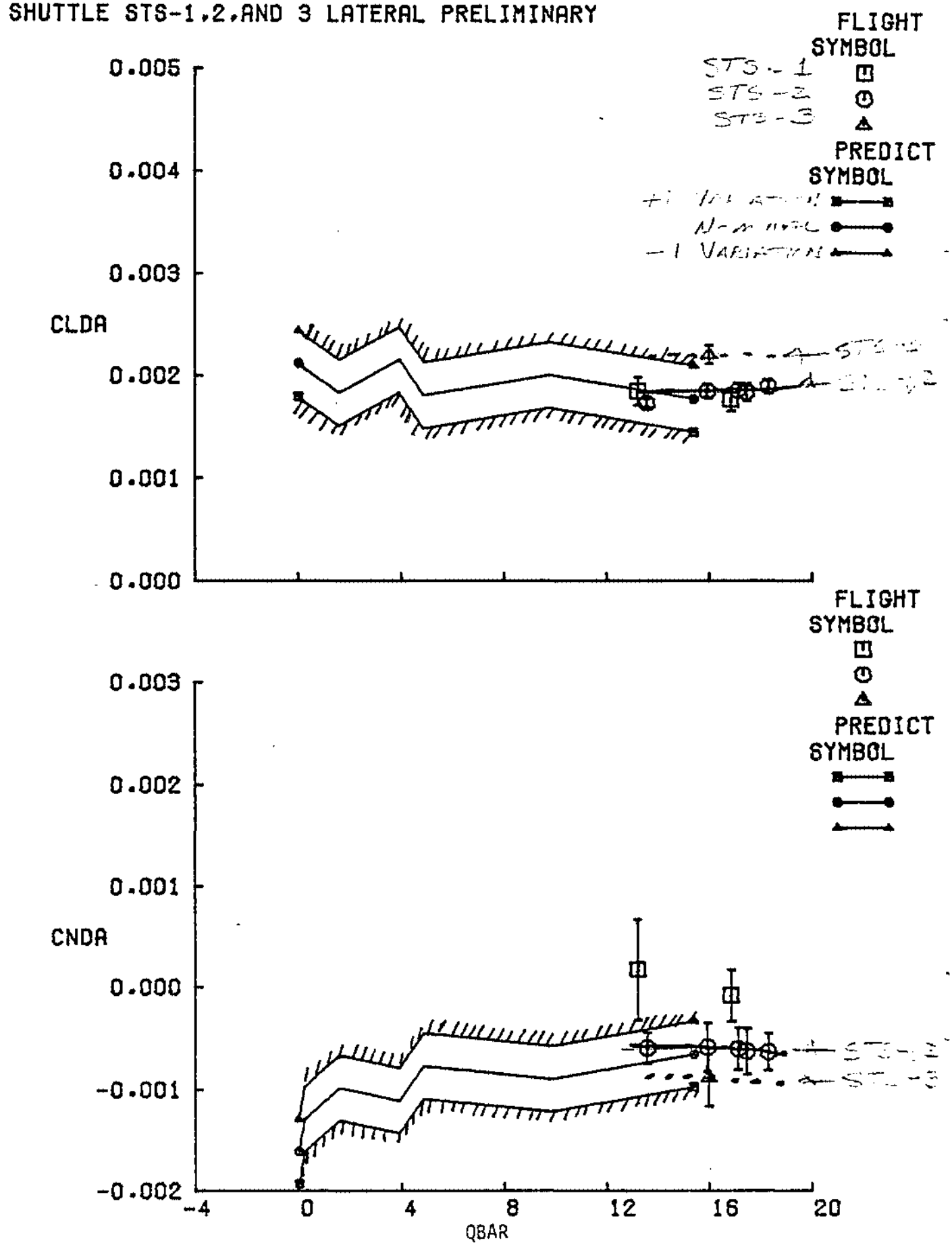

66 Figure 10a Lateral-Directional Derivatives Versus Dynamic Pressure

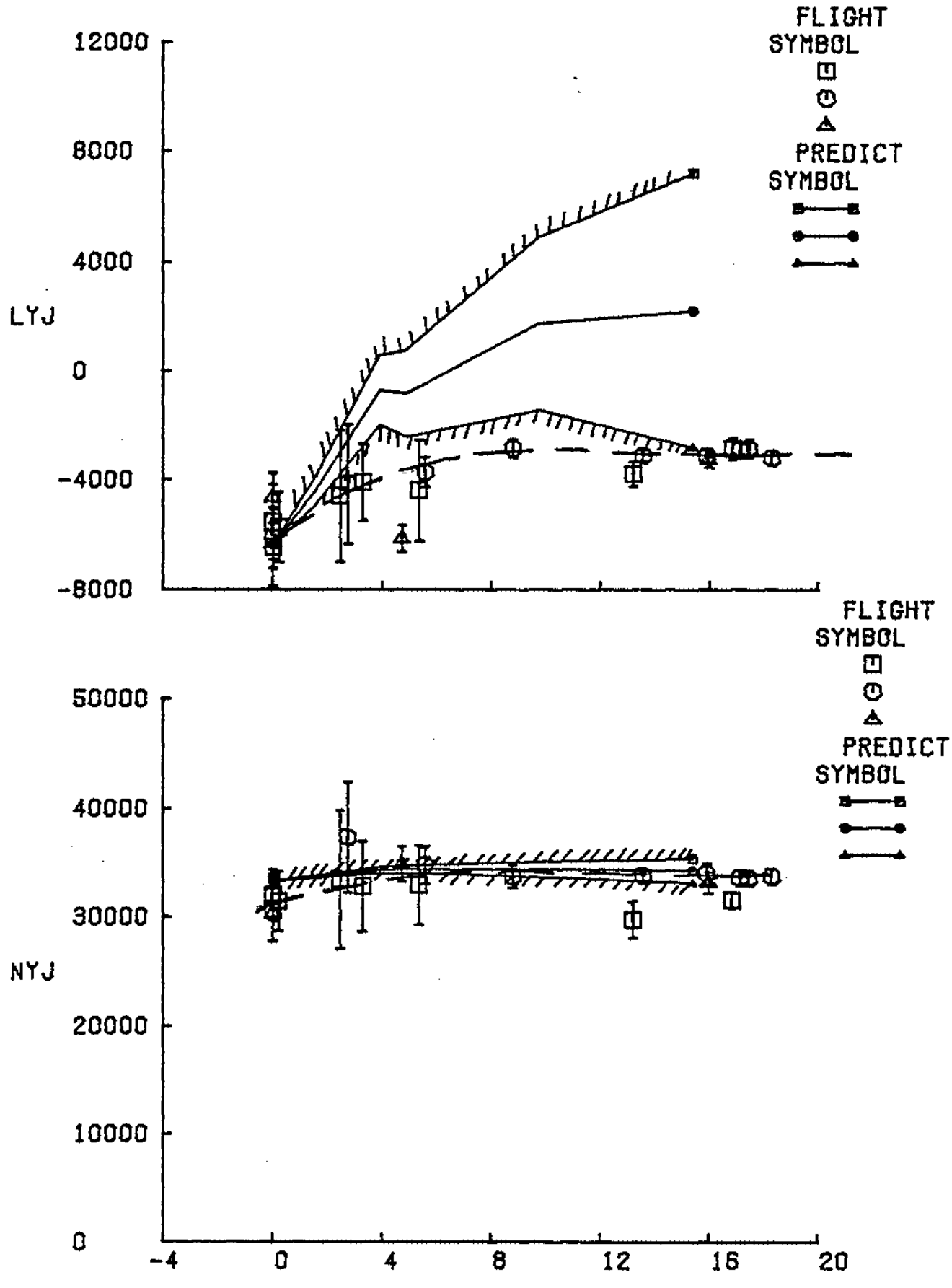

Figure 10b (Continued)

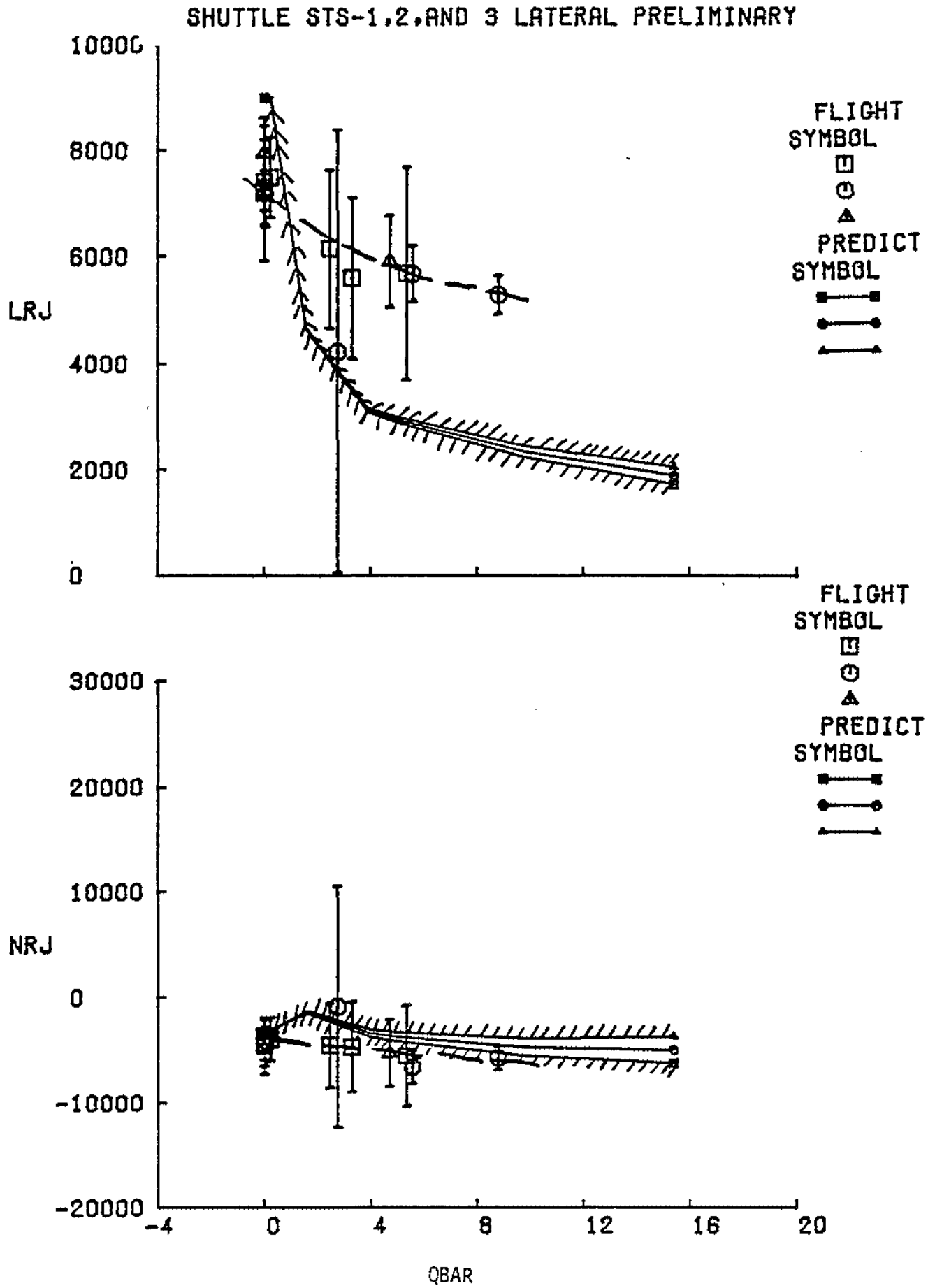

Figure 10c (Continued)

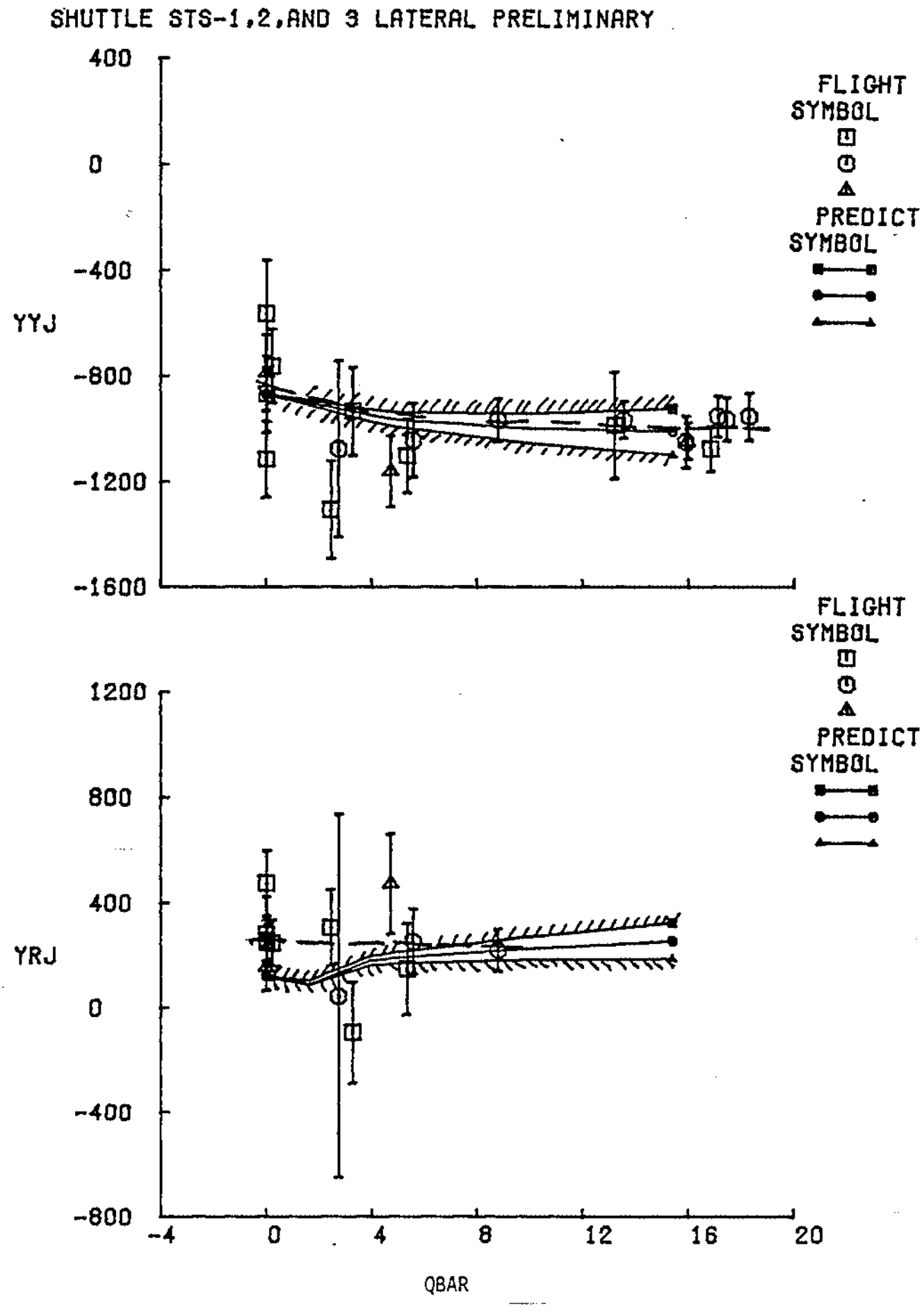

Figure 10d (Concluded)

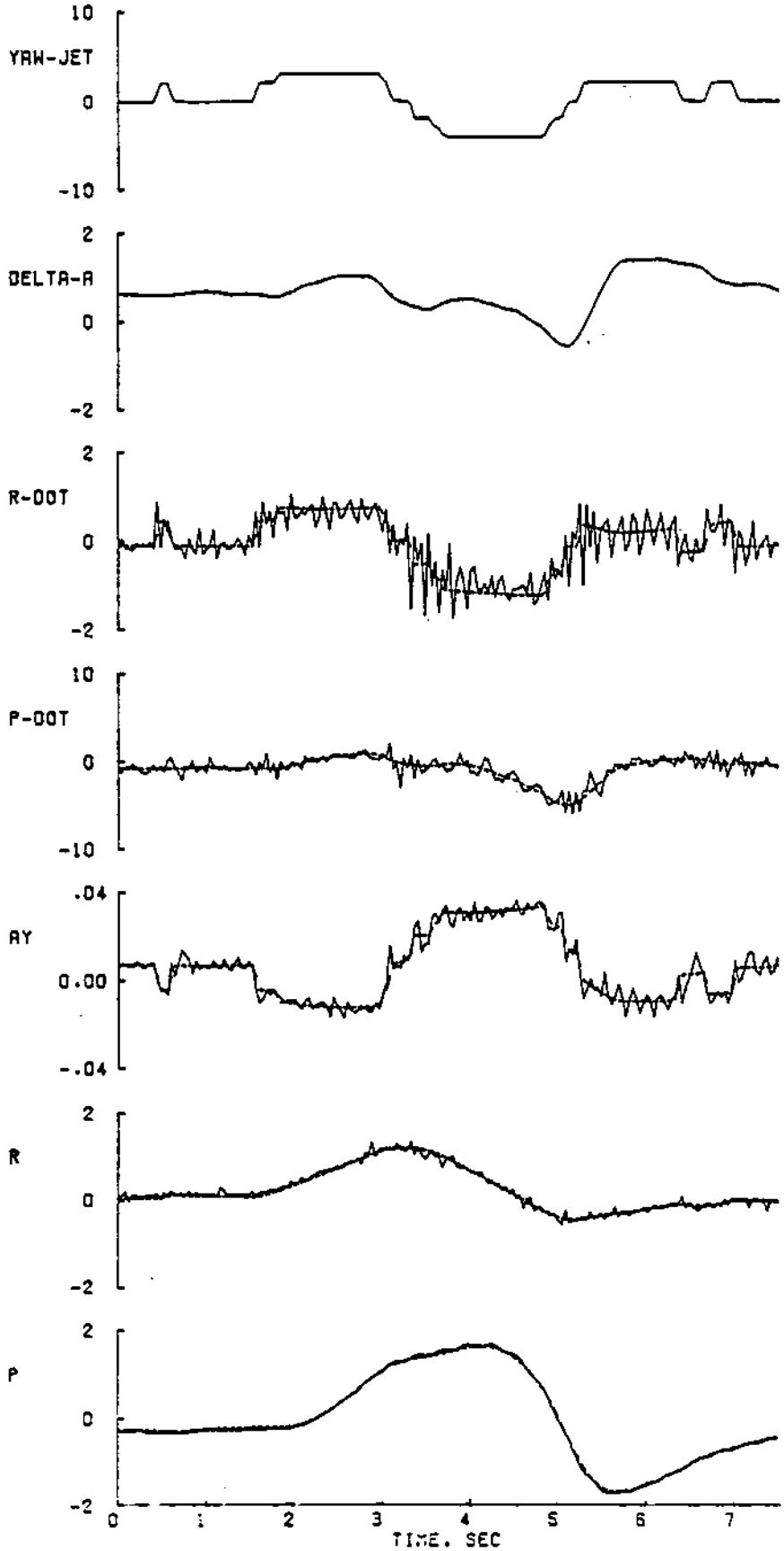

Figure 11 ACIP Noise Contamination Example

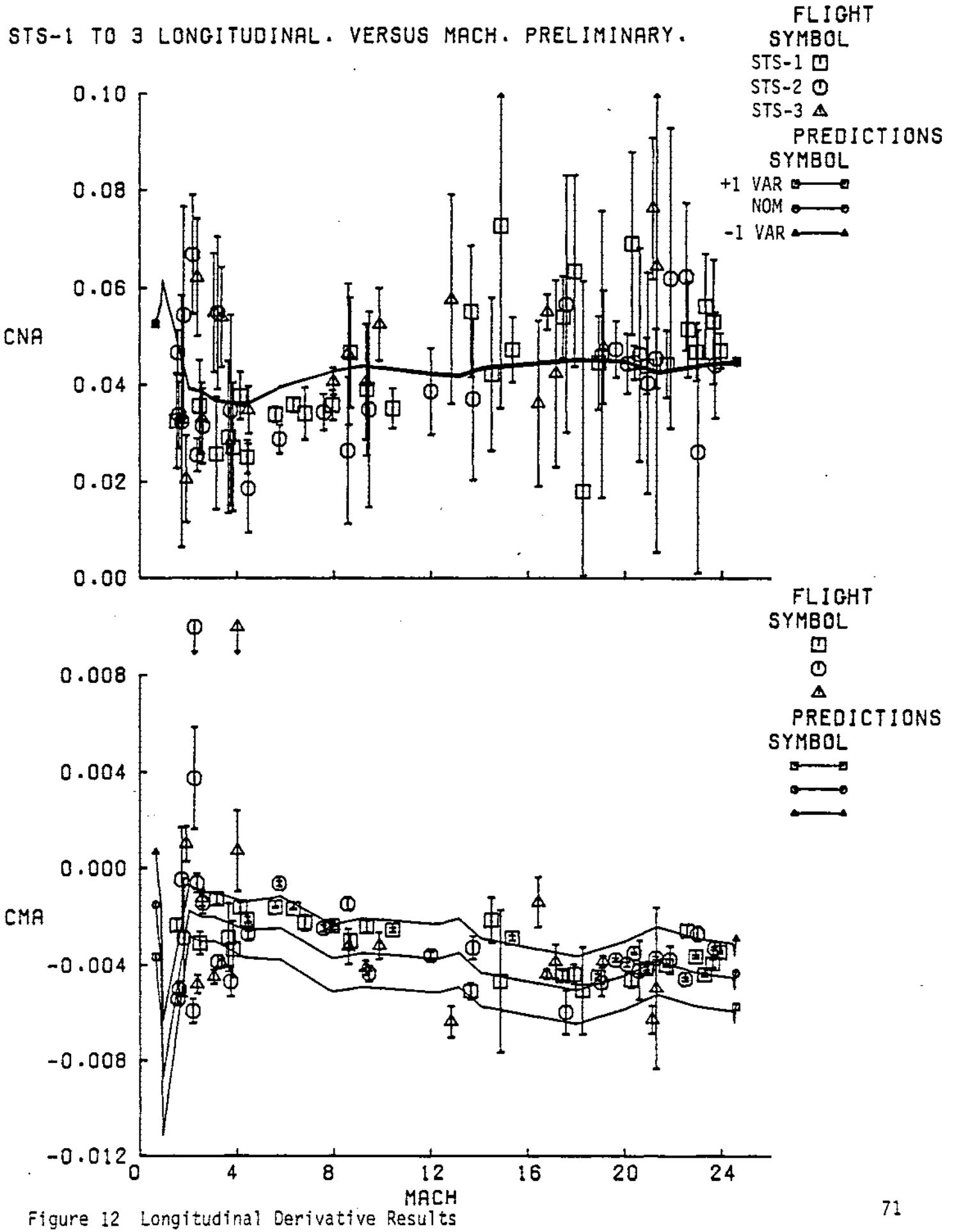

Figure 12 Longitudinal Derivative Results

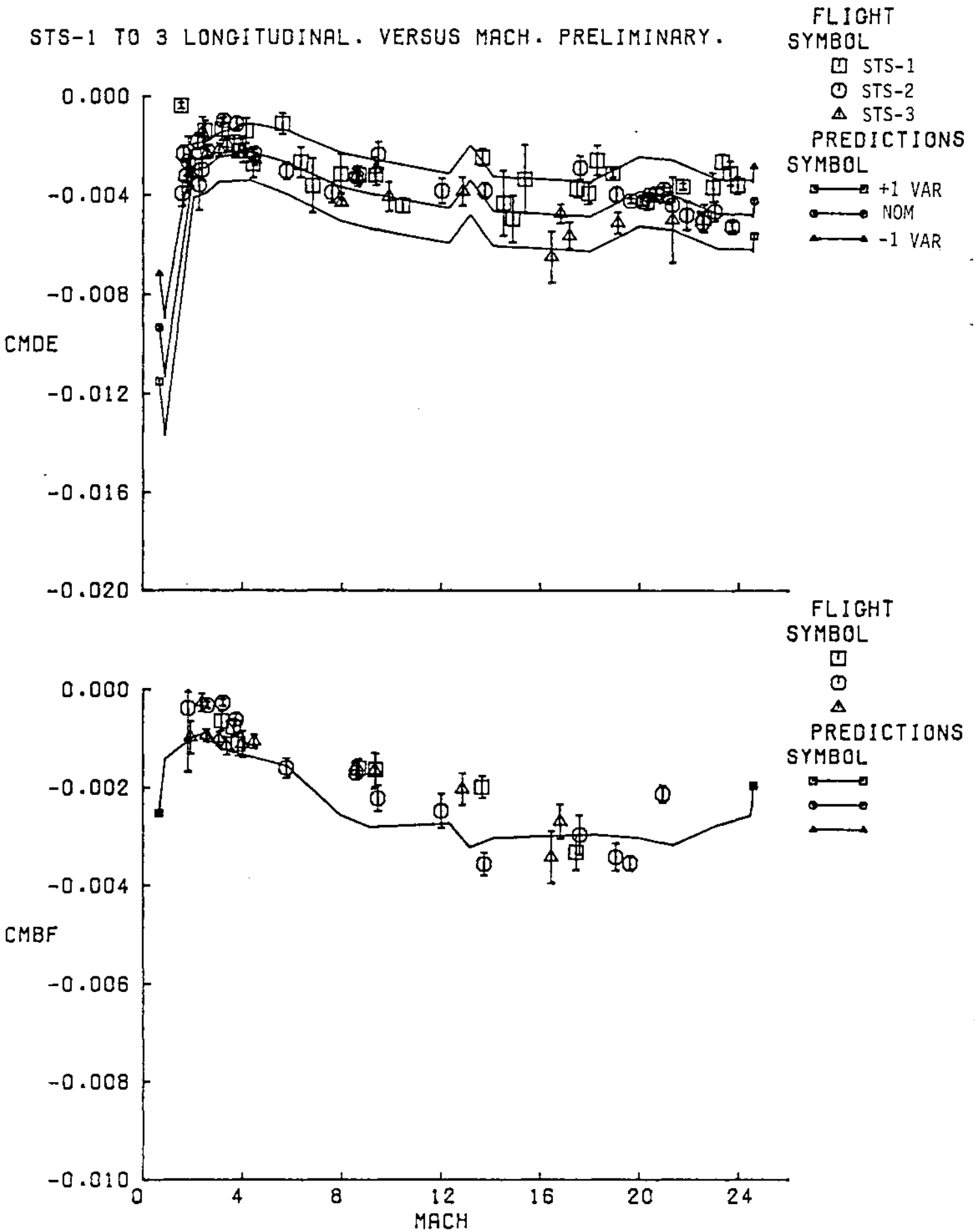

Figure 13 Longitudinal Derivative Results

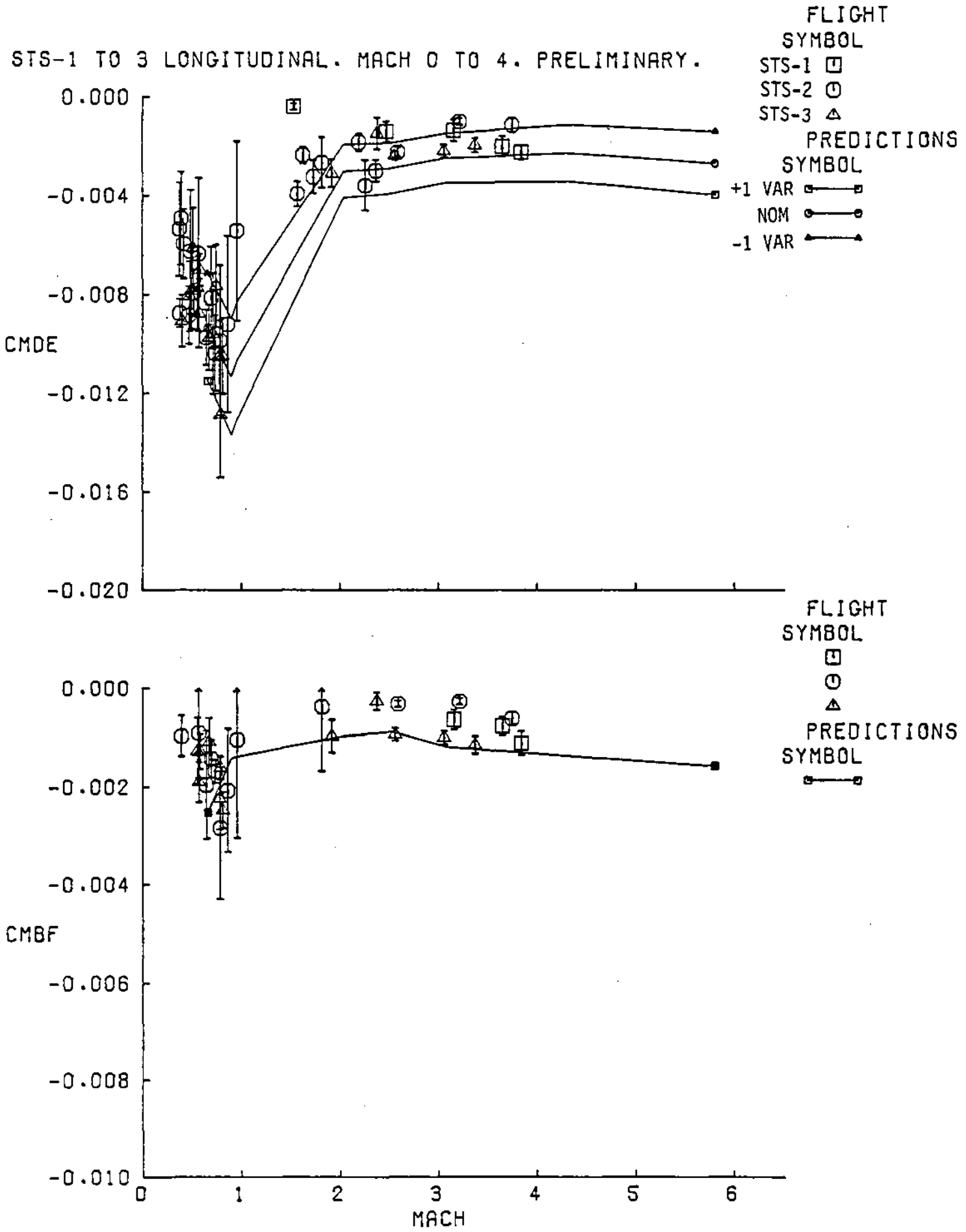

Figure 14 Longitudinal Derivative Results - Low M Regime

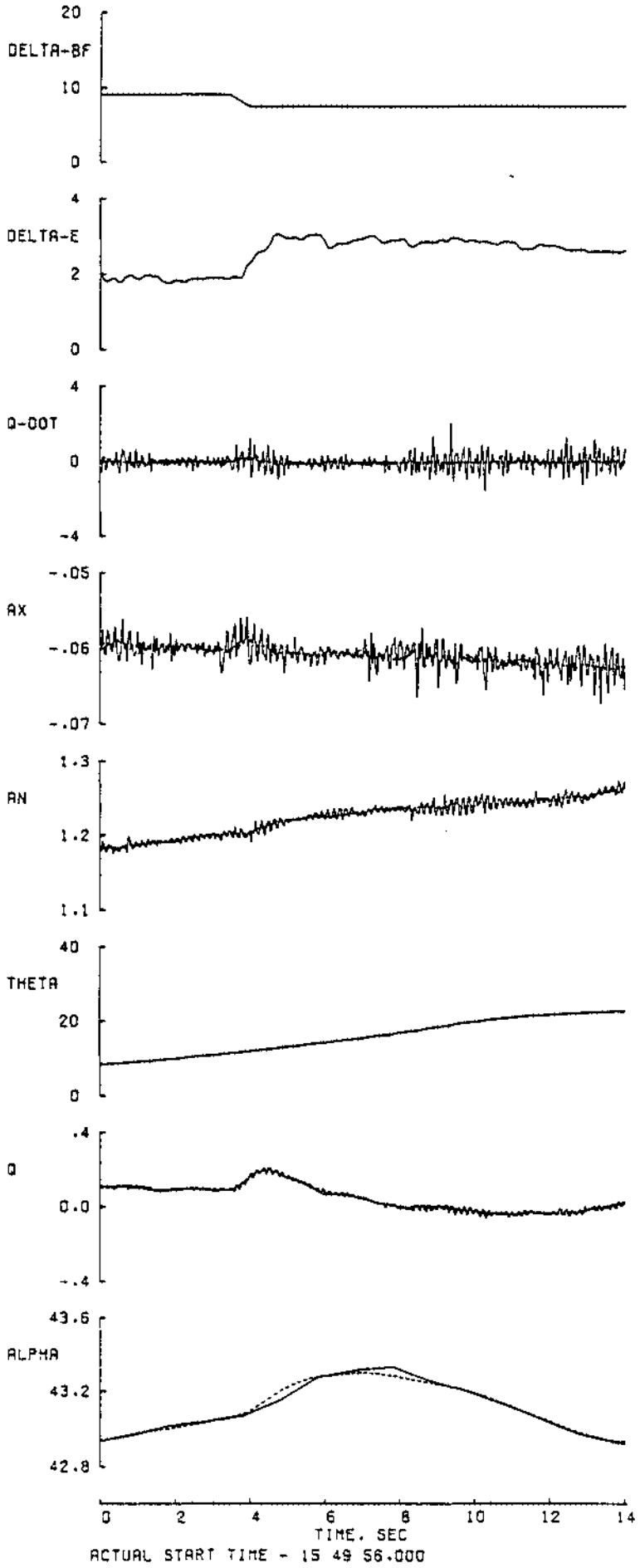

Figure 15 Body Flap Maneuver Results - STS-3

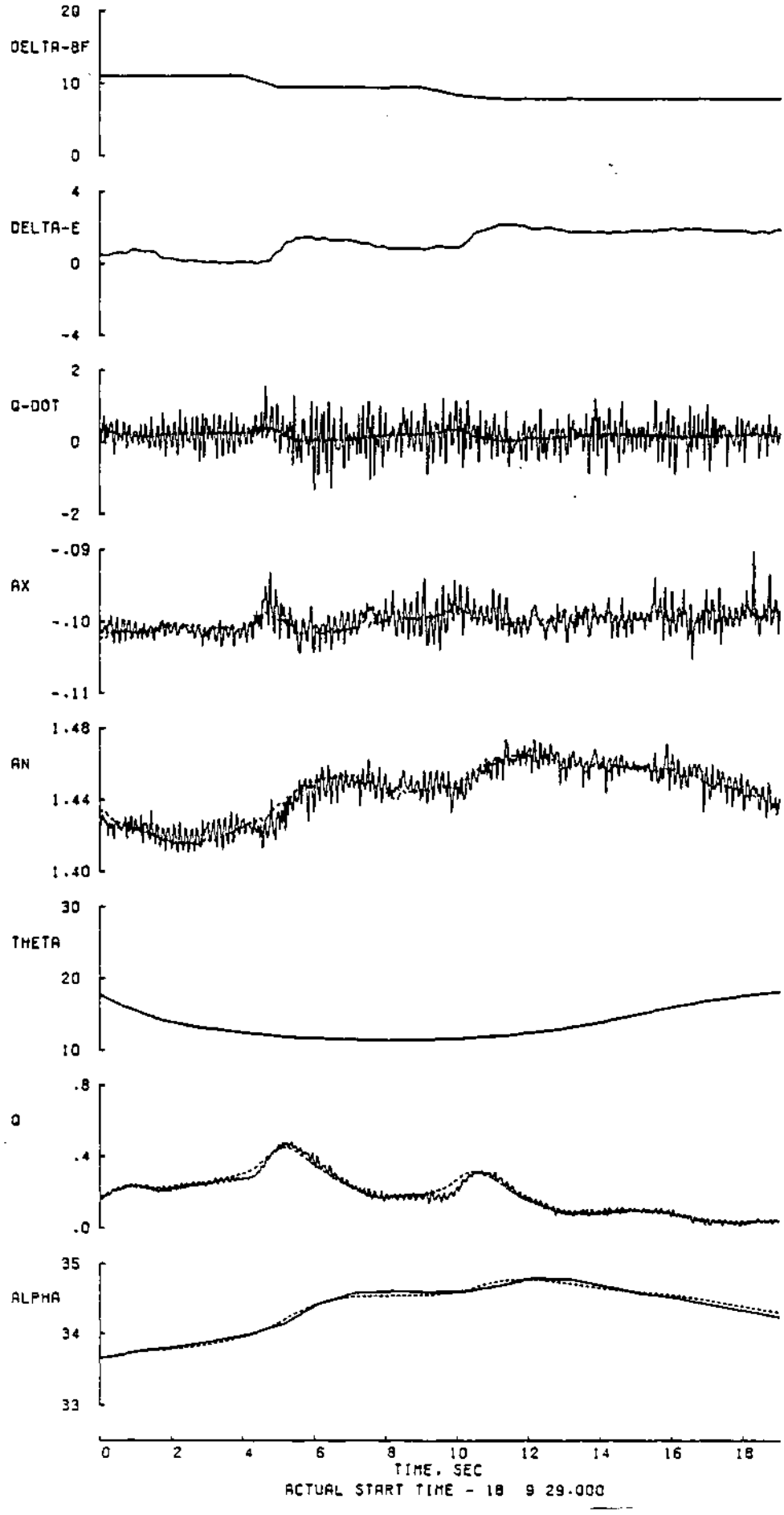

Figure 16 Body Flap Maneuver Results - STS-1

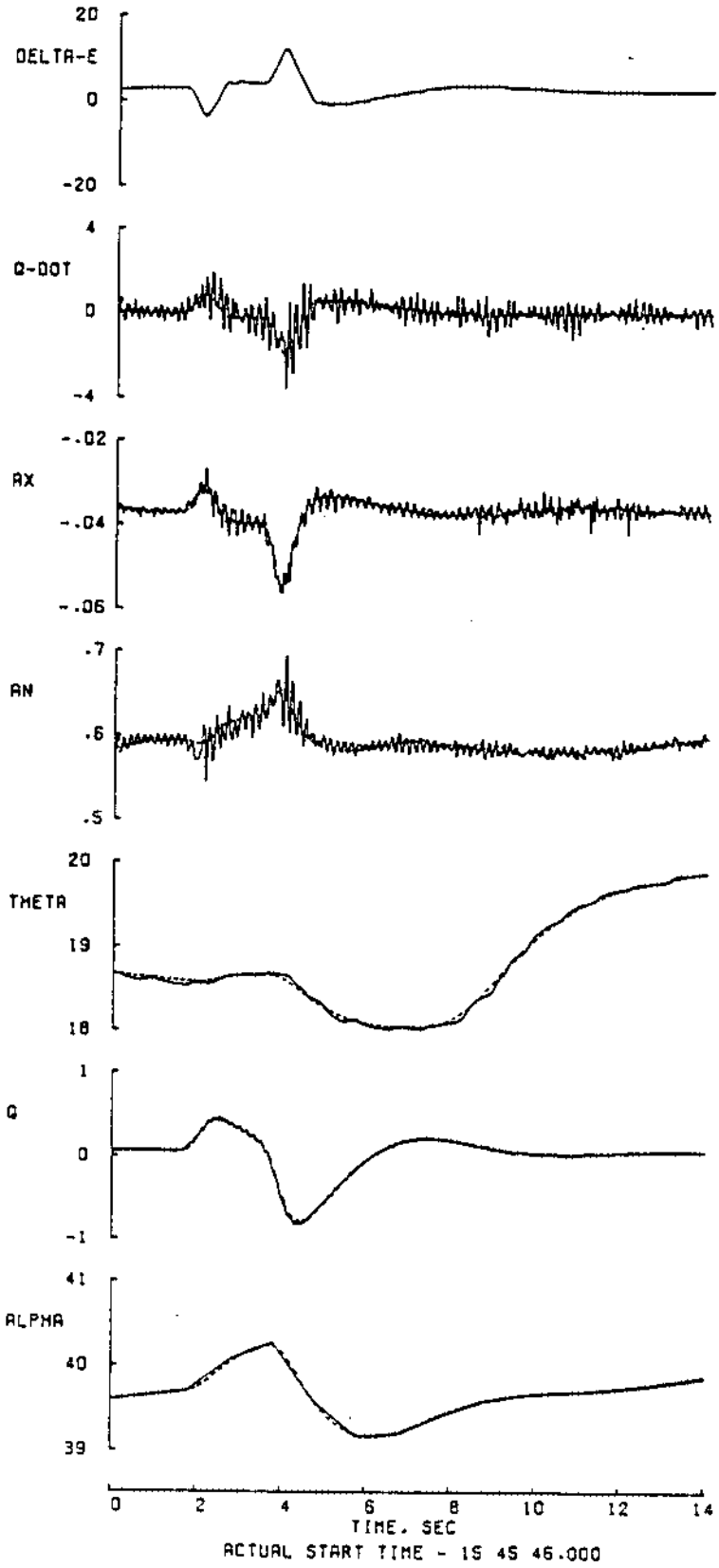

 Figure 17 Curve Fit with Second Order Derivative

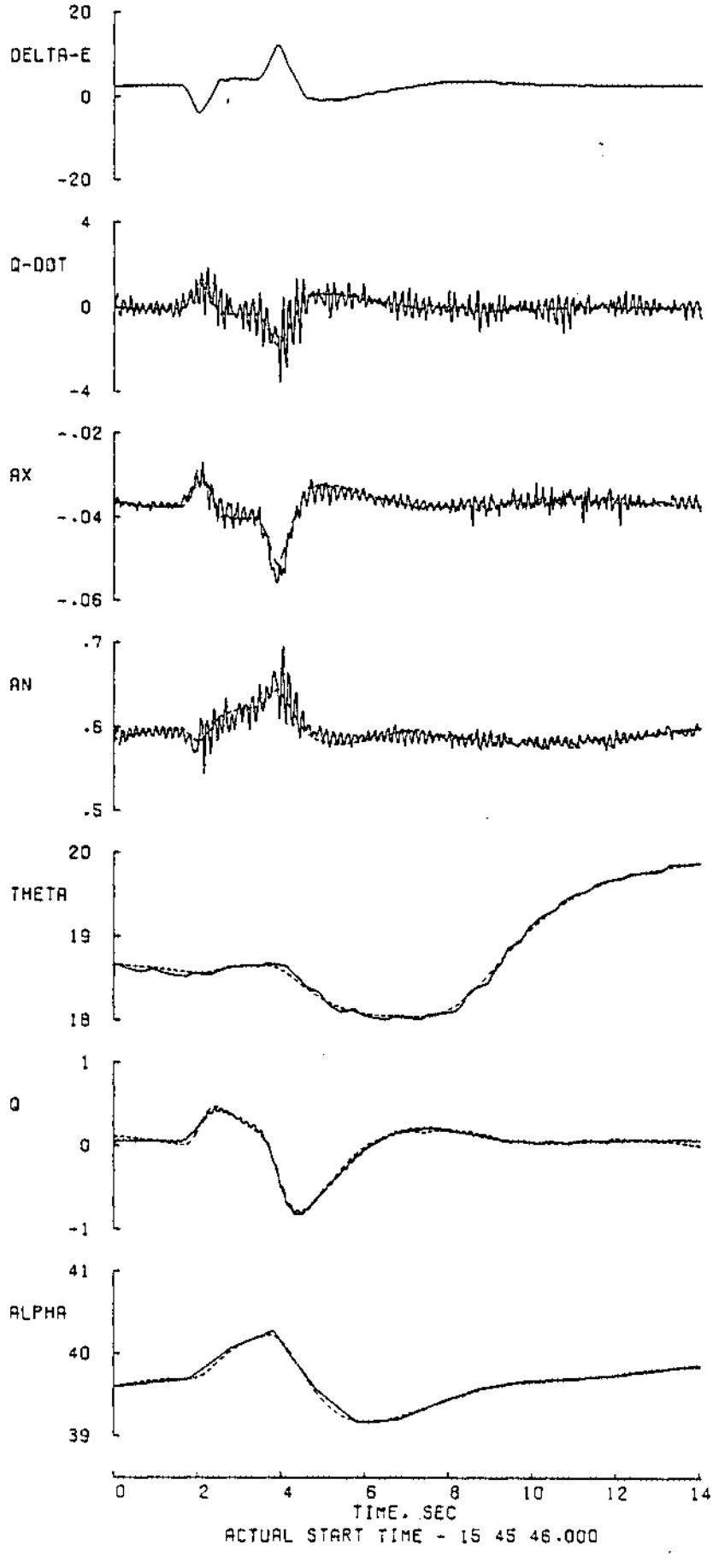

Figure 18 Curve Fit Without Second Order Derivative

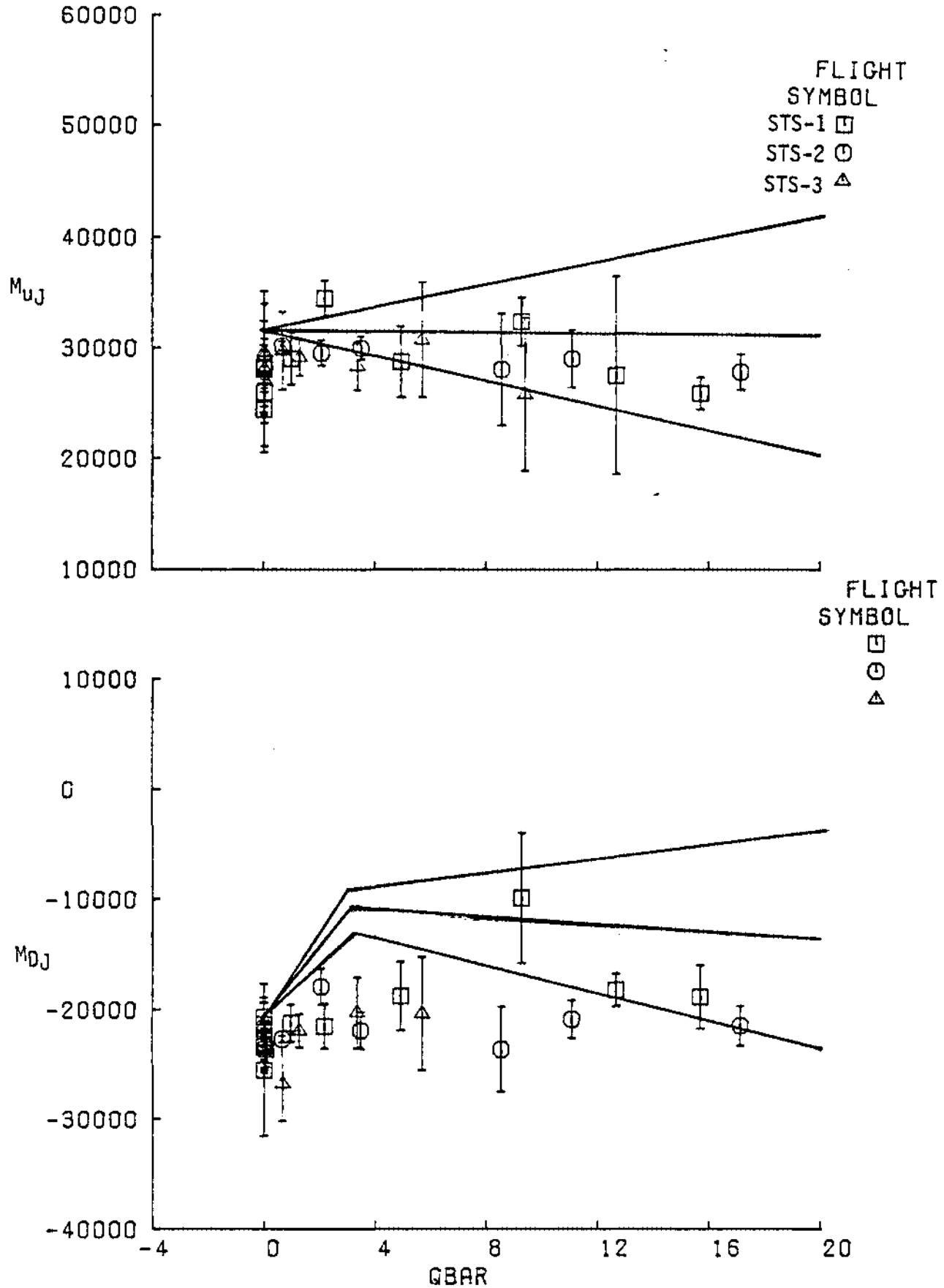

Figure 19 Moments From Pitch RCS Jets

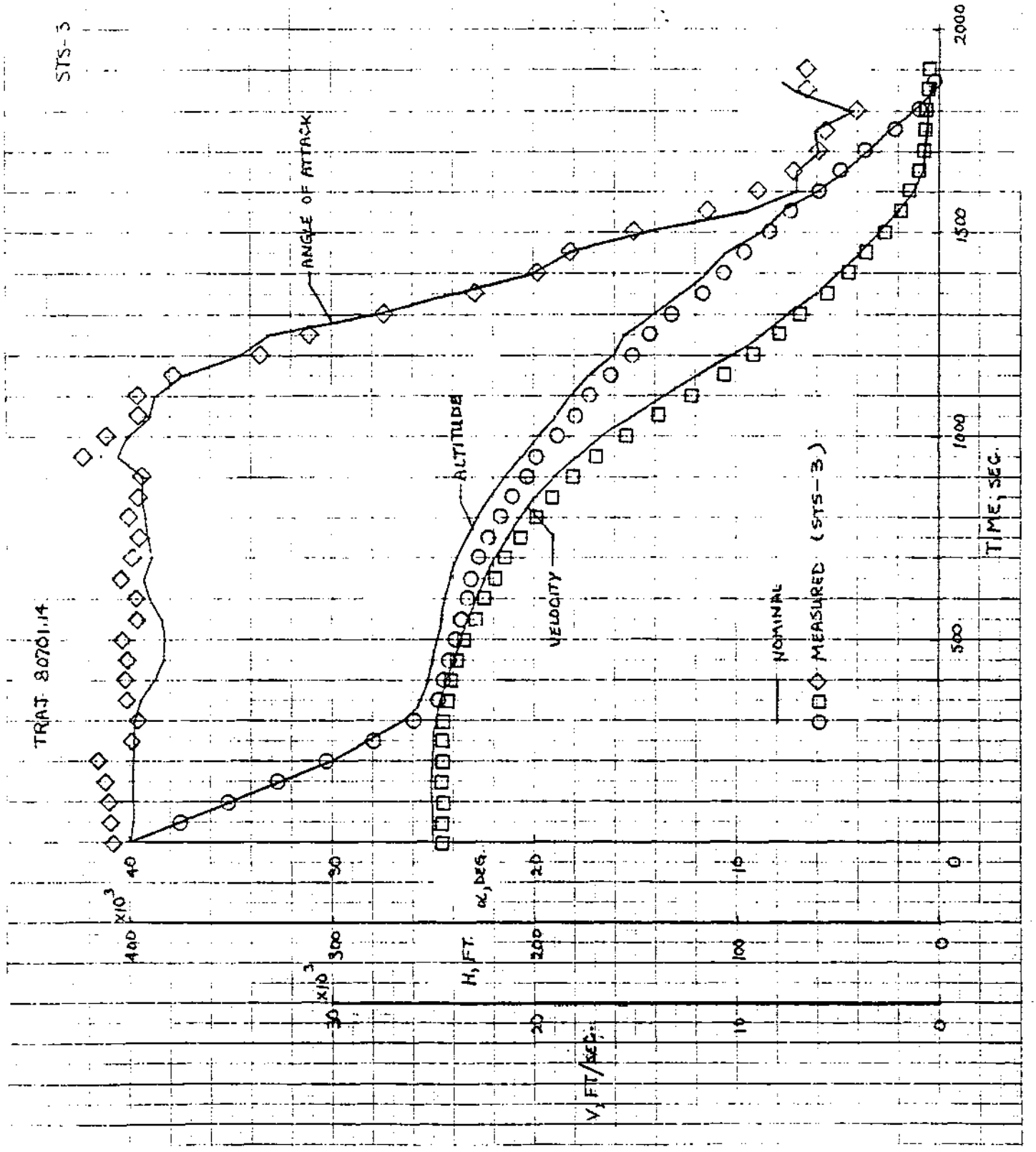

Figure 20 - Trajectory Comparison of Flight vs Predicted

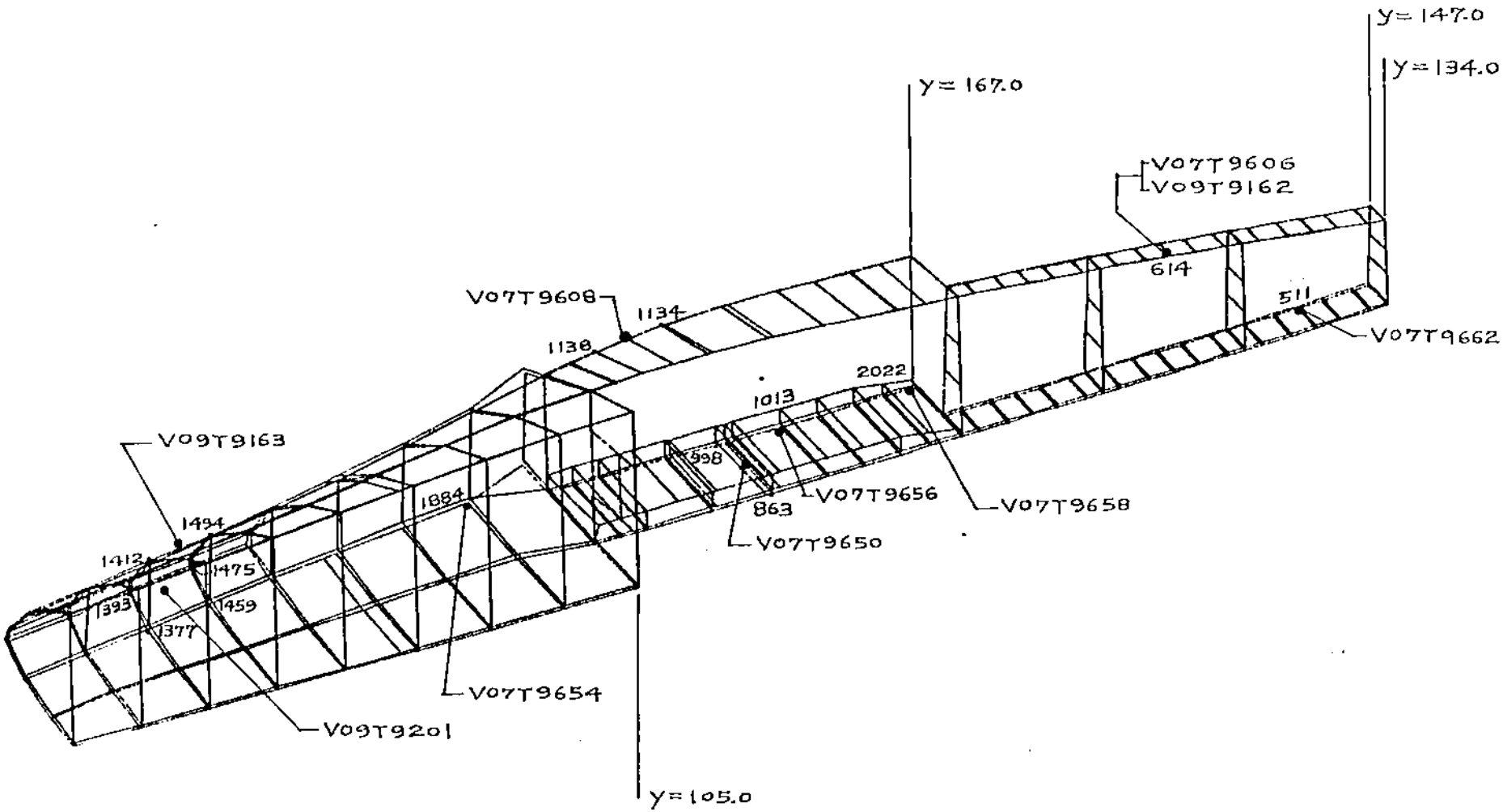

FIGURE 21 WS134 TPS TC LOCATIONS.

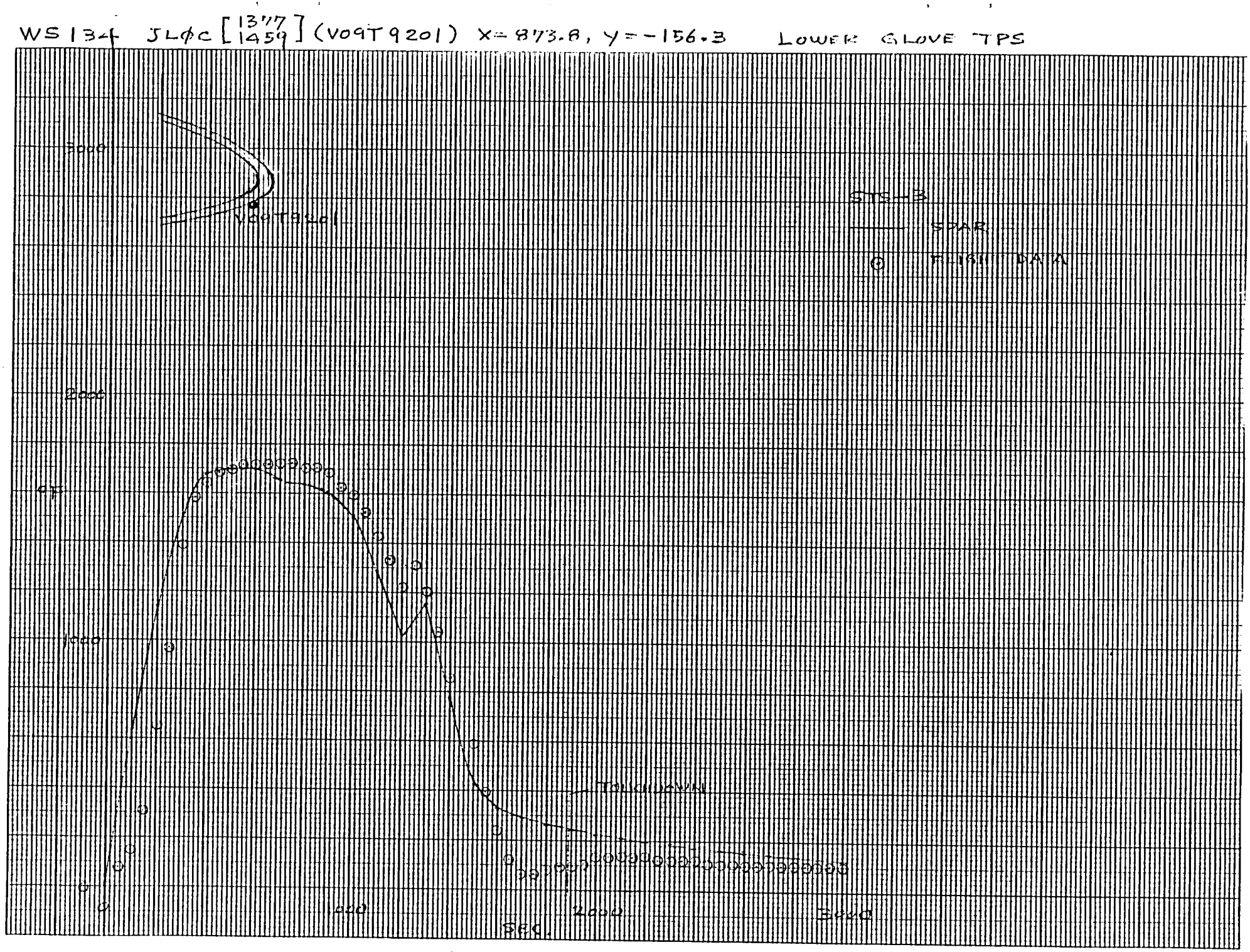

Figure 22 - TPS Surface Temperatures - WS 134

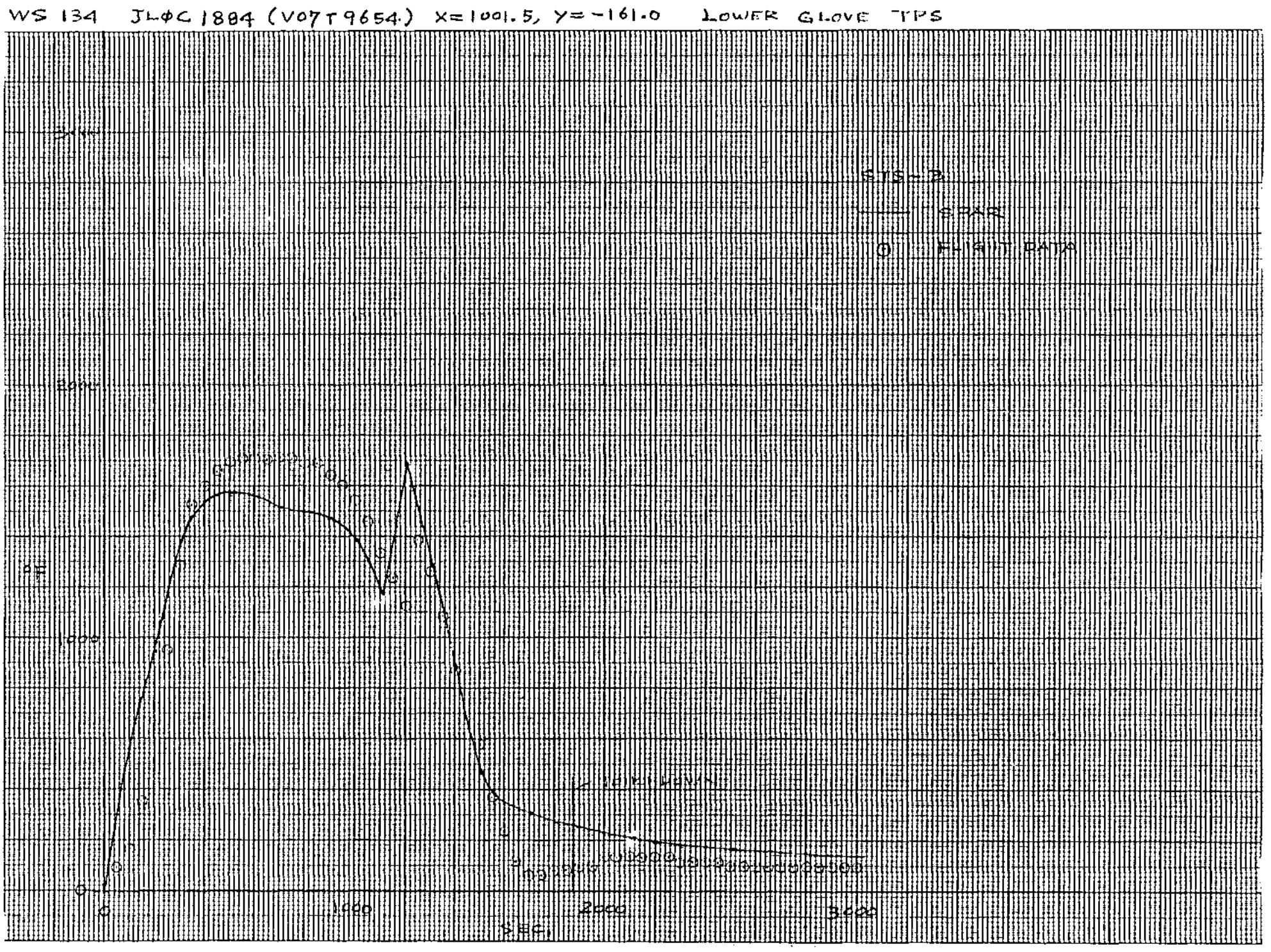

Figure 23 - TPS Surface Temperatures - WS 134

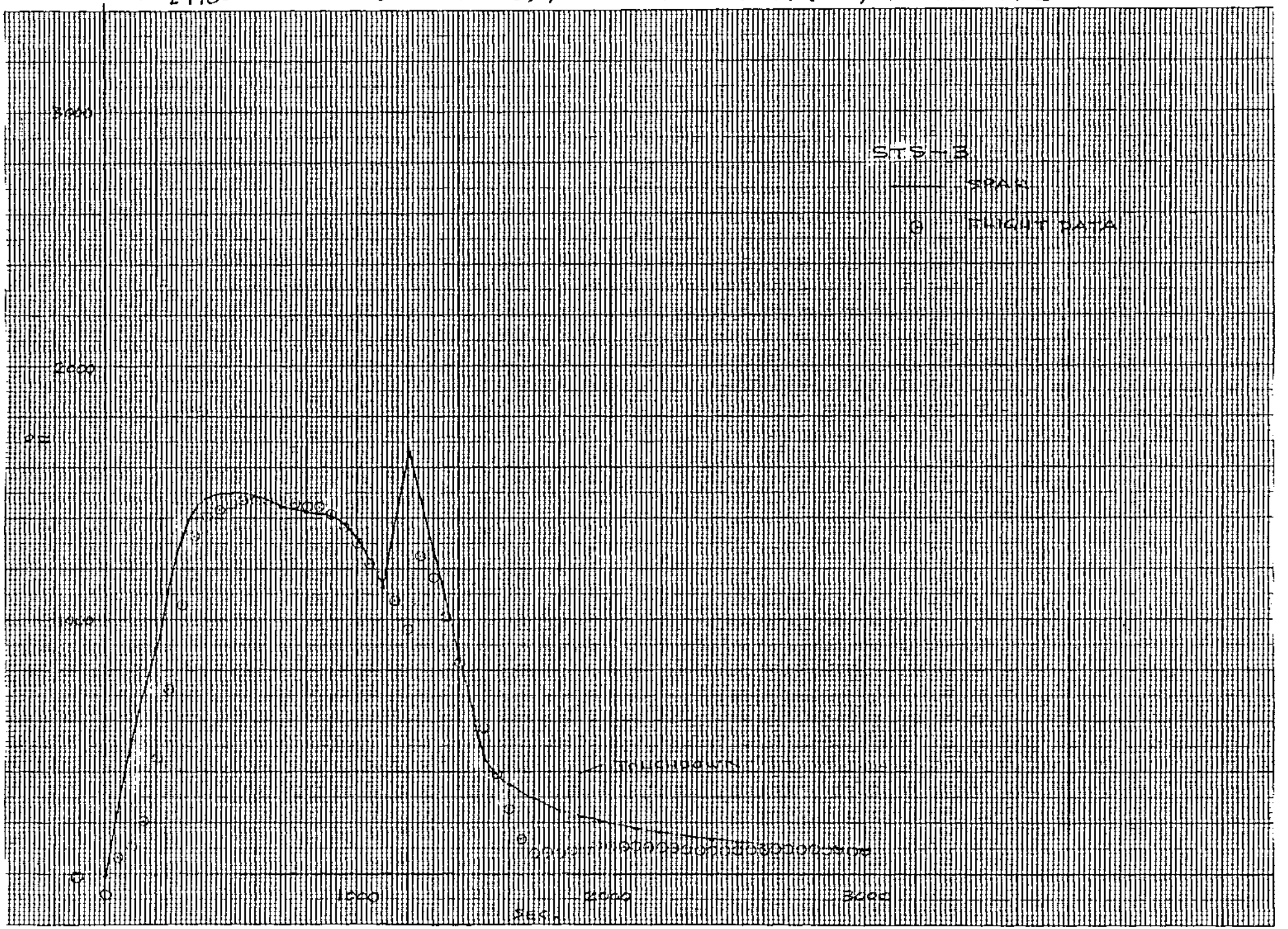

Figure 24 - TPS Surface Temperatures - WS 134

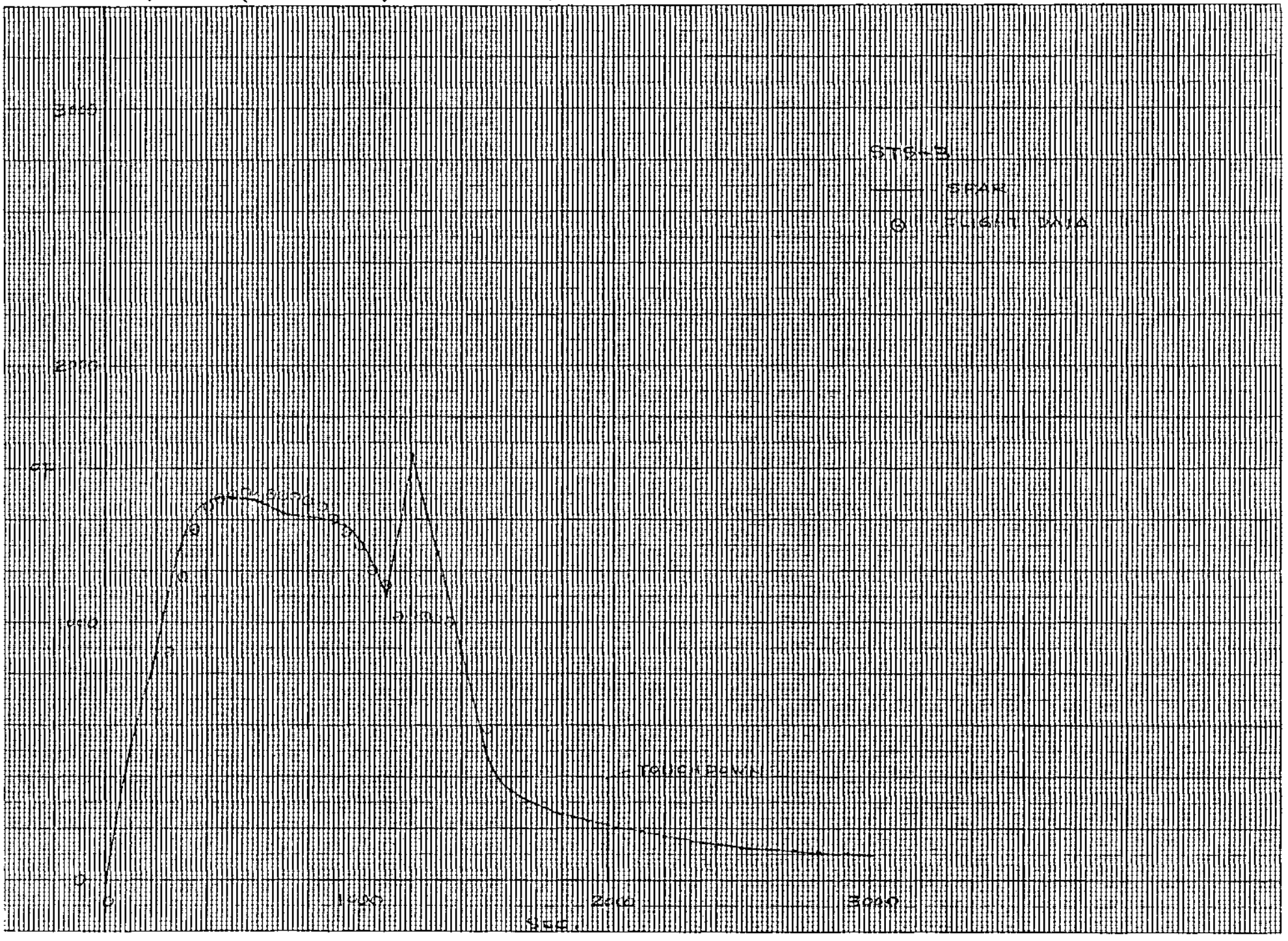

Figure 25 - TPS Surface Temperatures - WS 134

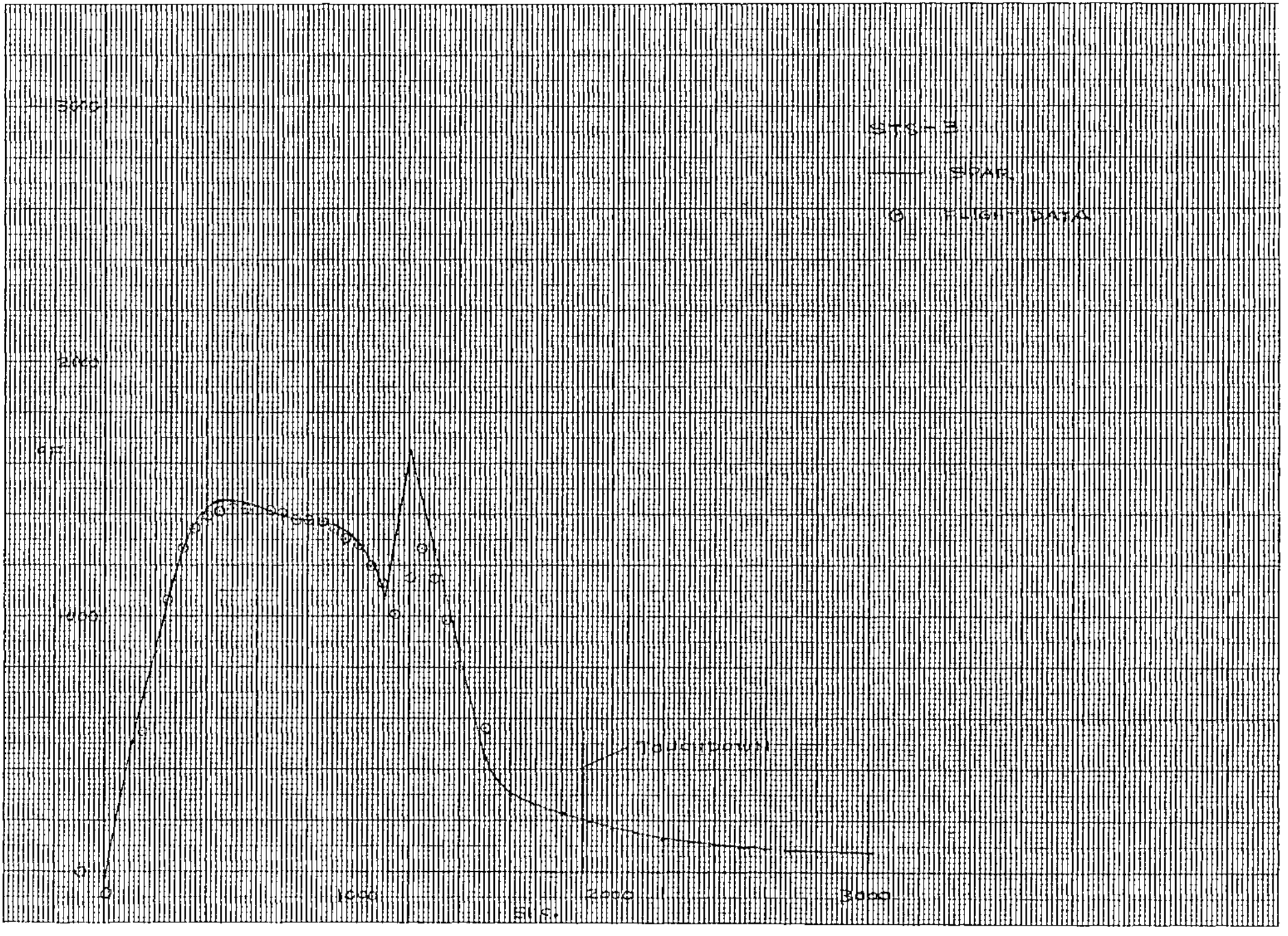

Figure 26 - TPS Surface Temperatures - WS 134

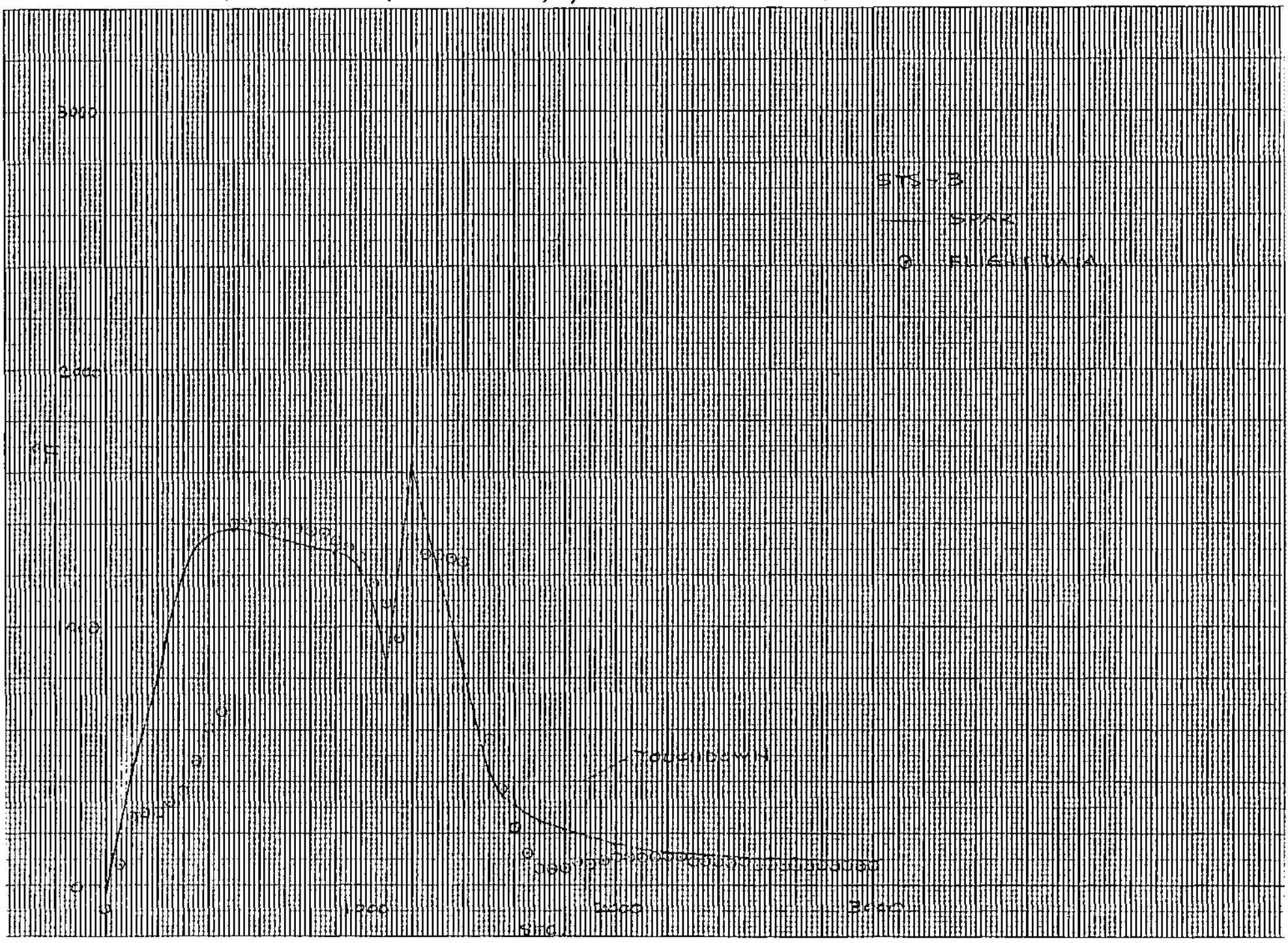

Figure 27 - TPS Surface Temperatures - WS 134

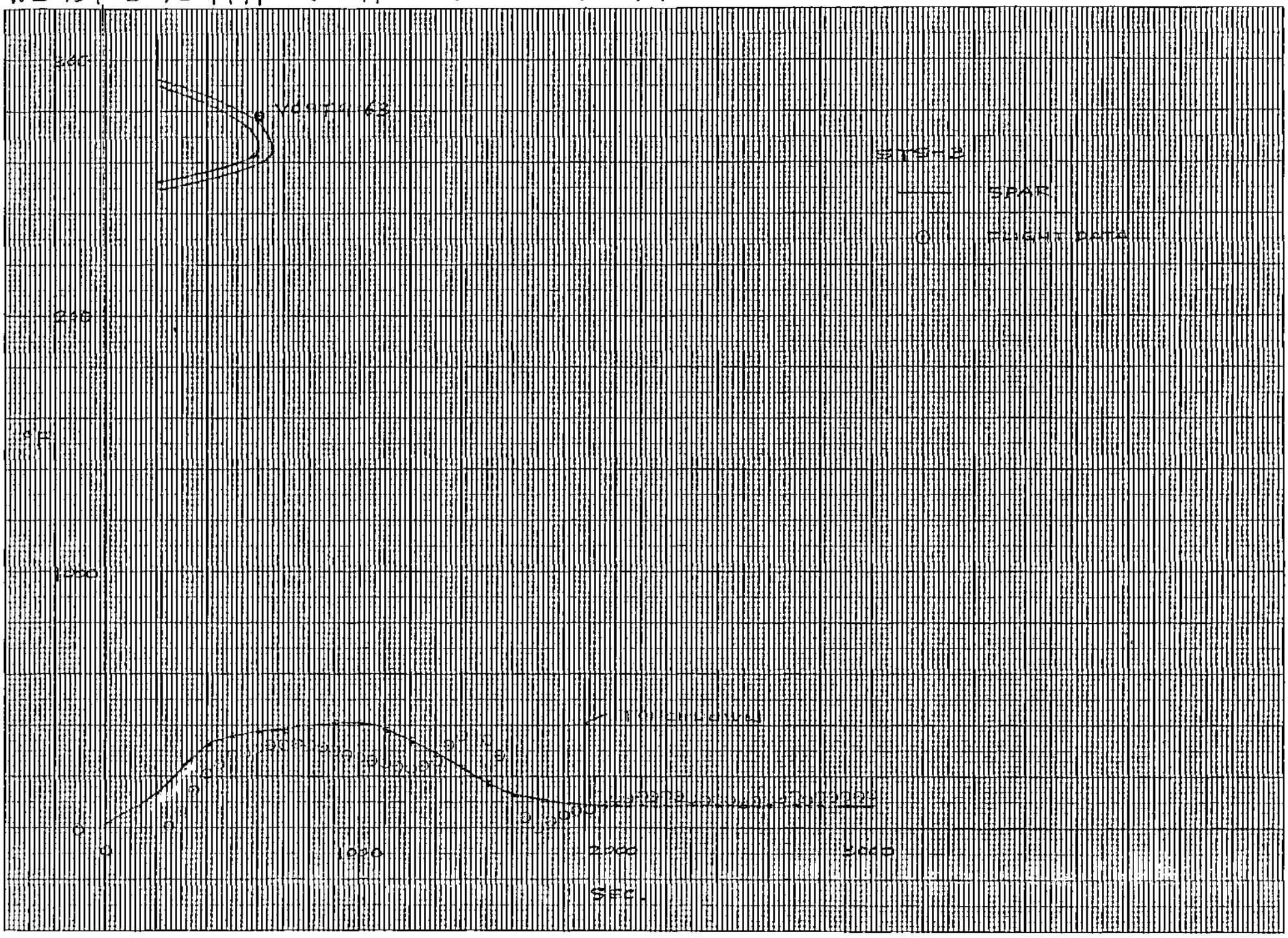

Figure 28 - TPS Surface Temperatures - WS 134

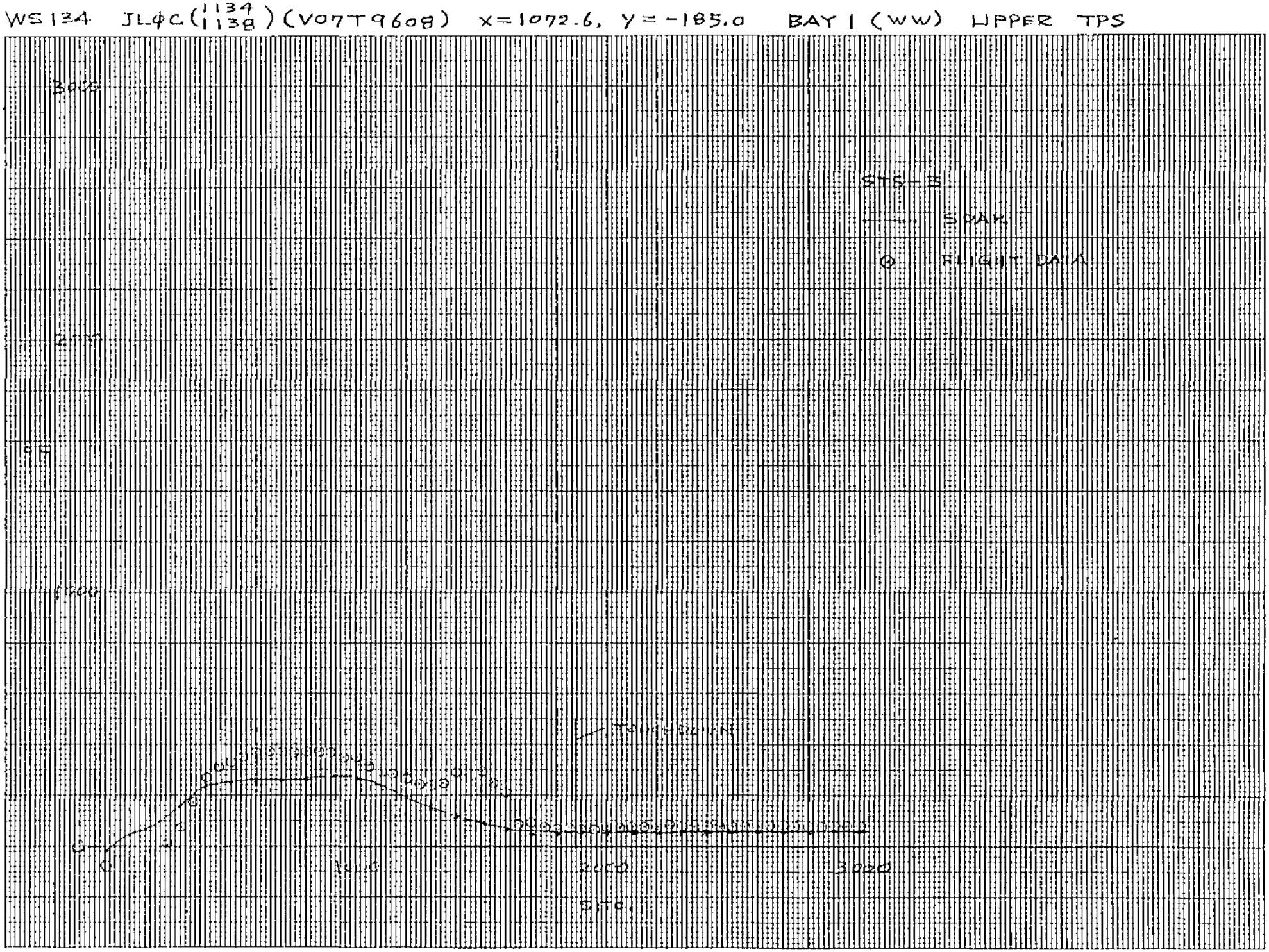

Figure 29 - TPS Surface Temperatures - WS 134

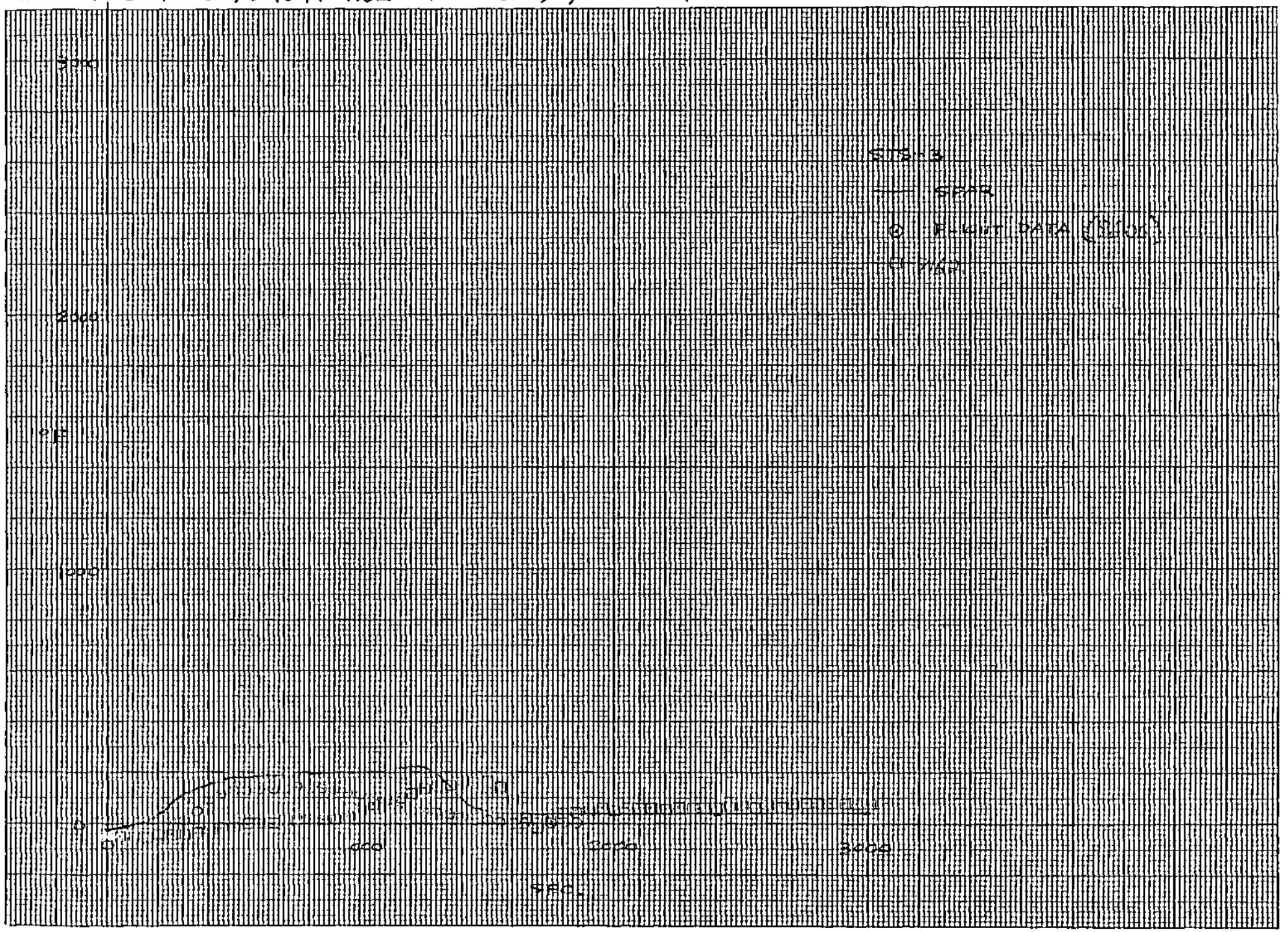

Figure 30 - TPS Surface Temperatures - WS 134

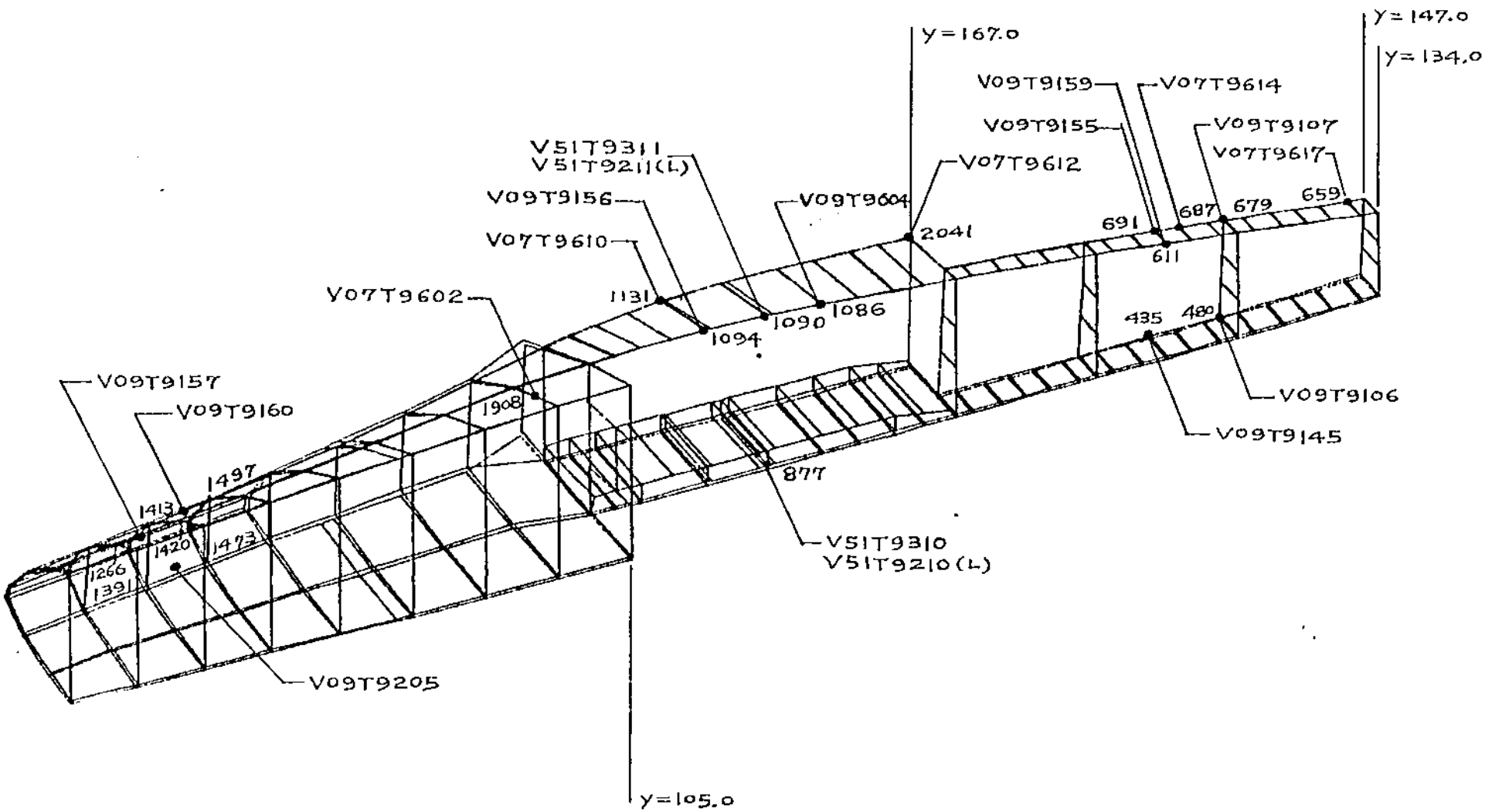

FIGURE 31 WS 134 ALUMINUM STRUCTURE TC LOCATIONS.

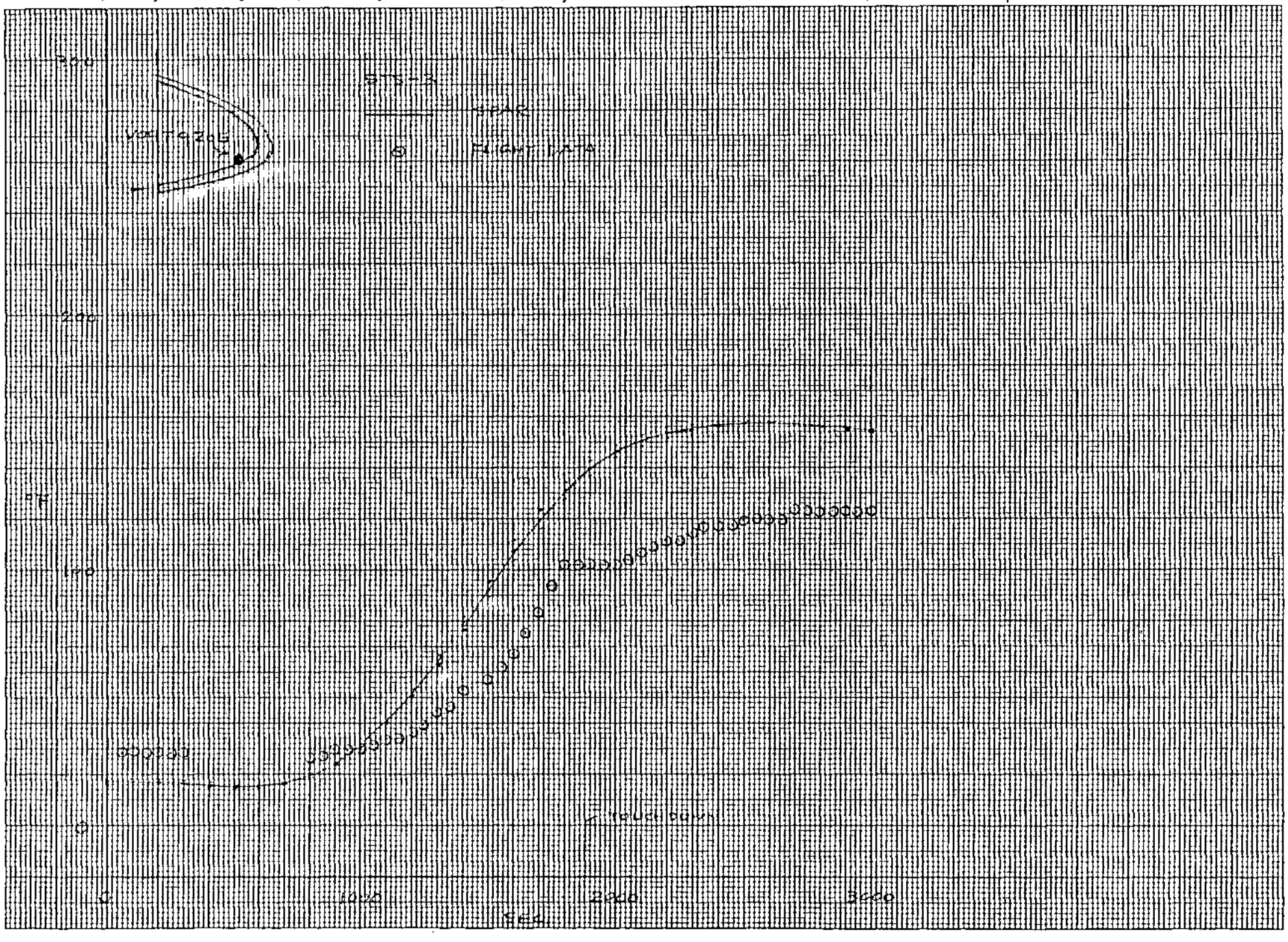

Figure 32 - Structural Temperatures - WS 134

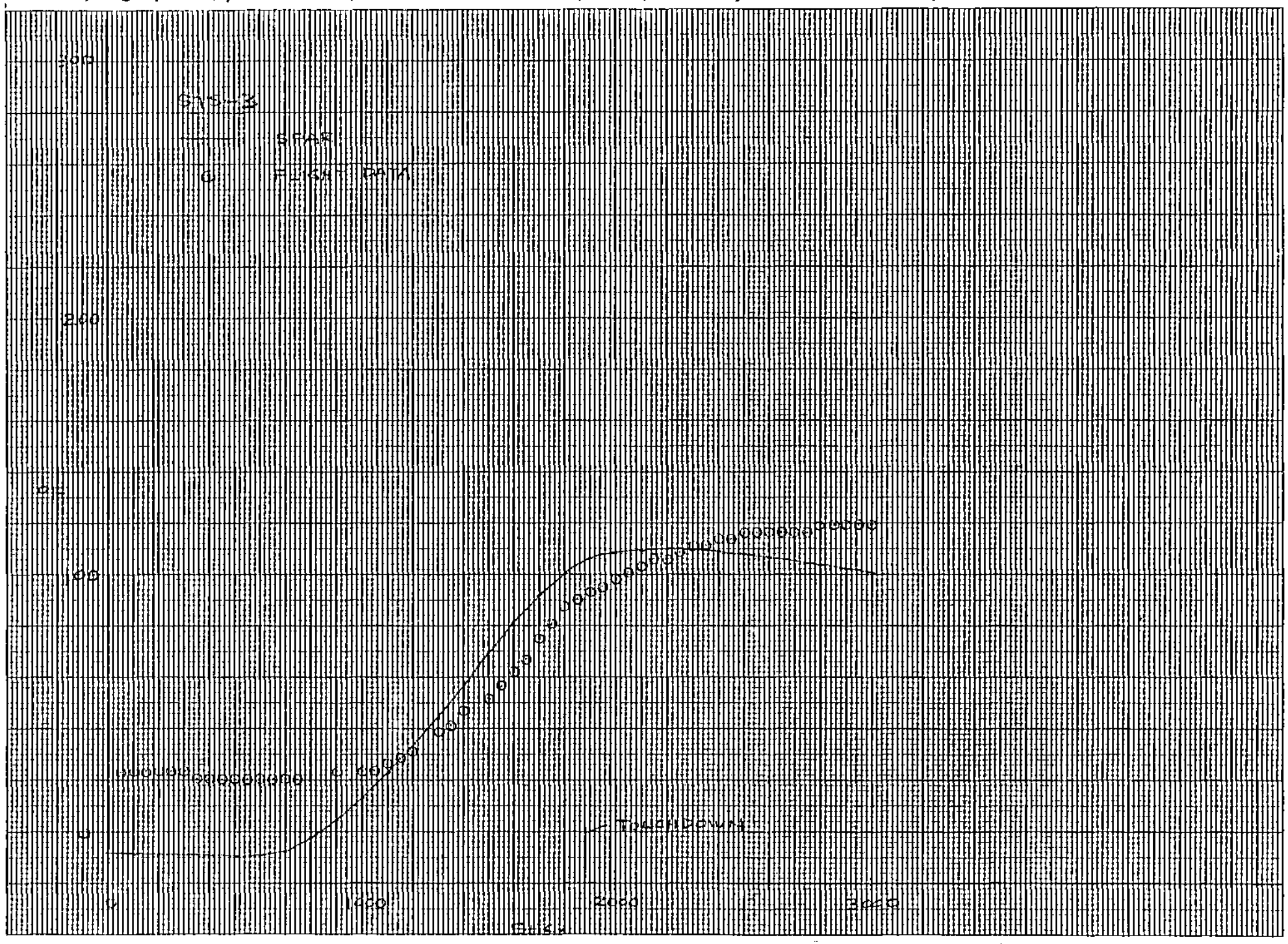

Figure 33 - Structural Temperatures - WS 134

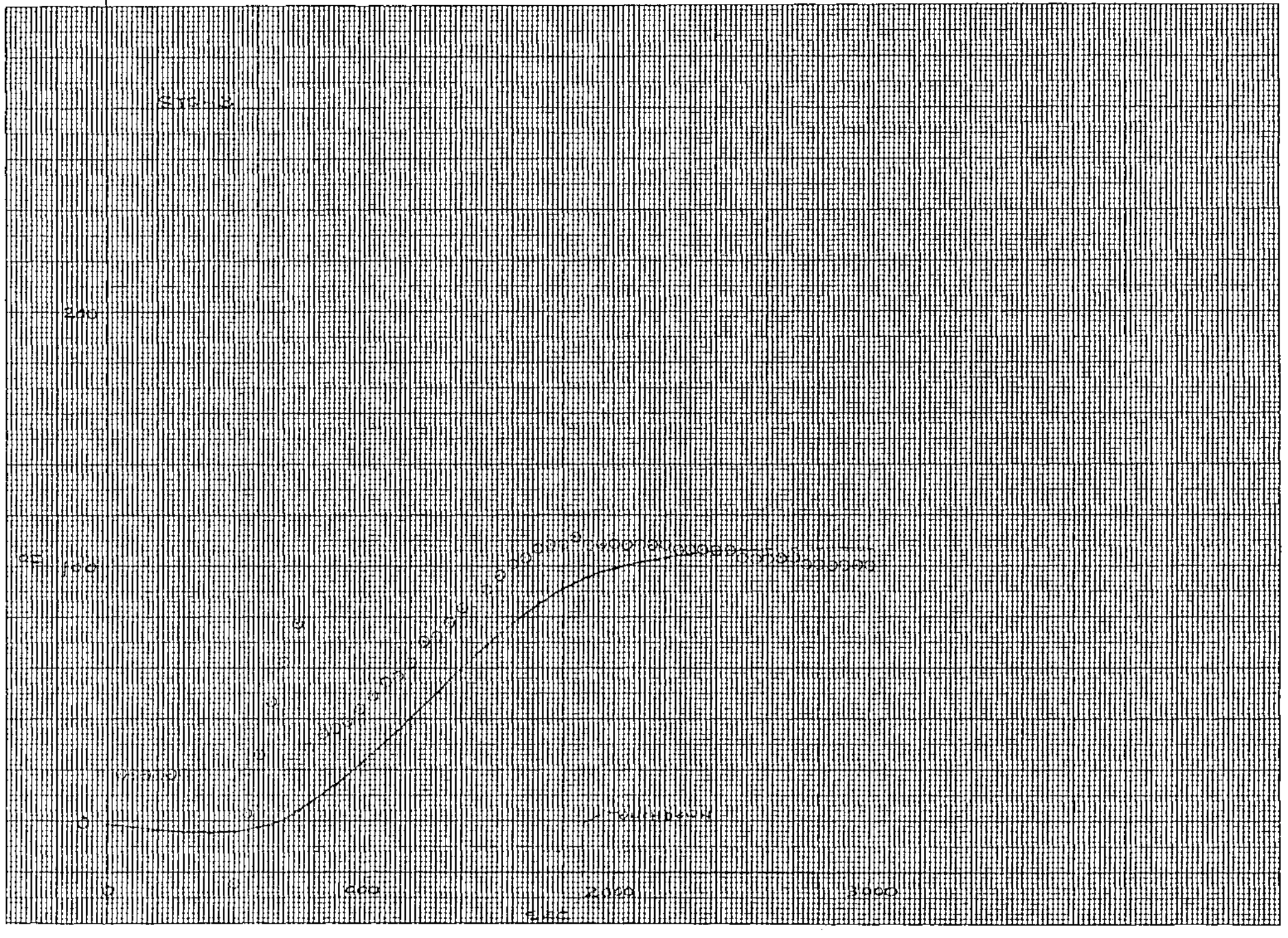

Figure 34 - Structural Temperatures - WS 134

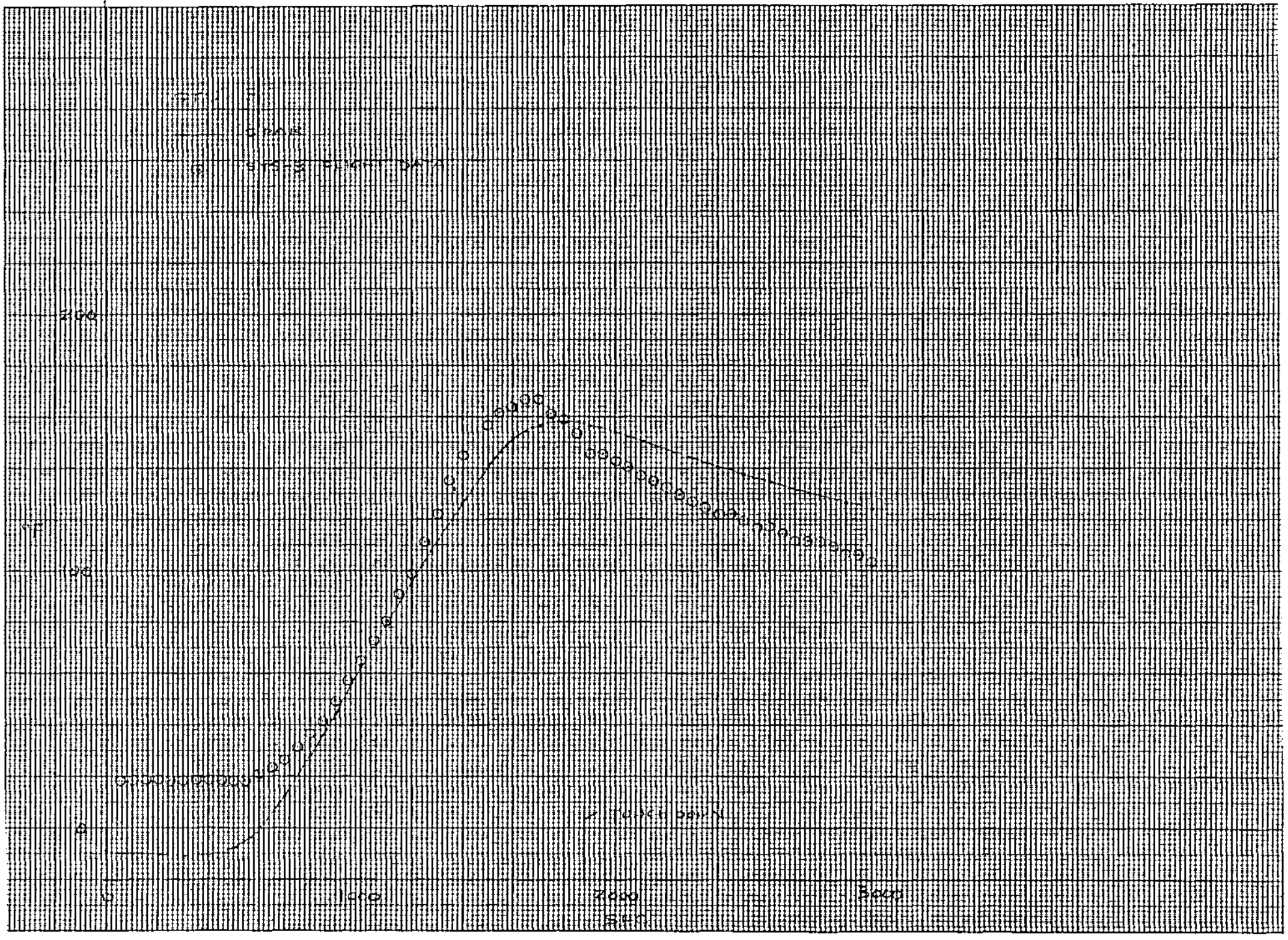

Figure 35 - Structural Temperatures - WS 134

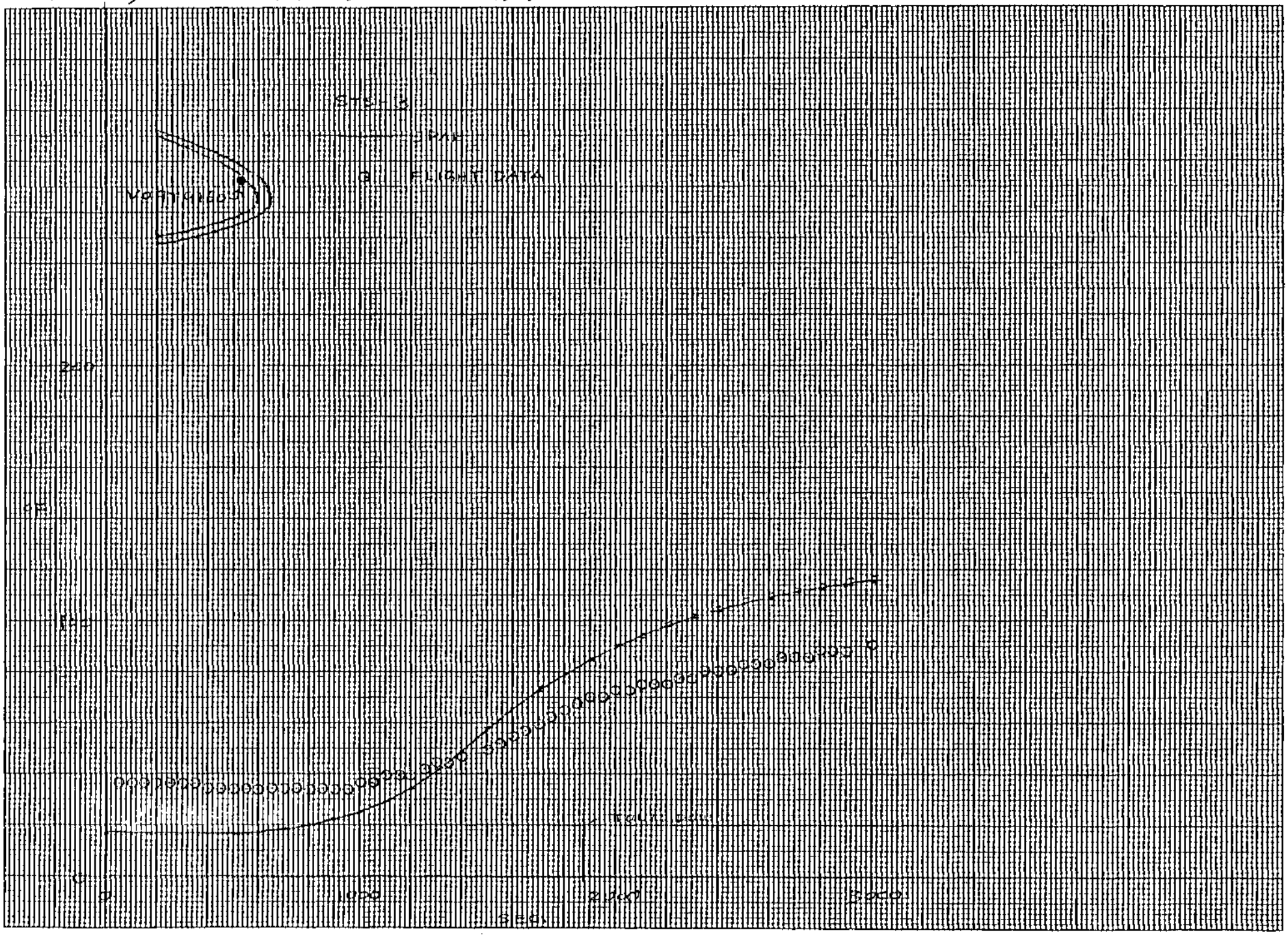

Figure 36 - Structural Temperatures - WS 134

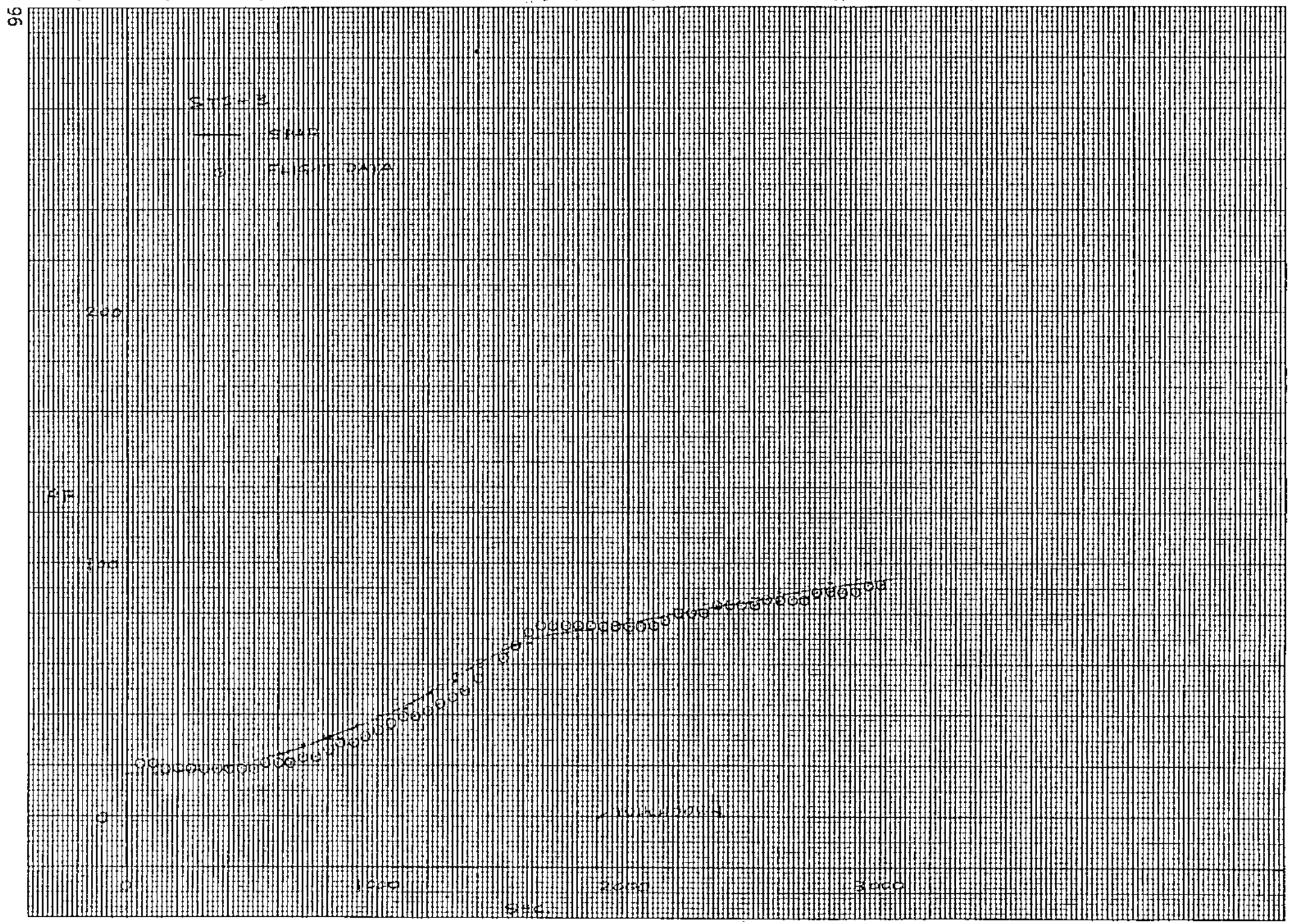

Figure 37 - Structural Temperatures - WS 134

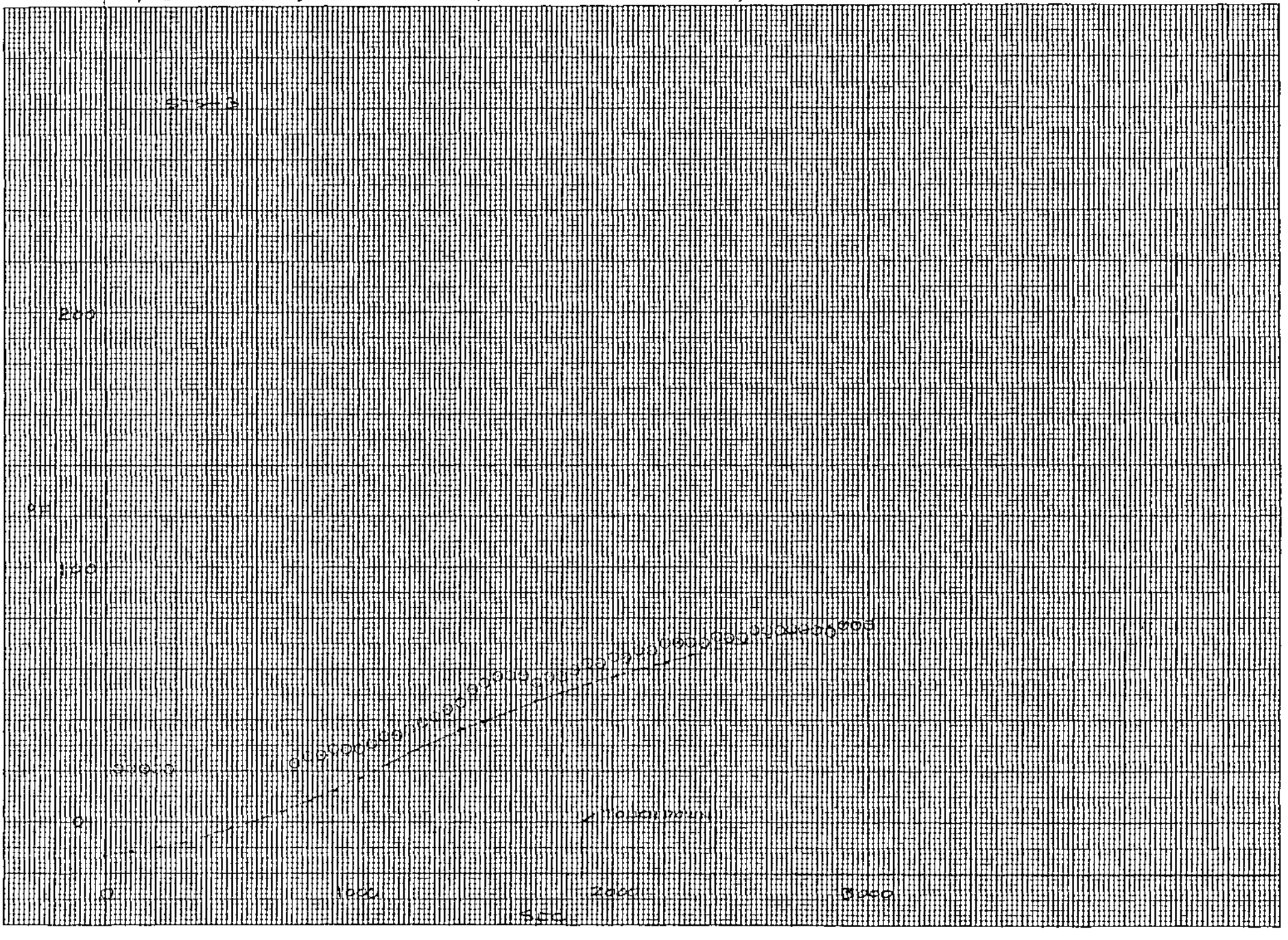

Figure 38 - Structural Temperatures - WS 134

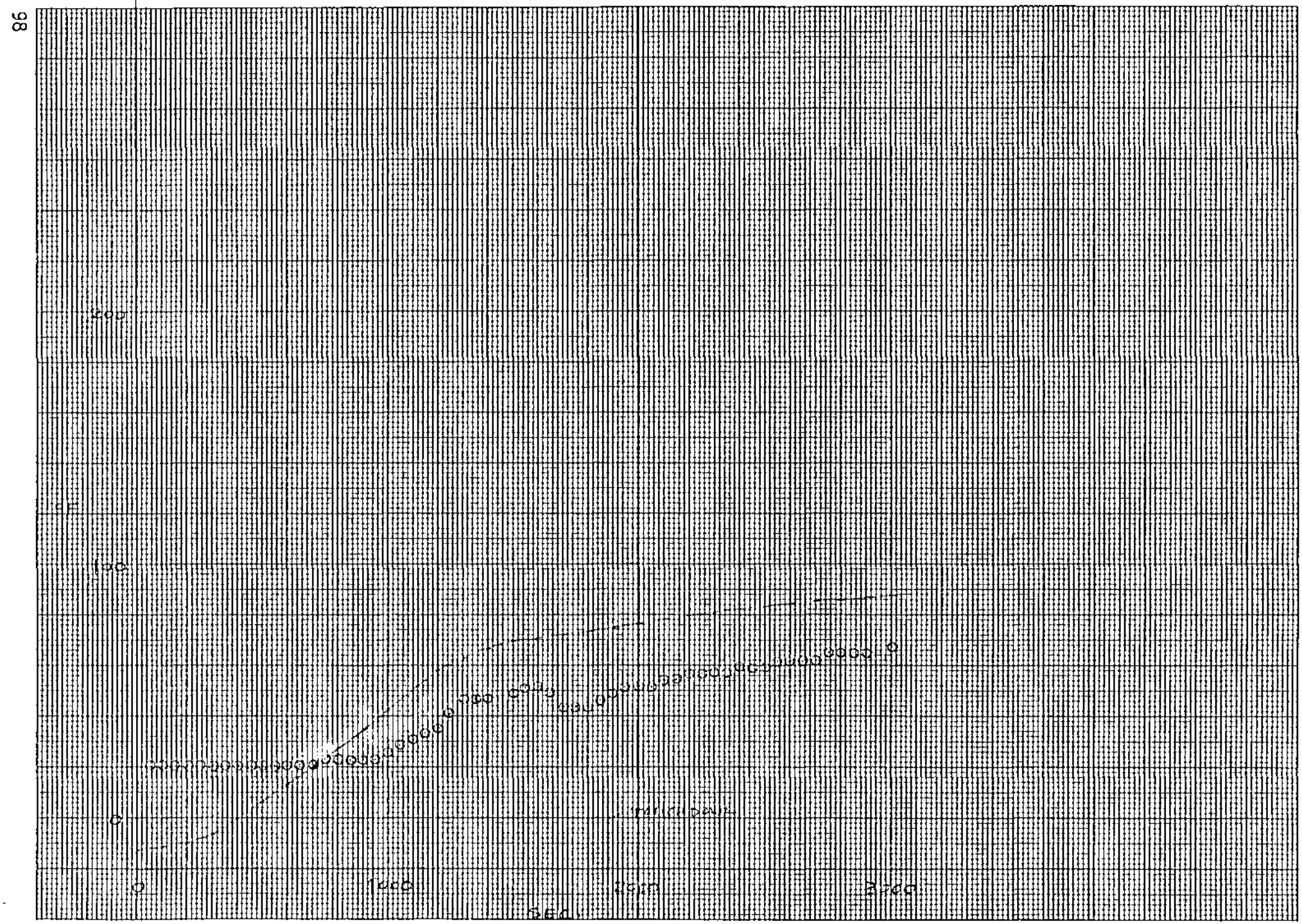

Figure 39 - Structural Temperatures - WS 134

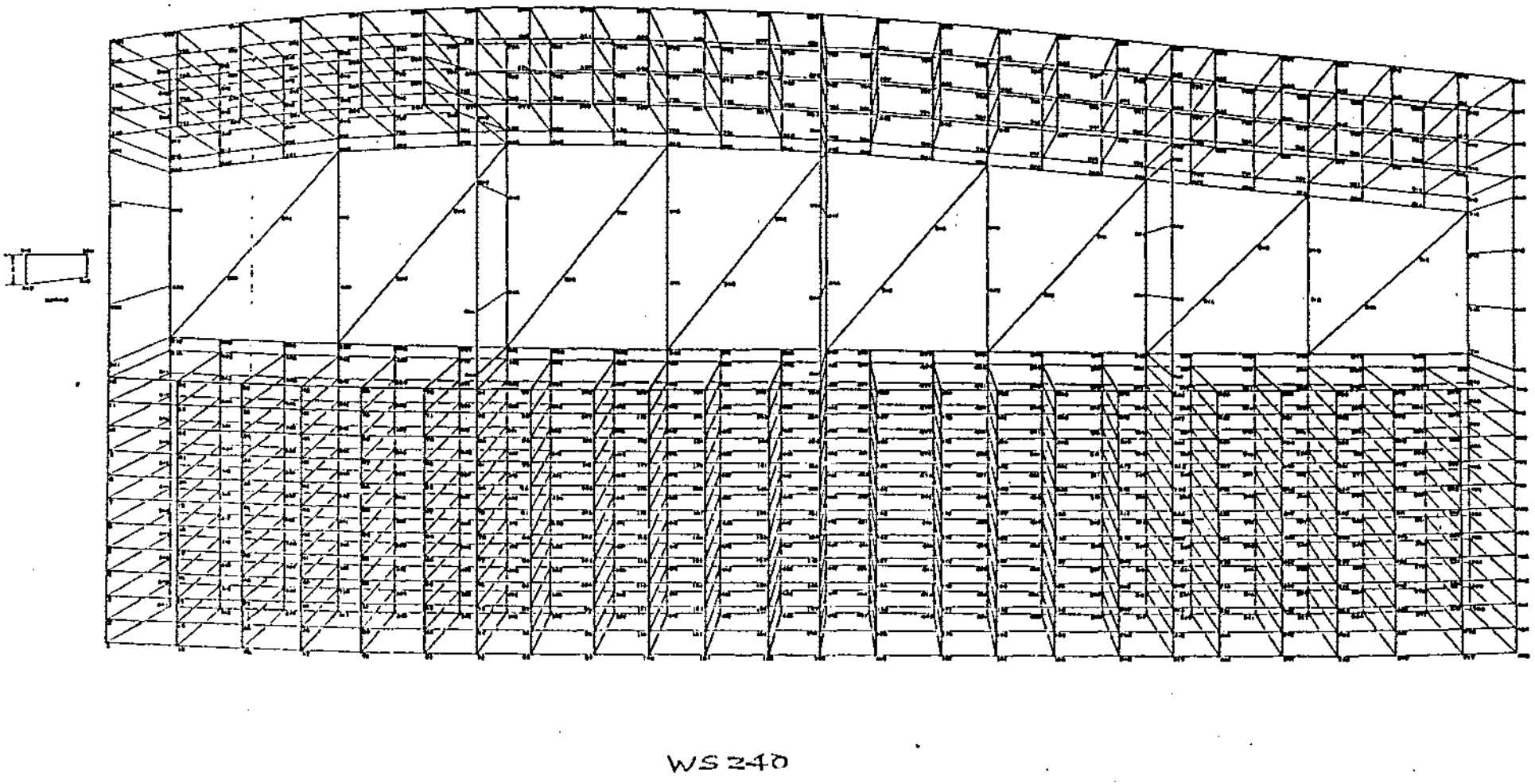

Figure 40 - SPAR Thermal Model of WS 240

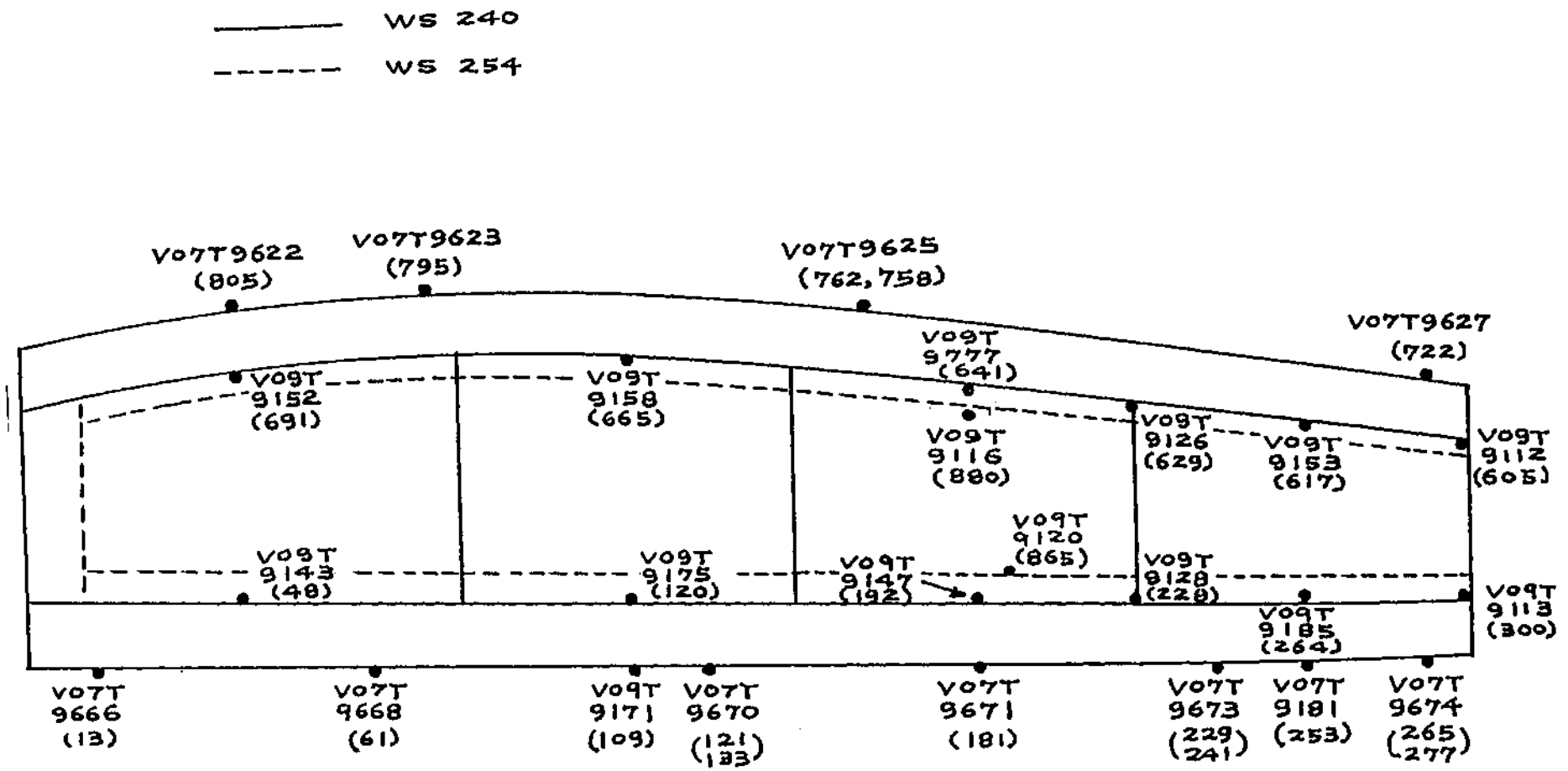

FIGURE 41. WS240 TC LOCATIONS.

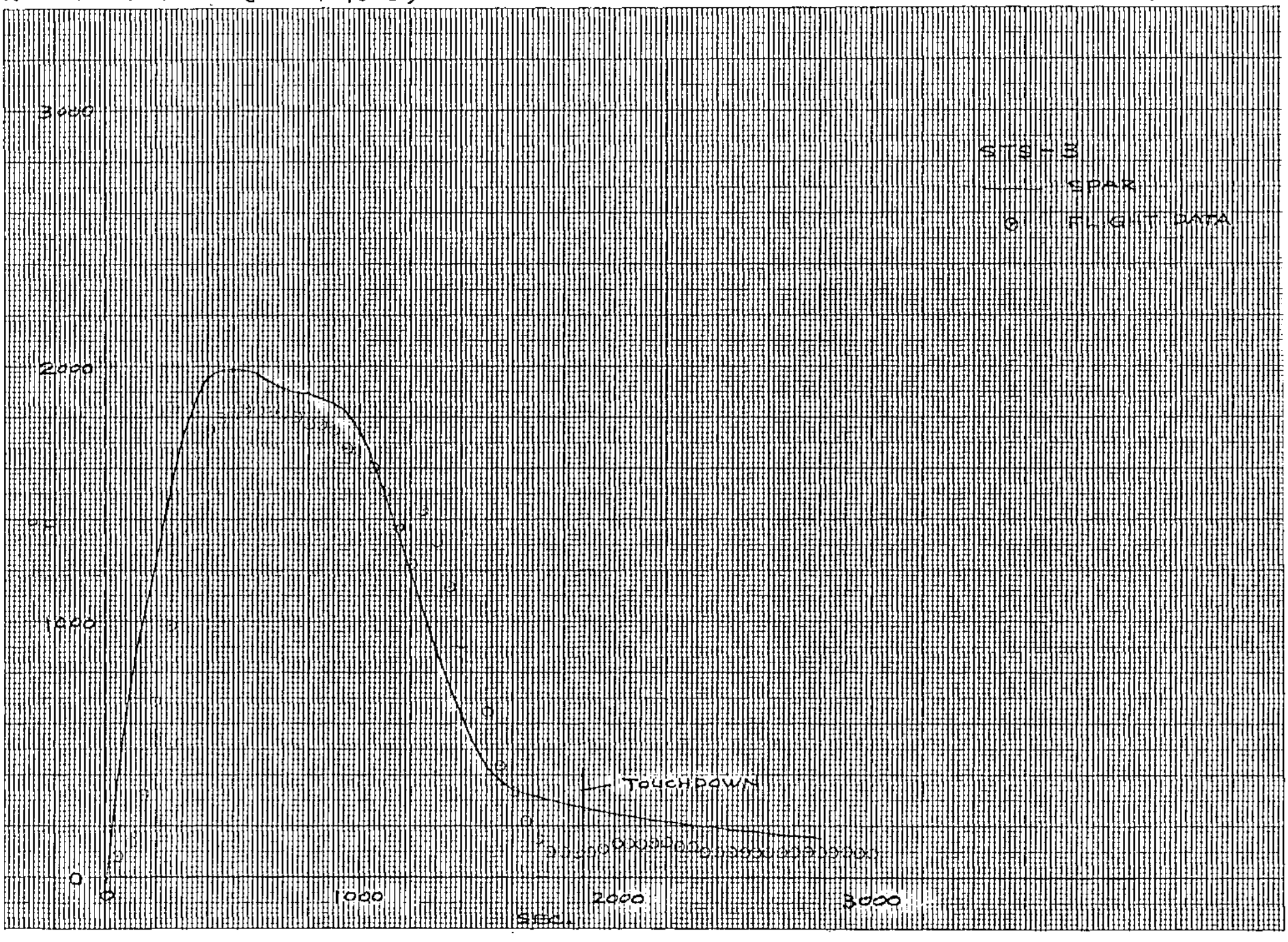

Figure 42 - TPS Surface Temperatures - WS 240

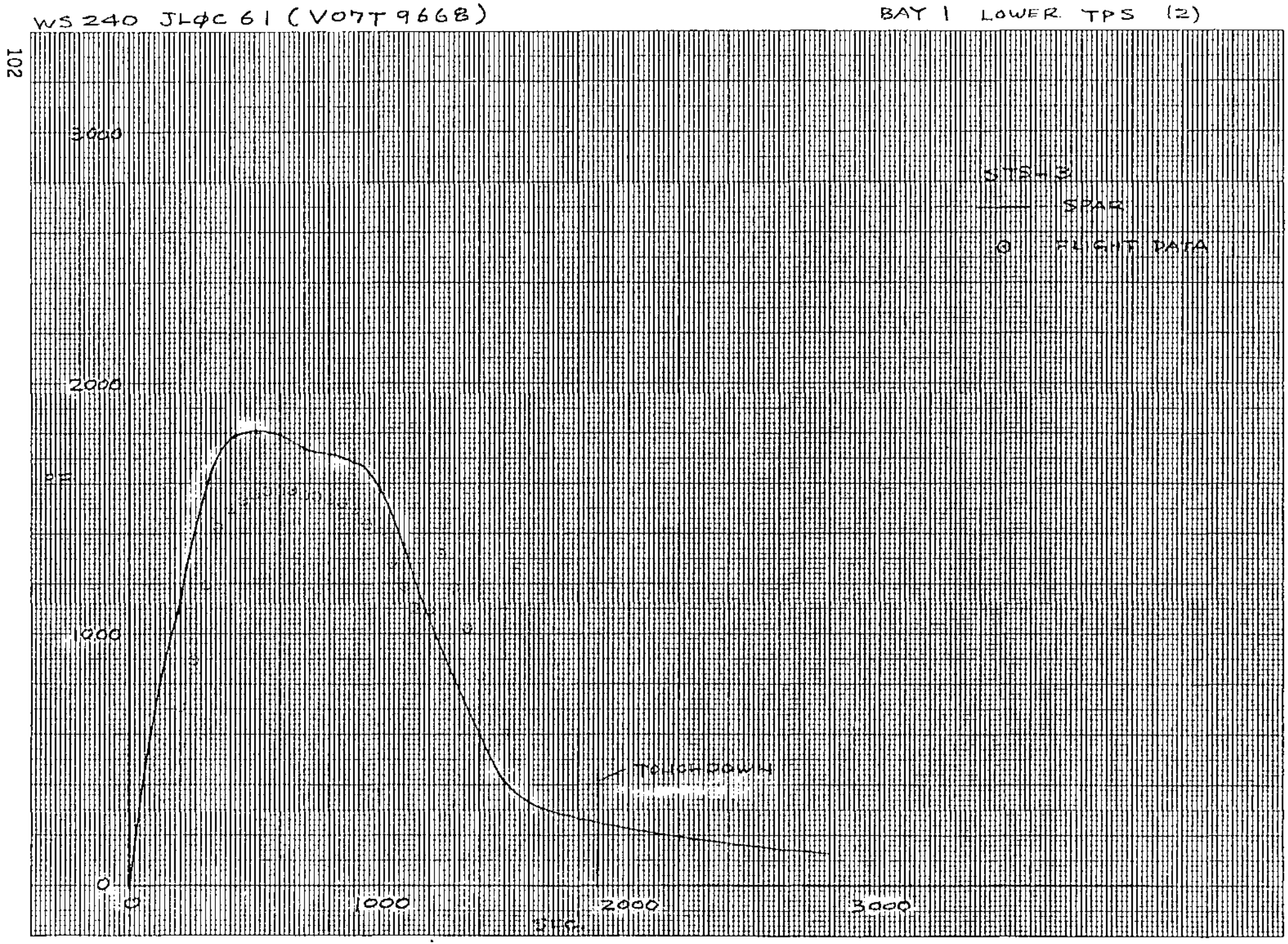

Figure 43 - TPS Surface Temperatures - WS 240

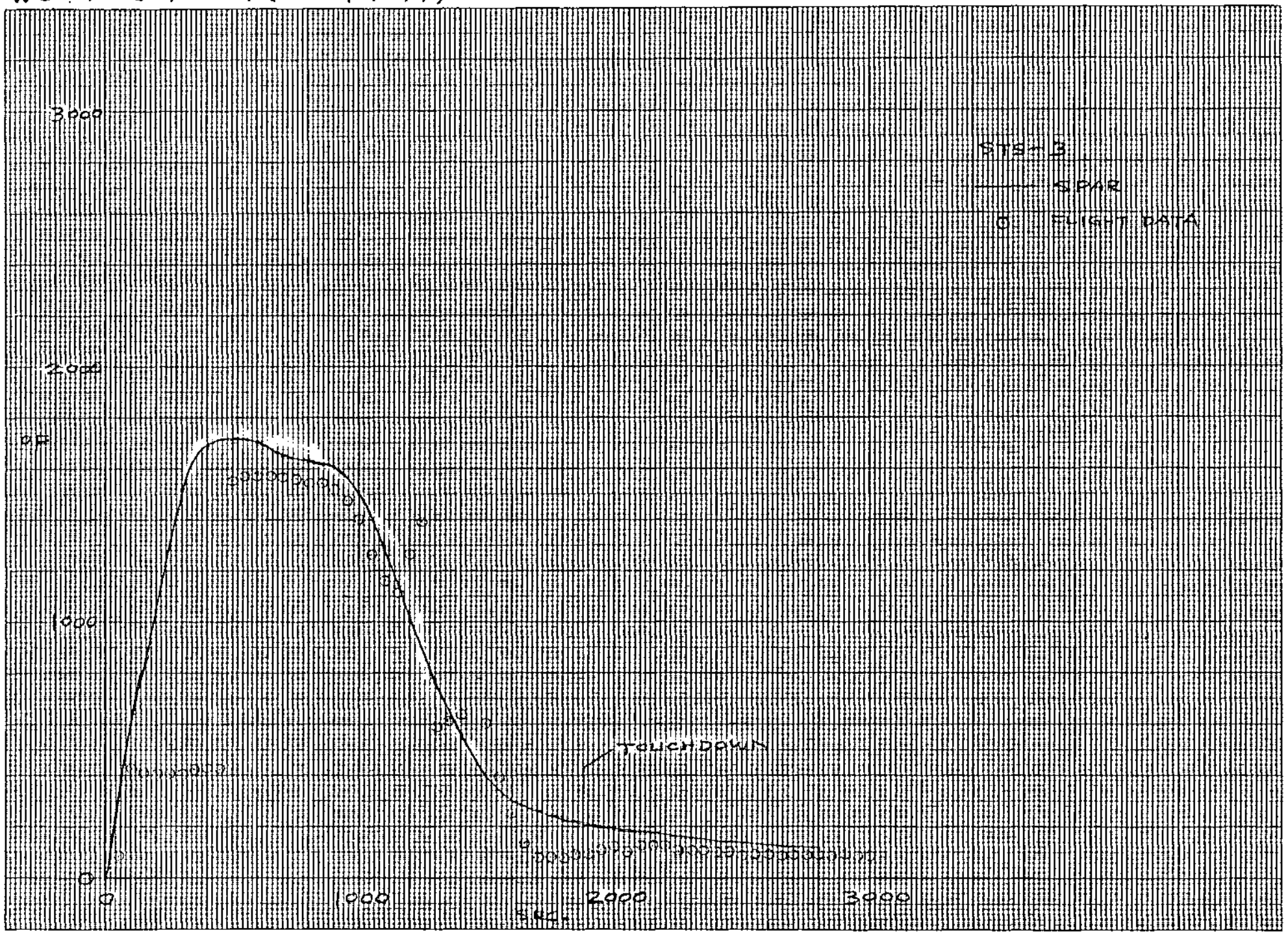

Figure 44 - TPS Surface Temperatures - WS 240

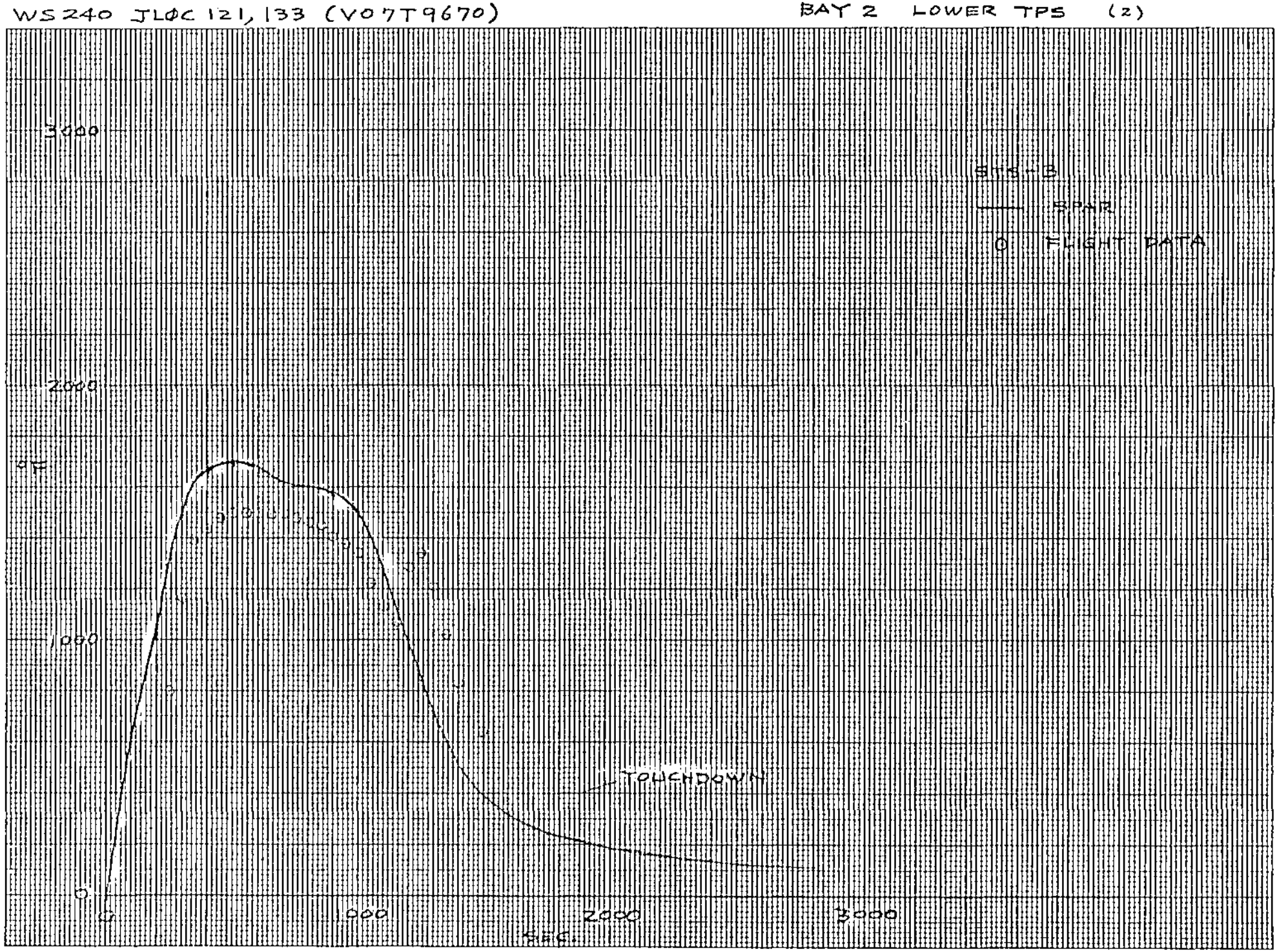

Figure 45 - TPS Surface Temperatures - WS 240

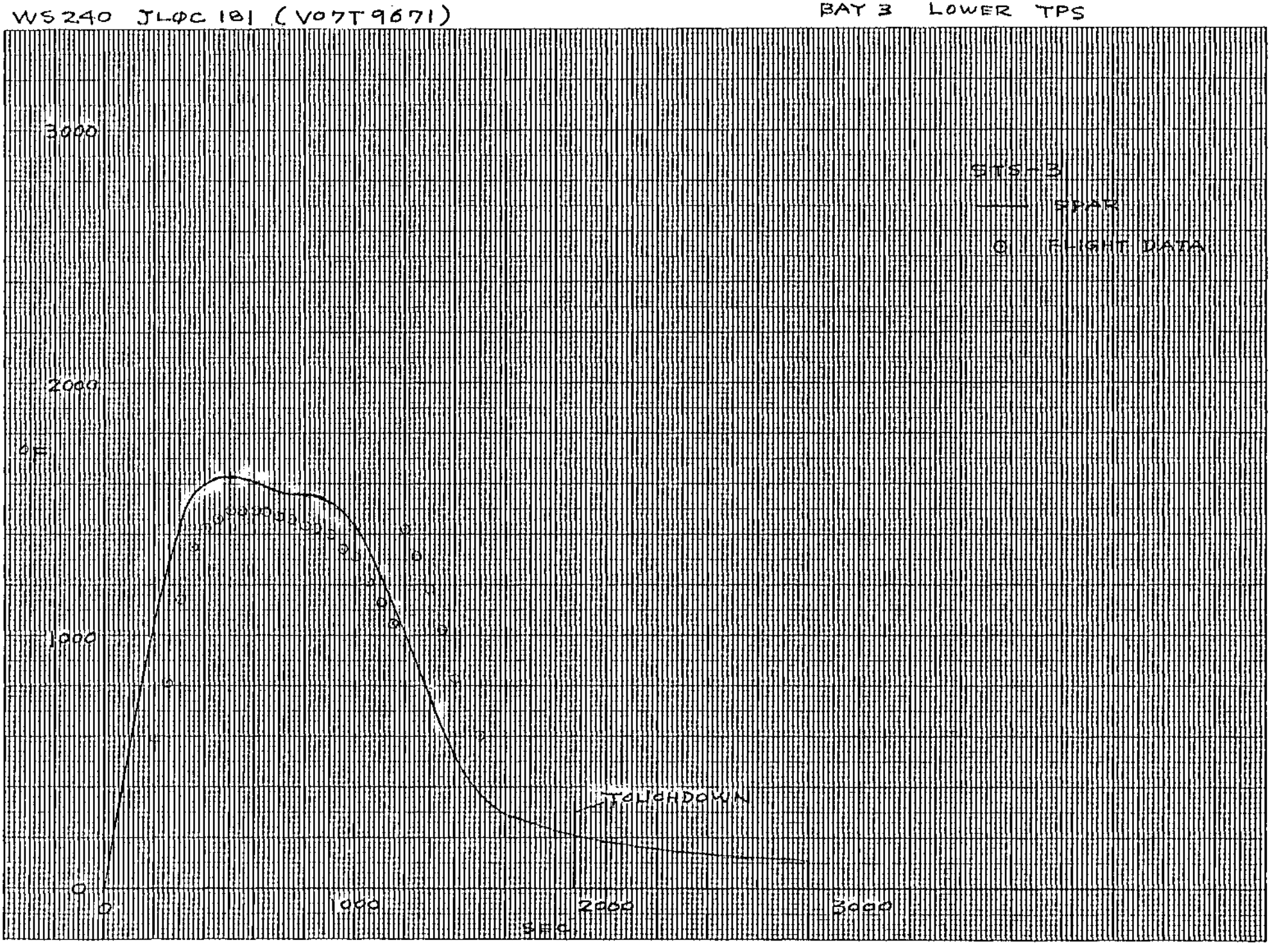

Figure 46 - TPS Surface Temperatures - WS 240

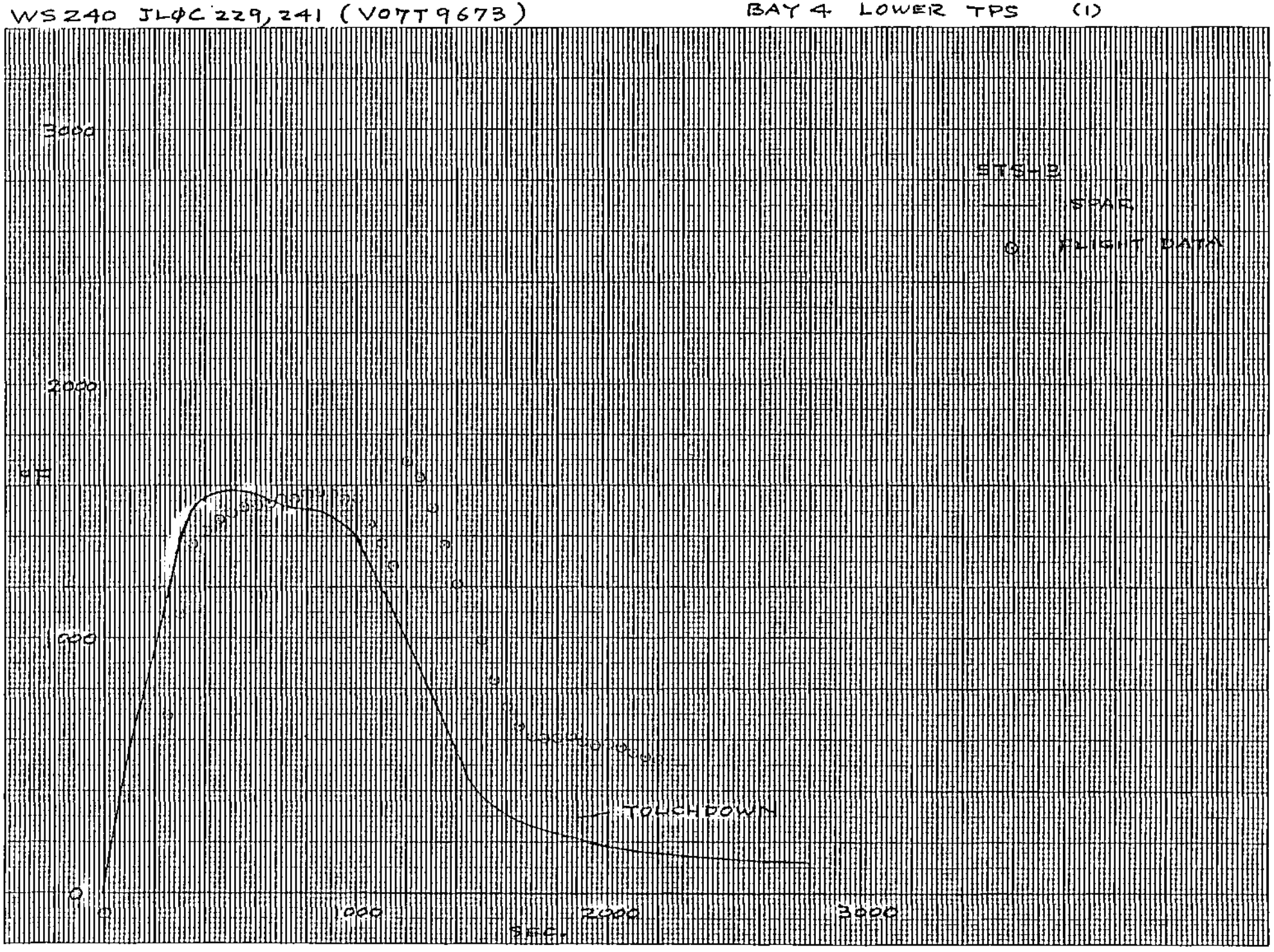

Figure 47 - TPS Surface Temperatures - WS 240

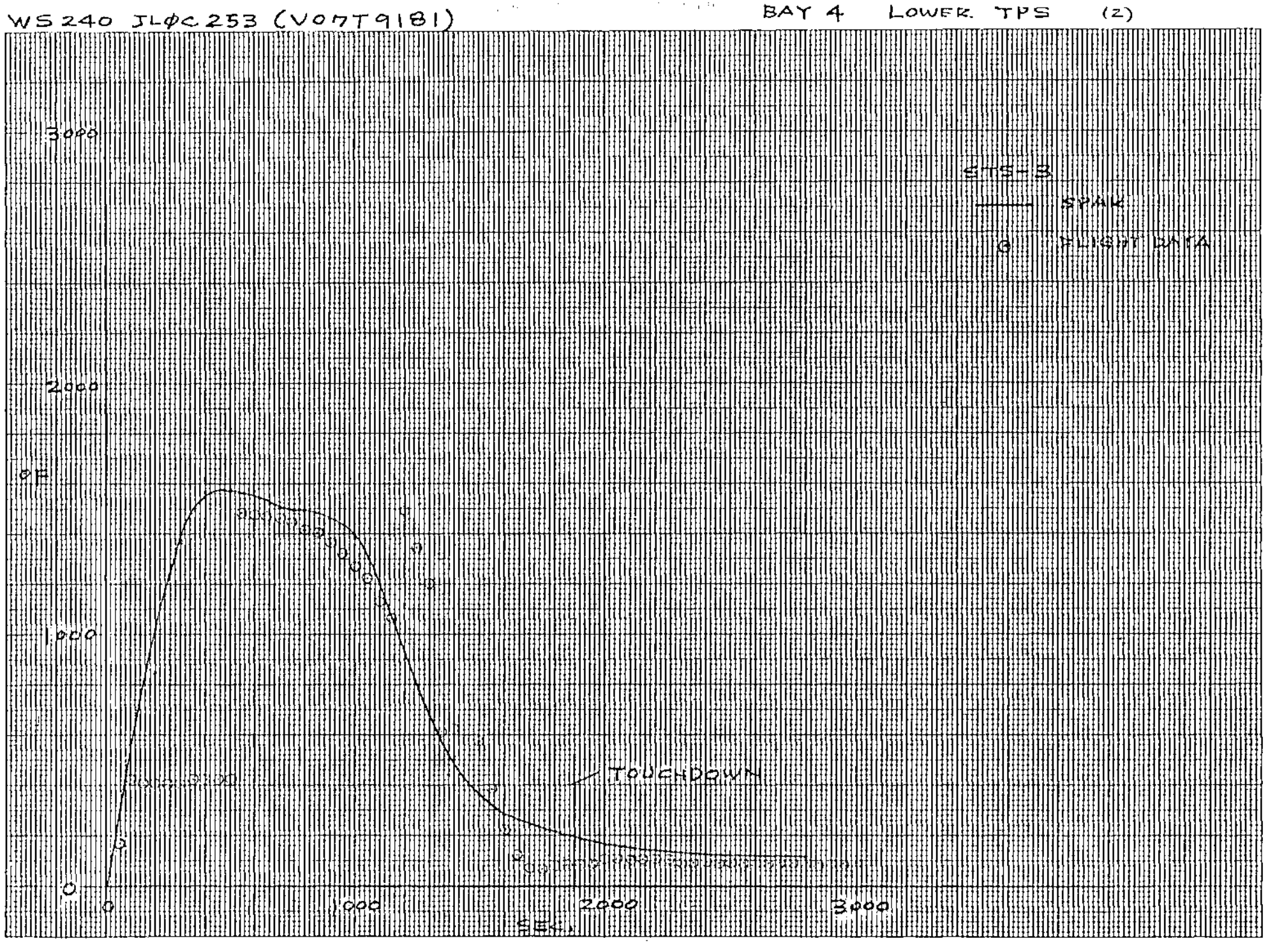

Figure 48 - TPS Surface Temperatures - WS 240

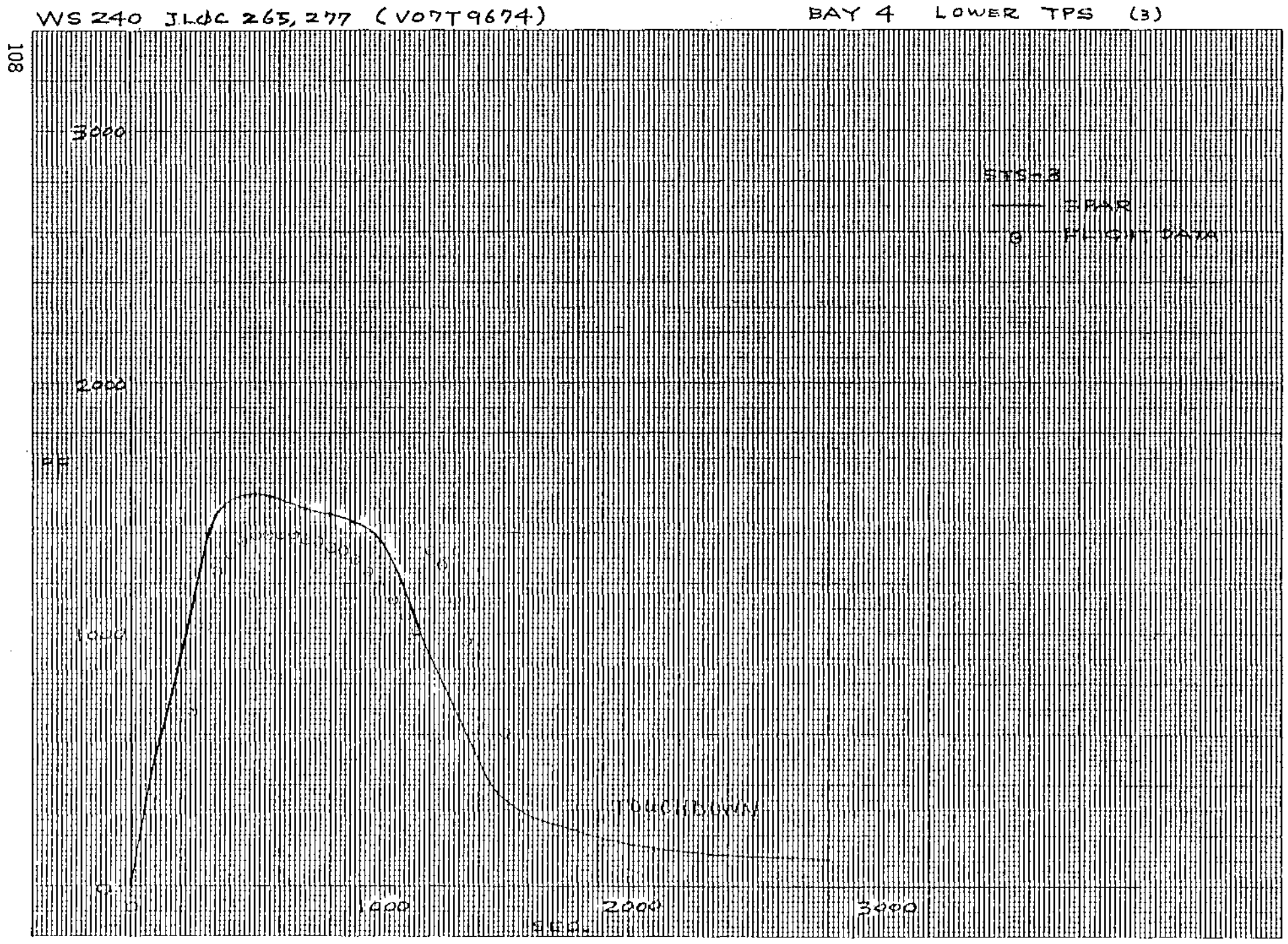

Figure 49 - TPS Surface Temperatures - WS 240

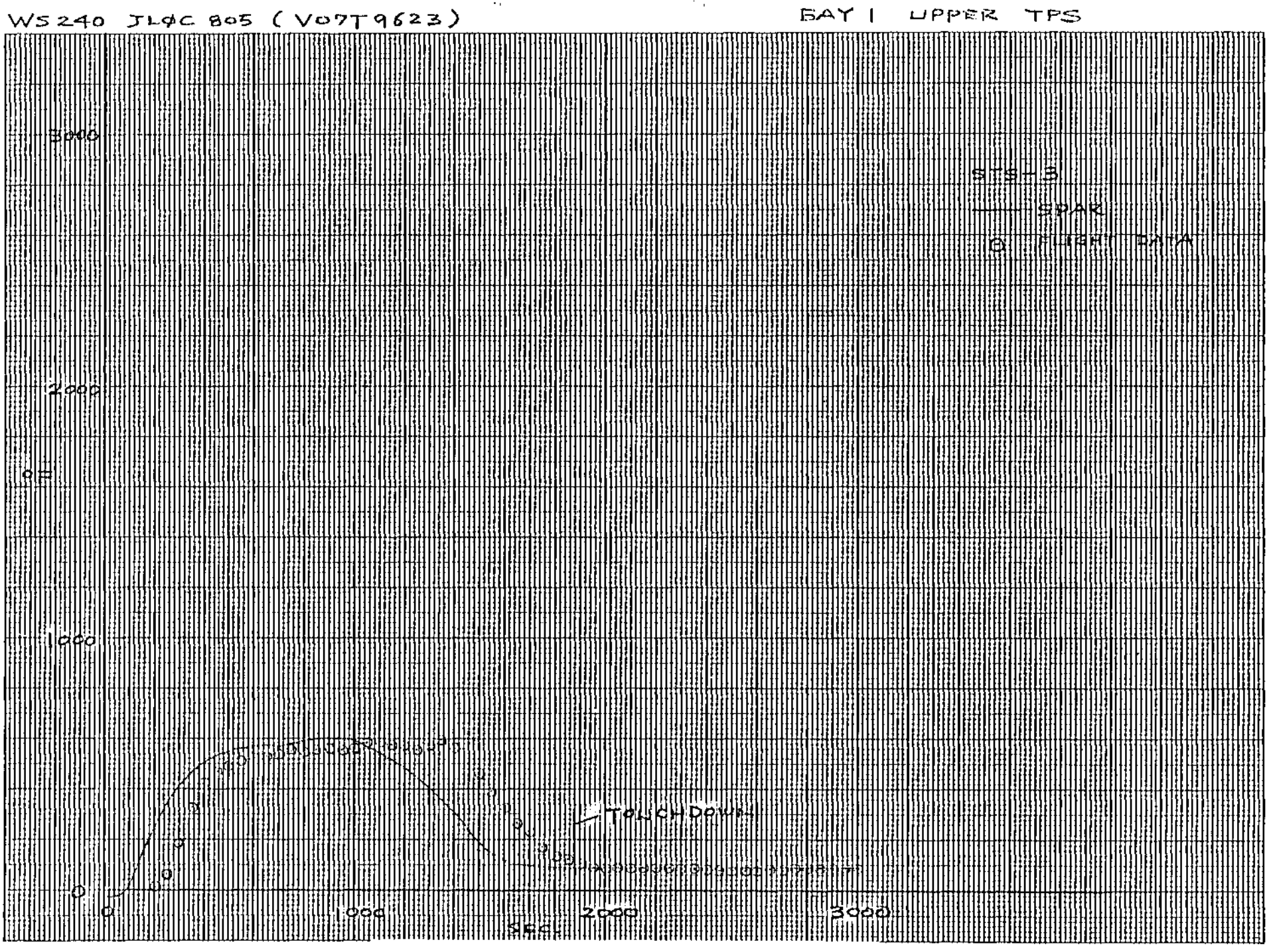

Figure 50 - TPS Surface Temperatures - WS 240

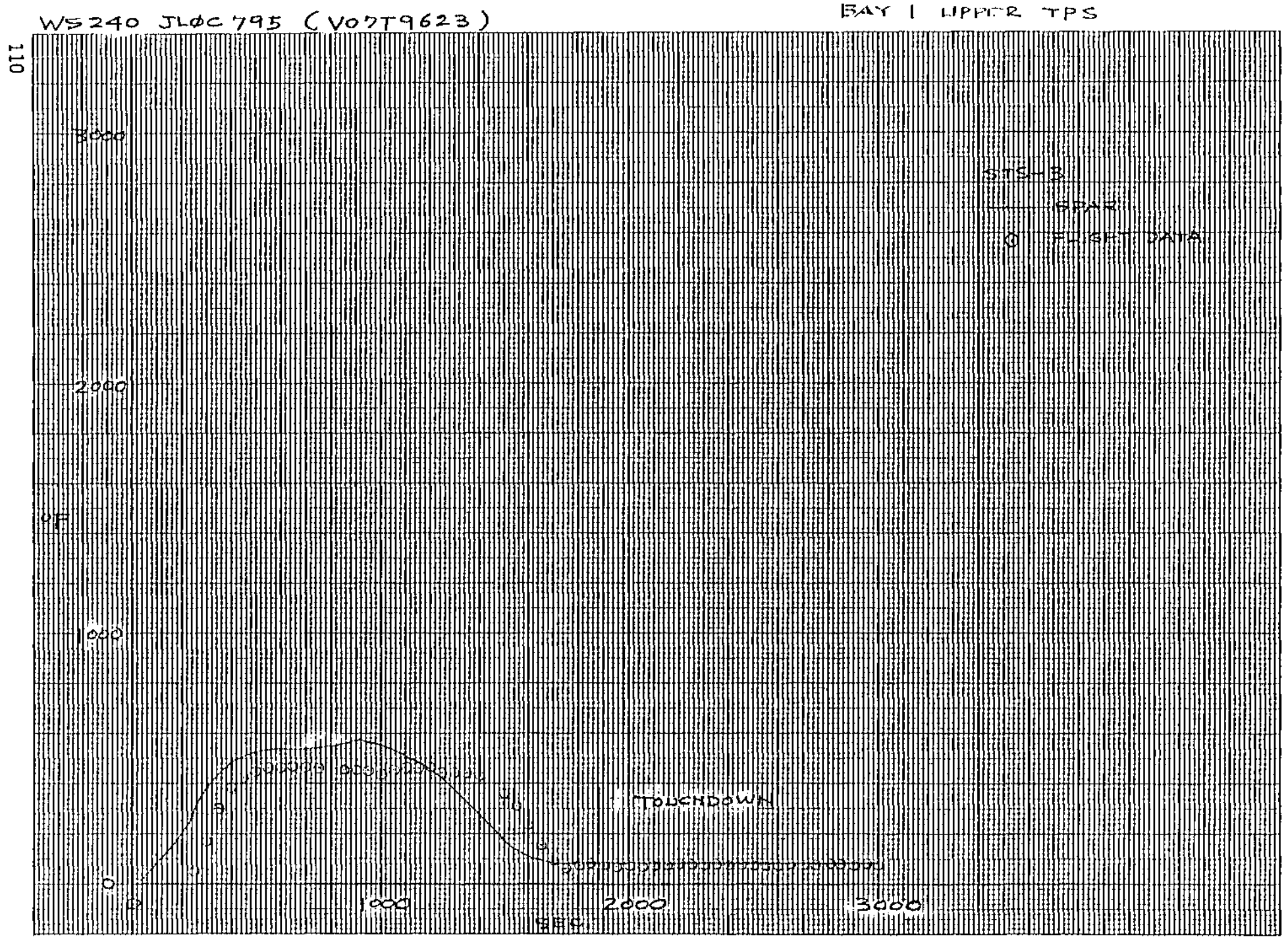

Figure 51 - TPS Surface Temperatures - WS 240

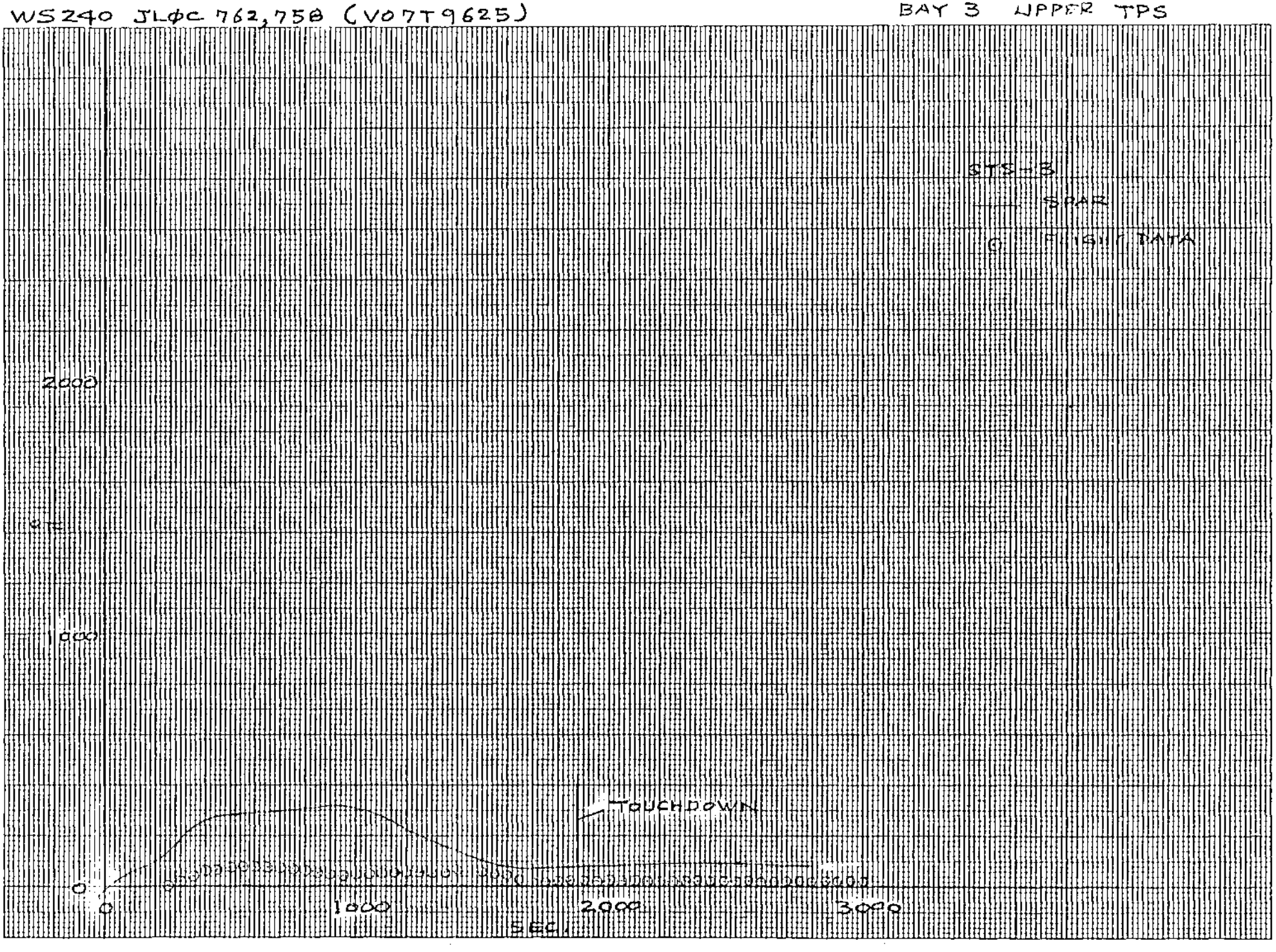

Figure 52 - TPS Surface Temperatures - WS 240

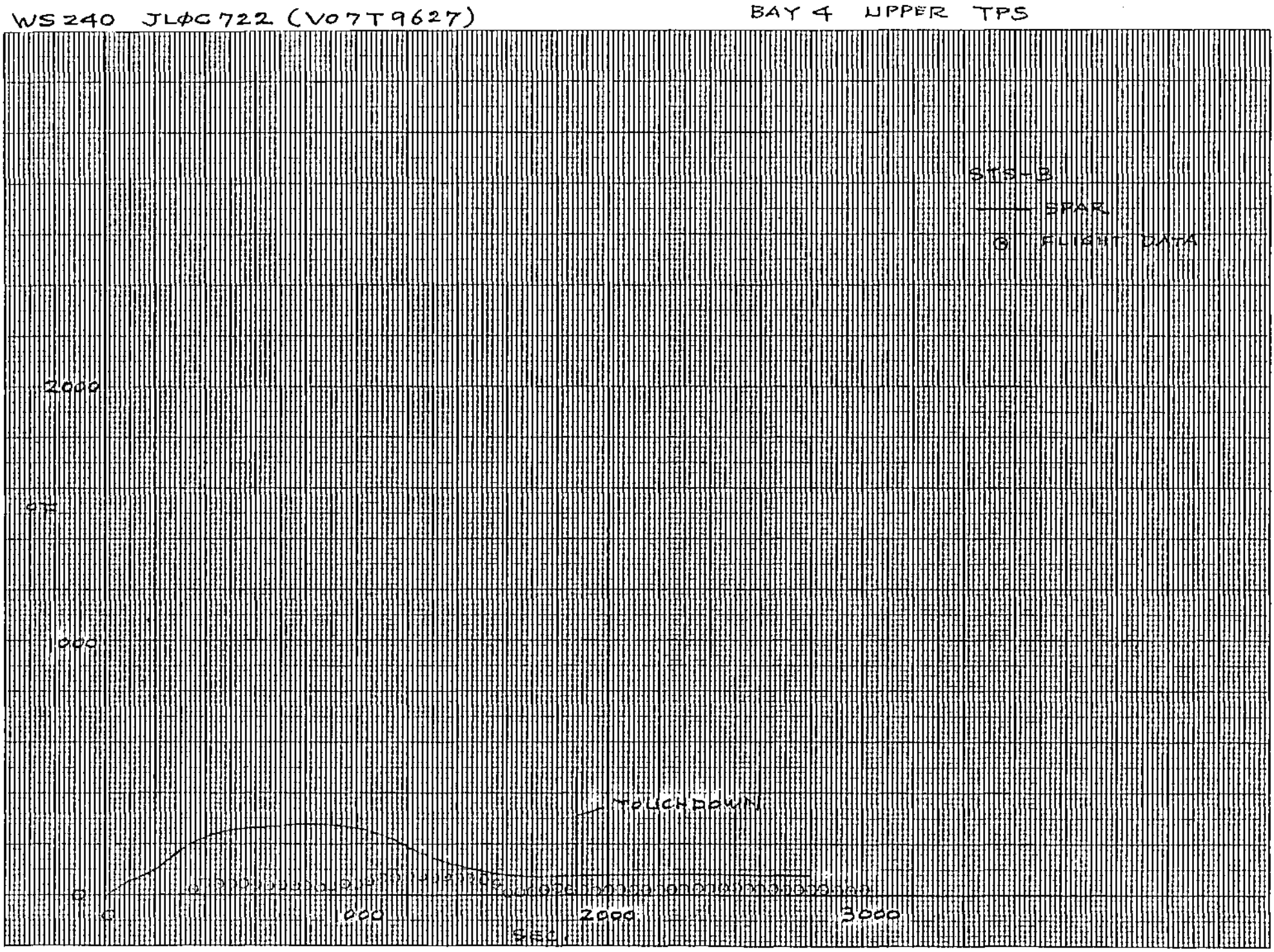

Figure 53 - TPS Surface Temperatures - WS 240

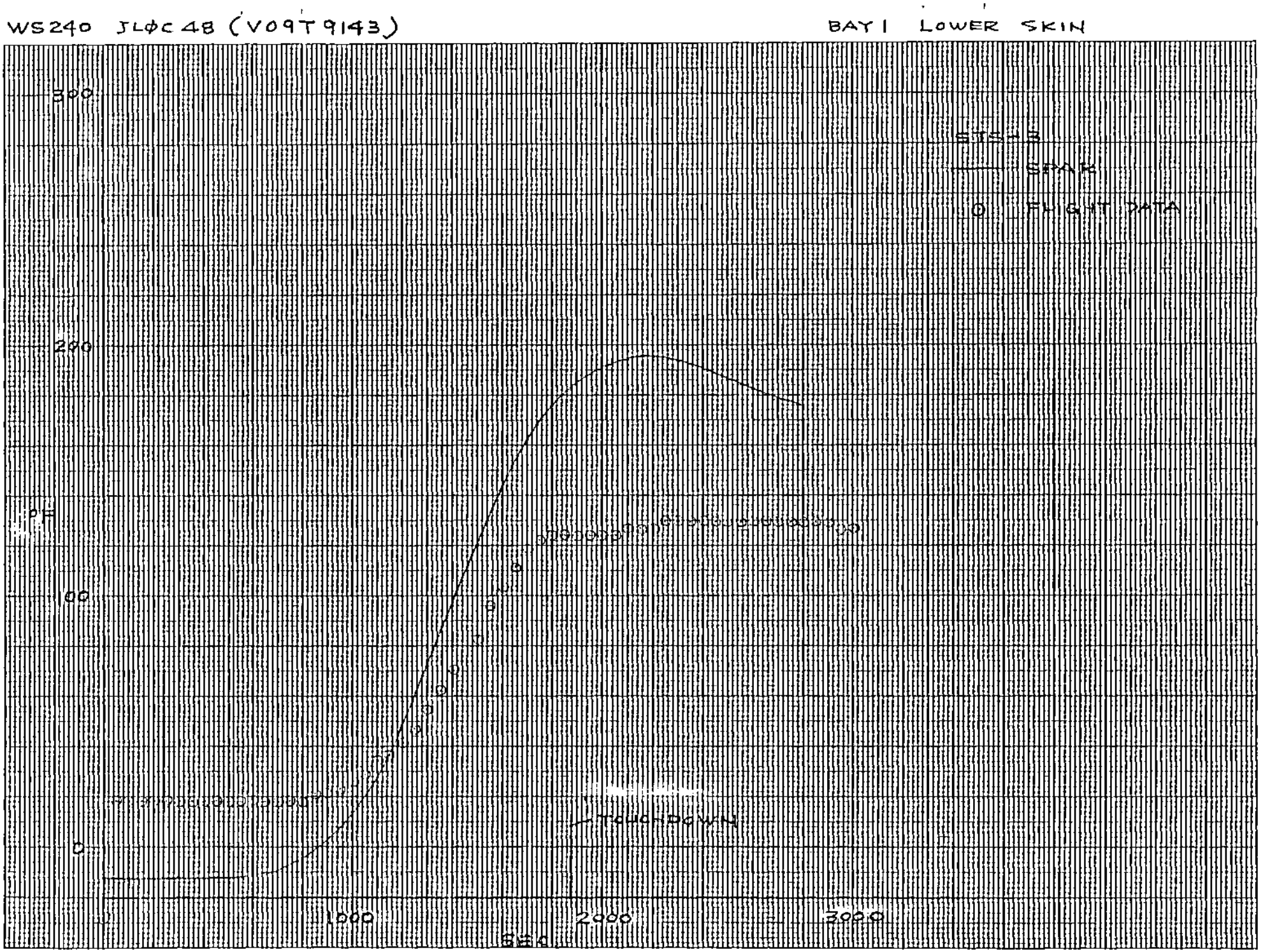

Figure 54 - Structural Temperatures - WS 240

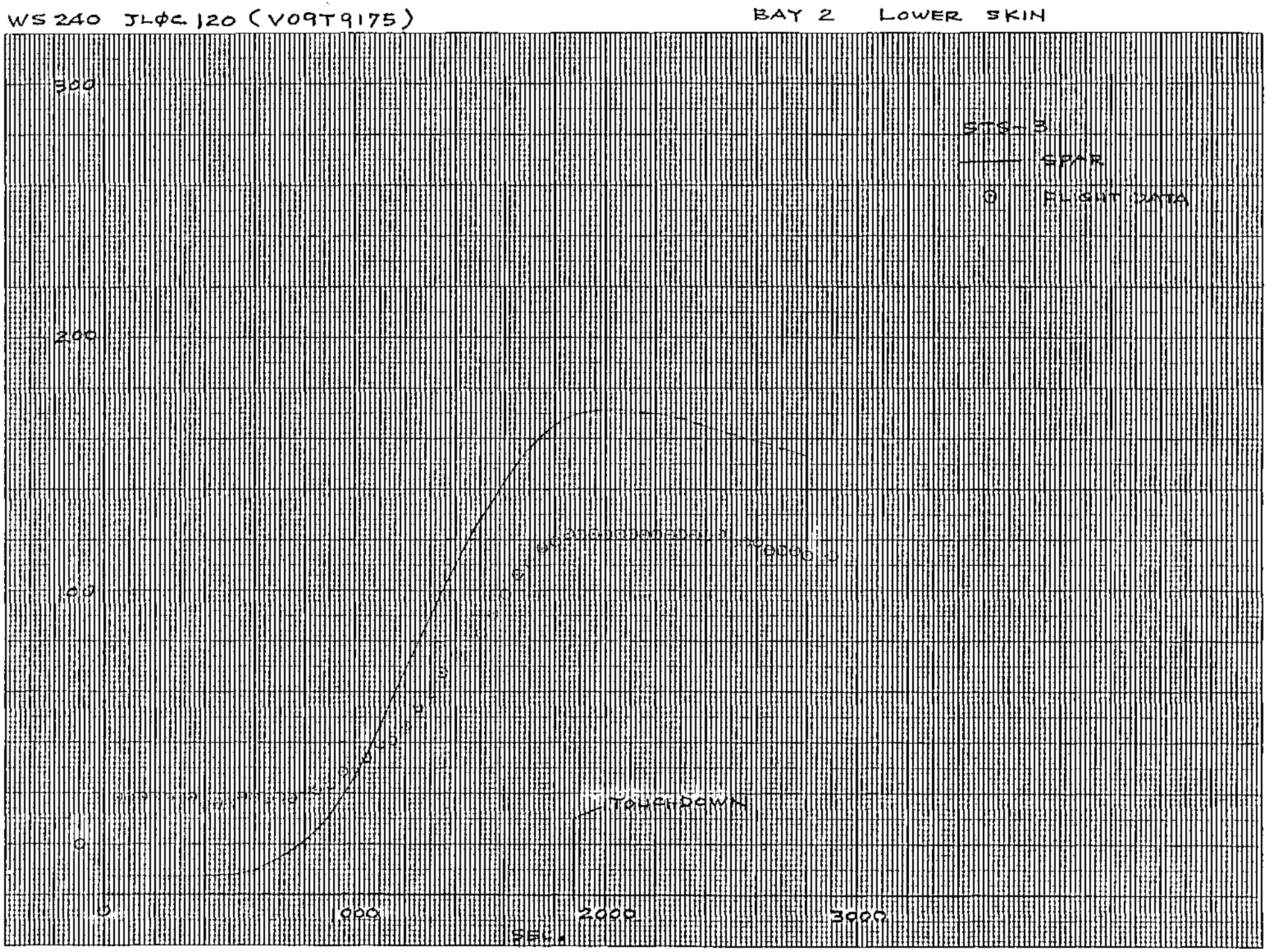

Figure 55 - Structural Temperatures - WS 240

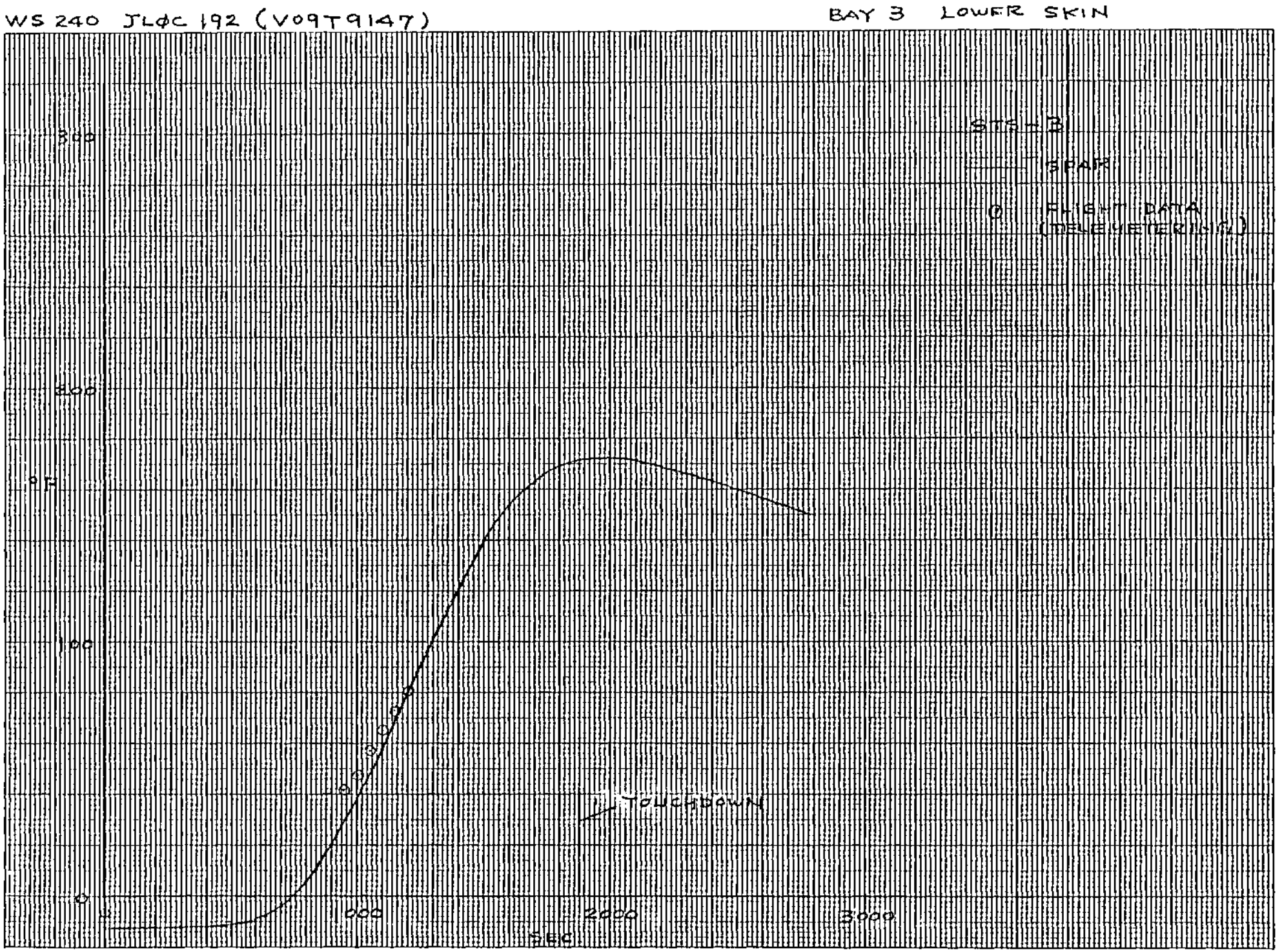

Figure 56 - Structural Temperatures - WS 240

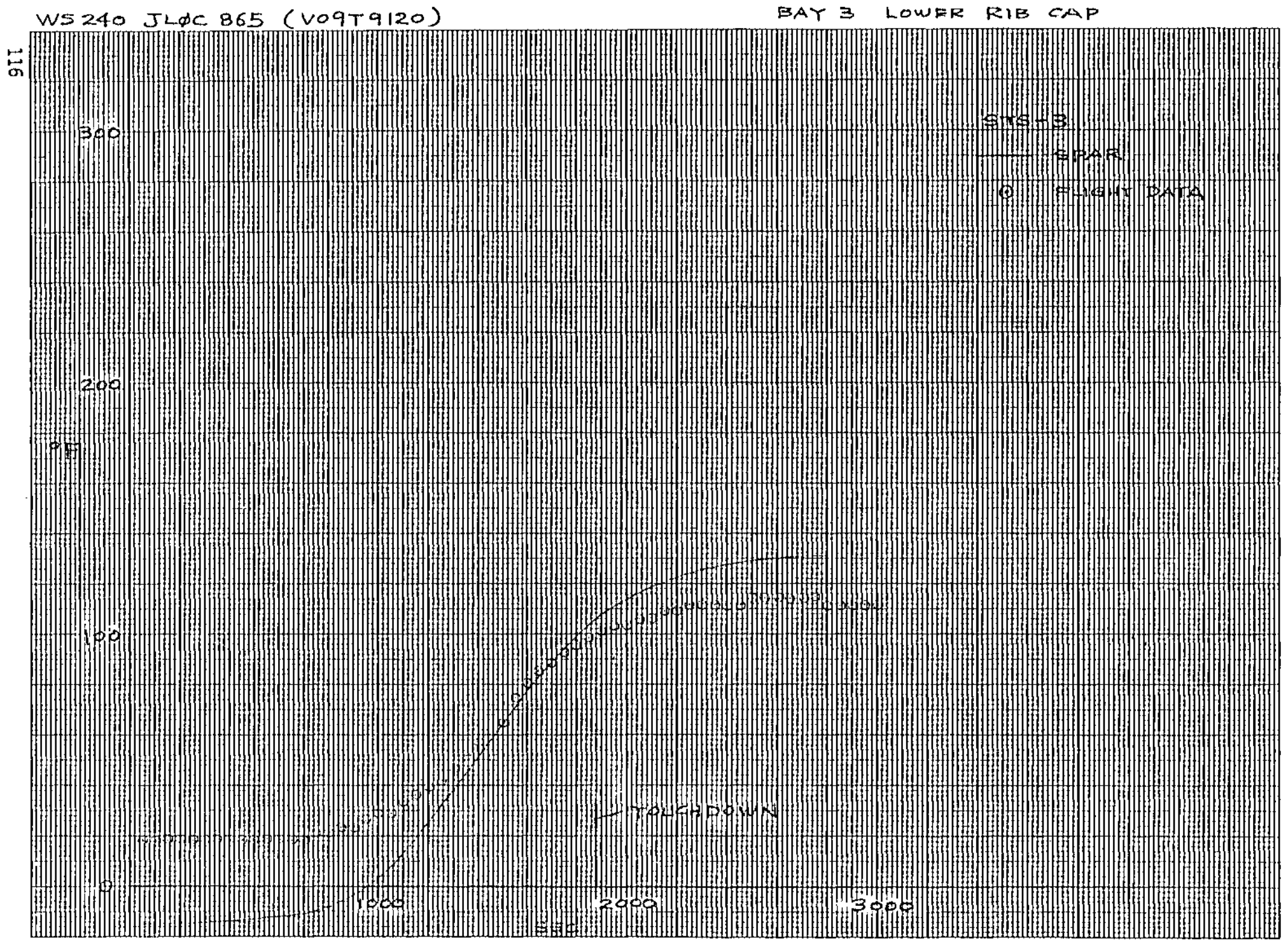

Figure 57 - Structural Temperatures - WS 240

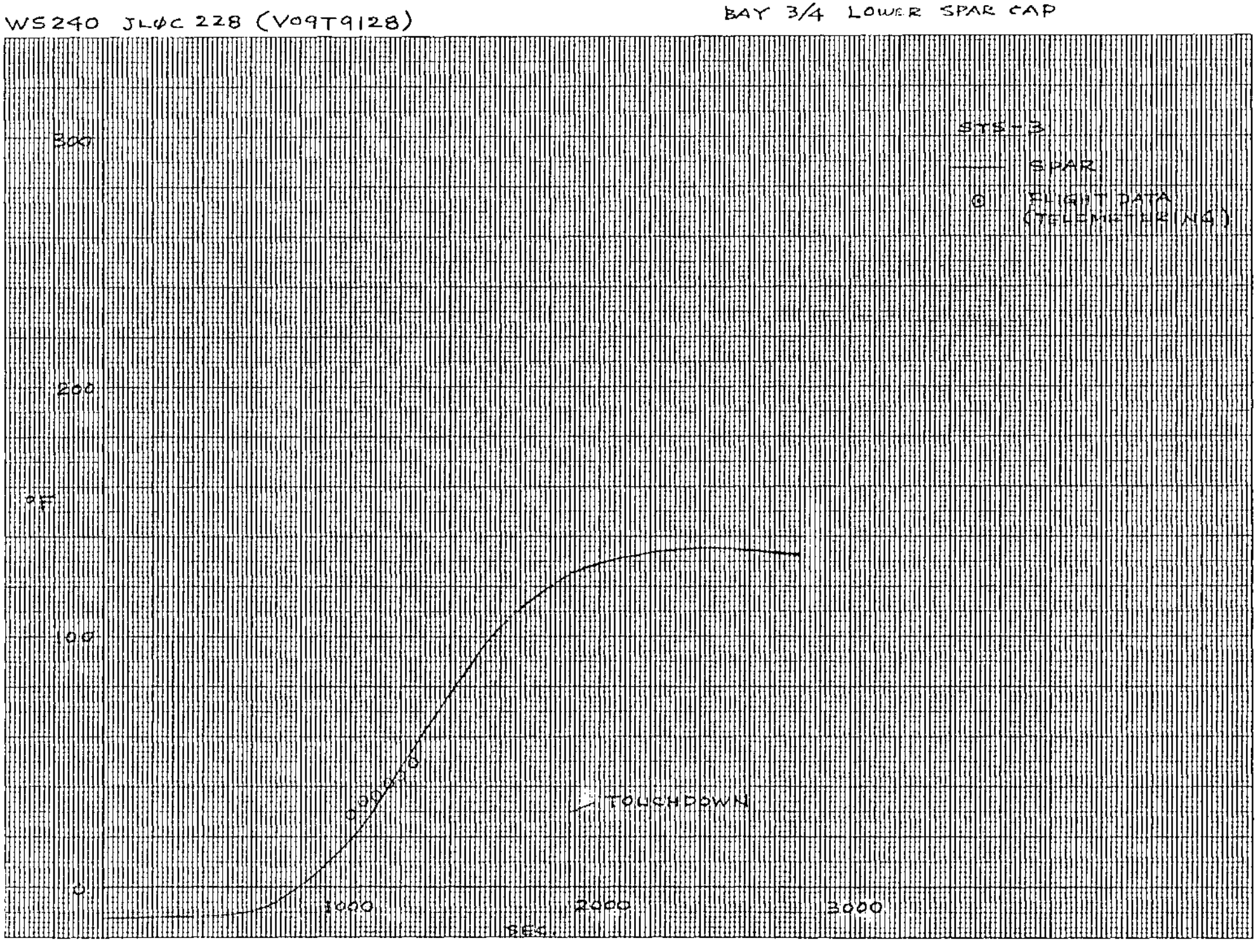

Figure 58 - Structural Temperatures - WS 240

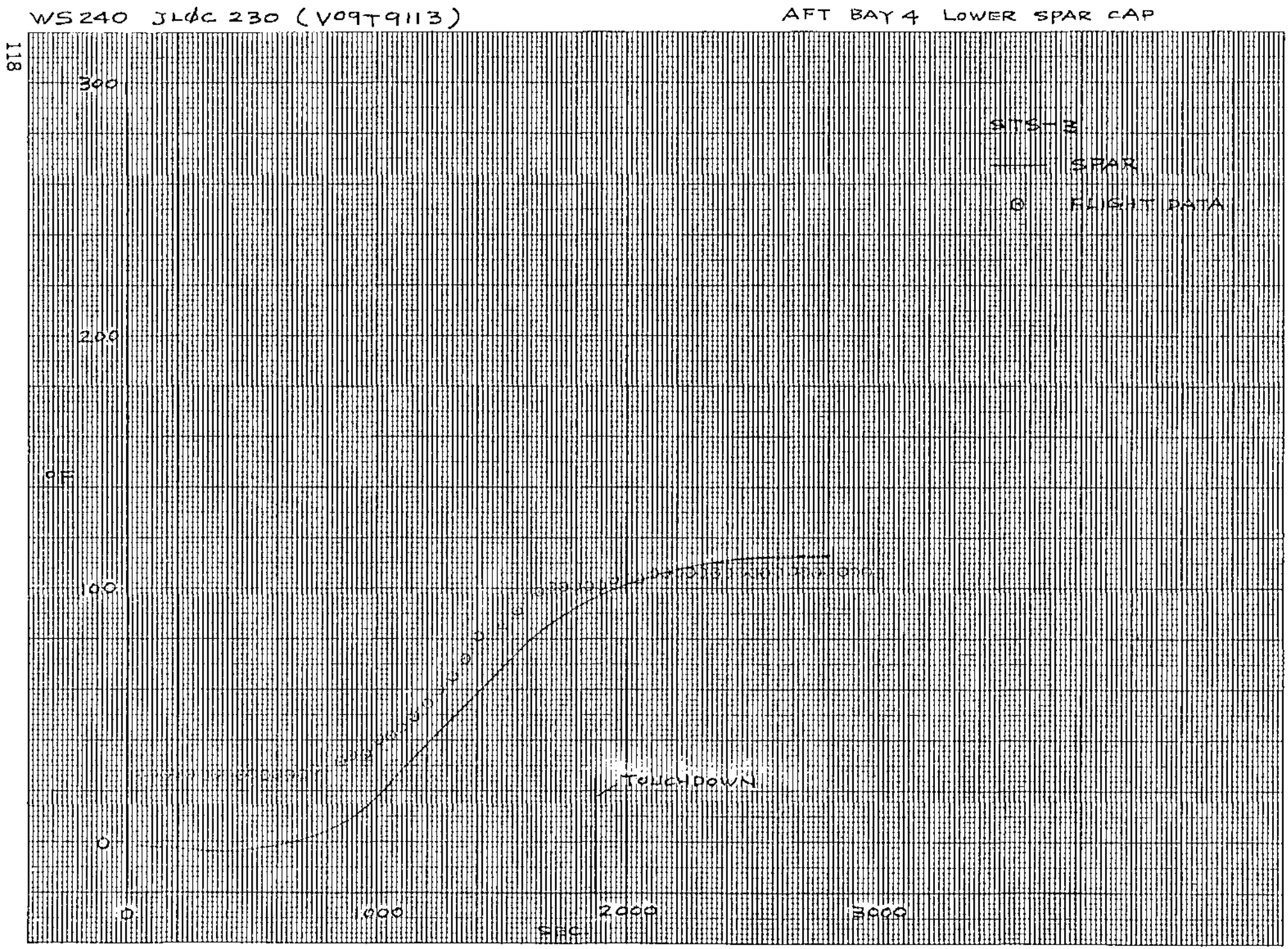

Figure 59 - Structural Temperatures - WS 240

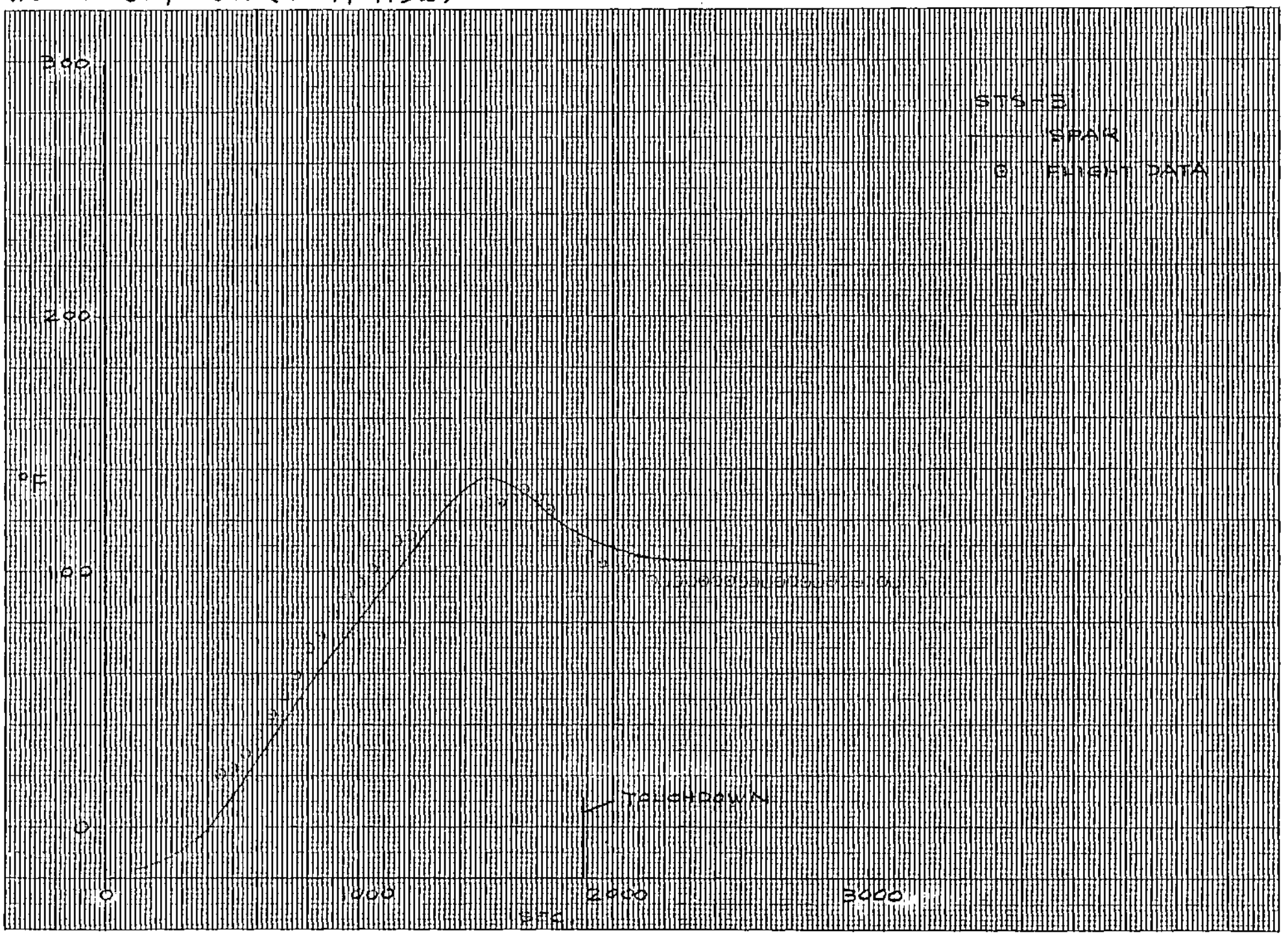

Figure 60 - Structural Temperatures - WS 240

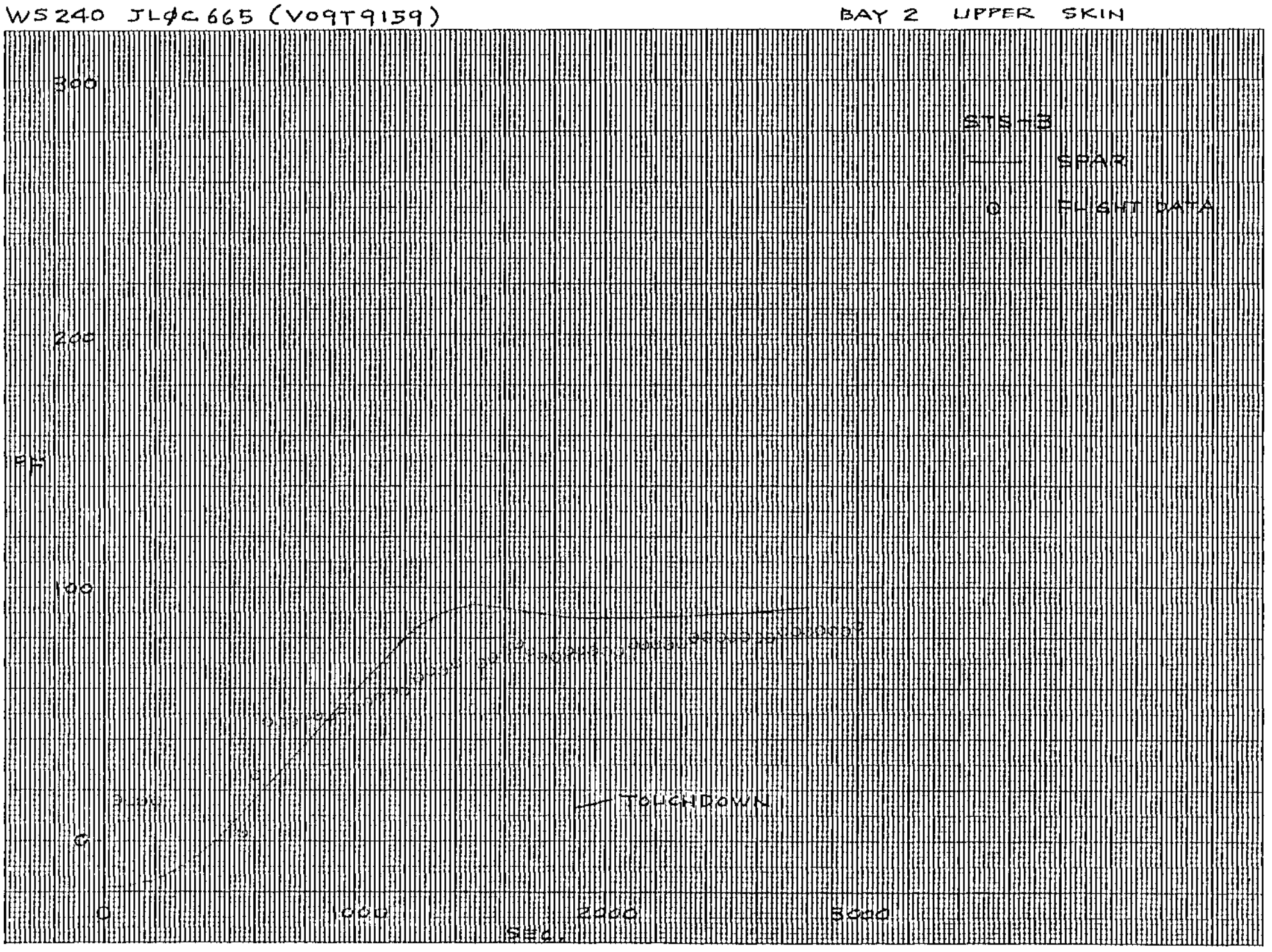

Figure 61 - Structural Temperatures - WS 240

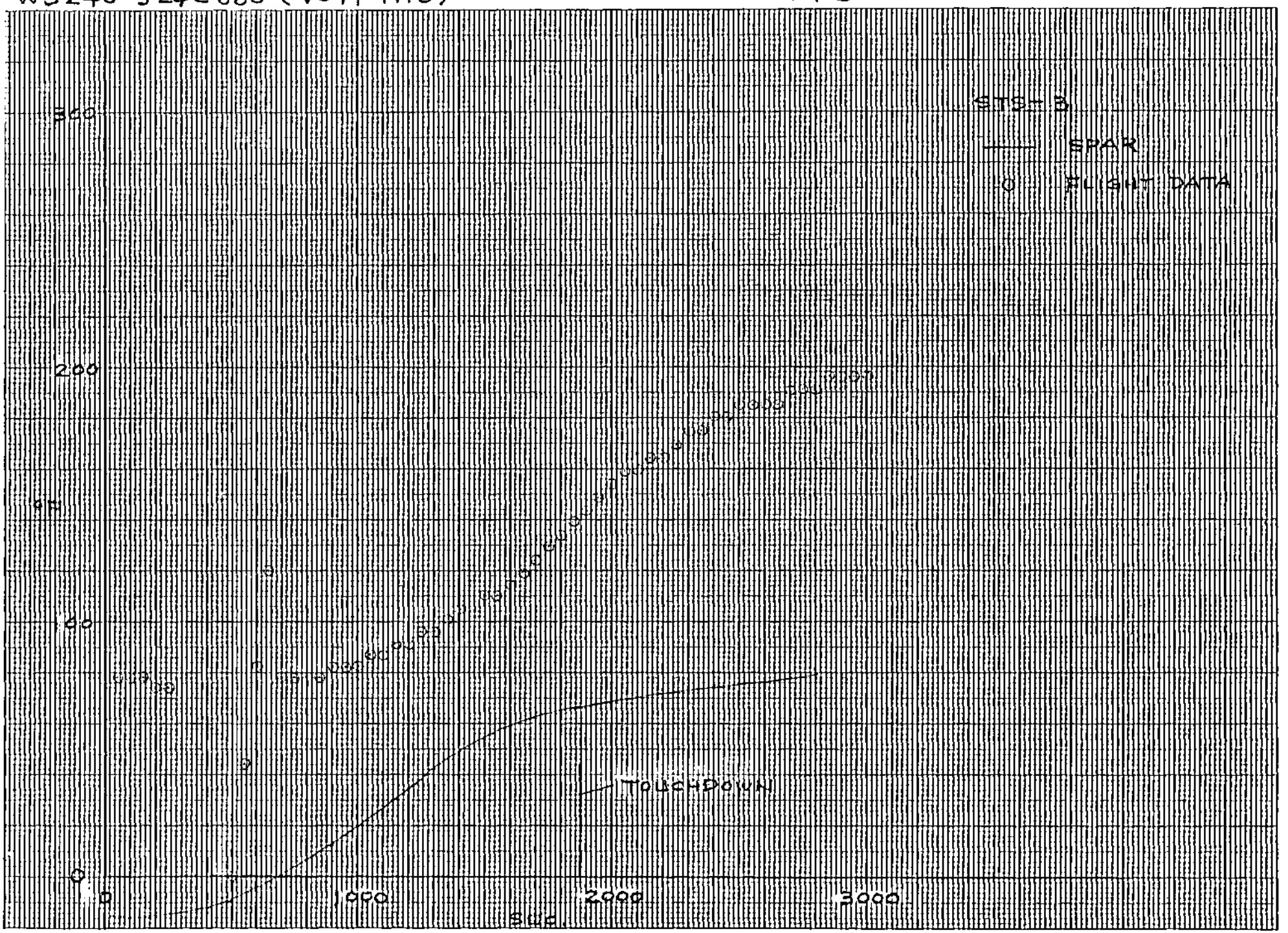

Figure 62 - Structural Temperatures - WS 240

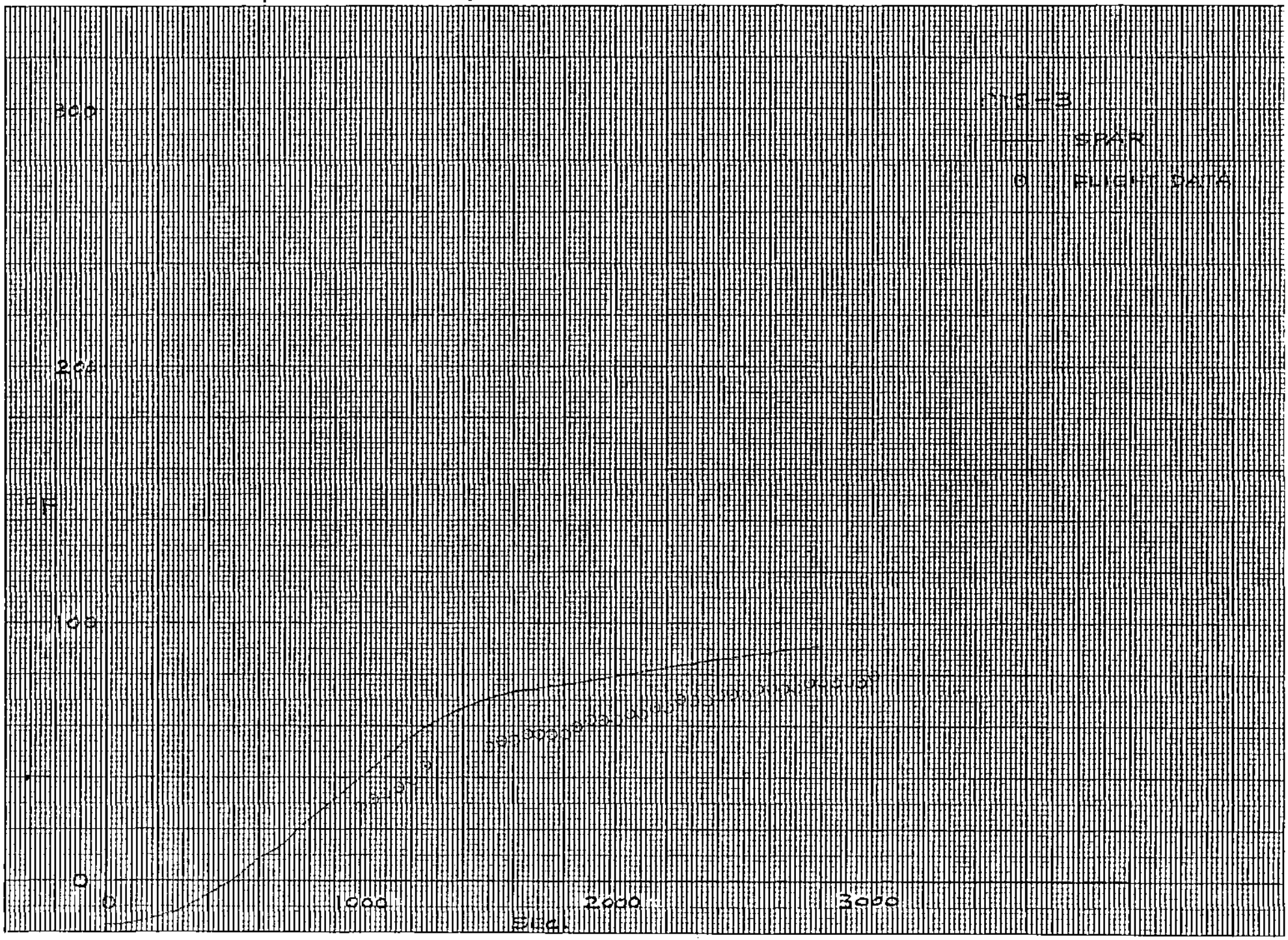

Figure 63 - Structural Temperatures - WS 240

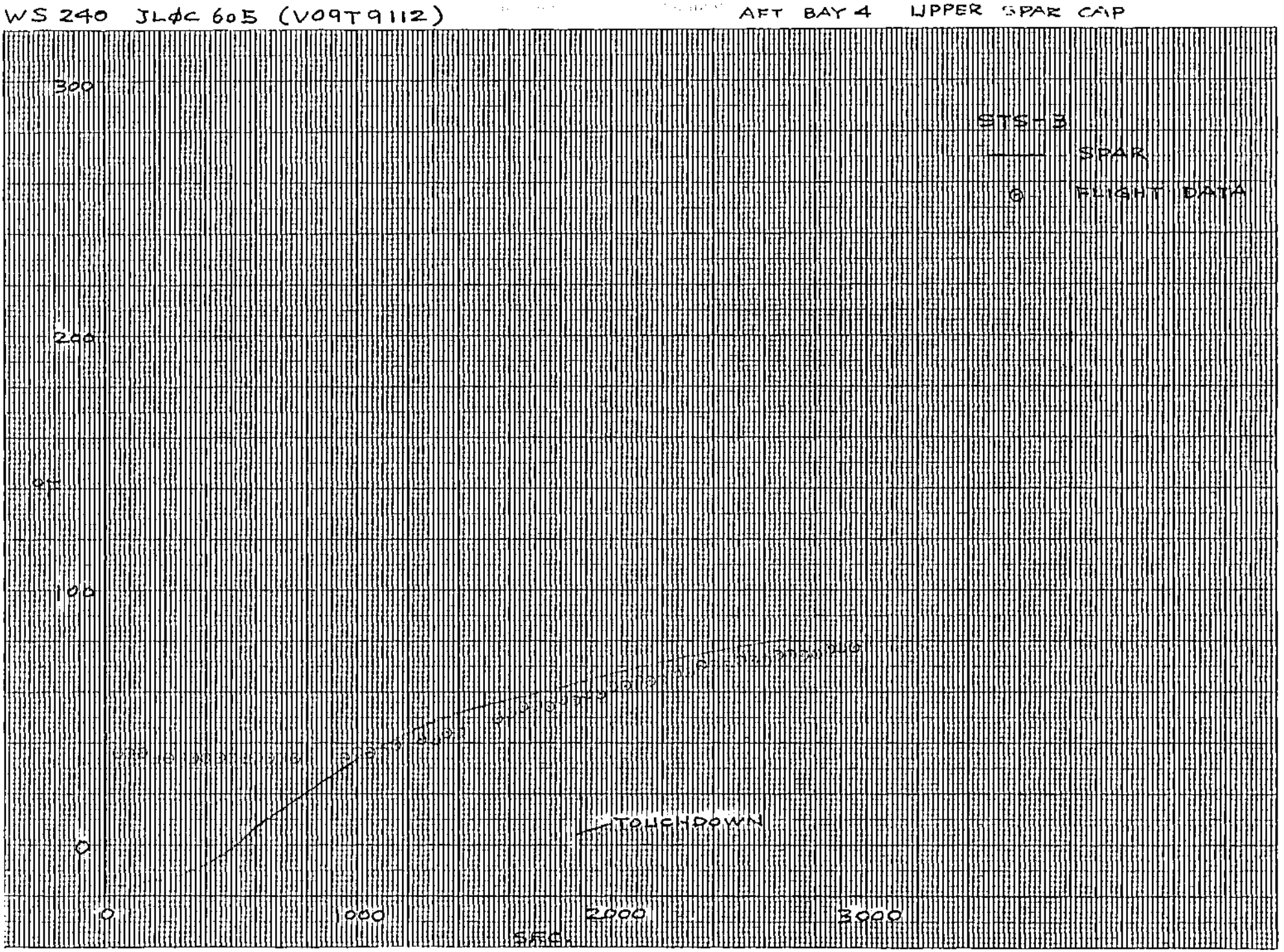

Figure 64 - Structural Temperatures - WS 240

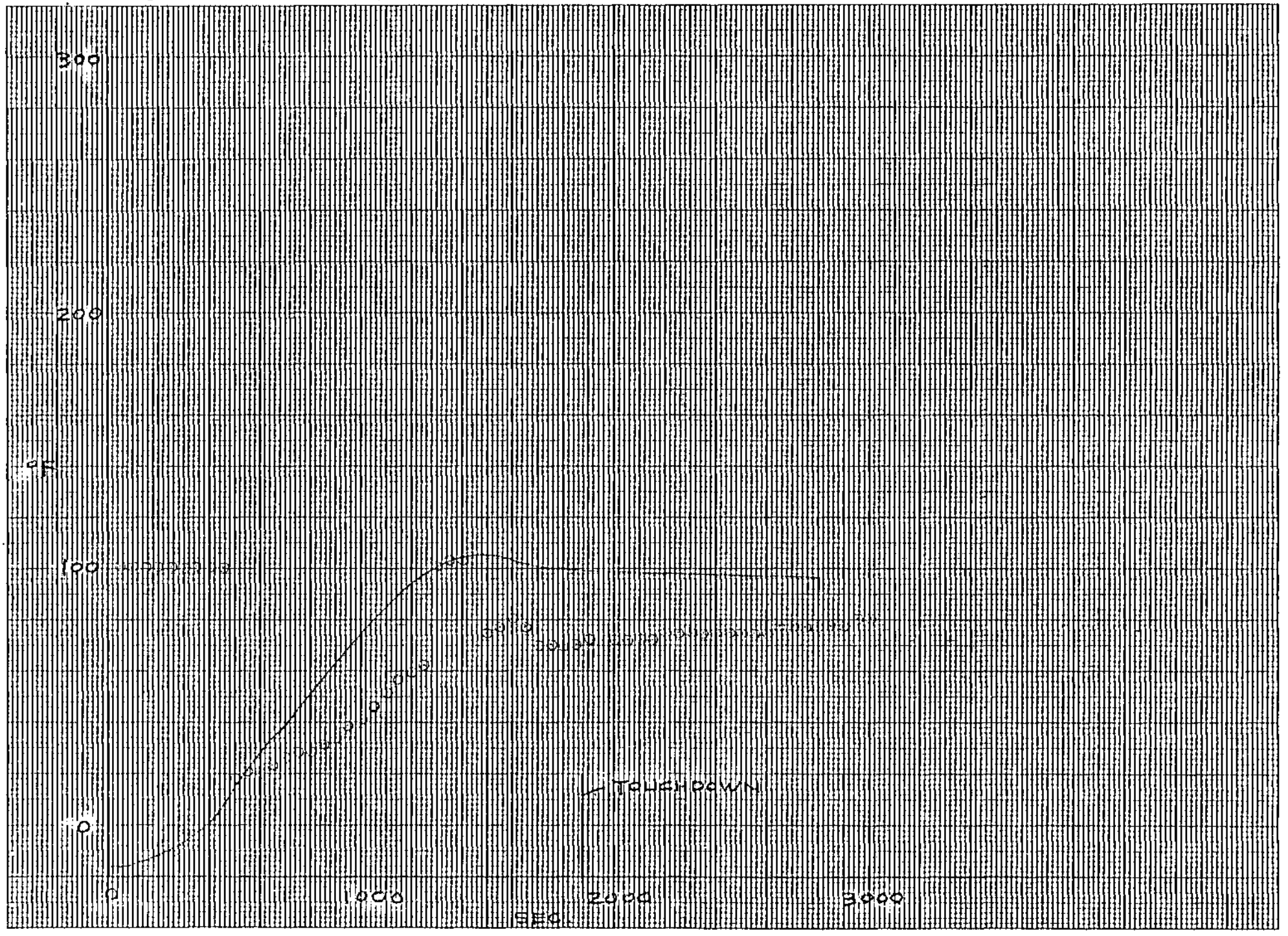

Figure 65 - Structural Temperatures - WS 240

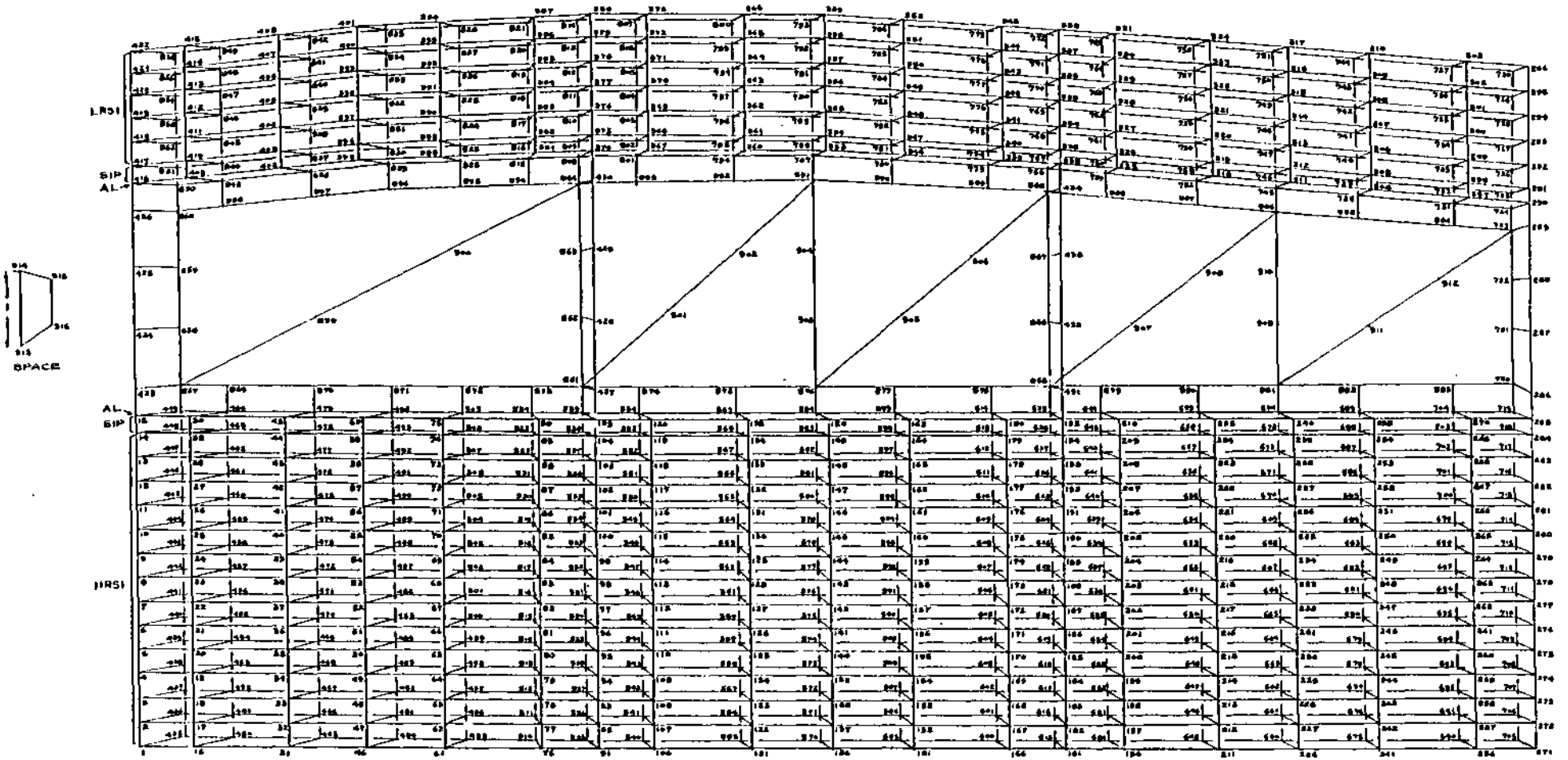

Figure 66 - SPAR THermal Model - WS 240

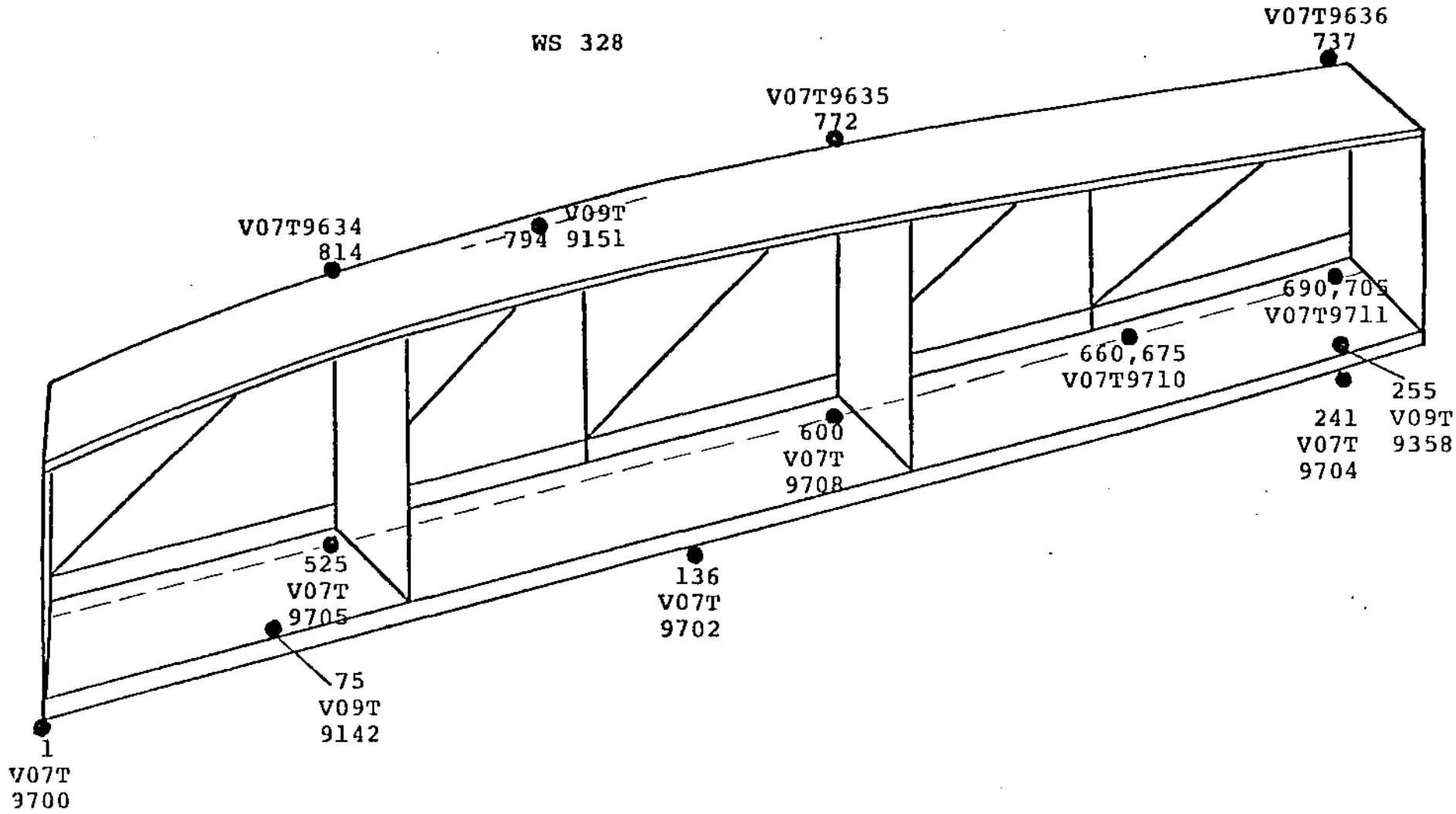

Figure 67 - Temperature Measurement Locations - WS 328

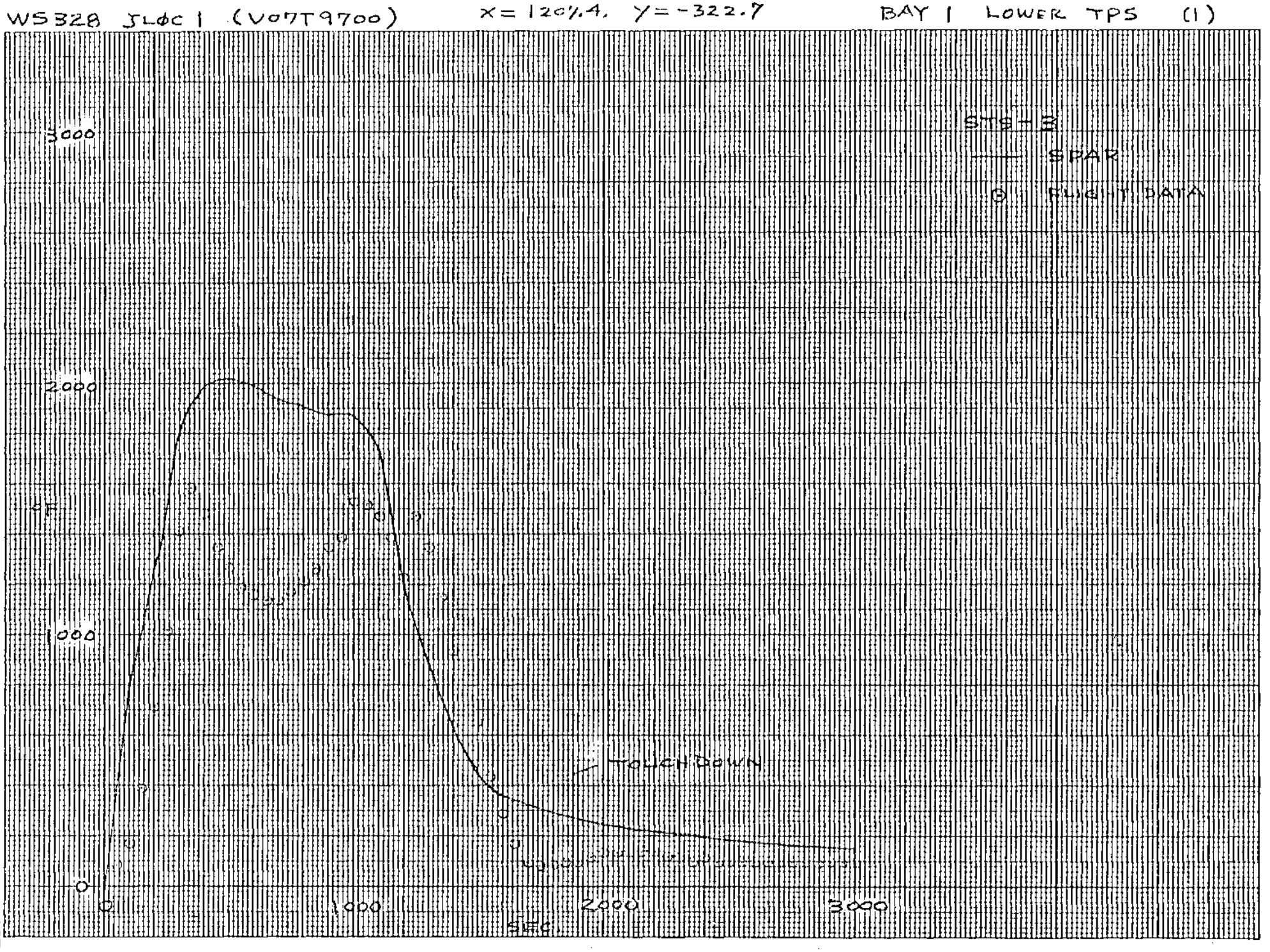

Figure 68 - TPS Surface Temperatures - WS 328

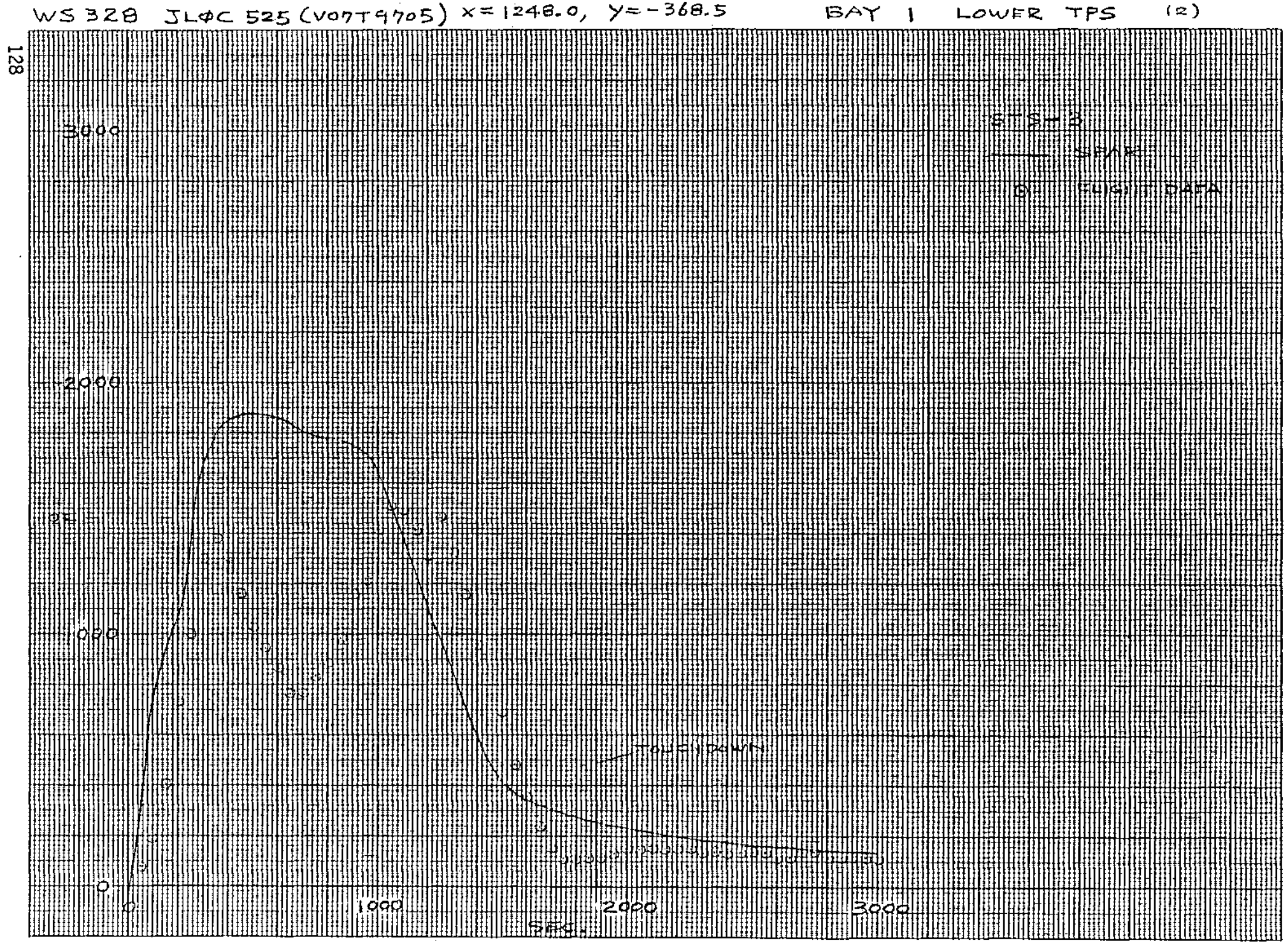

Figure 69 - TPS Surface Temperatures - WS 328

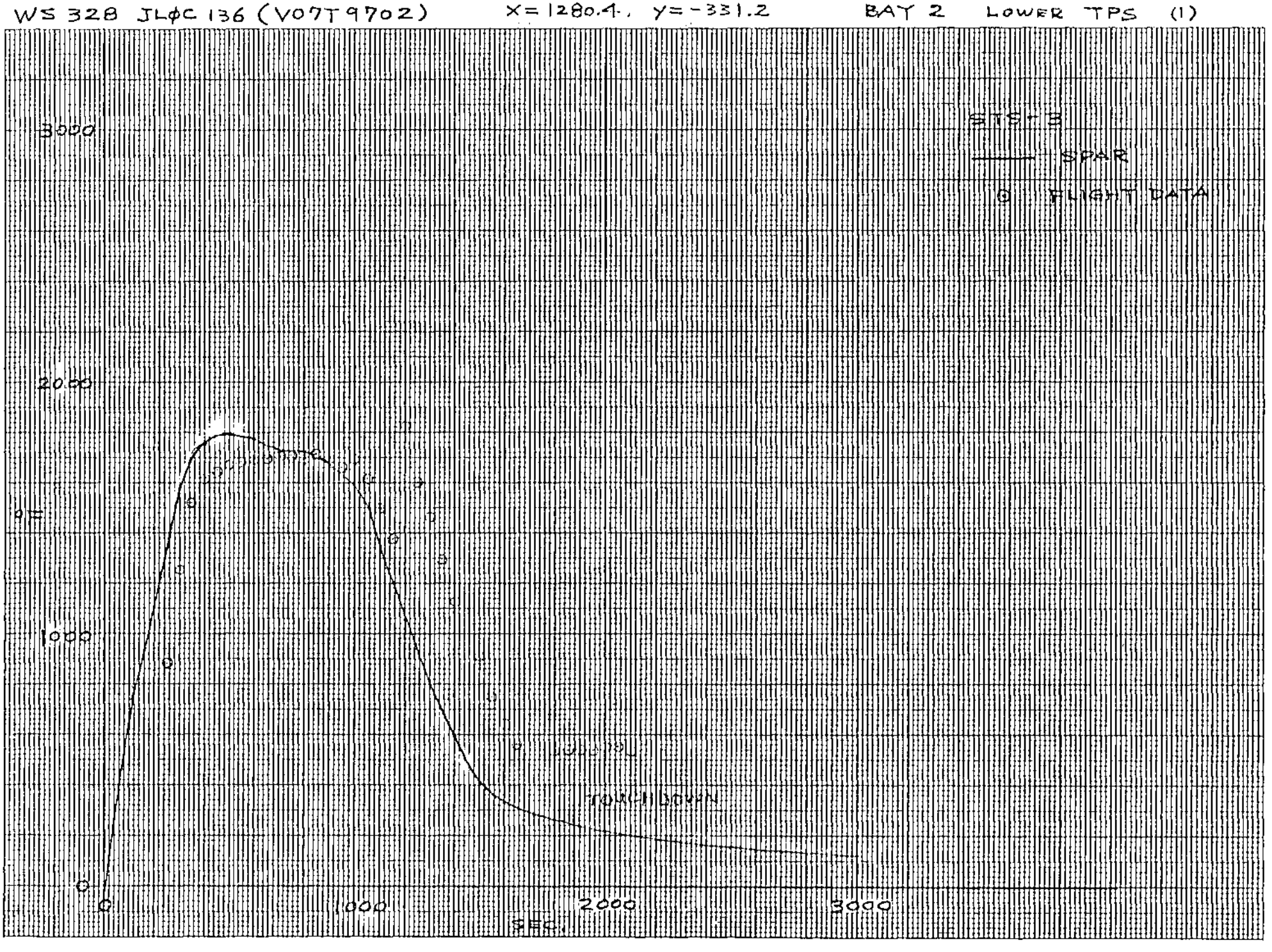

Figure 70 - TPS Surface Temperatures - WS 328

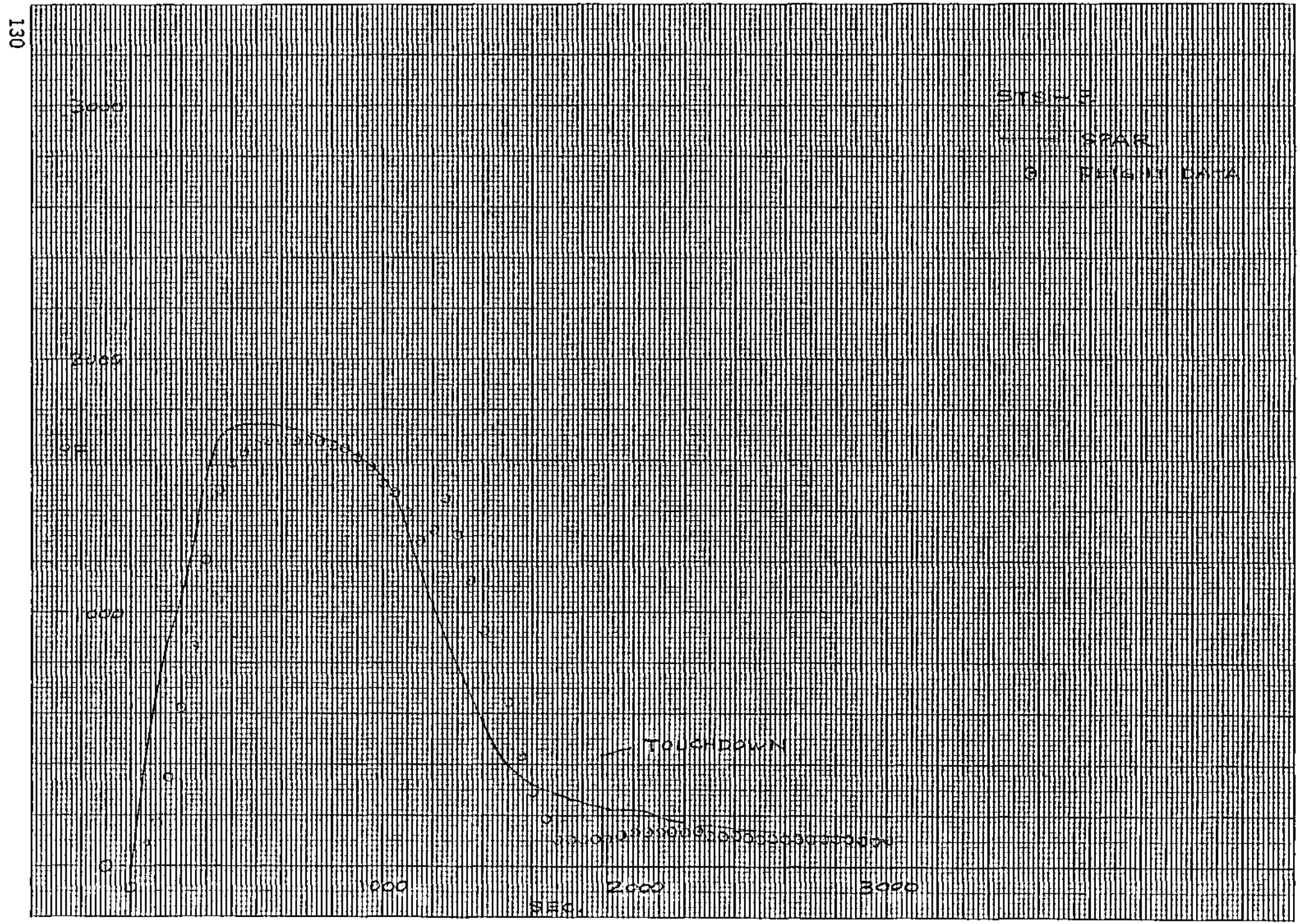

Figure 71 - TPS Surface Temperatures - WS 328

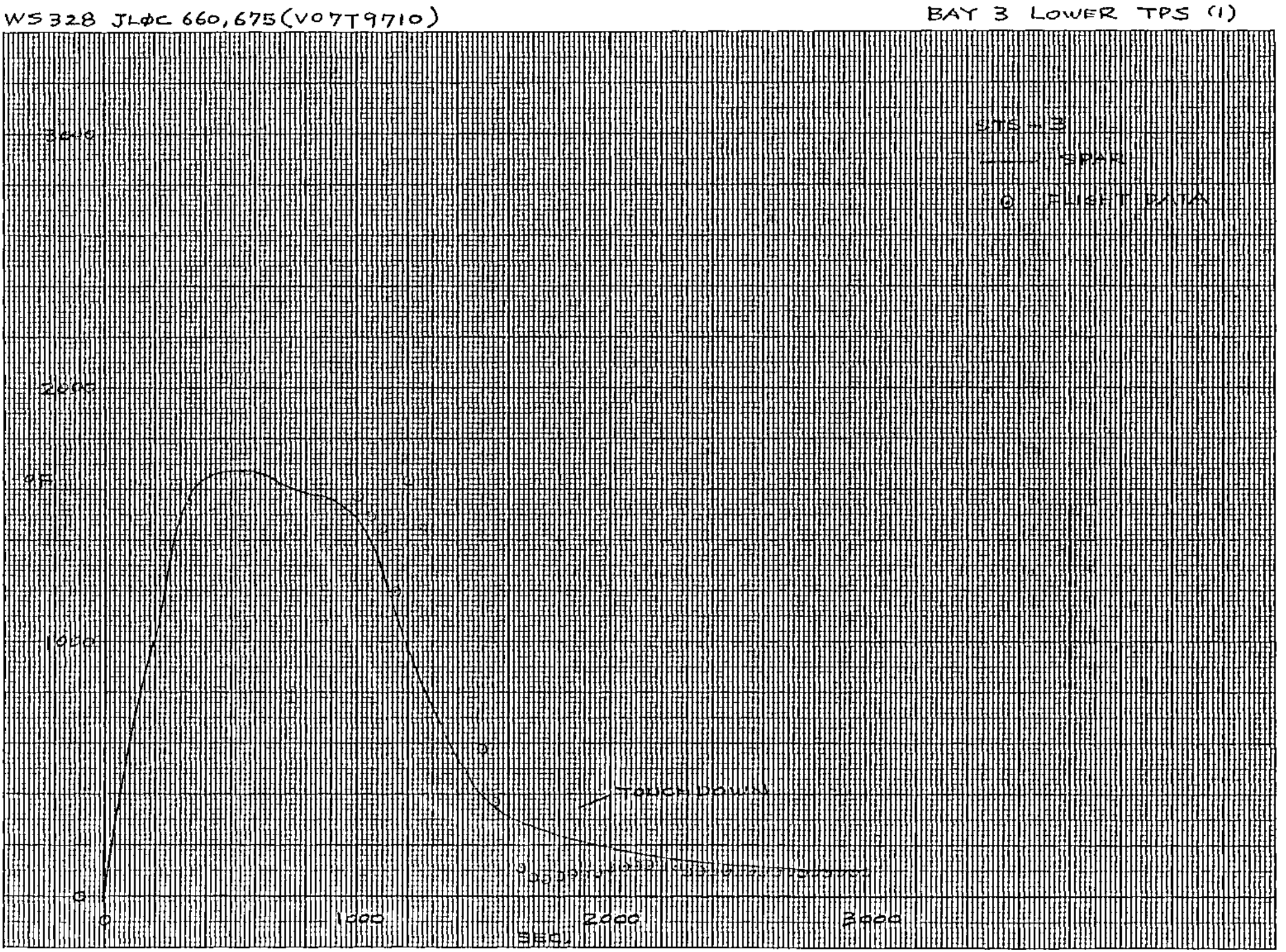

Figure 72 - TPS Surface Temperatures - WS 328

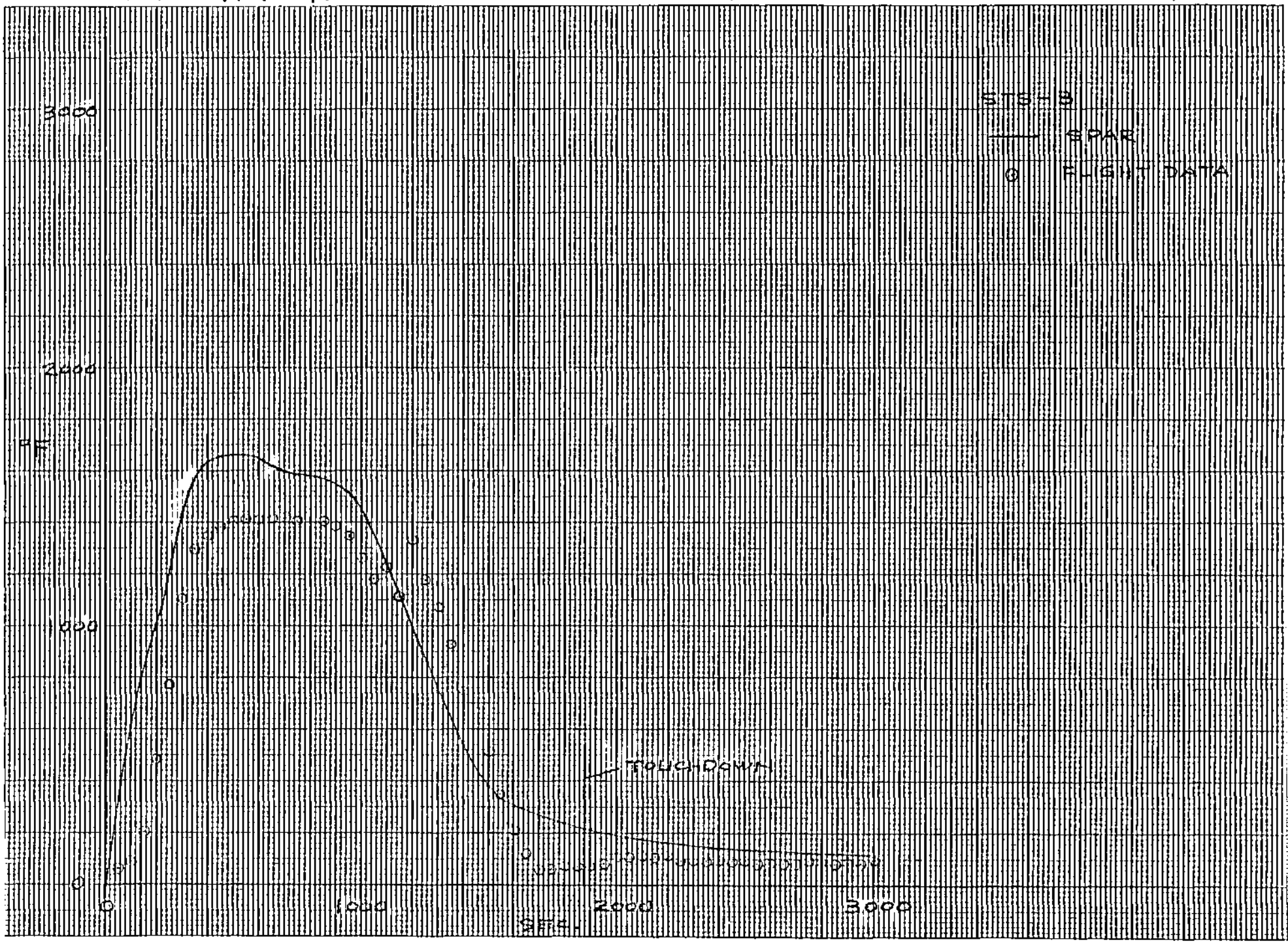

Figure 73 - TPS Surface Temperatures - WS 328

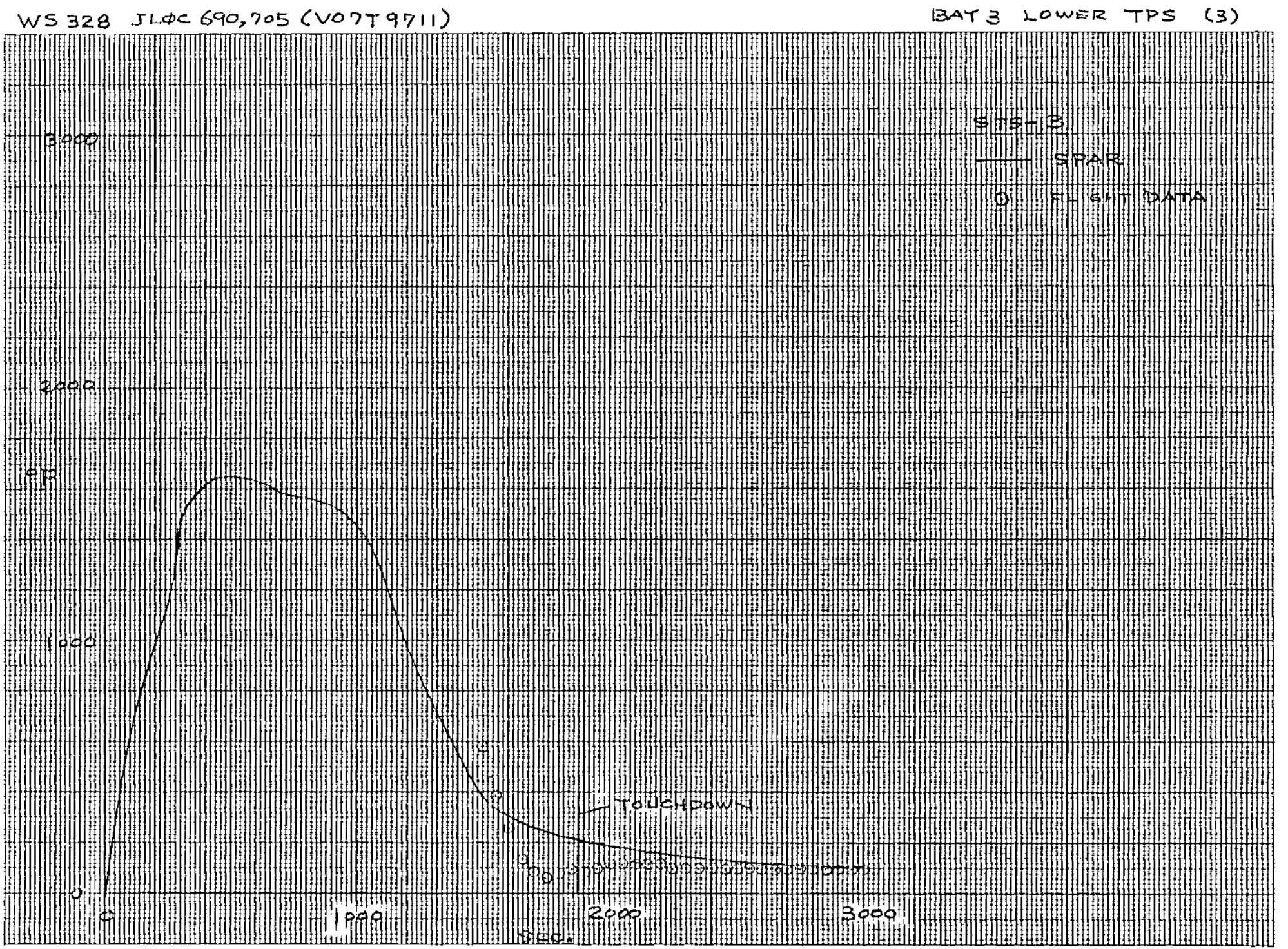

Figure 74 - TPS Surface Temperatures - WS 328

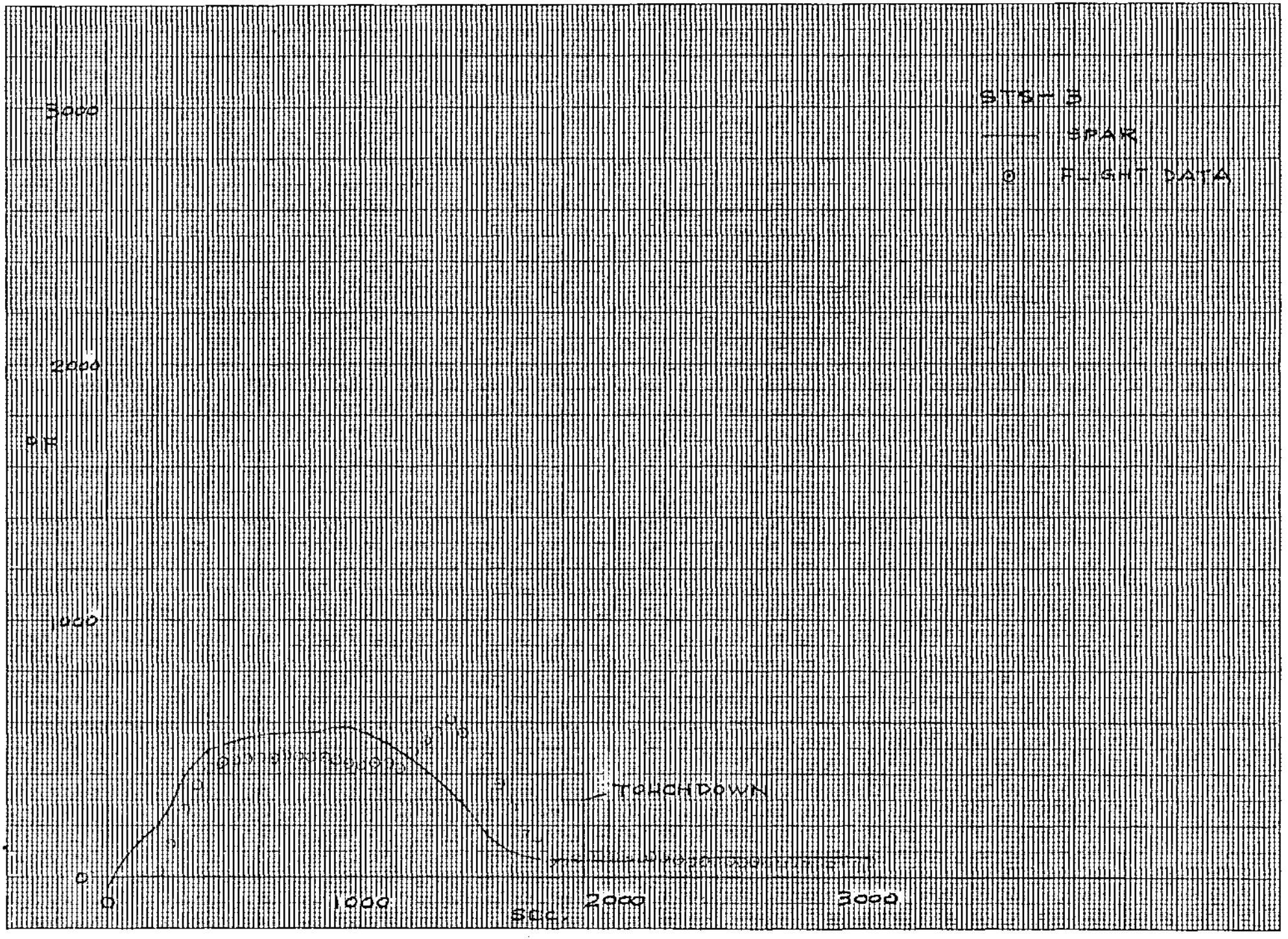

Figure 75 - TPS Surface Temperatures - WS 328

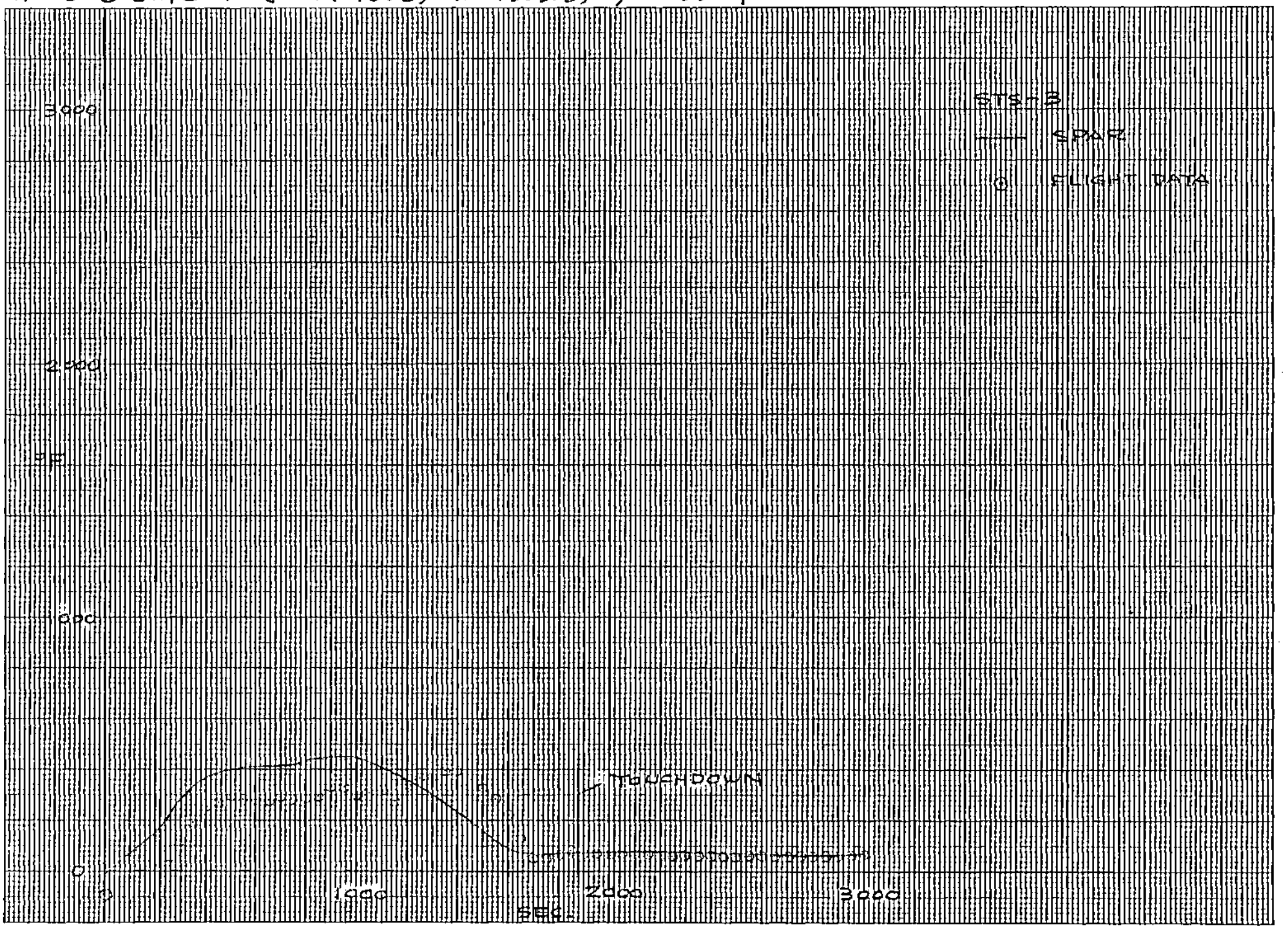

Figure 76 - TPS Surface Temperatures - WS 328

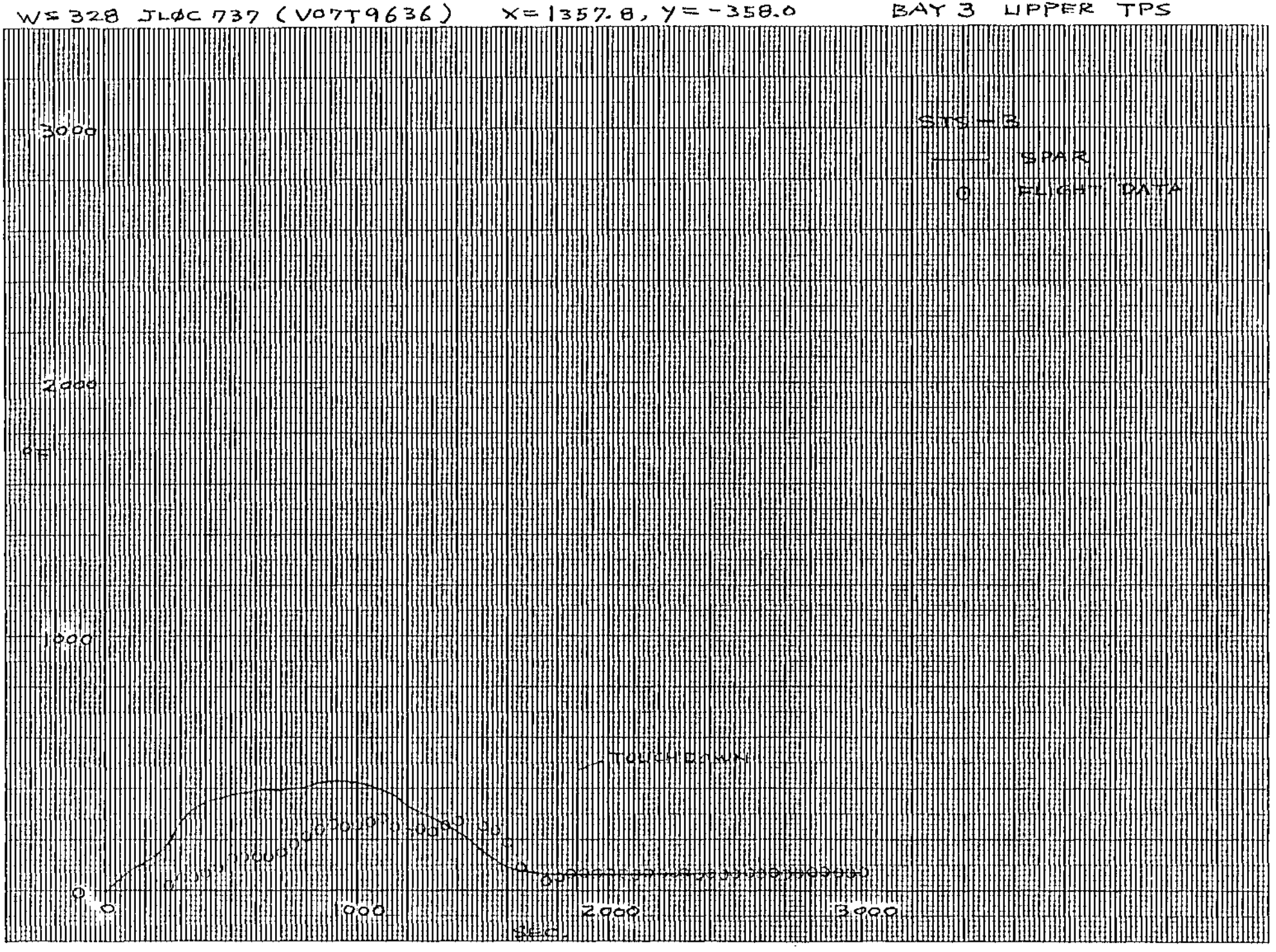

Figure 77 - TPS Surface Temperatures - WS 328

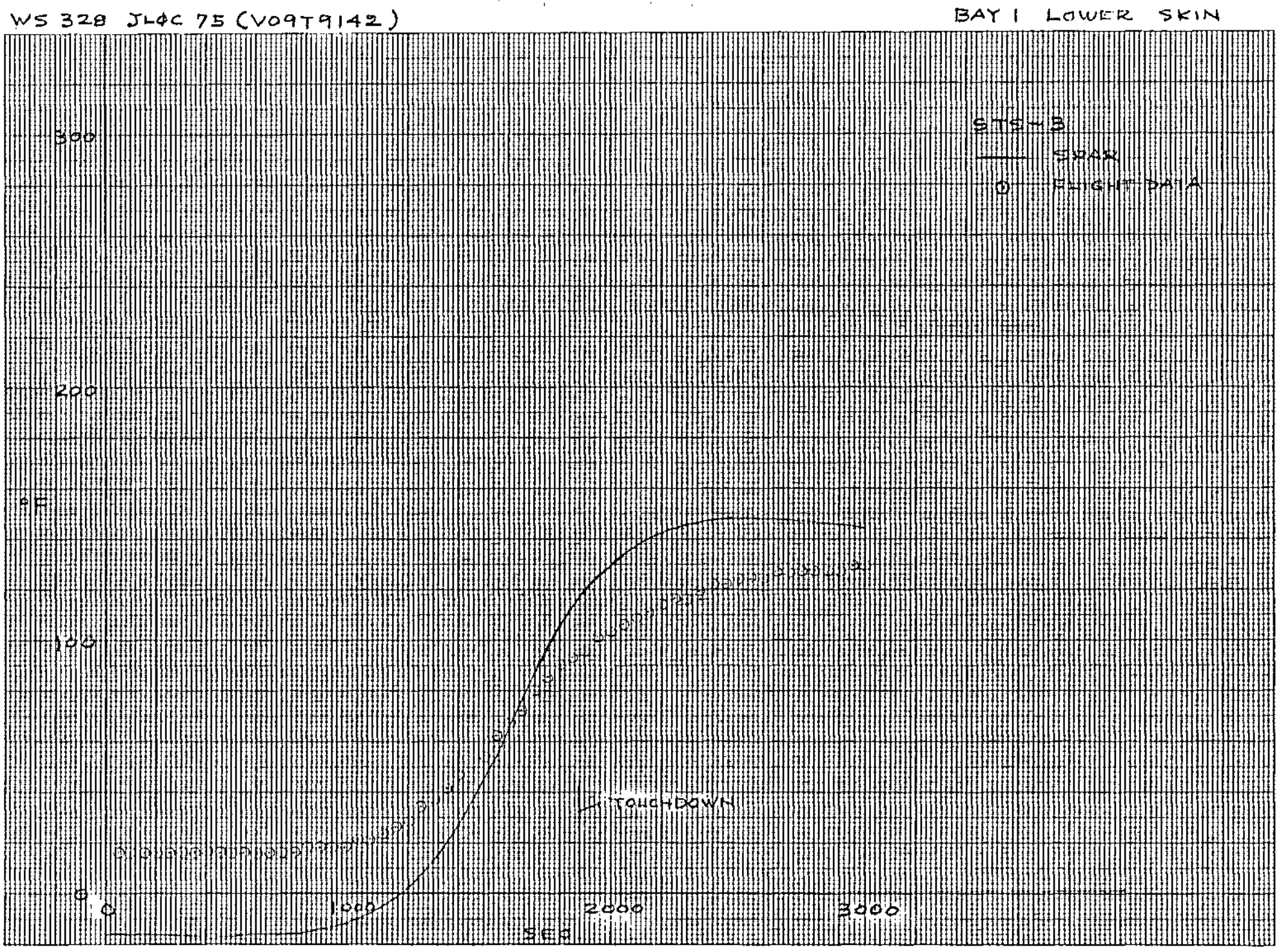

Figure 78 - Structural Temperatures - WS 328

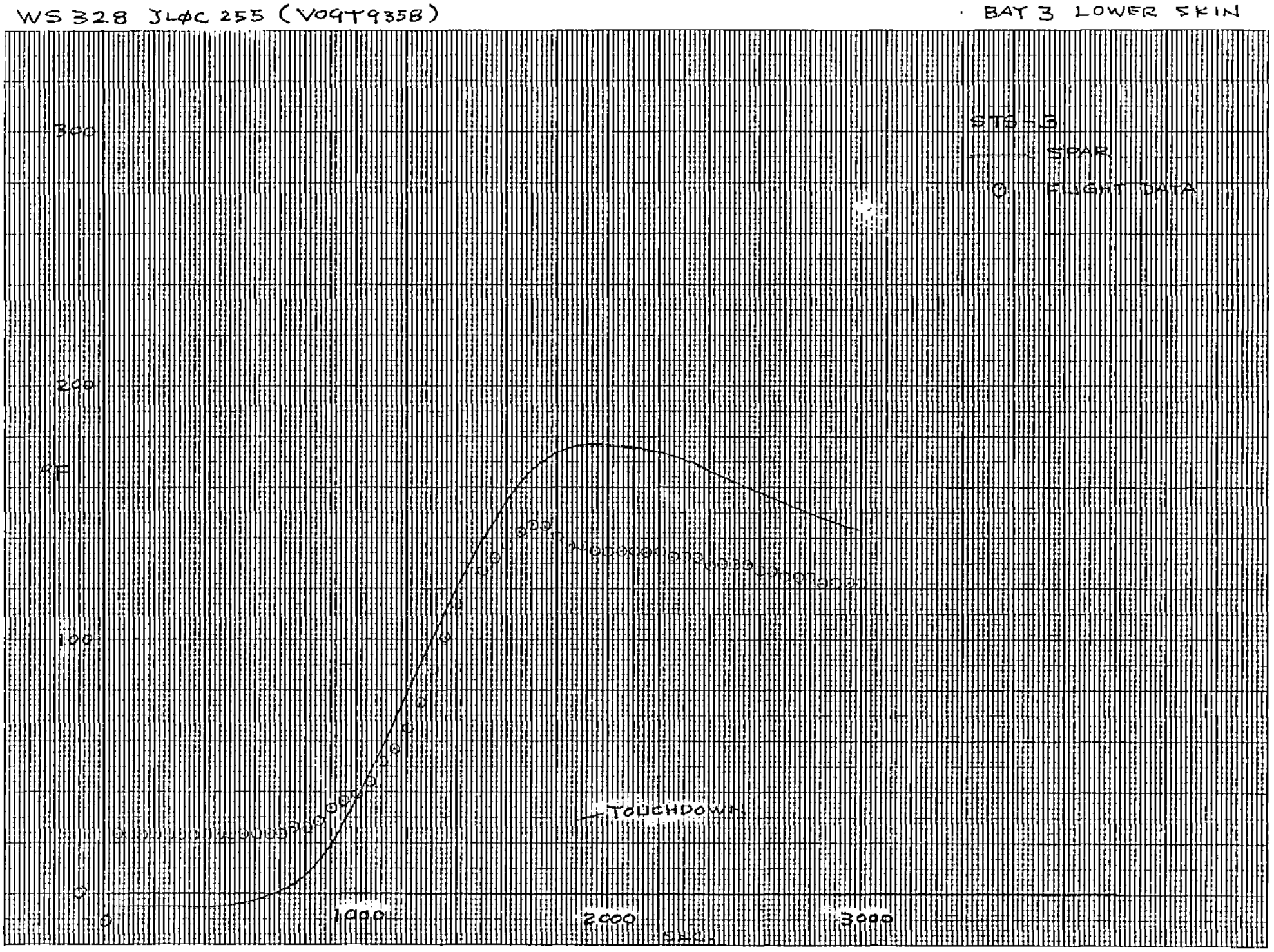

Figure 79 - Structural Temperatures - WS 328

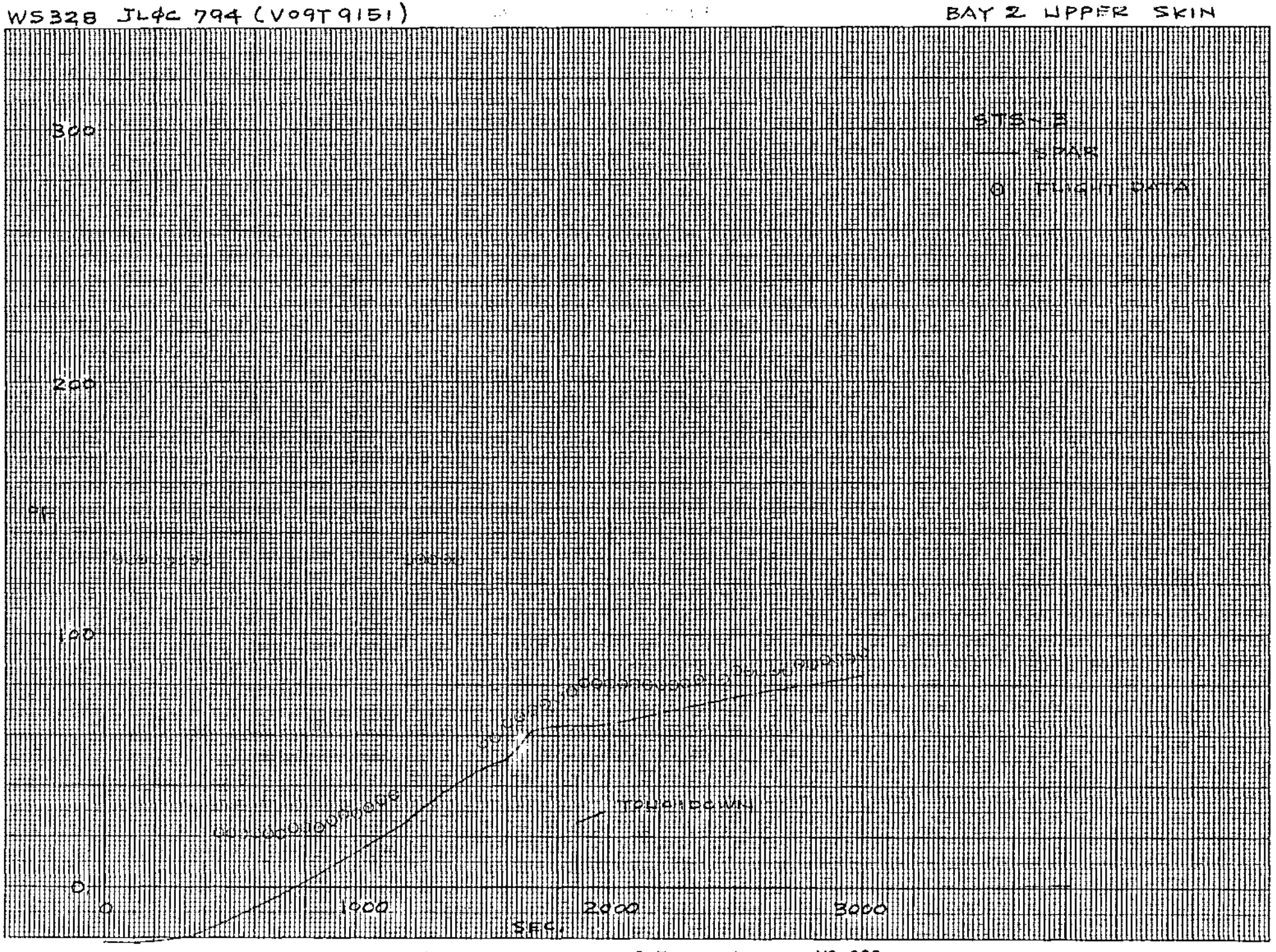

Figure 80 - Structural Temperatures - WS 328

Conclusions

There did not appear to be any indication of pilot induced oscillations during the approach and landing.

The handling qualities in the approach and landing do not appear adequate for satisfactory landings from an emergency takeover from the autoland system at low altitude.

Serious control difficulties were seen during nose wheel letdown due to the elevator rate limit.

The ACIP recorder package is vital to future estimation, but the ACIP instrumentation package needs to be periodically calibrated and aligned. In addition, the ACIP recorder should be moved to a different vibration environment to provide higher quality data.

Recommendation

It is therefore recommended that new locations be investigated for installation of the ACIP instrumentation package that would result in higher frequency noise contamination and also allow easier access for recalibration in between flights.

REFERENCES

1. Maine, Richard E.; and Iliff, Kenneth W.: User's Manual for MMLE3, A General FORTRAN Program for Maximum Likelihood Parameter Estimation. NASA TP-1563, 1980.
2. Iliff, Kenneth W.; Maine, Richard E., and Montgomery, T.D. Important Factors in the Maximum Likelihood Analysis of Flight Test Maneuvers. NASA TP-1459, 1979.
3. Iliff, Kenneth W.: Aircraft Identification Experience AGARD. LS-104, 1980.
4. Iliff, Kenneth W.; Maine, Richard E.; and Cooke, Douglas R.,
   Selected Stability and Control Derivatives from the First Space Shuttle Entry. AIAA Paper 81-2451, November, 1981.
5. Preliminary Analysis of STS-1 Entry Flight Data, NASA TM-81363, 1981.
6. Preliminary Analysis of STS-2 Entry Flight Data. NASA TM-81371, 1981.

1. Report No.	2. Government Accession No.	3. Recipient's Catalog No.
NASA TM-81373		

4. Title and Subtitle	5. Report Date
PRELIMINARY ANALYSIS OF STS-3 ENTRY FLIGHT DATA	August 1982
	6. Performing Organization Code: RTOP 989-10-00
7. Author(s)	8. Performing Organization Report No.
	10. Work Unit No.
9. Performing Organization Name and Address: NASA Ames Research Center, Dryden Flight Research Facility, P.O. Box 273, Edwards, California 93523	11. Contract or Grant No.
	13. Type of Report and Period Covered: Technical Memorandum
12. Sponsoring Agency Name and Address: National Aeronautics and Space Administration, Washington, D.C. 20546	14. Sponsoring Agency Code

15. Supplementary Notes

16. Abstract

Dryden has completed a preliminary analysis of the data obtained during entry of the STS-3 flight. Planned maneuvers were performed during this flight, as was done on STS-2, which significantly enhance the quality of the data for analysis.

On this flight, transfer of control from the auto system to the pilot was accomplished at approximately 200 feet before touchdown. The handling qualities of the orbiter in the approach and landing do not appear adequate for consistently satifactory landings from an emergency takeover from the autoland system at low altitudes. In addition, serious control difficulties were seen during nose wheel letdown due to the elevator rate limit.

The ACIP Recorder Package is vital to future estimation, but the ACIP Instrumentation Package needs to be periodically calibrated and aligned. The ACIP Recorder should be moved to a different vibration environment to provide higher quality data.

17. Key Words (Suggested by Author(s))	18. Distribution Statement
Orbiter Stability and control Performance Heating Derivative extraction	Unclassified - Unlimited Subject category 18

19. Security Classif. (of this report)	20. Security Classif. (of this page)	21. No. of Pages	22. Price*
Unclassified	Unclassified	149	A07

For sale by the National Technical Information Service, Springfield, VA 22161